A Muon and Neutron Study of Multiferroic Materials

Heather Joanne Lewtas
University of Oxford

A thesis submitted for the degree of
Doctor of Philosophy
at the
University of Oxford
Michaelmas Term 2010

A Muon and Neutron Study of Multiferroic Materials

Heather Joanne Lewtas
Linacre College, University of Oxford
Michaelmas Term 2010

Abstract of Thesis Submitted for the Degree of Doctor of Philosophy

In this thesis multiferroic materials are investigated through a number of different experimental techniques, particularly μ^+SR, neutron scattering and impedance spectroscopy. The magnetic and dielectric properties of materials, which form multiferroic states through different mechanisms, are explored. Inelastic neutron scattering studies have been made of $LuMnO_3$ and $LuFe_2O_4$. Large reciprocal space maps have been made of $LuFe_2O_4$ and an initial spin wave dispersion found. The exchange parameters have been estimated from the data and are shown to support ab initio calculations. The spin wave dispersion of $LuMnO_3$ has been mapped throughout the Brillouin zone and the exchange parameters extracted by comparison with a spin-wave model. Comparisons have then been made with other members of the hexagonal manganite family. The analysis is supported by thermal expansion and magnetization studies. The first experiment on a multiferroic combining the μ^+SR technique and applied electric fields was performed as a proof of principle experiment on $HoMnO_3$. The effect of the electric field on the magnetism has been detected and calculations performed to try and identify muon stopping sites. The family of rare earth chromites have been studied through magnetization and heat capacity experiments as well as μ^+SR. The varying entropy and energy level splitting within the family is examined and the debate as to whether they are multiferroic is addressed. An instrument to study dielectric properties at cryogenic temperatures through impedance spectroscopy was designed and constructed. Multiferroics investigated in this thesis using neutron scattering and μ^+SR were then studied with this apparatus to look for coupling between magnetic and ferroelectric order parameters. A dielectric anomaly associated with the magnetic transition temperature was observed in $LuFe_2O_4$ which is evidence of the coupling between the order parameters.

For my Family.

Acknowledgements

I am greatly indebted to the following people and I wish to thank them:

- Stephen Blundell and Andrew Boothroyd, for their help, advice and guidance. Whenever anyone said "You're lucky to have them as supervisors" I could honestly say "yes I am".
- Moon-Sun Nam, Arzhang Ardavan and Paul Goddard for help and advice when it came to cryostats and instrument design and Robert Story and Tony Hickman for helping me when things went wrong.
- Tom Lancaster and Francis Pratt for their help on μSR experiments and their expertise analysing results. Peter Baker for his help with characterization, μSR, Latex and many other things.
- Martin Rotter for neutron and calculation expertise and collaborations. B. Roessli, J. Kulda, J. Gavilano and P. Bourges for technical assistance and advice while performing neutron experiments. Stew Bland and Roger Johnson for their resonant X-ray expertise.
- Prabhakaran Dharmalingam, B. M. Wanklyn, Peter Clack and Fred Wondre for making, aligning and cutting crystals. H. Müller for collaborations on thermal expansion measurements and David Walker for collaborations on high temperature dielectric measurements.
- Graeme Johnstone , Andrew Steele, Alice Taylor, Rhiannon Jones, Isabel Franke, Peter Babkevich, Lucian Pascut and Jack Wright for making working here fun and Bill Hayes for many papers and tea time conversations.

Thank you to my whole family and to Adam for everything and my friends Rachel and Dragana with whom I have had so much fun and who are always at the end of the phone.

Contents

List of Figures

Chapter 1

Introduction to Multiferroic Systems

Contents

1.1 Introduction

Multiferroic materials have experienced a resurgence of interest in recent years following the discovery in 2003/4 of compounds that display large cross-coupling effects between magnetic and ferroelectric order parameters [1, 2, 3]. Particular interest has been aroused by the possibility of new magnetoelectric coupling mechanisms [4, 5, 6] and the potential for exploitation in technological applications [7, 8, 9]. The objective of this thesis was to undertake measurements to characterize the magnetic and dielectric properties of multiferroic materials and provide insight into these coupling mechanisms. In this chapter I present an overview of the phenomenology of multiferroic materials, the types of magnetic and ferroelectric order that are found, and the possible ways in which they are coupled.

1.2 Magnetic Ordering

The magnetic properties of materials are a consequence of some atoms and ions behaving as elementary magnetic dipoles under certain circumstances with their relative orientation influenced by external magnetic fields. In a diamagnetic material an applied magnetic field induces a magnetic moment in the substance that opposes the applied field. However in paramagnetic materials the applied field induces a magnetic moment that aligns parallel to the field.

The magnetic moment of an ion comes from the electrons in unfilled electronic shells. The spin, $\boldsymbol{s}_i$, and orbital angular momentum, $\boldsymbol{l}_i$, of the individual electrons combine to give the total spin, $\boldsymbol{S} = \sum_i \boldsymbol{s}_i$, and total orbital angular momentum $\boldsymbol{L} = \sum_i \boldsymbol{l}_i$. Due to spherical symmetry, over full shells, these sum to zero so only unfilled shells contribute. The resultant spin and orbital angular momenta are coupled by the spin-orbit interaction to give the total angular momentum, $\boldsymbol{J}$.

In systems where the energy of the Coulomb repulsion is greater than that from the spin-orbit interactions Hund's rules can be used to find the angular momentum quantum numbers of the most energetically favourable state, the ground state in a magnetic material. The rules state that S and L must be maximised to minimise the Coulombic repulsion between the electrons [10]. The effective magnetic moment can be calculated from the spin-orbit interaction as

$$\mu_{\text{eff}} = g_J \mu_B \sqrt{J(J+1)}, \tag{1.1}$$

where μ_{eff} is the Bohr magneton and g_J is the Landé g-value given as

$$g_J = \frac{3}{2} + \frac{S(S+1) - L(L+1)}{2J(J+1)}. \tag{1.2}$$

However when the magnetic ion is considered not as a free ion but to sit in a local environment created by the electric fields of the surrounding ions other effects must be taken into account.

1.2.1 Environment

To understand the magnetic properties of transition metal ions in solids it is necessary to take into account the effect that the surrounding atoms in the material have on the energy of an atom. In crystal field theory the surrounding atoms are replaced by negative point electric charges and bonding between the atoms and the transition metal ions is ignored. The interaction between the metal and the ligand is electrostatic only. The differing angular dependencies of the electron density of s, p and d orbitals means that they are affected differently by the local environment. A common case is an octahedral environment of ligands around a central metal ion. s orbitals have spherical symmetry, their energy is raised because of the increased repulsion between the electrons in the orbital and the negative ligand point charges but it is raised equally because of the symmetry and the orbitals remain degenerate. Similarly p orbitals lie along the axes pointing directly at the point charges so they all have the same degree of interaction. d orbitals however fall into two categories; t_{2g} levels that point between the axes (orbitals d_{xy}, d_{xz} and d_{yz}) and e_g levels that point along the axes (orbitals d_{z^2} and $d_{x^2-y^2}$). Figure 1.1 shows that d_{xy} orbitals have a lower overlap with p orbitals from the neighbouring ligands and will therefore have a lower electrostatic energy. This means that the d orbitals will not be degenerate. Other local environment symmetries may effect the crystal field in other ways, for example in a tetrahedral environment orbitals along the axes will be further away from the charge density of atoms on four corners of a cube than orbitals between the axes.

1.2.2 Exchange Interactions

Exchange interactions are important to understand when considering the phenomena of long range ordering and the interaction of magnetic ions. These interaction terms are due to Coulomb interactions produced when electron wavefunctions overlap in a

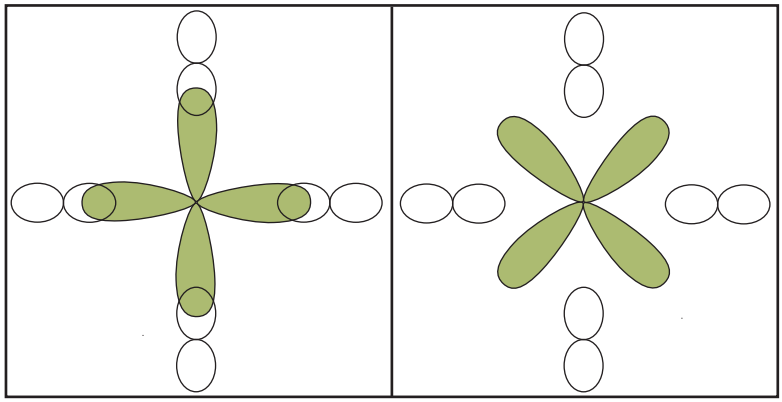

Figure 1.1: Left panel shows the overlap of the $d_{x^2-y^2}$ orbitals (green) with the oxygen p orbitals (white) in an octahedral environment. Right panel shows the overlap of the magnetic d_{xy} orbitals (green) with the oxygen p orbitals (white) in an octahedral environment.

material [10]. The Heisenberg Hamiltonian for the exchange interaction terms is given by

$$\mathcal{H} = -\sum_{ij} J_{ij} S_i \cdot S_j \tag{1.3}$$

which is a sum over all pairs of spins i and j where J_{ij} is the exchange constant between the i^{th} and j^{th} spins. The magnetic order can be seen clearly in the sign of J_{ij}:
$J < 0$ antiferromagnetic alignment,
$J > 0$ ferromagnetic alignment.

In a ferromagnet the spins are aligned parallel with a resultant net magnetic moment. In an antiferromagnet the spins are antiparallel and so the moments cancel. There are different ways of constructing this order as shown in Figure 1.2. A ferrimagnet is similar to an antiferromagnet in that the spins oppose each other yet the opposing moments are unequal so there is a spontaneous magnetization. Many more complex magnetic structures can arise such as helical order where the ordering propagates along a particular direction with each spin being rotated by a fixed angle relative to its neighbours. Magnetic order can be commensurate, where the period of the order is equal to an integer number of lattice units, or incommensurate where this is not the case.

The different forms of exchange which influence the ordering are explained as fol-

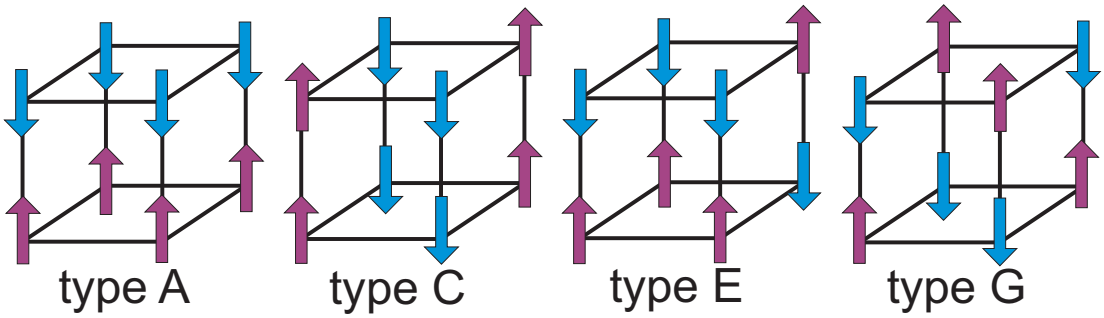

Figure 1.2: Four types of antiferromagnetic order shown here on a simple cubic lattice.

lows:

Direct Exchange — When the electrons on neighbouring magnetic atoms interact with no intermediary. Often this is not the important mechanism in a system as there is insufficient direct overlap of the electron shells of the neighbouring ions.

Superexchange — This is an indirect exchange between two non-neighbouring magnetic ions which is mediated by a non-magnetic ion, often oxygen. Figure 1.3 illustrates the principle with two transition metal ions separated by an oxygen ion. Assuming that the moment on the transition metals ions is due to a single unpaired electron in a d orbital and the oxygen has two p electrons it can be seen that antiferromagnetic coupling is favoured as it lowers the energy of the system by favouring electron hopping and allowing the electrons to become delocalized over the whole structure.

RKKY Interaction — Exchange interactions between magnetic ions in metals can be mediated by conduction electrons. A local moment spin polarizes the conduction electrons which then couple to a neighbouring local moment. This is an indirect exchange and is also known as itinerant exchange. This can be important in muon interactions, Section 2.2.4.

Double Exchange — Ferromagnetic exchange interactions are favoured as the magnetic ions can show mixed valency allowing the electrons to hop into a vacancy without having to change spin direction. Electrons in lower lying orbitals of the magnetic ions will have parallel spins in both valencies so any higher energy hopping electron needs to have its spin aligned with the lower level electrons both of where it

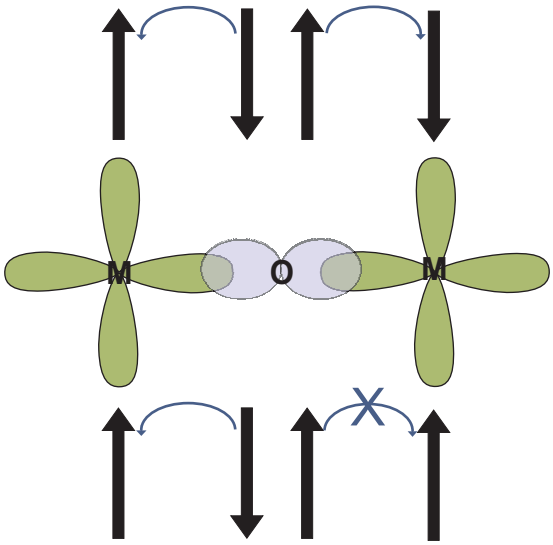

Figure 1.3: Superexchange interaction showing the favouring of antiferromagnetic order.

hopped from, and to. To minimise the kinetic energy the ions must then be ferromagnetically coupled.

Dzyaloshinskii-Moriya Interaction — Also known as the anisotropic exchange interaction, the spin-orbit interaction takes on the role of mediator of the exchange. This interaction favours non-collinear spin ordering. The Hamiltonian is written as

$$\hat{\mathcal{H}}_{DM} = \mathbf{D} \cdot \mathbf{S}_1 \times \mathbf{S}_2 \tag{1.4}$$

where vector **D** vanishes if the crystal field has an inversion symmetry at the mid point of the vector joining the two spins, $\mathbf{r}_{1,2}$, Figure 1.4. It is proportional to $\mathbf{x} \times \mathbf{r}_{1,2}$ where $\mathbf{r}_{1,2}$ is the vector connecting the magnetic ions and **x** is the displacement of the oxygen from this line. The energy of the interaction increases with **x**, the degree of inversion symmetry breaking [6]. The interaction forces the spins to preferentially lie at right angles to each other in a plane perpendicular to **D**. The effect of this is often to cant the spins at a small angle. When this occurs in antiferromagnets it can result in a small ferromagnetic moment in a direction perpendicular to the antiferromagnetic alignment, canted antiferromagnetism.

1.2.3 Frustration

Frustration occurs when the geometry of the crystal lattice or conflicting forces mean the system is unable to minimise all the interaction energies simultaneously. In mag-

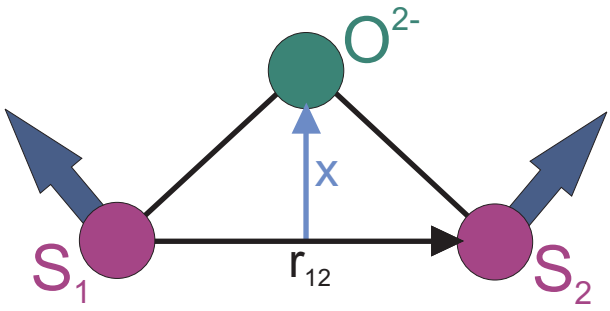

Figure 1.4: Dzyaloshinskii-Moriya interaction where $\mathbf{r}_{1,2}$ is the vector connecting the magnetic ions and **x** is the displacement of the oxygen from this line.

netism the conflict arises as neighbouring spins wish to be aligned antiparallel. Geometric magnetic frustration is frustration that arises from the geometry of the lattice as shown in Figure 1.5. Antiferromagnetic nearest neighbour interactions on a triangular lattice are frustrated as all three bonds cannot be satisfied simultaneously. The system will exist in multiple equally unsatisfied states.

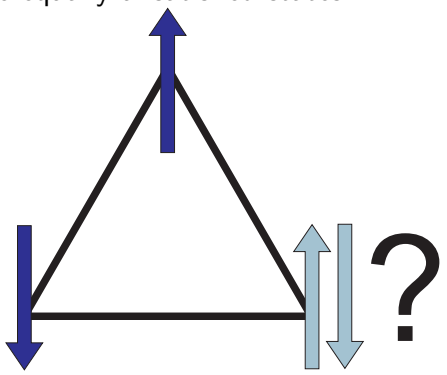

Figure 1.5: Frustration on a triangular lattice.

Frustration plays an important role in most chapters of this thesis. The hexagonal manganites, Chapters 4 and 5, need to relieve their spin frustration by forming 120° spin structures and trimerizing. $LuFe_2O_4$, Chapter 7, shows both charge and spin frustration influencing many of its properties. In the rare earth chromites, Chapter 6, the entropy signatures show signs of frustration which provides further insight into the systems.

1.2.4 Excitations

Order in a crystal can be disrupted by excitations. An ordered array of atoms in a crystal lattice can be disrupted by a thermally excited lattice vibration. The quantization of this lattice vibration is called a phonon and its behaviour can be described by a

dispersion relation. A dispersion relation defines the relationship between the angular frequency, ω, and the wave vector, q (or between the energy, $\hbar\omega$, and momentum, $\hbar q$).

Spin Wave Excitations

A magnetic system can be perfectly ordered at absolute zero but above this temperature the order can be disrupted by excitations called spin waves which are quantized as magnons. A spin wave can be conceptualized as single spins flipped from their ground state order which then propagate through the system. As with phonons this can be described by a dispersion relation and can be used to find out about the exchange interactions in the material. This analysis is seen in Chapters 4 and 7.

As an example the ground state of the system can be said to consist of all the spins lying along the $+z$ direction. In 1D the Heisenberg Hamiltonian, equation 1.3, can be written as

$$\mathcal{H} = -J\sum_i [S_i^z S_{i+1}^z + (S_i^+ S_{i+1}^- + S_i^- S_{i+1}^+)], \tag{1.5}$$

where the exchange J will be negative for a ferromagnetic system and S_i is the spin operator acting on site i. S_i^- and S_i^+ are the annihilation and creation operators that destroy or create a flipped spin on site i. The ground state with all spins fully aligned is defined such that $\mathcal{H}|0\rangle = E_0|0\rangle$ where $E_0 = NS^2J$ and N is the number of spins in the chain. The excitation is created by flipping a spin j to produce the excited state $|j\rangle = S_j^-|0\rangle$, Figure 1.6. The Hamiltonian can then be applied to this excited state giving:

$$\mathcal{H}|j\rangle = (-NS^2J + 2SJ)|j\rangle - SJ|j+1\rangle - SJ|j-1\rangle. \tag{1.6}$$

If the Fourier transform $|q\rangle = \sum_j \exp(iqr_j)|j\rangle$ is then introduced where r_j is the position of spin j the result is

$$\mathcal{H}|q\rangle = (-NS^2J + 2JS(1-\cos(qa)))|q\rangle \tag{1.7}$$

where a is the spacing between the spins in the chain. The energy of the excitation can then be given in the dispersion relation $\hbar\omega = 2JS(1-\cos(qa))$. From this it can be seen that when data is fit to the dispersion relation the value of J can be extracted.

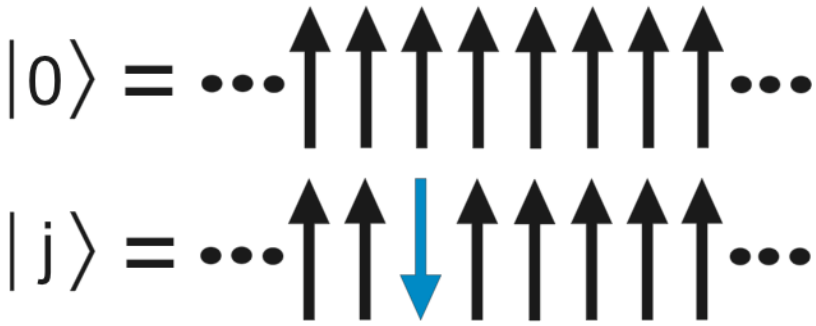

Figure 1.6: Spin wave excitations showing the ground state and the excited state.

1.3 Ferroelectricity

A ferroelectric is an insulating system with two or more states of non-zero electric polarization in zero applied field, referred to as spontaneous polarization [11]. To be ferroelectric it must be possible to switch between the states of polarization using an applied electric field through the coupling of the field to the polarization. The observation of polarization-electric field (P-E) hysteresis loops is considered necessary to establish whether a material is ferroelectric. These measurements allow the switching of the direction of spontaneous polarization by an applied electric field to be observed.

To exhibit spontaneous polarization a system must have a non-centrosymmetric arrangement of ions. The presence of ferroelectricity is determined by the balance between short range repulsions that favour symmetric structures and long range Coulomb forces that favour the ferroelectric state. The short range repulsions between adjacent electron clouds need to be countered by bonding that stabilises shifts in ion arrangements. At high temperatures the short range repulsions dominate resulting in an unpolarized state. However when the temperature decreases the stabilizing forces become stronger than the repulsions and the non-centrosymmetric, ferroelectric state becomes stable. This local off-centring of ions can form long range cooperative ordering yielding a net polarization through the dipole-dipole interaction [11]. Sometimes competing effects overcome this interaction and the dipoles cancel each other out so there is no net polarization, this state is known as antiferroelectric.

While ferroelectricity was observed earlier in hydrogen bonded materials such as Rochelle salt it was the 1949 discovery of ferroelectricity in the relatively simple structure of the perovskite oxide $BaTiO_3$ that allowed the phenomena to be more fully understood. It has been found in these perovskite structures that the hybridization

of the transition metal $3d$ and oxygen $2p$ orbitals is essential for stabilizing the ferroelectric distortion [12]. In this mechanism charge moves from filled $2p$ orbitals to d states of the transition metal ions which must be empty for this mechanism to occur. The necessity of empty d orbitals could be for a variety of reasons. However, as will be described in the rest of this chapter there are ways for a system to stabilize ferroelectricity even when the d^0 requirement is not fulfilled.

Although not definitive indicators of ferroelectricity other electrical measurements are often made to investigate properties. Pyroelectricity, the generation of a transient voltage when a material is heated or cooled, is required but is not sufficient for ferroelectricity. These measurements are often made because coupling of magnetic and ferroelectric order parameters have been seen as anomalies in the pyroelectric signals at magnetic ordering transition temperatures. Dielectric measurements are also often utilised for the same reason and are described further in Chapter 3.

1.4 Domains and Domain Walls

Magnetic and ferroelectric domains and domain walls play a significant role in material properties especially of those materials investigated in this thesis. Domains are regions of the material with different orientations of the magnetic or ferroelectric order. An applied magnetic or electric field can then cause the domains to align. Domain walls are the interfaces separating the regions [13].

Domains form to minimise the total energy of the material, for example in a magnetic material a single ferromagnetic domain would minimise the exchange energy but it would maximise the magnetostatic energy, or the electrostatic energy for a single ferroelectric domain. There are many factors that influence the size and shape of domains. Magnetic domain walls are typically a few hundred Ångströms thick in contrast to ferroelectric domain walls which are only a few lattice constants thick.

1.5 Multiferroics

Multiferroic materials exhibit two or more ferroic properties in the same phase. The properties are ferroelectricity, ferromagnetism and ferroelasticity, although in practice ferroelasticity is often excluded and ferrotoroidic order included [14, 15]. Ferroelastic materials exhibit a spontaneous stable deformation in response to an applied stress and can be switched hysteretically. In ferrotoroidic materials the order parameter is the

curl of the magnetization or polarization. In most cases the term *multiferroic* is used to describe a system with magnetic and ferroelectric order as is the case in the materials investigated in this thesis. The classification has also been broadened to include antiferroic orders. There are 31 point groups that allow spontaneous polarization and 31 that allow spontaneous magnetization, there are 13 point groups that are to be found in both sets. Multiferroic materials are uncommon and many of their characteristics are not well understood.

The symmetry requirements for the different order parameters are shown in Table 1.1 which displays the same information as is clarified in Figure 1.7. In a ferromagnetic material spatial inversion results in no change to the magnetic moment however, under time reversal the orbit and therefore the magnetic moment will switch. In a ferroelectric material, represented as a positive point charge that lies asymmetrically in a crystal unit cell, time reversal has no effect, Figure 1.7. However under spatial inversion the polarization is reversed. A multiferroic therefore needs to exhibit a lack of both time and spatial inversion symmetries.

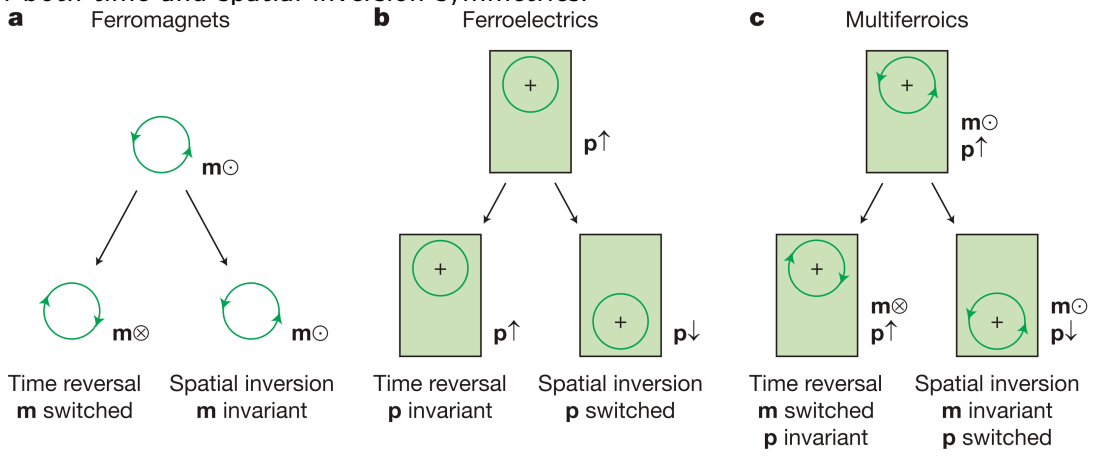

Figure 1.7: Spatial and time inversion symmetry in multiferroics [9]. a) a magnetic moment depicted as a charge tracing an orbit experiences no change under spatial inversion however time invariance reverses the orbit and therefore the moment direction. b) a ferroelectric is depicted as a positive point charge in a unit cell. Time invariance has no effect however spatial inversion reverses the polarization direction. c) a multiferroic breaks both spatial and time inversion symmetry.

The origin of magnetism is basically the same in all insulating magnetic materials, the existence of localized electrons in partially filled d or f shells of transition metal or rare earth ions, which have a corresponding magnetic moment. However the absence of d electrons is an advantage for ferroelectricity [16]. Most ferroelectrics are transition

metal oxides where the non-centrosymmetry arises from the shifting of cations and anions inside the crystal as the positive transition metal ions like to form 'molecules' with the negative oxygen ions [6]. These movements are stabilised by the formation of covalent bonds from the hopping of electrons from filled oxygen shells to empty transition metal d shells. This mutual exclusion means that alternate ways of uniting ferroelectricity and magnetism are needed and there are many different mechanisms that try to fill this gap.

Why the presence of d electrons suppresses the tendency for a distortion removing the centre of symmetry is not well understood although there have been many attempts at clarification [17, 18]. One suggestion is the possibility that transition metal ions with occupied d shells are too large to be displaced from the centre of an oxygen octahedra as commonly found in ferroelectric perovskites however there is not a systematic correlation when the size of the ions is investigated so this is probably not the deciding factor [17]. There is no full solution to the problem and it may be that it is just a matter of the magnetic ion being stable at the centre of its octahedra. It is possible that materials will be found where this is not the case.

Table 1.1: Spatial Inversion and Time Inversion Symmetry

	Spatial Inversion?	Time Inversion?
Ferroelastic	Yes	Yes
Ferroelectric	No	Yes
Ferromagnetic	Yes	No
Multiferroic	No	No

The alternative possibilities for uniting ferroelectricity and magnetism in multiferroics can be grouped in various ways according to different characteristics. They can be grouped into proper and improper ferroelectrics. Proper ferroelectrics have a structural instability towards the polar state, associated with the electronic pairing that is the main force behind the transition [6]. Improper ferroelectrics result when the polarization is a product of a more complex lattice distortion or when it appears as an accidental product of other ordering.

They can also be grouped into type-I and type-II multiferroics. Type-I multiferroics are those in which the ferroelectricity and magnetism have different sources. In this

case the order parameters are largely independent of each other although there is usually some coupling between them. They are often good ferroelectrics and the onset temperatures of the magnetic and ferroelectric transitions can be well above room temperature. Type-II multiferroics are those in which the magnetism causes the ferroelectricity, this implies that there will be a strong coupling between the two. The polarization in these materials however is often much smaller than in type-I materials.

1.5.1 Type-I Multiferroics

There are many different mechanisms in the type-I subclass but the main ones are described below.

Electronic Lone Pair creates charge Asymmetry

Steriochemically active $6s^2$ lone pairs, also called dangling bonds, have a high polarizability and are the source of the ferroelectricity in this mechanism. Ions such as Tl^{1+}, Pb^{2+} and Bi^{3+} have $6s^2$ lone pairs. The electron criteria here is for p^0 instead of d^0 which occurs in the Bismuth lone pair. The pair of s electrons in the valence shell (the lone pair) should have spherical symmetry if they retain purely s character. However the active $6s^2$ lone pair causes the empty Bi $6p$ orbital to become closer in energy to the oxygen $2p$ orbital. A hybridization between the two p orbitals then occurs and this leads to the cation, Bi in this case, being displaced within its oxygen surroundings towards the anion and the ferroelectric criteria of non-centrosymmetry occurring [19]. This mechanism is reported most often in materials $BiFeO_3$ and $BiMnO_3$ (ABO_3). The magnetism comes from the partially filled d shells of the B ion, Mn or Fe in the examples.

Ferroelectricity due to Charge Ordering

The ferroelectric mechanism for this multiferroic is 'electronic ferroelectricity' which occurs in the situation where the electric dipole depends on the electron correlations instead of the covalent bonding between anions and cations to stabilize the dipolar arrangement [20]. The general mechanism through which the electron correlations or charge order can induce ferroelectricity can be thought of as the mixture of site-centered and bond-centered charge ordering, Figure 1.8. Ferroelectricity arises when both types of charge order occur simultaneously. The sites are inequivalent in valency and the bonds become inequivalent with the strong and weak ones alternating. This

mechanism allows for the possibility that a material could be controlled by the charge, spin and orbital degrees of freedom of the electron.

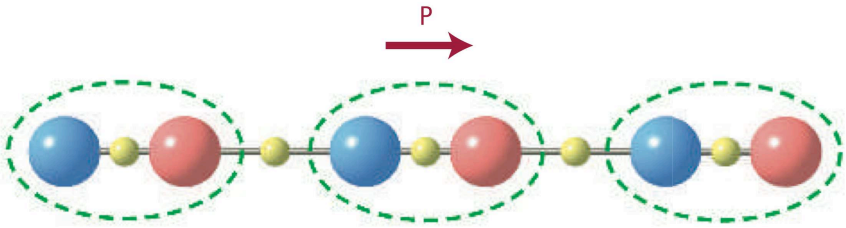

Figure 1.8: The multiferroic mechanism from charge ordering is shown [6]. The sites are inequivalent as the charges differ (red/blue spheres correspond to cations with more/less positive charge) and the bonds alternate between long and short. The ions with the shorter bonds are shown circled in green. The polarization direction is indicated by the red arrow.

Type-I ferroelectricity due to charge ordering occurs in several different classes of material such as perovskites of the type $Pr_{1-x}Ca_xMnO_3$, magnetite Fe_3O_4 and $LuFe_2O_4$. The specific mechanism behind the multiferroic behaviour of charge ordered $LuFe_2O_4$ is fully described in Chapter 7.

Geometric Ferroelectricity

Geometric ferroelectrics are improper ferroelectrics that exhibit frustration and undergo a lattice distortion, the main example is the hexagonal manganite family, $RMnO_3$ [21]. In the hexagonal manganites this lattice distortion is a buckling of the R-O planes and tilting of the manganese oxygen bipyramids [22]. Figure 1.9 shows the lattice distortion and resultant dipoles as green arrows. There are two dipoles in one direction for every one opposing them so the system gains a polarization and is a ferroelectric system. This mechanism is explained in more detail in Chapters 4 and 5 as it is exhibited by both $LuMnO_3$ and $HoMnO_3$.

1.5.2 Type II Multiferroics

Type II multiferroics are a more recent discovery, in these materials the magnetism causes the ferroelectricity which implies there is a strong coupling between them. The discovery of type-II systems was made in $TbMnO_3$ [1] and $TbMn_2O_5$ [2]. Broadly this classification can be grouped into materials with spiral or collinear magnetic ordering.

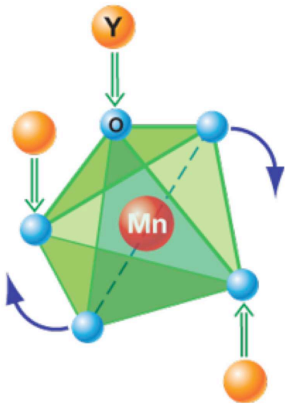

Figure 1.9: The multiferroic mechanism in hexagonal $YMnO_3$ showing the movement of the rare earth, Y, and the tilting of the MnO_5 block [23]. The Mn ion remains at the centre. The green arrows show the dipoles.

Spiral magnetic orders

In this class of multiferroics ferroelectricity occurs in the spiral magnetic phase of materials such as $TbMnO_3$, $Ni_3V_2O_6$ and $MnWO_4$. The spiral magnetism is caused by the magnetic frustration of the system. While a material with a sinusoidal spin density wave remains centrosymmetric spiral magnetism breaks spatial and time inversion symmetry, Figure 1.10, allowing an electric polarization.

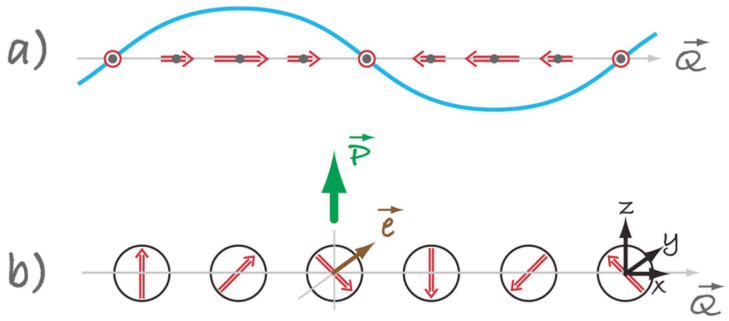

Figure 1.10: Spiral magnetic order as a mechanism for ferroelectricity [23]. a) Shows a sinusoidal spin density wave with the spins pointing along a single direction although they vary in magnitude, this is centrosymmetric. b) Cycloidal spiral ordering showing the wave vector of the spiral, **Q**, and the spins rotating in the xz plane with spin rotation axis, **e**. The resultant polarization direction is shown by the green arrow.

The exchange striction, where the ions move to satisfy the energy considerations

of the exchange interactions, in this case is associated with the Dzyaloshinskii-Moriya interaction, the anti-symmetric part of the exchange coupling. Ferroelectricity appears when the wave vector of the spiral, **Q**, does not coincide with the spin rotation axis, **e** [4]. The polarization is then proportional to the vector product **P**$\propto$ **[e x Q].**

Collinear magnetic orders

In collinear magnetic order all the magnetic moments align along a particular axis. Ferroelectricity appears in these materials without the involvement of the spin-orbit interaction, the polarization is a result of exchange striction. The magnetic coupling varies with the atomic position which is observed in Ca_3CoMnO_6 [24] where the system consists of a chain of Co^{2+} and Mn^{4+} ions, Figure 1.11.

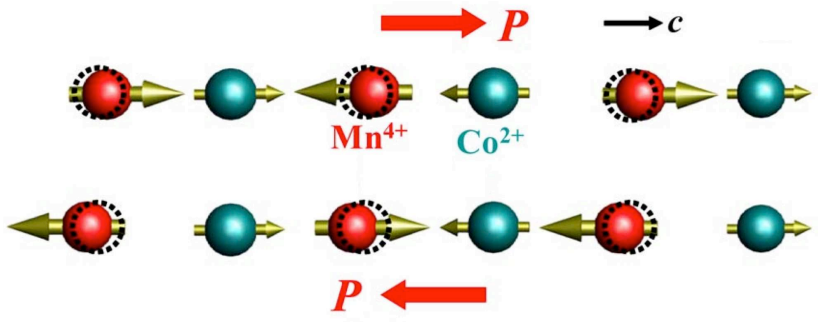

Figure 1.11: Collinear magnetic order as a mechanism for ferroelectricity [24]. Up-up-down-down spin order and alternating ionic order are shown. The undistorted atomic positions are shown with dashed circles. The electrical polarization is indicated by the red arrow.

At high temperatures the distances between the ions is constant and there is inversion symmetry. Magnetic order is needed to break the inversion symmetry, as shown in Figure 1.11, the magnetic order is up-up-down-down. The Mn^{4+} ions move towards the Co^{2+} ions aligned ferromagnetically and the bonds of those aligned antiferromagnetically are stretched, the fact that the valency on neighbouring sites alternates breaks inversion symmetry. The figure shows two possible ways of combining the magnetic and charge order which produce polarizations in opposite directions.

Ferroelectricity can also arise in collinear structures without the need for a mixed valence system. In the orthorhombic manganites, RMnO$_3$, with small rare earth ions, R, the Mn orders in the same manner as above (up-up-down-down) in the basal plane. The oxygen ions act as intermediaries for the exchange which depends on both the

distance between the Mn ions and the Mn–O–Mn bond angle. The exchange striction causes the oxygen ions to shift perpendicular to the Mn–Mn bonds which produces a polarization along the direction of the movement [25].

1.6 Magnetoelectric Coupling

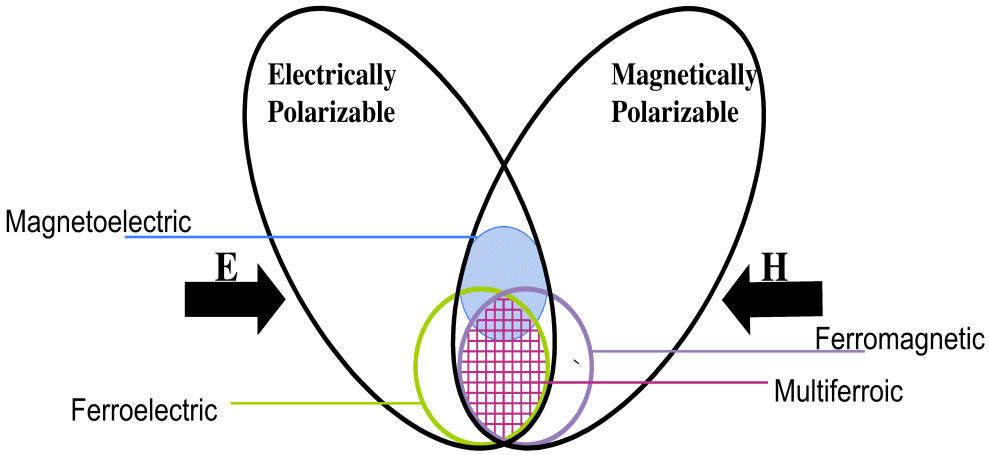

Figure 1.12: Magnetoelectric coupling is an independent phenomena that can, but need not necessarily, arise in materials that are both magnetic and electrically polarizable. Ferromagnets form a subset of magnetically polarizable materials and ferroelectrics a subset of electrically polarizable materials. Multiferroics occur when these two groups intersect.

The linear magnetoelectric effect is the induction of magnetization by an electric field or of polarization by a magnetic field. Magnetoelectric coupling can occur directly or indirectly via strain. It occurs whatever the nature of the electric and magnetic order parameters [7]. The overlap of magnetoelectric and multiferroic materials is incomplete as shown in Figure 1.12.

Contributions to the magnetoelectric effect are obtained by expanding the free energy,

$$F(\mathbf{E},\mathbf{H}) = F_0 - \frac{\varepsilon_0 \varepsilon_{ij} E_i E_j}{2} - \frac{\mu_0 \mu_{ij} H_i H_j}{8\pi} - \alpha_{ij} E_i H j + \cdots \tag{1.8}$$

where **H** and **E** are the magnetic and electric field respectively, ε_0 and μ_0 are the permittivity and permeability of free space, ε_{ij} and μ_{ij} are the relative permittivity and permeability and α_{ij} is the linear magnetoelectric tensor. The fourth term on the right of the equation describes the linear magnetoelectric coupling.

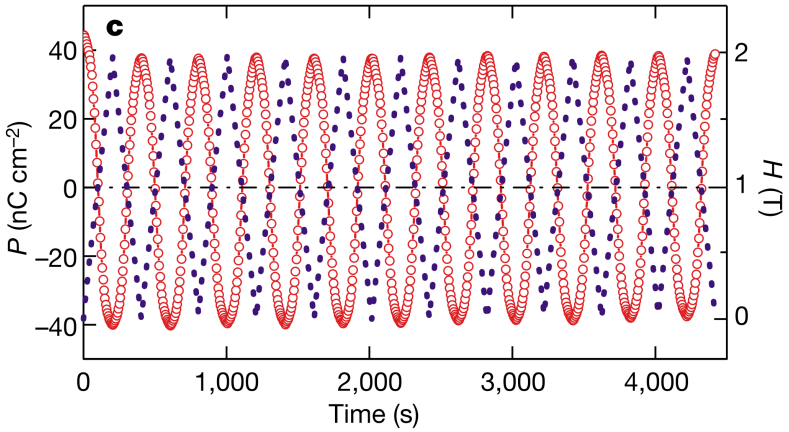

Figure 1.13: Polarization flipping by an applied magnetic in $TbMn_2O_5$ demonstrating magnetoelectric coupling [2].

An example of magnetoelectric coupling in multiferroic $TbMn_2O_5$ is shown in Figure 1.13. The linear magnetolectric effect is symmetry forbidden in hexagonal manganites, RMnO$_3$, however ferroelectric and antiferromagnetic domain walls have been shown to be coincident. Coupling via walls could then occur either because the local magnetization in the domain wall has reduced magnetic symmetry [3] or the local magnetization interacts with the strain from the ferroelectric wall [26].

1.7 Applications of Multiferroics

Applications such as transducers and magnetic field sensors have been suggested for multiferroics although most focus tends to be on data storage techniques. Multiferroics may have a future as devices for reading magnetic storage systems. At the moment read heads depend on magnetoresistive materials which generate heat and are sensitive to thermal noise however capacitive readings under magnetic fields can be done with no or very little heat produced [27]. They can also be more sensitive than resistive measurements which could allow the magnetic bit density to be increased. Four state memory has already been demonstrated [28], the idea being that magnetization and polarization could both encode information which could be read by a resistance measurement. In practice coupling would be likely to occur between the

two order parameters however an advantage of this would be the ability for data to be written electrically and read magnetically. This would demonstrate the advantages of ferroelectric random access memory and magnetic data storage while avoiding the disadvantages of generating the large local fields needed to write and the problems of reading FeRAM [9].

1.8 Plan of the Thesis

A variety of multiferroic materials and mechanisms are investigated in this thesis. The electrical properties of several multiferroics are investigated using impedance spectroscopy in Chapter 3. Given the coupling of magnetic and ferroelectric properties discussed in this chapter it is important to be able to investigate both order parameters. The aim of this investigation was to create instrumentation that could measure dielectric properties of multiferroic materials. Coupling of the order parameters was seen in these experiments.

The spin wave dispersions in multiferroics $LuMnO_3$ and $LuFe_2O_4$ are investigated in Chapters 4 and 7 respectively. These are type-I multiferroics through the geometric ferroelectric and charge ordered mechanisms respectively. The exchange parameters have been calculated from inelastic neutron data. The magnetic properties and magnetostrictive behaviour of $LuMnO_3$ have also been observed.

The magnetic and dielectric properties of the rare earth chromites are measured in Chapter 6. They are investigated for multiferroicity taking into account the conditions laid out previously in this chapter. Type-I multiferroic hexagonal $HoMnO_3$ is investigated with μSR (Muon Spin Rotation, Relaxation and Resonance) in Chapter 5. Using this technique the effect on the magnetic properties of applying an electric field have been seen in an effort to more fully understand the magnetoelectric coupling.

Bibliography

[1] T. Kimura, T. Goto, H. Shintani, K. Ishizaka, T. Arima and Y. Tokura, Nature **426**, 55 (2003).

[2] N. Hur, S. Park, P. A. Sharma, J. S. Ahn, S. Guha and S-W. Cheong, Nature **429**, 392 (2004).

[3] Th. Lottermoser, M. Fiebig, Phys. Rev. B **70**, 220407(R) (2004).

[4] M. V. Mostovoy, Phys. Rev. Lett. **96** 067601 (2006).

[5] J. J. Betouras, G. Giovannetti and J. van den Brink, Phys. Rev. Lett. **98**, 257602 (2007).

[6] S.-W. Cheong and M. Mostovoy, Nature Materials **6**, 13 (2007).

[7] M. Fiebig, J. Phys. D: Appl. Phys. **38**, R123 (2005).

[8] Y. Tokura, Science **312**, 1481 (2006).

[9] W. Eerenstein, N. D. Mathur and J. F. Scott, Nature **442**, 759 (2006).

[10] S. J. Blundell, *Magnetism in Condensed Matter*, Oxford University Press, Oxford, (2003).

[11] K. Rabe, Ch. H. Ahn and J.-M. Triscone, *Physics of Ferroelectrics A Modern Perspective*, Springer, Berlin, (2007).

[12] R. E. Cohen, Nature **358**, 136 (1992).

[13] H. Béa and P. Paruch, Nature Materials **8**, 168 (2009).

[14] B. B. van Aken, J.-P. Rivera, H. Schmid and M. Fiebig, Nature **449**, 702 (2007).

[15] K. M. Rabe, Nature **449**, 674 (2007).

[16] N. S. P. Bhuvanesh and J. Gopalakrishnan, J. Mater. Chem. **7(12)**, 2297 (1997).

[17] N. A. Hill, J. Phys. Chem. B. **104**, 6694 (2000).

[18] D. I. Khomskii, J. Mag. and Mag. Mater. **306**, 1 (2006).

[19] R. Seshadri and N. A. Hill, Chem. Mater. **13**, 2892 (2001).

[20] N. Ikeda, H. Ohsumi, K. Ohwada, K. Ishii, T. Inami, K. Kakurai, Y. Murakami, K. Yoshii, S. Mori, Y. Horibe and H. Kitô, Nature **436**, 1136 (2005).

[21] Th. Lonkai, D. G. Tomuta, U. Amann, J. Ihringer, R. W. A. Hexdrikx, D. M. Többens and J. A. Mydosh, Phys. Rev. B **69**, 134108 (2004).

[22] B. B. Van Aken, T. T. M. Palastra, A. Filippetti and N. A. Spaldin, Nature Materials **3**, 164 (2004).

[23] D. I. Khomskii, Physics **2**, 20 (2009).

[24] Y. J. Choi, H. T. Yi, S. Lee, Q. Huang, V. Kiryukhin and S.-W. Cheong, Phys. Rev. Lett. **100**, 047601 (2008).

[25] B. Lorenz, Y.-Q. Wang and C.-W. Chu, Phys. Rev. B **76**, 104405 (2007).

[26] M. Fiebig, Th. Lottermoser, D. Frölich, A. V. Goltsev, and R. V. Pisarev, Nature **419**, 818 (2002).

[27] M. A. Subramanian, T. He, J. Chen, N. S. Rogado, T. G. Calvarese and A. W. Sleight, Adv. Mater. **18**, 1737 (2006).

[28] M. Gajek, M. Bibes, S. Fusil , K. Bouzehouane, J. Fontcuberta, A. Barthélémy and A. Fert, Nature Materials **6**, 296 (2007).

Chapter 2

Experimental Procedures

Contents

This chapter introduces the experimental methods that were used for the measurements presented in this thesis. The principles of each technique are explained and the experimental apparatus and methodology described. Section 2.1 describes the bulk techniques of magnetic susceptibility and heat capacity. Sections 2.2 and 2.3 describe the microscopic techniques of μSR and neutron scattering respectively. μSR and neutron scattering are complementary techniques for investigating magnetic materials: μSR probes local magnetic correlations on relatively long time scales, while neutron scattering probes local and extended correlations on relatively short time scales.

2.1 Bulk Measurement Techniques

2.1.1 Magnetization Measurements

Most magnetization measurements in this thesis have been taken using a Quantum Design Superconducting Quantum Interference Device (SQUID) magnetometer also called a Magnetic Properties Measurement System (MPMS). The sample environment is a Helium flow cryostat that can maintain a temperature between 1.8–400 K in magnetic fields of $\pm$7 T. The sample is placed in a gel capsule, held in alignment with closely packed cotton wool and sealed with Kapton tape, in a straw. The straw is translated vertically within three superconducting coils. To ensure that the correct magnetic susceptibility value is obtained the sample is positioned within the detection coils while in the paramagnetic phase. A small field is applied, vertically as seen in Figure 2.1, to induce a magnetic moment sufficient to be measured by the detection coils as the sample is passed through them. The resultant response allows the sample to be positioned correctly within the coils. Movement of the sample through the superconducting pick-up coils induces a current proportional to the sample magnetization. These current changes in this superconducting circuit produce changes in magnetic field near the SQUID which acts as a magnetic flux-to-voltage converter. The magnetization of the sample is then given as the amplitude of the output voltage curve which is a function of the sample position.

DC magnetic susceptibility measurements (the sample is oscillated at a frequency of a few Hz) were used to measure the zero field cooled (ZFC) and field cooled (FC) responses. For ZFC measurements the sample is cooled in as close to zero field as possible after which the measuring field is applied and data is collected while warming. For FC measurements data are taken after the measuring field has been applied at

high temperatures and then the sample cooled in that field, data are then collected while cooling. AC magnetic susceptibility can be used to look at dynamic fluctuations of magnetic moments in the sample. It has two components, one in phase (χ' real part) and one out of phase (χ'' imaginary part) with the drive current, where ϕ is the phase difference and ω the measurement frequency. Results from these measurements are seen in Section 5.3.1.

The SQUID magnetometer only reaches frequencies up to 1 kHz and so for higher frequency measurements a Physical Properties Measurement System (PPMS) was used. This system is similar to the MPMS system although it has a lower sensitivity.

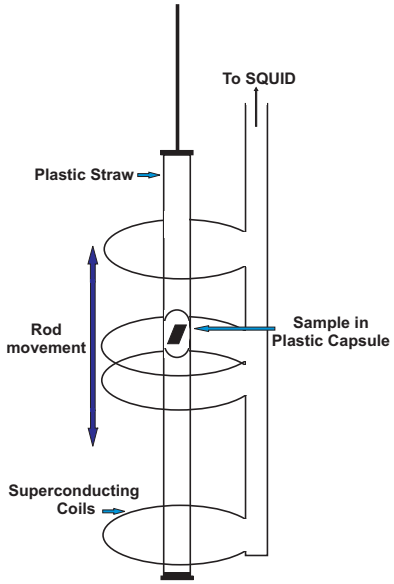

Figure 2.1: Diagram of sample positioning within the pick-up coils of the SQUID magnetometer.

2.1.2 Heat Capacity Measurements

Heat capacity investigations can provide information on the lattice, electronic and magnetic properties of a material. It affords a way of discovering how the entropy of a sample changes as a function of temperature or magnetic field. Heat capacity measurements in this thesis were performed using the PPMS. The sample sits on an alumina platform with a layer of Apiezon grease between the two to ensure thermal conductance, K_g, between them. Attached to the platform is a thin film heater to provide the heat pulse, $P(t)$, and a thermometer to measure the platform temperature. C_a, referred to as the addendum, is the heat capacity of the platform and the grease when no sample is attached. Small wires provide the thermal and structural connection

from the platform to the heat sink or thermal bath with thermal conductance K_w. All these components and values are indicated in Figure 2.2. The vacuum is sufficient that the thermal links are dominated by the conductance of the wires.

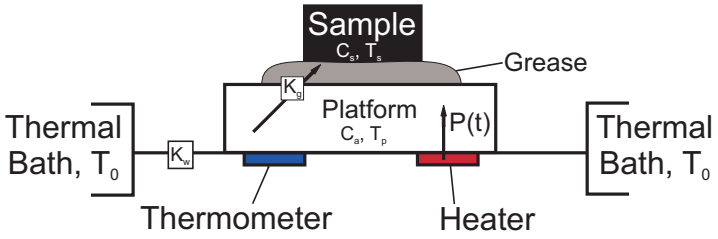

Figure 2.2: Diagram of heat capacity sample mount also showing the thermal conductance values K_w and K_g.

During a measurement a heat pulse is applied for a fixed time which is then followed by a cooling period of the same duration. The heat capacity software then fits the temperature response to a model that accounts for the thermal relaxation of the platform to the bath and from the platform to the sample. This is done using the 'two-tau' model which accounts for temperature differences between the sample and the platform. Equations 2.1 and 2.2 express the model where T_s is the temperature of the sample,

$$C_a \frac{dT_p}{dt} = P(t) - K_w (T_p(t) - T_0) + K_g (T_s(t) - T_p(t)), \quad (2.1)$$

$$C_s \frac{dT_s}{dt} = -K_g (T_s(t) - T_p(t)). \quad (2.2)$$

2.2 μSR

2.2.1 Muon Properties

The term μSR stands for $\mathbf{M}$uon $\mathbf{S}$pin $\mathbf{R}$otation, $\mathbf{R}$elaxation and $\mathbf{R}$esonance. Essential features of the muon and the technique make it an ideal method for investigating the local magnetic fields within a system [1]. Table 2.1 describes two of the important features. The lifetime of the muon, $\tau_\mu \approx 2.2$ μs, is long compared to most condensed matter processes allowing timescales intermediate to those of NMR or AC susceptibility and neutron scattering to be investigated [2]. The muon has a large gyromagnetic

Mass m_μ	105.6584389(34) MeV/c^2
	$=$ 206.7682 m_e
	$\approx$ 1/9 m_p
Charge	$\pm e$
Spin	1/2
Lifetime τ_μ	2.197019(21) μs

Table 2.1: Fundamental properties of the muon where m_e and m_p are the masses of the electron and proton, respectively [3, 4].

ratio, $\gamma_\mu = 2\pi\times1.355\times10^8$ HzT^{-1}, which determines the interaction between the magnetic field and the muon spin at the stopping site of the muon meaning that μSR is sensitive to magnetic fields down to 10^{-5} T.

For a μSR experiment muons need to have low enough energy to be stopped in a sample with a volume typically less than 1 cm^3. The decay of π^+ produces muons in this energy range. The pions are produced when a proton beam hits a target, typically of a light material with a high melting point such as graphite or beryllium, via the following reactions,

$$p + p \rightarrow \pi^+ + p + n, \text{ and } \; p + n \rightarrow \pi^+ + n + n, \tag{2.3}$$

where p is a proton and n a neutron. The pion then decays in 26 ns via the following reaction

$$\pi^+ \rightarrow \mu^+ + \nu_\mu. \tag{2.4}$$

The most common way positive muons are produced is when the decay above happens when the pion is stationary on the surface of the target, from surface muon beams. Positive muons are produced in this method as π^- stopped in a graphite target will be captured by the carbon nuclei [5]. If negative muons are needed then the pion needs to decay in flight. This occurs in facilities such as RIKEN-RAL in the UK but was not utilized in any experiment in this thesis. The neutrino is only produced with negative helicity (spin antiparallel to momentum) so as to conserve angular and linear momentum in reaction 2.4. The μ^+ also has negative helicity within the rest frame of the pion. The result of this is that the muons produced in this reaction are 100 $\%$

spin polarised with their spin antiparallel to their momentum.

2.2.2 Muon Stopping and Decay

After the muons are implanted in the sample they lose energy by electron scattering and ionization processes, then undergo electron capture and loss reactions all of which reduces the energy from around 4 MeV to a few hundred eV in about a picosecond. As these processes are all Coulombic, not interacting with the muon spin, the thermalisation occurs with little depolarization. Any lattice damage caused by the muons is ignored as it is assumed that the muon will thermalise well away from any damaged area closer to the material surface. Once the muon is thermalised the spin polarization evolves depending on the local magnetic field environment. The muon experiences a magnetic field distribution from dipolar interactions with neighbouring nuclear and electronic spins, from the external field and from the hyperfine fields caused by the spin density at the muon stopping site. The evolution of the polarization can be detected when the muon decays.

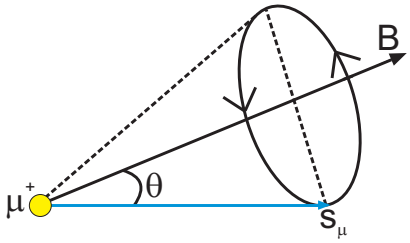

Figure 2.3: Diagram of the muon with spin $\mathbf{s}_\mu$ precessing about a magnetic field.

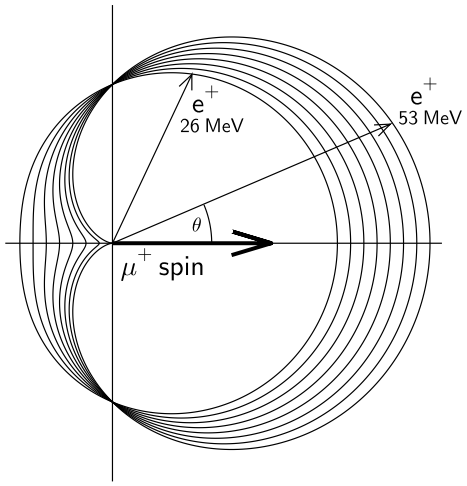

Figure 2.4: Angular distribution of positrons from the parity violating muon decay.

The evolution of the polarization can be understood by thinking of the precession of the spins in a magnetic field [1]. If the local field is at angle θ to the muon spin direction when it is implanted then the muon spin will precess about the field as in Figure 2.3. It will precess with angular frequency ω_μ,

$$\omega_\mu = \gamma_\mu B, \tag{2.5}$$

where $\gamma_\mu = ge/2m_\mu$ is the gyromagnetic ratio of the muon, g the g-factor and B is the local field.

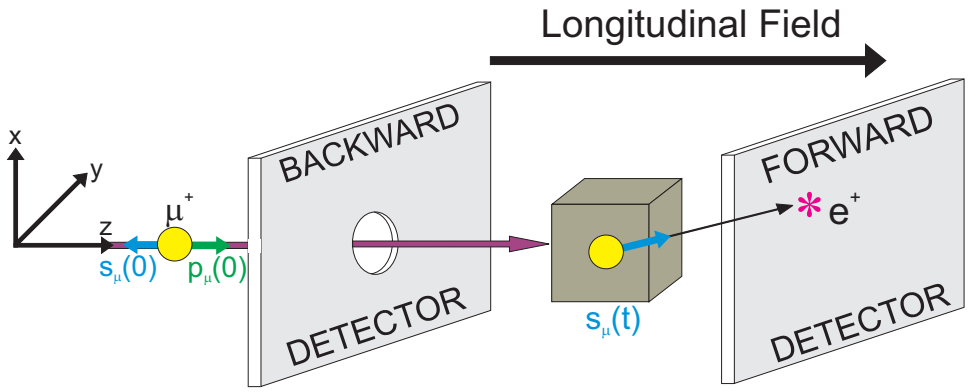

Figure 2.5: A diagram of the muon implantation and decay within a sample between forward and backward detectors in a longitudinal field geometry.

Independent of the local environment the implanted muon will decay via the weak interaction in 2.197 μs into a positron and two neutrinos,

$$\mu^+ \rightarrow e^+ + \nu_e + \bar{\nu}_\mu. \tag{2.6}$$

The decay is anisotropic with the positrons most likely to be emitted along the direction of the muon spin at the time of decay. This is due to the fact that the decay is also a parity violating process and that linear and angular momentum are conserved. The probability of the decay per unit time, at angle θ to the μ^+ spin direction can be calculated in equation 2.7 [2],

$$dW\,(\varepsilon,\theta) = \frac{n(\varepsilon)}{\tau_\mu}[1 + a(\varepsilon)\cos(\theta)]d\varepsilon d\cos(\theta) \tag{2.7}$$

$$a(\varepsilon) = (2\varepsilon - 1)\,/\,(3 - 2\varepsilon) \tag{2.8}$$

$$n(\varepsilon) = \varepsilon^2(3 - 2\varepsilon) \tag{2.9}$$

where ε is the normalised positron energy, which has a distribution of values. In the three body decay the positron can have an energy ranging from zero (antiparallel neutrinos carry away all the energy) to $E_{\max}$=52.8 MeV. The emission of positrons

is weighted in favour of being parallel to the muon spin polarization by a factor of $1 + a(\varepsilon)\cos(\theta)$, with the maximal cardioid shape when the positron energy is equal to $E_{\max}$ (a(ε)=1) and being a circle in polar co-ordinates when the energy is equal to half $E_{\max}$, Figure 2.4. So even if all positron energies were to be detected the net positron emission would be in the direction of the muon polarization.

The experiments in this thesis were performed in a longitudinal field geometry as in Figure 2.5. In this arrangement a field is applied along the z-axis. This is also the layout for the zero field (ZF) geometry where the applied field is zero. In the presence of no component of magnetic field perpendicular to the initial muon spin direction no oscillatory behaviour will be seen. In the zero field geometry a precession signal will only be seen if an internal coherent magnetic field exists within the sample i.e. long range magnetic order exists. The ZF geometry is a very sensitive way of detecting weak internal magnetism to $\sim 10^{-5}$ T. In a transverse field geometry the applied field is perpendicular to the initial spin polarization. The muon spins will precess about this field.

2.2.3 μSR Sources and Instruments

The spin polarized muons are transported to the sample through a series of dipole guiding magnets and quadrupole focusing magnets. The magnetic fields conserve the polarization by changing the trajectory of the muons at the same rate as the spin is rotated so at all times the spin is antiparallel to the momentum. To remove contaminant particles (for example muons that have decayed into positrons in flight) from the muon beam a combination of electric and magnetic fields are used. The electrostatic and magnetic forces will cancel only for particles of the correct velocity thus only allowing muons through.

To determine how the spin polarization evolves as a function of time the decay positrons are detected by arrays of detectors placed at fixed angles around the sample. Detectors are grouped in symmetrically opposite arrangements such as forward and backward detectors as seen in Figure 2.5. An asymmetry function, $A(t)$, is defined by

$$A(t) = \frac{N_F(t) - \alpha N_B(t)}{N_F(t) + \alpha N_B(t)}, \tag{2.10}$$

where $N_F(t)$ and $N_B(t)$ are the count rates in the forward and backward detectors respectively and α accounts for any inequivalency in the detection efficiency in the

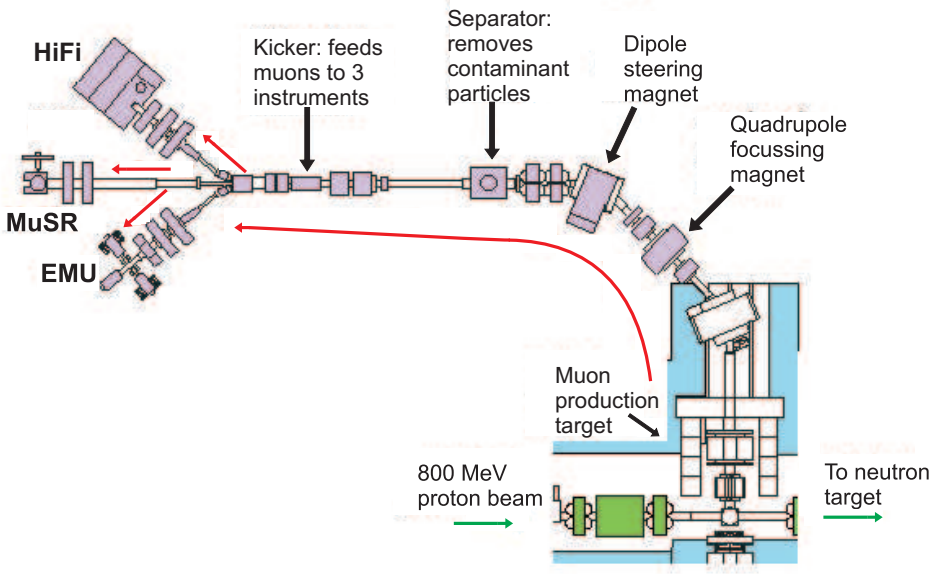

Figure 2.6: A diagram of the ISIS, Rutherford Appleton Laboratory beamlines. A separator is used to remove unwanted particles. A kicker is used to divert single pulses into the different instruments.

two arrays. The parameter α is determined by applying a weak transverse field to the sample in its paramagnetic state.

After a positron is detected there is a period of deadtime, $\tau_d \sim$ 10 ns, where the detector is effectively off. This limits the speed of data acquisition. This means that the true count rate, r, will differ from the observed count rate, r_{ob}, as seen in equation 2.11,

$$r = \frac{r_{ob}}{(1 - r_{ob}\tau_d)}. \tag{2.11}$$

Pulsed Sources

Pulsed and continuous sources have different advantages and limitations. Pulsed sources are most effective for slow relaxation processes where features are happening over longer times. The most intense source of pulsed neutrons and muons in the world is at the ISIS facility at the Rutherford Appleton Laboratory in the UK. The experiments in Chapter 5 were performed at this facility on the EMU beamline. A proton pulse from a synchrotron is fired at a target at regular intervals producing a pulsed beam at ~50 Hz. Several muons are implanted in the sample simultaneously at a time t_0 and timing events are measured relative to this. An advantage of this method is that after the muons are implanted no more arrive for 20 ms, which means

that the random time-independent background will be small so data can be reliably taken to longer times. However a disadvantage is that if there is a very fast precession frequency or relaxation rate then the muons at the start of the pulse will have dephased before those at the end are implanted. The pulse is said to have reached the sample only when its centre has impacted at t_0, and data cannot be recorded until the whole pulse has arrived after t_0+t_{offset}.

The EMU spectrometer is a 96 detector instrument which operates mainly in the longitudinal geometry [6]. A Helmholtz coil is used to provide the magnetic field at the sample site. Collimation is used to adjust the beam size incident on the sample.

Continuous Sources

Continuous sources are better for observing fast muon spin rotation frequencies or relaxations. The Paul Scherrer Institute (PSI) in Villigen, Switzerland has a continuous muon source and experiments in Chapter 6 were taken at this facility on the instrument GPS (General Purpose Spectrometer) [7]. At PSI protons are accelerated in a cyclotron and on hitting graphite targets produce a continuous beam of muons. Muons arriving at the instrument are detected by muon counters before hitting the sample which triggers the timing electronics. The detection of a decay positron stops the timer and the experiment is then repeated in this way for several million events. The timing electronics allows unwanted events, such as another muon entering the sample before the first has decayed, to be rejected. A separator is not necessary at PSI as there is a thin scintillation detector placed before the sample which can distinguish between muons and positrons by the light they generate in the detector. As in EMU, Helmholtz coils allow the application of a magnetic field to the sample. However in contrast to EMU five positron detectors are located forward, backward, above, below and right of the beam direction.

2.2.4 Muon Spin Interactions

An important issue for interpreting μSR data is to determine where the muon stops in the sample. μSR is a probe of local magnetic fields and so determining the local environment is essential for understanding the results. The magnetic field at the muon site is given here by $\mathbf{B}$ and is the sum of seven terms [8, 9],

$$\mathbf{B} = \mathbf{B_0} + \mathbf{B_{dia}} + \mathbf{B_{con}} + \mathbf{B_{trans}} + \mathbf{B_{dip}} + \mathbf{B_L} + \mathbf{B_{dem}}. \tag{2.12}$$

$\mathbf{B}_0$ Externally applied magnetic field.

$\mathbf{B}_{dia}$ Diamagnetic field which only needs to be considered for superconductors.

$\mathbf{B}_{con}$ Contact hyperfine field resulting from non zero spin density induced at the μ^+ sites from the RKKY mechanism in metals.

$\mathbf{B}_{trans}$ Transferred hyperfine field from non-zero spin density induced at the μ^+ sites from covalency effects in insulators.

$\mathbf{B}_{dip}$ Dipole Field contribution, see equation 2.13.

$\mathbf{B}_L$ Lorentz field is a macroscopic contribution which is needed for insulating ferromagnets.

$\mathbf{B}_{dem}$ Demagnetization field is a macroscopic contribution which depends on the bulk magnetisation and the shape of the sample. This is needed for insulating ferromagnets.

It is the dipole field that will dominate in the antiferromagnetic materials studied in this thesis and as such equation 2.13 for the dipole field can be used to find possible muon stopping sites [5, 10]. $\mathbf{B}_{dip}$ is produced by moments, μ_i, located at sites $\mathbf{r}_\mu - \mathbf{r}_i$, where $\mathbf{r}_\mu$ is the muon site, and the sum runs over all magnetic ion positions, $\mathbf{r}_i$, and is given by

$$\mathbf{B_{dip}}\left(\mathbf{r}_\mu\right) = \frac{\mu_\mathbf{0}}{\mathbf{4}\pi} \sum_{\mathbf{i}} \frac{\mathbf{3}\left(\mu_\mathbf{i} \cdot \hat{\mathbf{n}}_\mathbf{i}\right)\hat{\mathbf{n}}_\mathbf{i} - \mu_\mathbf{i}}{\left|\mathbf{r}_\mu - \mathbf{r}_\mathbf{i}\right|^\mathbf{3}}. \tag{2.13}$$

The unit vector between the muon and magnetic ion sites is $\widehat{\mathbf{n}}_i = (\mathbf{r}_\mu - \mathbf{r}_i)/\left|\mathbf{r}_\mu - \mathbf{r}_\mathbf{i}\right|$. The calculation is done for around 10^4 unit cells so that the observed precession frequencies can be compared to the calculated fields within the material [9]. The data analysis of the muon experiments in this thesis was done using WiMDA, a program written by Dr. F. L. Pratt. [11] and with dipole field calculation programs written by S. J. Blundell, P. J. Baker, T. Lancaster and A. Steele.

2.3 Neutron Scattering

Neutron scattering is an appropriate technique for investigating correlated electron systems by virtue of the properties of the neutron and the availability of experimental

instrumentation. The de Broglie wavelength of thermal neutrons is comparable to the interatomic distances in solids allowing diffraction to probe the structures. The neutron also possesses a magnetic moment and so interacts with the magnetic moments of unpaired electrons in a sample allowing magnetic orders to be characterized. The energy of neutrons produced at experimental facilities is similar to the energy of many excitations making neutron scattering ideal for studying phonons and magnons. They also interact weakly with matter allowing them to penetrate cryostats and other obstacles in the experiment.

2.3.1 Neutron Sources

There are two types of neutron source available for neutron scattering experiments, reactor and spallation sources, both of which were used for experiments in this thesis. The reactor source Orphée at the Laboratoire Léon Brillouin (LLB), Saclay, France was used for some experiments in Chapter 4 and the reactor source at Institut Laue-Langevin (ILL), Grenoble, France was used for experiments in Chapter 7. A reactor source produces a high flux of neutrons at a steady rate through nuclear fission of ^{235}Uranium. More neutrons than are needed to maintain the chain reaction are produced and these neutrons are then used for the scattering experiments.

$$^{235}\mathrm{U} + \mathrm{n} \rightarrow 2.5\mathrm{n} + 200\,\mathrm{MeV} + \mathrm{nuclei} \tag{2.14}$$

A moderator is introduced to slow the neutrons down from MeV to meV energies resulting in a Maxwell-Boltzmann distribution of velocities. The neutron beam is constrained to be monochromatic with an array of orientated crystals arranged to select a particular wavelength. The neutrons then pass through wave guides to the scattering instruments.

The "continuous" spallation source at SINQ, Paul Scherrer Institut (PSI), Switzerland was used for experiments in Chapter 4. Spallation sources produce a relatively low flux of neutrons which also have a broad range of energies. Spallation occurs when high energy protons hit the nuclei of heavy atoms causing high energy particles, including neutrons, to be ejected and absorbed by other nuclei resulting in the emission of 20-40 neutrons per incident proton. The neutron beam can also be pulsed as at ISIS, Rutherford Appleton Laboratories in the UK however this type of source was not used so shall not be described further. The spectrum of the neutron is then adjusted

with a moderator as with a reactor source.

2.3.2 Neutron Scattering Instruments

Elastic and inelastic neutron experiments are either carried out at a fixed incident wavelength at a reactor source or with a broad band of wavelengths at a pulsed source. For inelastic measurements triple axis spectrometers are normally used at reactor sources and time-of-flight spectrometers are used at pulsed sources. The research in this thesis was all conducted at continuous sources on triple-axis spectrometers so only that instrument shall be described.

Triple Axis Spectrometer

The triple axis spectrometer (TAS) is ideal for looking at excitations at a particular point in, or direction in ($\mathbf{Q}$,ω) space. Figure 2.7 shows a diagram of a triple axis instrument. The initial and final energies of the neutrons are selected by the monochromator and analyser respectively. In the monochromator a material such as single crystal pyrolytic graphite or Heusler crystals select a monochromatic beam from a broad distribution of neutron wavelength through Bragg reflection, defining the wave vector $\mathbf{k_i}$ incident on the sample. At the analyser the beam is Bragg reflected so only neutrons with a particular final wave vector $\mathbf{k_f}$ are recorded in the detector.

Moderated neutrons emerge in all directions and, while the diffraction from the monochromator and analyser provide some constraint on the angular divergence of the beam, collimators provide adjustable control. Collimators are typically parallel plates of neutron absorbing material [12]. Filters are included as Bragg diffraction from the monochromator also allows higher order reflections of the narrow wavelength band that has been selected. These higher order neutrons will result in extra peaks in a diffraction pattern or inelastic spectrum. Pyrolytic graphite filters or nitrogen cooled beryllium filters are commonly used. They act to stop the transmission of neutrons above a particular wavelength or to optimally transmit a particular wavelength but have transmission troughs at the second and third harmonics.

Neutron detectors generally use gaseous $^3\mathrm{He}$ in a process shown in equation 2.15. Neutrons are not charged so cannot be detected directly by gas ionization so they need to make another atom release a charged particle. The absorber, $^3\mathrm{He}$, and the

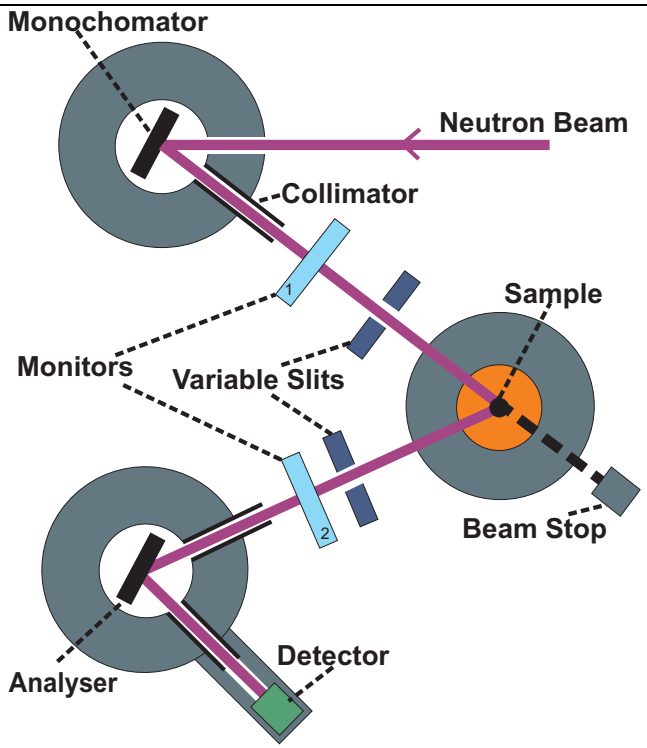

Figure 2.7: A schematic of a triple axis spectrometer used for neutron experiments.

neutron produce a proton which ionizes the gas which is collected by an anode wire. The signal is proportional to 0.77 MeV so the signal from a neutron event can be distinguished from the different energies that would arise from high energy neutron or gamma rays [13].

$$^{3}\mathrm{He} + n \rightarrow ^{3}\mathrm{H} + p + 0.77\,\mathrm{MeV} \tag{2.15}$$

Beam monitors are placed on all instruments so that allowances can be made automatically for variation in beam strength during measurements. The monitor is placed in the direct beam but attenuation is usually much less than 1% [14]. The two main types of monitor are gas detectors, as described above, and scintillation detectors. In scintillation detectors a neutron absorber such at ^{6}Li is mixed with a scintillator such as ZnS and the resultant burst of light when an incoming neutron is absorbed and secondary particles formed is amplified by a photomultiplier.

For some experiments in Chapter 7 a triple axis instrument was used that allows many data points to be collected simultaneously using a detector known as FlatCone [15]. This allows inelastic responses to be mapped over extended regions of ($\mathbf{Q}$,ω)

space without increasing the measurement time. It is a bank of multidetectors made up of 31 individual channels covering a scattering range of 75^o with each channel containing two analyser crystals and a $^3\mathrm{He}$ detector. It allows scanning along a third axis without the need to reorient the crystal.

2.3.3 Neutron Scattering Theory

The following is a brief description of the main concepts in neutron scattering, it is covered in detail in several books [14, 16].

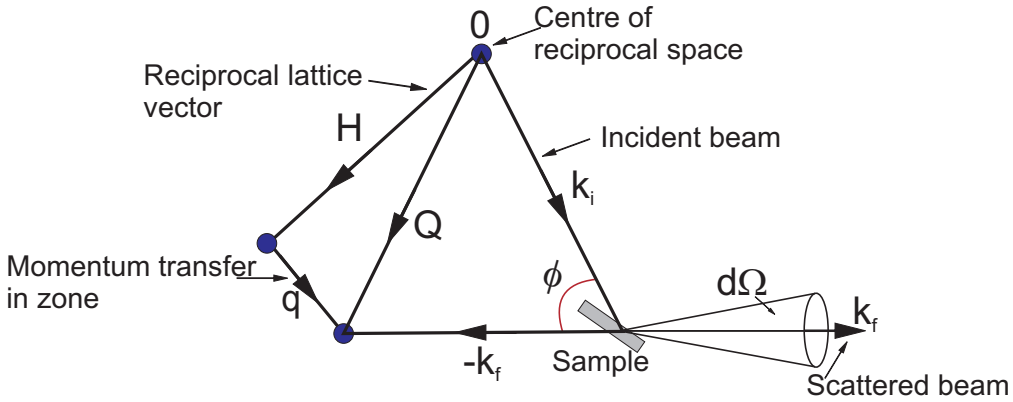

Figure 2.8: Scattering diagram of triple axis spectrometer in reciprocal space, relating the incident and final wavevectors to the scattering wave vector. Also depicted is the solid angle into which the neutron is scattered.

In the experiment a neutron with initial wavevector $\mathbf{k}_i$ is incident on the sample and is then scattered through an angle ϕ into the final wavevector $\mathbf{k}_f$ as seen in Figure 2.8. The momentum transferred to the sample is $\hbar\mathbf{Q}$, where $\mathbf{Q}$ is the scattering wavevector, as defined in equation 2.16.

$$\mathbf{Q} = \mathbf{k}_i - \mathbf{k}_f \tag{2.16}$$

In inelastic scattering events the neutron loses or gains energy, energy conservation results in equation 2.17, where E_i and E_f are the incident and final energies of the neutron respectively and $\hbar\omega$ is the energy of excitation of the sample. For elastic scattering $\hbar\omega = 0$.

$$E_i - E_f = \hbar\omega = \frac{\hbar^2}{2m_n}\left(\mathbf{k}_i^2 - \mathbf{k}_f^2\right) \tag{2.17}$$

A neutron is detected when it emerges from the sample within a solid angle $d\Omega$, shown in Figure 2.8 and has an energy within a small range, dE_f, of values around E_f. The total cross section is defined in equation 2.18, where I_0, the incident flux, is taken to be the number of neutrons hitting a unit area, perpendicular to the neutron beam, in a unit time,

$$\sigma_{tot} = \frac{\text{number of neutrons scattered in all directions per second}}{(I_0)}. \tag{2.18}$$

In a neutron scattering experiment it is the double differential cross-section that is measured,

$$\frac{d^2\sigma}{d\Omega\, dE_f} = \frac{\begin{array}{c}\text{number of neutrons scattered per second into the solid angle } \mathrm{d}\Omega \\ \text{in the direction } \theta, \phi \text{ with final energy between } E_f \text{ and } E_f + dE_f\end{array}}{I_0\, d\Omega\, dE_f}. \tag{2.19}$$

It can also be defined in terms of the scattering function, S($\mathbf{Q}, \omega$), of the system,

$$\frac{d^2\sigma}{d\Omega\, dE_f} = b^2 \frac{k_f}{k_i} NS\left(\mathbf{Q}, \omega\right), \tag{2.20}$$

which gives the probability that the scattering changes the energy of the system by $\hbar\omega$ and changes its momentum by $\hbar\mathbf{Q}$ where N is the number of atoms and b is the scattering length.

The Neutron Coherent Elastic Scattering Cross Section

The double differential cross-section can be expressed as the sum of coherent and incoherent components. Coherent scattering results in elastic Bragg scattering and inelastic phonon scattering and is due to coherent interference from nuclei in a material. The incoherent scattering is seen as an isotropic background and is due to a variance in scattering lengths.

When only considering the coherent scattering the differential cross section can be expressed as in equation 2.20. This equation holds if the material consists of only a single element. If not, the site dependent scattering lengths must be included in $S\left(\mathbf{Q}, \omega\right)$ by including the atomic density operator $\rho_{\mathbf{Q}}\left(t\right) = \sum_l e^{i\mathbf{Q}\cdot\mathbf{r}_l(\mathbf{t})}$ which is then time averaged. For a lattice with more than one unit cell where $\mathbf{r}_j$ is the position of

the j^{th} atom, the elastic differential cross section then becomes

$$\frac{d\sigma}{d\Omega} = N\frac{(2\pi)^3}{\upsilon_0}\sum_{\mathbf{G}}\delta\left(\mathbf{Q}-\mathbf{G}\right)\left|F_N\left(\mathbf{G}\right)\right|^2 \tag{2.21}$$

where,

$$F_N\left(\mathbf{Q}\right) = \sum_j \overline{b}_j \exp\left(i\mathbf{Q}\cdot\mathbf{r}_j\right)\exp\left(-W_j\left(\mathbf{Q},T\right)\right) \tag{2.22}$$

and where υ_0 is the unit cell volume and the vectors $\mathbf{G}$ are reciprocal lattice vectors. This would describe a perfectly rigid lattice but the atoms actually fluctuate with thermal motion about their equilibrium positions. As the temperature increases the intensity of Bragg peaks decreases because of the increase in thermal motion. This decrease in intensity is described by the Debye-Waller factor, $W_j(\mathbf{Q},T) = \frac{1}{2}\langle(\mathbf{Q}\cdot\mathbf{u}_j(T))^2\ \rangle$ where $\mathbf{u}_j(T)$ is the displacement of the j^{th} atom from its equilibrium position.

2.3.4 Magnetic Neutron Scattering

Magnetic Elastic Scattering

The neutron possesses a magnetic dipole moment that can interact with the magnetic field from unpaired electrons. The interaction occurs through the magnetic field due to the orbital motion of the electrons and the magnetic field due to the spin dipole moment of the electron itself. The magnetic moment of a neutron is given by

$$\boldsymbol{\mu}_n = -\gamma\mu_N\boldsymbol{\sigma}, \tag{2.23}$$

where μ_N is the nuclear magneton, γ is a numerical constant equal to 1.913 and σ is the Pauli spin operator which has eigenvalues of ±1. The interaction potential between the neutrons and the local magnetic field from the unpaired electrons, $\mathbf{B}(\mathbf{r})$, can be given in terms of the spatial coordinate $\mathbf{r}$ using

$$V_M\left(\mathbf{r}\right) = -\boldsymbol{\mu}_n\cdot\mathbf{B}\left(\mathbf{r}\right), \tag{2.24}$$

or by taking the Fourier transform, wavevector $\mathbf{Q}$,

$$V_M\left(\mathbf{Q}\right) = -\boldsymbol{\mu}_n\cdot\mathbf{B}\left(\mathbf{Q}\right) = -\mu_0\boldsymbol{\mu}_n\cdot\mathbf{M}_\perp\left(\mathbf{Q}\right), \tag{2.25}$$

where $\mathbf{M}_{\perp}$ is the component of the electron magnetic moment perpendicular to the scattering wavevector $\mathbf{Q}$, which is given by

$$\mathbf{M}_{\perp}(\mathbf{Q}) = \widehat{\mathbf{Q}} \times \left\{ \mathbf{M}(\mathbf{Q}) \times \widehat{\mathbf{Q}} \right\}. \tag{2.26}$$

When systems are magnetically ordered magnetic elastic scattering can be observed as magnetic Bragg peaks. For unpolarized neutron scattering, the cross section for magnetic scattering is given by

$$\frac{d\sigma}{d\Omega} = N_m \frac{(2\pi)^3}{V_{0m}} \left(\frac{\gamma r_0}{2}\right)^2 \sum_{\alpha\beta} \left\langle \left(\delta_{\alpha\beta} - \widehat{Q}_{\alpha}\widehat{Q}_{\beta}\right) F_M^{\alpha}(\mathbf{G}) F_M^{\beta *}(\mathbf{G}) \right\rangle \delta(\mathbf{Q} - \mathbf{G}), \tag{2.27}$$

where N_m is the number of magnetic unit cells in the crystal, V_{0m} is the volume of the magnetic unit cell, r_0 is the classical electron radius and $\mathbf{G}$ is now the magnetic reciprocal lattice vector. In the summation the indices α and β are the Cartesian coordinates x, y and z and $\delta_{\alpha\beta}$ is the Kronecker delta. $\langle ... \rangle$ represents the averaging over symmetrically equivalent magnetic domains. The magnetic unit cell structure factor $F^{\alpha}(\mathbf{Q})$ is given by

$$F_M^{\alpha}(\mathbf{Q}) = \sum_j \mu_{\alpha}^j f_j(\mathbf{Q}) e^{i\mathbf{Q}\cdot\mathbf{r_j}} e^{-W_j(\mathbf{Q},\mathbf{T})}, \tag{2.28}$$

where the summation j runs over all the magnetic ions in the unit cell, μ_{α}^j is the α component of the magnetic moment of the j$^{\text{th}}$ ion and $f_j(\mathbf{Q})$ is the magnetic form factor and r$_j$ is the position of the j$^{\text{th}}$ ion in the magnetic unit cell.

Magnetic Inelastic Scattering

In an inelastic magnetic scattering process the neutron gains or loses energy from the scattering. The neutron experiments in this thesis concentrate on inelastic measurements. Equation 2.29 is the cross section for inelastic magnetic neutron scattering in the dipole approximation,

$$\left(\frac{d^2\sigma}{d\Omega dE_f}\right) = \left(\frac{\gamma r_0}{2}\right)^2 f^2(\mathbf{Q}) e^{-2W(Q,T)} \frac{k_f}{k_i} S(\mathbf{Q},\omega), \tag{2.29}$$

where $S(\mathbf{Q},\omega)$ is the response function and describes how only the component of S perpendicular to $\mathbf{Q}$ contributes to the scattering amplitude and is given by

$$S(\mathbf{Q},\omega) = \sum_{\alpha\beta} \langle (\delta_{\alpha,\beta} - \widehat{Q}_\alpha \widehat{Q}_\beta) S^{\alpha\beta}(\mathbf{Q},\omega) \rangle \tag{2.30}$$

where $S^{\alpha\beta}(\mathbf{Q},\omega)$ are the space and time Fourier transforms of the time dependent spin-spin correlation functions. For the case of localised excitations with sharply defined energy difference the response function can also be written as,

$$S(\mathbf{Q},\omega) = \sum_{ij} \rho_i \left| \langle j \left| \widehat{\mu}_\perp \right| i \rangle \right|^2 \delta\left(E_i - E_j - \hbar\omega\right), \tag{2.31}$$

where $|i\rangle$ and $|j\rangle$ are the initial and final eigenfunctions of the system corresponding to the eigenvalues E_i and E_j. $\widehat{\mu}_\perp$ is the magnetic moment operator perpendicular to $\mathbf{Q}$, $\hbar\omega$ is the energy loss of the scattered neutron and ρ_i is the thermal population factor of the initial state $|i\rangle$.

The Principle of Detailed Balance

The detailed balance factor, $e^{\frac{\hbar\omega}{k_B T}}$ describes the difference between the probability of the neutron losing or gaining energy, so that

$$S(\mathbf{Q},\omega) = e^{\frac{\hbar\omega}{k_B T}} S(-\mathbf{Q},-\omega) \tag{2.32}$$

where T is the temperature and k_B the Boltzmann constant. The probability that the system is initially in the higher energy state is lower by the detailed balance factor. When the temperature is very low the probability of the neutron gaining energy is therefore also very low.

2.4 Impedance Spectroscopy

Measurements of the dielectric properties of materials have been carried out using impedance spectroscopy. Apparatus for the measurements was designed and built for use in cryogenic and high magnetic field environments (see Chapter 3). In impedance spectroscopy a sinusoidal potential perturbation is applied to the system and the current response is observed. The response is a sine wave at the same frequency but with a different phase and amplitude from the potential signal. The signal generator used in these experiments was a *Solartron 1260 Frequency Response Analyser* (FRA). The equipment was controlled by the software SMaRT.

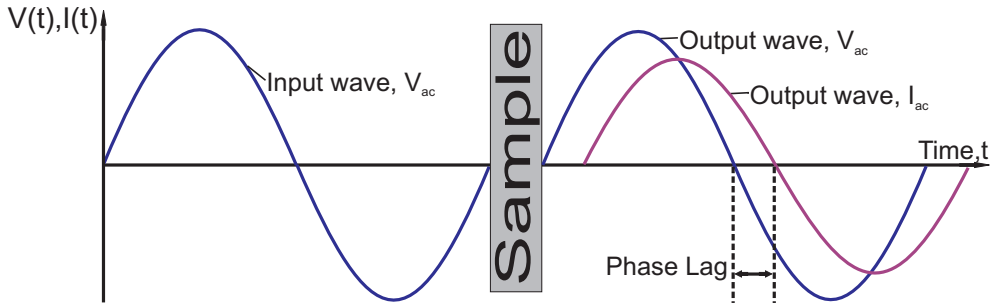

Figure 2.9: Input signal from the FRA and output signals after passing through the sample

The FRA determines the impedance of a sample through the single sine correlation technique. This determines the complex frequency response by measuring a single frequency at a time. The response is obtained by sweeping the applied signal frequency. The measured signal is multiplied by reference sine and cosine waves derived from the signal generator and integrated over a whole number of cycles. This process rejects harmonic responses and significantly reduces random noise. The *Solartron 1260* has a 1 MΩ input resistance and 35 pF internal input capacitance. When the *Solartron 1260* is used as a stand alone device the deviations due to the voltage divider effect become significant when the measured impedance exceeds Z=10 kΩ.

This limitation of the *Solartron 1260* is addressed with the inclusion of the *Solartron Dielectric Interface 1296* where the problems of large impedances in the low frequency regime are overcome. When analyzing low conductivity, low loss materials such as polymers, rubber, and the materials investigated in this thesis, it can be difficult to obtain accurate results due to the high impedance values of the materials. The *Dielectric Interface 1296* enhances the low frequency sensitivity for highly resistive materials and increases the impedance measurement range to 100 TΩ. It takes a reference measurement on a precision capacitor which is automatically substituted for the sample then a second measurement is made of the sample itself. The two results can then be used to find an accurate estimate of the permittivity of the material, the first measurement is used to eliminate the effects of extraneous capacitance.

Bibliography

[1] S. J. Blundell, Contemp. Phys. **40**, 175 (1999).

[2] A. Schenck, *Muon Spin Rotation Spectroscopy*, Adam Hilger Ltd, Bristol, UK (1985).

[3] D. B. Chitwood, T. I. Banks, M. J. Barnes, S. Battu, R. M. Carey, S. Cheekatmalla, S. M. Clayton, J. Crnkovic, K. M. Crowe, P. T. De- bevec, S. Dhamija, W. Earle, A. Gafarov, K. Giovanetti, T. P. Gor- ringe, F. E. Gray, M. Hance, D. W. Hertzog, M. F. Hare, P. Kammel, B. Kiburg, J. Kunkle, B. Lauss, I. Logashenko, K. R. Lynch, R. Mc- Nabb, J. P. Miller, F. Mulhauser, C. J. G. Onderwater, C. S. Özben, Q. Peng, C. C. Polly, S. Rath, B. L. Roberts, V. Tishchenko, G. D. Wait, J. Wasserman, D. M. Webber, P. Winter, and P. A. Żołnierczuk, Phys. Rev. Lett. **99**, 032001 (2007).

[4] Review of Particle Physics, J. Phys. G: Nucl. Part. Phys. **33**, 1 (2006).

[5] S. L. Lee, S. H. Kilcoyne and R. Cywinski, *Muon Science: Muons in Physics, Chemistry and Materials*, IOP Publishing, Bristol, UK (1999).

[6] http://www.isis.stfc.ac.uk/instruments/emu/

[7] A. Amato, GPS User Guide, 2009 http://lmu.web.psi.ch/facilities/gps/gps.html

[8] P. Dalmas de Réotier and A. Yaouanc, J. Phys.: Condens. Matter **9**, 9113 (1997).

[9] A. Schenck, F. N. Gygax, *Handbook of Magnetic Materials Volume 9*, Elsevier Science B.V., Amsterdam, (1995).

[10] M. Z. Uritskiĭ, V. Yu. Irkhin, Phys. of Solid State **42**, 399 (2000).

[11] F. L. Pratt, Physica B **289-290**, 710 (2000).

[12] G. Shirane, S. M. Shapiro, J. M. Tranquada, *Neutron Scattering with a Triple Axis Spectrometer*, Cambridge University Press, (2002).

[13] A. Oed, Nuclear Instruments and Methods in Physics Research A **525**, 62 (2004).

[14] B. T. M. Willis and C. J. Carlile, *Experimental Neutron Scattering*, Oxford University Press, Oxford, (2009).

[15] M. Kempa, B. Janousova, J. Saroun, P. Flores, M. Boehm, F. Demmal and J. Kulda, Physica B **385-386**, 1080 (2006).

[16] G. L. Squires, *Introduction to the Theory of Thermal Neutron Scattering*, Dover Publications, Inc. (1996).

Chapter 3

Impedance Spectroscopy

Contents

The history of impedance spectroscopy began with the introduction of impedance into electrical engineering by Oliver Heaviside in the 1880s. It was followed by increasingly complex interpretations and representations and the adoption of this technique in a wide variety of fields. Impedance spectroscopy is ideal for studying multiferroics as the time scales involved are perfect for looking at dipole motion and domain wall motion. Apparatus for measuring dielectric constants using impedance spectroscopy has been designed and built. Using this apparatus three main materials were investigated which are either multiferroic or can provide insight into multiferroic systems.

3.1 Dielectric Behaviour

Impedance spectroscopy can be divided into two categories, electrochemical impedance spectroscopy, involving measurements on materials such as solid and liquid electrolytes, and measurements on dielectric materials. The work in this thesis investigates insulating materials, which are often referred to as dielectric materials.

The dielectric constant of the material is one of the most important parameters used to characterize insulators and describes the response of a solid to an electric field. A dielectric material located between two parallel conducting plates comprises a capacitor, Figure 3.1. The capacitance, C, of the system is equal to the ratio of the charge on the metal plates, q, to the potential difference between them, V,

$$C = \frac{q}{V}. \tag{3.1}$$

When there is a dielectric material between the plates the capacitance will increase by an amount equal to the dielectric constant also known as the relative permittivity, ε_r, where

$$\varepsilon_r(\omega) = \frac{\varepsilon(\omega)}{\varepsilon_0} \qquad \varepsilon_r = \lim_{\omega \to 0} \varepsilon_r(\omega) = \frac{\varepsilon_s}{\varepsilon_0} \tag{3.2}$$

where ε_0 is the permittivity of free space and ε_s is the static permittivity. Therefore

$$q = \frac{\varepsilon_0 \varepsilon_r A V}{d} \qquad \text{and} \qquad C = \frac{\varepsilon_0 \varepsilon_r A}{d} \tag{3.3}$$

where A is the area of the plates and d is the distance between them, Figure 3.1.

Impedance is defined as the ratio of a sinusoidal voltage applied across two terminals of a measurement cell, to the sinusoidal component of the current flowing

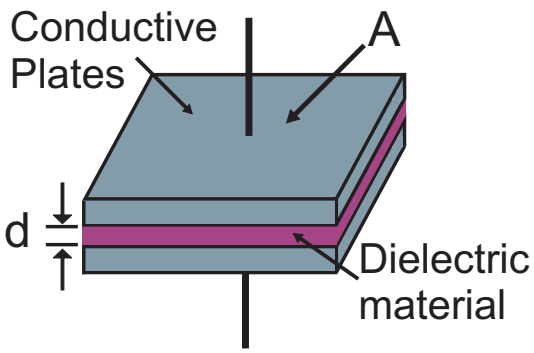

Figure 3.1: Parallel plate capacitor with a dielectric medium. The charge between two parallel plates creates an electric field, which is perpendicular to the plates. When a polarizing material is put between the plates it reduces the magnitude of the electric field.

between the terminals as a result of the applied potential difference. Assuming the measured material is not purely resistive, impedance will be a complex quantity as the current will be out of phase with the voltage [1].

3.1.1 Dielectric Relaxation with a Single Time Constant

When a polarizing material is subject to an external electric field, E-field, its response is typically a jump in the polarization followed by an increase to the static polarization, $\mathbf{P}_s$, at a rate that is proportional to the difference between the levels [2]. The time dependent response of the polarization can be characterized by,

$$\frac{d\mathbf{P}}{dt} = -\frac{1}{\tau}(\mathbf{P} - \mathbf{P}_s). \tag{3.4}$$

Debye coined the term 'relaxation time', τ, which he described as the time needed for the permanent molecular dipoles to reorient, or relax, following a change in the applied electric field. He found that the time lag between the average orientation of the moments and the E-field becomes noticeable when the frequency of the E-field is of the same order of magnitude as the reciprocal of the relaxation time. The Debye model of relaxation in a fluid like medium would be a set of non-interacting dipoles free to rotate against a viscous resistance. In a solid a more likely situation is the jumping by thermal excitation between two preferred orientations that are separated by a potential barrier [3]. This time dependent response can be modelled as an exponential function which means there is a lag time in the response to an oscillating

field. The time dependence of the polarization can be described as

$$\mathbf{P} = \varepsilon_0 \chi_e \mathbf{E} e^{i\omega t} \tag{3.5}$$

where $\mathbf{E}$ is the driving electric field and χ_e is the dielectric susceptibility which describes how easily the system polarizes. If the field remains for an infinitely long time the total polarization defines the static dielectric permittivity and shows the frequency dependence, given $(\varepsilon_s - 1)\varepsilon_0 \mathbf{E} = \mathbf{P}_s$.

The Debye interpretation requires independent uncorrelated dipole moments and is an idealised system. Debye equations for real, ε', and imaginary, ε'', permittivity are used to characterize dielectric relaxations,

$$\varepsilon'(\omega) = \varepsilon_{\infty +} \frac{(\varepsilon_s - \varepsilon_\infty)}{1 + \omega^2 \tau^2}, \tag{3.6}$$

$$\varepsilon''(\omega) = \frac{(\varepsilon_s - \varepsilon_\infty)\omega\tau}{1 + \omega^2 \tau^2}, \tag{3.7}$$

where ε_s is the dielectric constant at static conditions as described in equation 3.2 and ε_∞ is the dielectric constant at high frequency conditions.

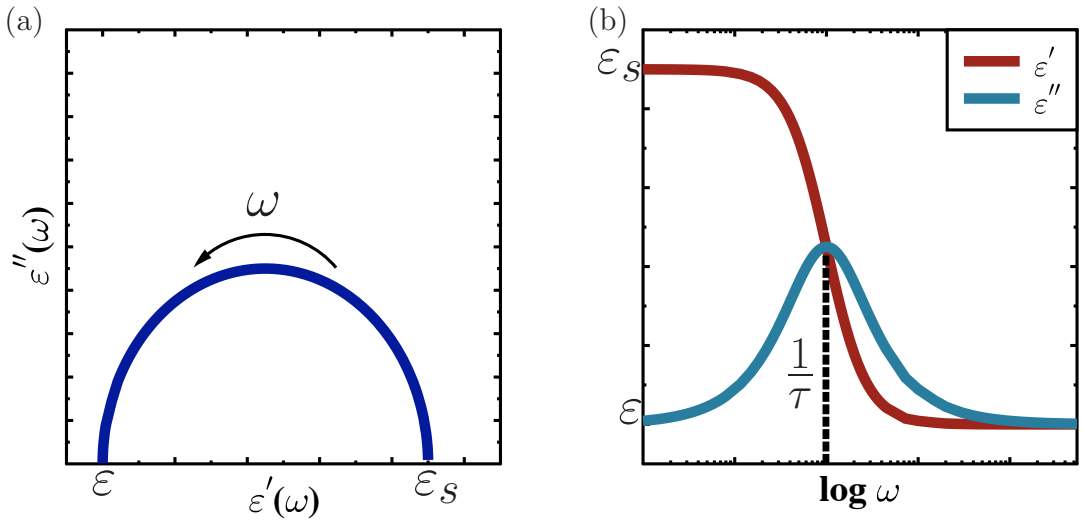

Figure 3.2: (a) Complex- plane Nyquist plot of a simple parallel RC circuit. (b) Bode plot.

These relaxations can be illustrated by means of different plot formats. Nyquist complex-plane plots are often used to display the data, in this method the imaginary impedance, -Im(Z)=Z″, or imaginary permittivity, -Im(ε)=ε'', is plotted against

the real impedance, Re(Z)=Z′, or real permittivity, Re(ε)=ε'. These plots have the disadvantage of not indicating the frequency directly, Figure 3.2(a). A semicircle is characteristic of the system relaxing with a single 'time constant'. The mid-point of the semicircle has a frequency $\omega_o = \frac{1}{RC}$. The macroscopic relaxation time, τ, for a Debye relaxation can be found from the frequency at which maximum loss occurs, ω_0. The relaxation time is dependent on the size of the molecular dipole and the micro-viscosity of its environment. Bode plots are used to show the frequency relationships, Figure 3.2(b). Three-dimensional Nyquist plots with a log-frequency axis can also be used to allow a more complete picture to be seen [4].

3.1.2 Frequency Dependence of Dielectric Constant

The value of dielectric constant varies with the frequency of the applied electric field and at certain frequencies energy is dissipated within the dielectric. The dielectric constant as a function of frequency is found to decrease by a series of sharp drops at certain frequencies and at each of these drops there is energy dissipation or dielectric loss, Figure 3.3. This suggests that at the frequencies where the discontinuities occur a polarization mechanism is turning off. It is turned off when it can no longer keep up with the applied field.

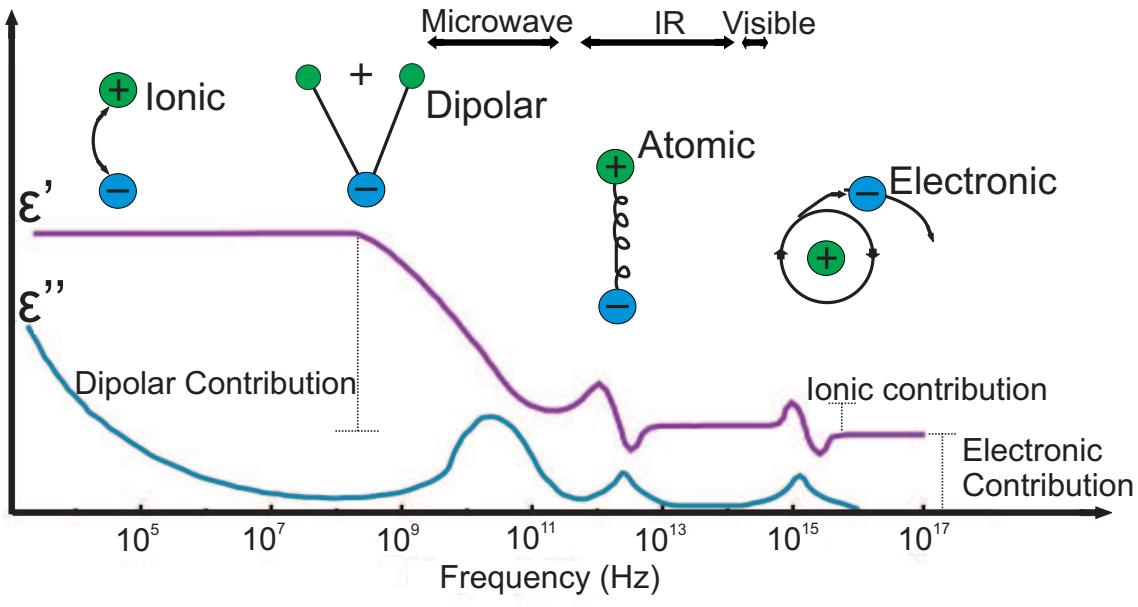

Figure 3.3: Dielectric response over a large frequency range showing the change in polarization processes.

When an AC current is passed through a capacitor the current leads the voltage

by 90°. When a dielectric is then inserted between the capacitor plates the molecules in the dielectric do not align instantaneously with the AC field. The angle by which the current leads the voltage is reduced. The magnitude of the reduction is known as the loss angle δ. The dissipation factor is then defined as $\tan(\delta)$ where,

$$\tan(\delta) = \frac{\varepsilon''}{\varepsilon'}. \tag{3.8}$$

Polar molecules have high dielectric power losses at certain frequencies, the maximum loss occurs at the point of inflexion in a dielectric constant-frequency curve, Figure 3.3. When the frequency of the applied E-field is low the dipoles can keep in phase with the changes in electric field and correspondingly the power losses are low. As the frequency is increased a point is reached when dipole reorientation is not completed before the E-field reverses and the dipoles become out of phase. This produces internal friction leading to the generation of heat. The dissipation factor is a measure of the energy per electric field cycle which is absorbed by the dielectric. When the frequency is further increased the dipoles do not have time to substantially move so the power loss is reduced. The dielectric loss is extremely dependent on temperature.

Often a particular technique only measures over a narrow frequency range so a technique is associated with a particular mechanism, this is not the case for impedance spectroscopy. The polarization mechanisms found in solids are described below and are illustrated on a broad logarithmic frequency scale in Figure 3.3.

Electronic Polarization – This is a process that arises from the displacement of electrons in neutral atoms with respect to the atomic nuclei they surround when subjected to an applied field, thus inducing a dipole moment.

Atomic Polarization – This is a process that arises when electrons in a molecule are shared asymmetrically and the electron cloud is shifted towards the stronger binding atom. The atoms acquire charges of opposite polarity so when an external field acts on them the equilibrium position of the atoms changes, inducing polarization.

Dipolar Polarization – In this process asymmetric charge distributions in dipolar molecules experience a torque in applied fields that orients them in the direction of the field. The time needed for the dipoles to relax is heavily dependent on the chemical surroundings of the dipole, the internal viscosity, and the temperature of the material. Usually dipoles are not able to rotate with an alternating E-field above frequencies of

10^9 Hz so above that their frequency contribution will not be observed [5].

Ionic Polarization – Ionic polarization is important in materials that have charge carriers that can migrate some distance through the bulk of the material. It is a mixture of ionic conductivity and interfacial or space charge polarization. This mechanism is a low frequency mechanism. Space charge polarization occurs when translating charge carriers become trapped at interfaces. The difference in the conductivity of the different materials leads to a build up of charge between them when a voltage is applied.

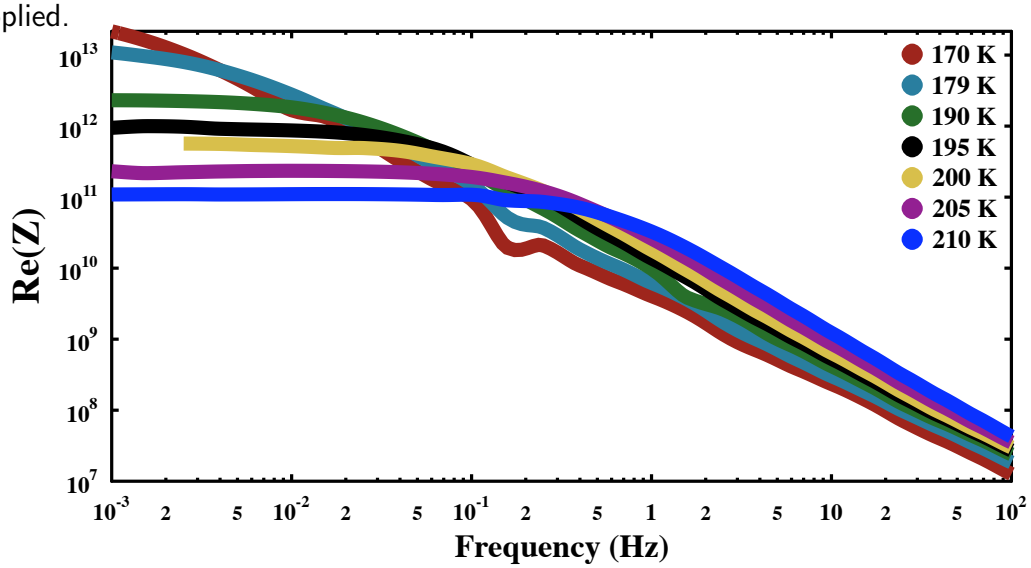

Figure 3.4: Real part of the impedance of $GdCrO_3$ at different temperatures.

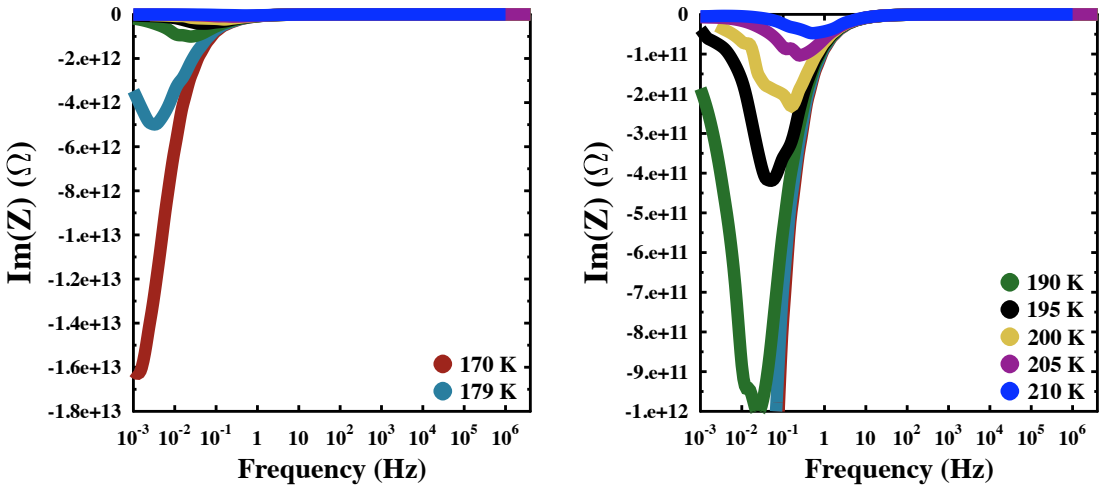

Figure 3.5: The imaginary part of the impedance for $GdCrO_3$ at several temperatures. There are large differences between the peak heights. The peaks move to lower frequency as the temperature decreases.

The Bode plots for $GdCrO_3$ at various temperatures are seen in Figures 3.4 and 3.5. Figure 3.4 shows the increase of impedance as temperatures decrease. Changes in the gradient of the real impedance between processes are mirrored in the peaks in the imaginary impedance, Figure 3.5. The relaxation features in Figure 3.5 are observed as peaks which shift toward higher frequencies with increasing temperature. For the data at 205 K (purple) the change in gradient in Figure 3.4 at approximately $2x10^{-1}$ Hz is observed in the peak in Figure 3.5, at the same frequency.

3.1.3 Equivalent Circuits

Impedance spectroscopy makes considerable use of equivalent circuits to represent the experimental frequency response. A significant advantage of impedance spectroscopy is the direct connection there often is between the behaviour of real systems and of idealized model circuit elements. The connection is not surprising as the laws which govern charge and potential do not change from electronic to ionic materials. The analogy between circuit elements and electrochemical processes is explained in this section. One danger of describing impedance results with equivalent circuits is that equivalent circuits are rarely unique with only the simplest circuits able to be classed as unambiguous. It is possible to have two different circuits that have the same overall impedance at all frequencies. Therefore it is necessary to keep the physical state of the material in mind.

Taking the two most basic circuit elements, the resistor and capacitor, the strengths of circuit modelling can be seen. If a sinusoidally varying potential is applied across a resistor the resultant current is,

$$v = V\sin(\omega t) \qquad \rightarrow \qquad i = \frac{V}{R}\sin(\omega t). \tag{3.9}$$

When the potential is applied to a capacitor current only flows when the potential is changing,

$$i = C\frac{dv}{dt} \qquad \rightarrow \qquad i = C\omega V\cos(\omega t) = C\omega V\sin(\omega t + \pi/2). \tag{3.10}$$

When these results are then put into the context of impedance, describing the restriction of current flow under conditions of changing potential, then

$$\text{For a resistor :} \quad Z(\omega) = R \qquad \text{For a capacitor :} \quad Z(\omega) = \frac{1}{j\omega C}, \tag{3.11}$$

where j represents the 90° phase shift. Impedances in parallel are combined as reciprocals so for a resistor and capacitor in parallel,

$$\frac{1}{Z(\omega)} = \frac{1}{R} + j\omega C \tag{3.12}$$

so,

$$Z(\omega) = \left(\frac{R}{1+\omega^2 C^2 R^2}\right) - j\left(\frac{\omega C R^2}{1+\omega^2 C^2 R^2}\right) \tag{3.13}$$

where the first term is the real, in-phase, component and the second term is the imaginary, out-of-phase, component.

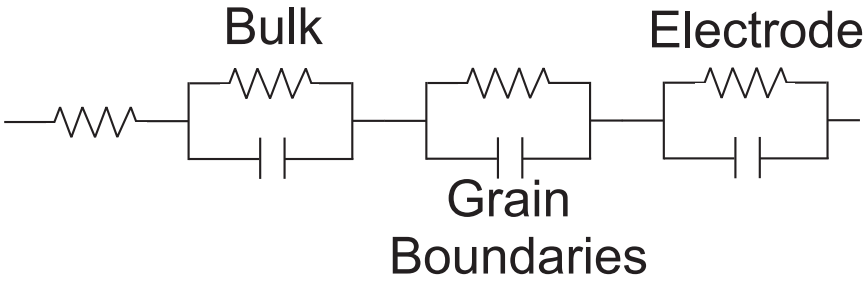

Figure 3.6: Equivalent circuit for a material. The parallel RC circuits represent the processes and the resistor in series is needed to represent the wires etc. leading to the parallel plate capacitor.

The fitting was done with unit weighting. Other circuit elements that introduce inductance, constant phase elements or Warburg impedance amongst others can be introduced but to make the models as unambiguous as possible they were kept as simple resistor capacitor circuits.

3.1.4 Material Properties

Single crystals are usually modelled as a pure resistance in parallel with a high-frequency ideal capacitor [1]. This would assume no electrode polarization. The contact resistance at the electrode is a consequence of current spreading from a high conductivity electrode into a low conductivity medium [6]. Solids in polycrystalline

form have multi-orientated grains that need to be accounted for. The grains, grain boundaries and electrode then need to be considered in the data analysis. The processes can often be differentiated by the capacitive range they occupy, Table 3.1.

Table 3.1: Capacitive Range

Process	Cacpacitance (F)
Bulk	10^{-12}
Grain Boundaries	10^{-11} to 10^{-8}
Sample/Electrode Interface	10^{-7} to 10^{-5}
Electrochemical Reaction	10^{-4}

A recently introduced representation of impedance data has been used as it enhances the discrimination between processes with relaxation frequencies that are very close [7, 8]. It is difficult to fit experimental data to equivalent circuits as it is hard to obtain a good fit when the difference between the relaxation frequencies of the contributing elements is small because there is uncertainty in the estimation of boundary frequencies [8]. This new representation allows the boundaries of the data representative of the bulk process to be identified so the fitting of this data is not influenced by the other processes.

In these graphs $L(\theta)$ defined as,

$$L(\theta) = \log\left(\frac{Z'}{Z''}\right) \tag{3.14}$$

can be plotted against $\log(f)$ and the change of slope is commensurate with a process changing into a transition between processes. The equation is then solved for each pair of successive points,

$$L\left(\theta\right)_i = \left(\alpha_\theta\right)_i \log\left(f_i\right) + \left(\lambda_\theta\right)_i, \tag{3.15}$$

the intercept, λ_θ, can then be plotted against the slope, α_θ, [7]. Each continuous line on the fit corresponds to a process and the change in direction provides a point at which a boundary of the frequency range of the processes can be drawn. These graphs can also be plotted in three dimensions using $\log(f)$ as the third axis. This is

useful as the slope against the intercept is not an explicit function of frequency and this can result in some overlapping.

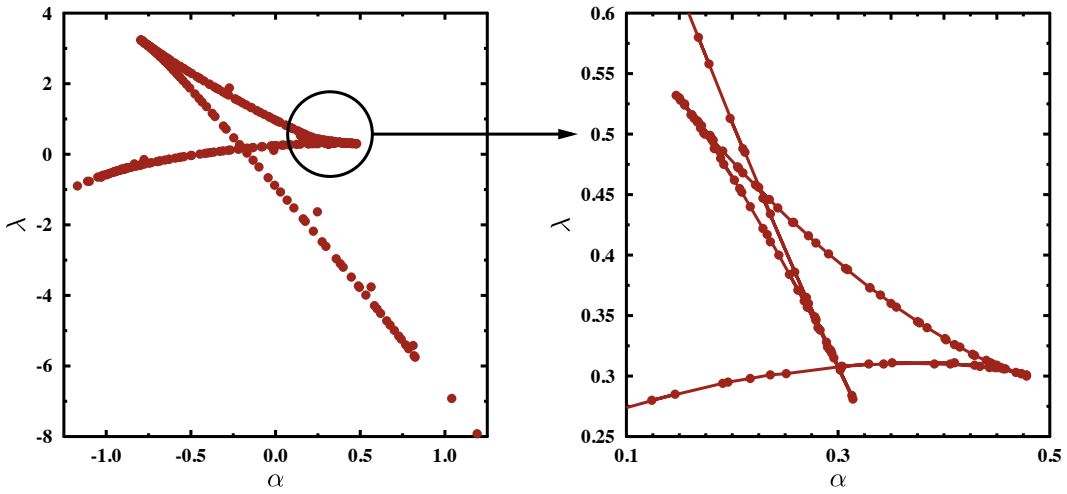

Figure 3.7: Alternative plotting to see the transition between processes. The data plotted describes $LaMnO_3$ at 124 K.

Graphs like Figure 3.7 can then be used to define the fitting boundaries for all the data. When processes are overlapping equivalent circuit fitting can lead to incorrect values which is why the fitting range is determined by the plots in Figure 3.7 which discriminate between the processes. The bulk, grain boundaries and electrode, Figure 3.6 can then be modelled by parallel resistor capacitor circuits. The contribution from the wires etc. is modelled with the resistor in series to the other elements, Figure 3.6.

3.1.5 Relevant Processes

Interfacial polarization was one of the first types of polarization to be recognized and is known as Maxwell-Wagner polarization [9]. The Maxwell-Wagner relation is due to the addition of charges at an interface which results in dielectric dispersion and losses. It describes the interfacial polarization due to capacitive barrier layers associated with grain boundaries or dislocations. These can also be described by an equivalent circuit [10]. Occasionally the Maxwell-Wagner effect at interfaces between sample and electrode gives rise to a large contact capacitance and results in a large dielectric constant. This can sometimes be mistaken for a bulk response. At the interface of electrodes in solids an inner layer capacitance is expected as there is a finite distance, even at the closest approach, between the ions and the interface, which

is of the order of a few angstroms.

Samples were cut to have two parallel faces with well-defined cross sections which were then polished. A rough electrode can be modelled with distributed circuit elements but a clearer picture arises if roughness is minimised. To avoid this problem an adhesive 10–15 nm layer of chromium was evaporated onto the parallel surfaces followed by a 200–250 nm layer of gold that would be in contact with the parallel plates. This removes the problem of the electrode not being in contact with the whole surface of the sample. The discontinuity in charge transfer at the interface between a sample and electrode results in an interfacial impedance. This is seen in many of the experimental results. Electrode effects usually occur at the lower end of the frequency range [1].

A behaviour known as relaxor ferroelectric behaviour is seen in some of the materials in this thesis. Polar nanoregions are believed to be responsible for the unusual physical properties which include a broad frequency and temperature dependent maximum in the dielectric permittivity and the freezing of the polarization below a peak temperature [11]. The absence of long-range ferroelectric order in zero field at any temperature is also a prerequisite for a relaxor ferroelectric. Polar nanoregions (PNR) are a network of randomly interacting dipolar entities which have a corresponding distribution of their size and dipolar strength [12]. In some ways this is reminiscent of a magnetic spin glass. The size of PNRs increases as the temperature decreases and then saturates. A high dielectric constant is typical of these materials [12]. Only disordered systems exhibit relaxor behaviour so disorder and/or frustration are important factors [12].

In some cases results that appear to show relaxor behaviour can in fact be due to conductive artefacts [13]. Relaxor behaviour can appear in heterogeneous materials as a result of the Maxwell-Wagner effect. As the Maxwell-Wagner effect does not require contact related depletion layers, it can be due to defects, it is not possible to simply change electrodes to remove the effect. This needs to be taken into account when analysing data [14].

3.2 Instrumentation

3.2.1 Frequency Response Analysis

The instrumentation and data analysis described in this chapter were for use in conjunction with a *Solartron 1260 Frequency Response Analyser* (FRA) and a *Solartron 1296 Dielectric Interface*. The *Solartron 1260* covers a frequency range of 10 μHz to 32 MHz.The frequency range used for the measurements described in this chapter was between 1 mHz and 32 MHz depending on the sample characteristics. A frequency response analyser determines the impedance of a sample by correlating a cell response with two synchronous reference signals [1] at each frequency. One reference signal is in-phase with the applied signal and one is 90° out of phase with it. Auto-integration averages the results over a number of cycles which is automated to yield statistically significant results [1].

The sine correlation technique rejects harmonics and DC offsets, noise effects are also significantly reduced. This technique is achieved by correlating input signals with reference sine waves and integrating over complete cycles. The frequency response analyser consists of a sine wave generator which sends a very pure sinusoidal excitation signal to the item under test and to one or more analysers. After it has passed through the test item the sine wave is then compared to the pure sine waves sent directly to the analysers. One analyser usually measures the voltage signal and the other the voltage waveform which is proportional to the current, Figure 3.8. The result of the correlation is made up of an imaginary and a real component and the magnitude and phase of the measured signal can be found. The correlation process can be considered as a highly tuneable bandpass filter.

The generated voltage can be varied between 0 to 3 V below 10 MHz and to 1 V above this. The steady state output of a linear system excited by a sine wave is its self a sine wave and is made linear by applying a suitably small perturbation. Impedance should be independent of the amplitude of the applied signal. Small applied voltages were used in this experiment which is an advantage of impedance spectroscopy compared to other techniques.

The measured system output is multiplied by the sine and cosine at the test frequency, ω. To avoid measurement errors the results of the multiplication are sent to integrators where they are averaged over a whole number of cycles which results in the unwanted frequency components going to zero. The longer the integration time

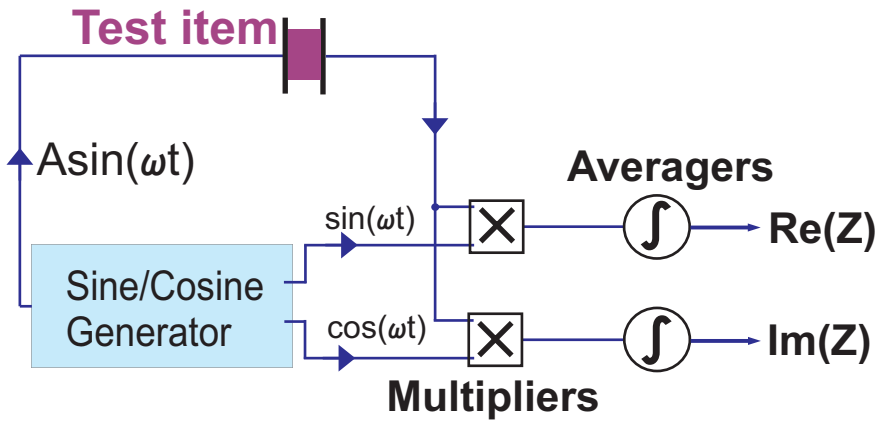

Figure 3.8: Frequency response analysis in the *Solartron 1260 FRA*. The outputs are the real impedance, Re(Z), and the imaginary impedance Im(Z).

the more complete the rejection of the noise.

The *Dielectric Interface 1296* extends the measurement capabilities of the *Solartron 1260*. The current measuring range is extended from 6 μA to 100 fA which enables the measurements of very high impedances. The *Dielectric Interface 1296* also increases the sensitivity of measurements at low frequency. It has the facility to enable the sample capacitance to be compared to high quality internal or external reference capacitors. For the purpose of these experiments only internal reference capacitors were used. Impedance measurements made with this interface can exceed 100 TΩ however the frequency range is slightly reduced to 10 μHz—10 MHz. This is useful for materials with low conductance (high impedance). Deviations due to the voltage divider effect occur when the measured impedance is 1% of the input resistance of the FRA [6]. The *1296* acts to greatly increase the input resistance extending the range over which this effect is not significant [15].

For dissipation factor ($\tan(\delta)$=$\varepsilon''/\varepsilon'$), measurements where ε'' is very small and ε' is large, the resolution of $\tan(\delta)$ is critical for an accurate measurement. The *Dielectric Interface* overcomes this issue by taking a reference measurement on a precision capacitor, which is substituted for the sample and then a measurement is made on the sample itself. The first measurement is used to eliminate the effects of extraneous capacitance.

3.2.2 Parallel Plate Electrode Puck

Many different practical aspects had to be taken into consideration in the design of a device to measure dielectric constants at cryogenic temperatures and high magnetic fields. The design of the puck for taking the measurements, shown in Figure 3.9, has combined the desire for quality results with the need for ease of use.

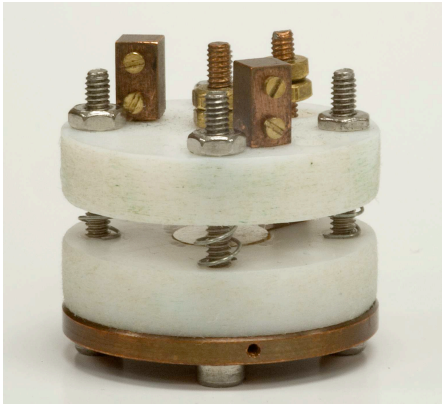

Figure 3.9: Photograph of the parallel plate capacitor puck with electrodes sunk into PTFE discs. The screws that hold the plates together are spring loaded.

The choice between 2, 3 or 4 point measurements had to take these aspects into account [16]. Two point measurements can include many errors however using the *Solartron 1260* and the *1296 Dielectric Interface* many of these can be corrected for by reference measurements and subtractions. 4 point measurements are ideal for bulk characterizations however reliable 4 point measurements are difficult in practice [17]. Taking these factors into consideration a set-up that can utilise both 4 point and 2 point contact arrangements was created to allow the greatest range of accurate measurements. The parallel plates for the two point measurement, discussed previously, were sunk into PTFE discs and connected to copper screw threads onto which connecting coaxial cables could be attached [18]. Electrodes are usually made of precious metals such as silver, gold or platinum [2]. Silver was chosen for the parallel plates in the instrument as there is minimal performance difference between these metals but a large cost advantage. The screws that hold the sample between the plates were spring loaded to ensure an even distribution of pressure. Holes were put in the top PTFE disc for extra cables when 4 point measurements were used. Small copper blocks with two screws in were mounted onto the disc so the extra coaxial cables could be screwed to the block and connected to smaller wires that could be attached to the sample with

silver paste.

The *Solartron 1260* is capable of making 4 point measurements [19] however in practice parallel plate measurements were found to be more reliable and were used for all the measurements in this thesis. This was established through extensive test measurements.

3.2.3 Cryogenic and Practical Considerations

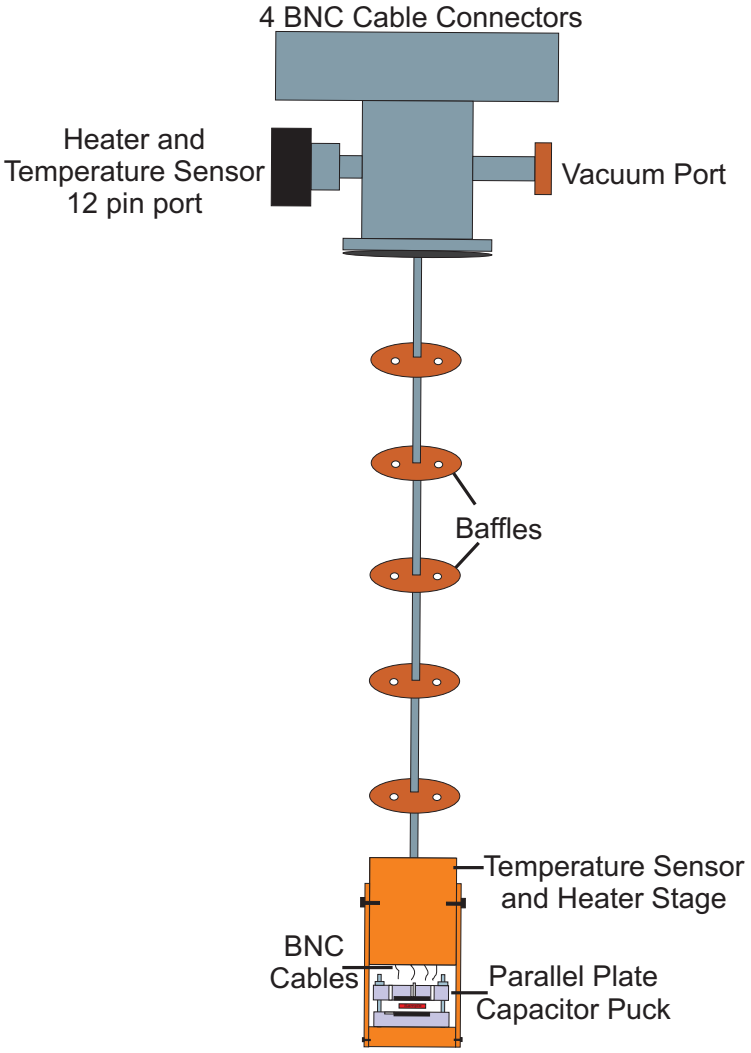

Figure 3.10: Diagram of impedance spectroscopy insert for cryostat, this is not to scale. Baffles were used to reduce the temperature gradient. The vacuum port was included for when it needed to be enclosed and the instrument needed to be pumped out.

The rest of the device was designed with thermal, magnetic field and noise constraints in mind. The puck was placed in a copper cylinder and a temperature sensor

attached to the connected copper block, as close to the puck as possible, to give the best thermal reading of the sample. GE varnish diluted with toluene and methanol was used to attach the temperature sensor. Cigarette paper was placed underneath the sensor and its wires to electrically isolate them from the copper block beneath. The temperature sensor was calibrated before being attached to the instrument by cycling it through the whole temperature regime possible on the cryostat alongside another sensor that was already calibrated. It was important when taking measurements to wait for a stable temperature especially with the sensor being slightly displaced from the sample. As the top of the insert is at room temperature while the bottom is at cryogenic temperatures baffles were placed along the length of the insert to reduce the temperature gradient, Figure 3.10. A manganin wire heater was wound around the top of the copper block. Approximately 150 Ωs is needed to produce the heat necessary to be able to sit stably at a constant temperature. 130 W/m wire was used so it was possible to calculate how much was needed. It was covered with GE varnish to prevent the insulation on the outside of the wires being damaged and causing electrical shorting.

The best way to prevent high frequency artefacts from the wires contaminating the signal is to keep them short so this was done to as great an extent as possible [20]. The wires for the sensors consisted of twisted pairs to cancel out the field induction. A break-out board was placed half way up the inner tube so that broken wires to the temperature sensor could be more easily replaced without having to replace the whole length making it much easier to find which wire was broken. The wires were attached to the rod between the baffles to reduce thermal vibration [15]. As the samples were not moisture sensitive it did not matter if condensation occurred on them when the insert was removed from the cryostat so the device was not placed in a shield, this means that the helium gas, introduced into the sample space through a needle valve, acts as an exchange gas and temperature control is much more effective. The device was constructed so it could be used in high magnetic fields but unfortunately due to liquid helium sourcing constraints this was not possible and would be a good opportunity for further work.

3.3 Dielectric Response Fitting

The preferred analysis method for fitting impedance spectroscopy data to equivalent circuits or mathematical models is complex least squares fitting [21]. This procedure

allows all the parameters of the model to be simultaneously adjusted resulting in an optimum fit.

3.3.1 Calibration

The data needs to be calibrated to take into account the resistance and induction of the apparatus that are not a result of the system under test. The following equation can be used to extract the actual impedance of the system,

$$Z = \frac{Z_p(Z_m - Z_s)}{Z_p - (Z_m - Z_s)}, \tag{3.16}$$

where Z_S is the shorted (close circuit) impedance and Z_p is the empty (open circuit) sample holder impedance [20]. Modern FRA analysers have a built in nulling procedure but it can also be performed externally. After calibration high frequency effects from the *Solartron 1260 FRA* will have been subtracted.

3.3.2 Kramers-Kronig Transforms

The Kramers-Kronig transformation allows the validity of the impedance data to be confirmed for a linear system over a wide range of frequencies. The relations were developed in the field of optics and are integral equations which constrain the real and imaginary components of complex quantities when the system they are applied to satisfies causality, linearity and stability. It is a retrospective check on the validity of the impedance data set. The imaginary component of impedance can be calculated from the real part through

$$Z_i(\omega) = \left(\frac{2\omega}{\pi}\right) \int_0^\infty \frac{Z_r(x) - Z_r(\omega)}{x^2 - \omega^2} dx, \tag{3.17}$$

and the real part can be obtained from the imaginary part through

$$Z_r(\omega) = Z_r(\infty) + \left(\frac{2}{\pi}\right) \int_0^\infty \frac{xZ_i(x) - \omega Z_i(\omega)}{x^2 - \omega^2} dx, \tag{3.18}$$

where $Z_i(\omega)$ and $Z_r(\omega)$ are the frequency dependent imaginary and real parts of the impedance respectively. Equation 3.17 is usually expressed with a minus sign which reflects the convention to present complex impedance with the coordinate system $(-Z_i(\omega)Z_r(\omega))$ [22].

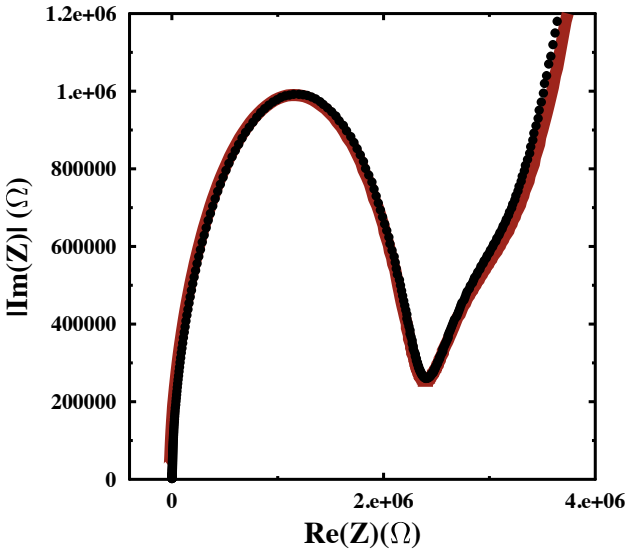

Figure 3.11: The black points are impedance data of $LaMnO_3$ at 124 K. The red line is the Kramers-Kronig transformation of this data. The transformation matches extremely well to the bulk response indicating good quality data. The only slight divergence is around the electrode response.

Figure 3.11 shows the impedance results from $LaMnO_3$ at 124 K in black and the Kramers-Kronig transformation of the data in red, where the real and imaginary parts have been calculated from each other. The data and the transformation map extremely well onto each other showing the validity of the data. The only slight divergence is observed in the region of the electrode response. Linearity was assured by using a sufficiently small amplitude perturbation. This means that the current response to a sinusoidal potential will be sinusoidal at the same frequency but of different phase. If a system is non-linear then the current will contain harmonics of the excitation frequency. Stability occurs when the system returns to its original state when the perturbation is removed.

3.4 Experimental Results

3.4.1 $LaMnO_3$ Impedance Analysis

$LaMnO_3$ is an A-type antiferromagnet with $T_N = 140$ K which is driven by orbital order. $LaMnO_3$ is not a multiferroic but was chosen as the test case for the instrumentation for two reasons. Work had been recently published looking at the dielectric behaviour of this compound where exactly the same equipment was used; the *So-*

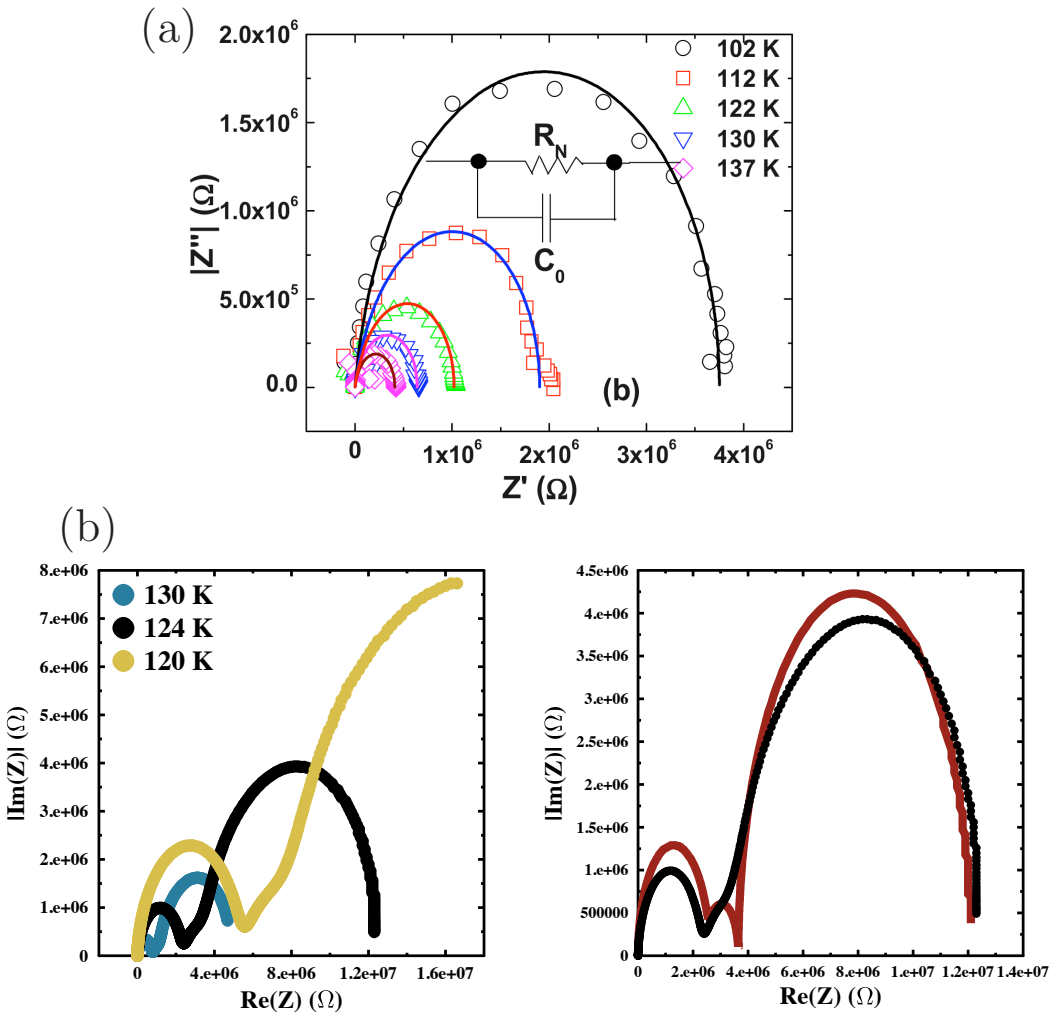

Figure 3.12: (a) Complex plane impedance plot of $LaMnO_3$ from [23] also showing the parallel circuit to which the plots are fitted. (b) The left panel shows impedance arcs of $LaMnO_3$ at different temperatures. This shows the change in arc size with temperature. The right panel shows the data at 124 K (black) and the fitting to three parallel resistor and capacitor elements in series (red). A better result is found when all three arcs are fitted separately.

Iartron 1260 and *Dielectric Interface 1296* [23]. The scope of their experiments was also in line with the aims of this study and the analysis was done using equivalent circuits. $LaMnO_3$ is also of the same family as many multiferroics so comparisons can be made especially as the work was conducted on a single crystal like the majority of materials in this thesis.

A single crystal of $LaMnO_3$ was aligned with X-ray Laue and was found to have the orthorhombic c-axis 24° from perpendicular to the flat gold coated faces. As the aim of this experiment was to compare these results to published results that had specified a single crystal grown in the same manner but not of a specified alignment this lack of perfect alignment was not considered a problem. Magnetic measurements on $LaMnO_3$ were performed with a Superconducting Quantum Interference Device (SQUID) magnetometer. The magnetic ordering transition temperature was found at 138 K.

The change in arc size with temperature is shown in Figure 3.12(b) this can be compared to the results of previous work shown in Figure 3.12(a) [23]. The larger arc was found to have a capacitance much greater than the range of a bulk response, and so is likely to be due to the electrode. It was possible in this study to acquire many more measurement points than were presented in the published data [23]. A resistor in series, as shown in Figure 3.6, represents the resistance of the things such as the leads used to connect the cells to the measuring system. This results in an offset along the real axis of a Nyquist plot and is seen as an identical contribution to all the measurements of every sample in the raw data.

The magnitude of the bulk response arcs, Figure 3.12(b), are of the same order as those seen in Figure 3.12(a) at equivalent temperatures. The right panel of Figure 3.12(b) shows the data for 124 K in black with a fit to three parallel resistor capacitor circuits in red. There are two main arcs with a possible third feature between them. When this feature is modelled as an arc it also has a capacitance much larger than a bulk response. The strength of the alternative representation, where the boundaries of the process can be clearly defined, is seen here in the ability to separate accurately the bulk response. The red fit looks faithful to the raw data however improved fits to the bulk response were found when the arc was fitted separately. The fitting frequency boundaries were found as in Section 3.1.4.

A relaxation process is seen in the graph of $\tan(\delta)$ against temperature, Figure 3.13. For a thermally activated dielectric relaxation process an activation energy can be found from the Arrhenius law,

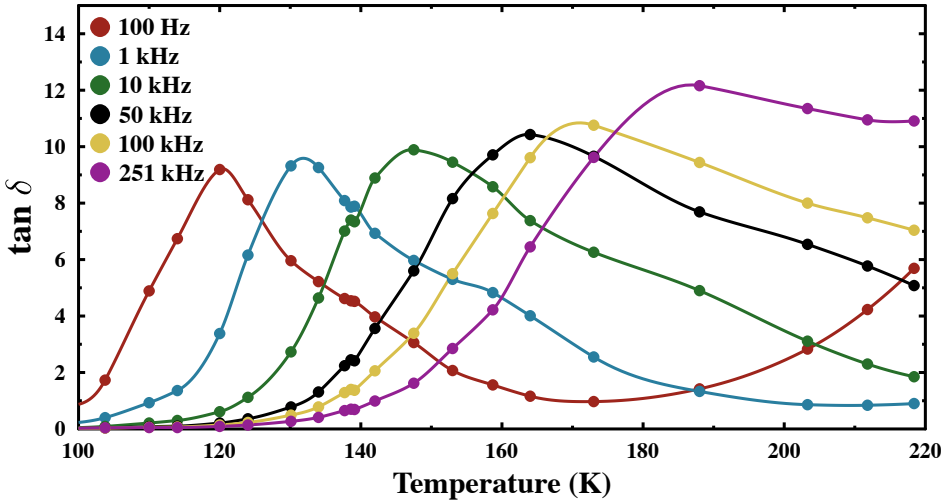

Figure 3.13: The dielectric loss change with temperature in $LaMnO_3$ at different frequencies is shown. The peaks become broader and show an increasing peak height at higher frequencies.

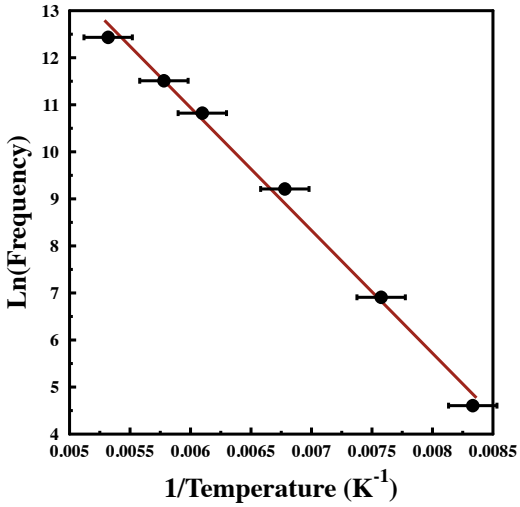

Figure 3.14: $LaMnO_3$ Arrhenius Plot of the natural log of frequency against the $\tan(\delta)$ peak positions. The best fit line is shown in red.

$$f = f_0 \exp(-E_a/k_B T_p) \tag{3.19}$$

where E_a is the activation energy, f_0 is the characteristic relaxation frequency at infinite temperature, k_B is the Boltzmann constant and T_p the peak temperature. The activation energy is the energy needed for the direction of the polar regions to be switched. The peaks were fitted with Gaussian line shapes and the resultant peak positions plotted against the natural logarithm of frequency and the best fit line found, Figure 3.14. The dielectric loss peaks give an Arrhenius relation with an activation energy of E_a=0.22±0.008 eV.

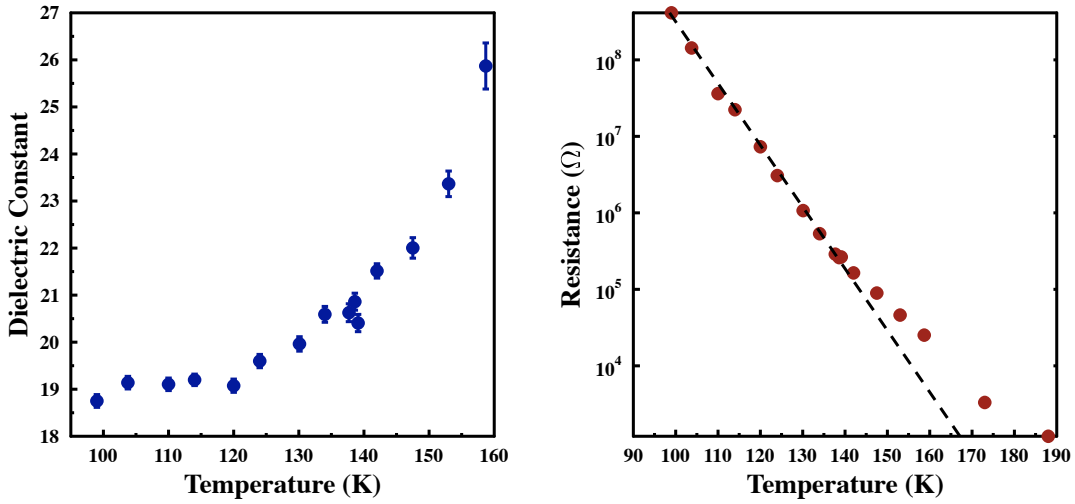

Figure 3.15: The dielectric constant of $LaMnO_3$ against temperature is shown on the left with the low temperature constant found to be between 18 and 19. The resistance in the same temperature range is shown on the right. A change of gradient is observed at around 140 K.

A static dielectric constant, $\varepsilon_s = \varepsilon'(T \to 0)$ of 16–21 in $LaMnO_3$ has been observed previously [14, 25, 26]. The low temperature value observed in Figure 3.15, extracted from capacitance values found from equivalent circuits, looks like it will lie between 18 and 19 which is in agreement with these results. Previous results have observed a dielectric anomaly at T_N, Figure 3.16 [23]. The equivalent dielectric constant values cannot be extracted from their capacitance data without knowing the dimensions of the sample. This was an unexpected result showing a coupling of the magnetic and electric order parameters that had not been observed in other studies [25]. However, using the same experimental techniques and equivalent circuit fitting this study was not able to reproduce the results. From the results observed

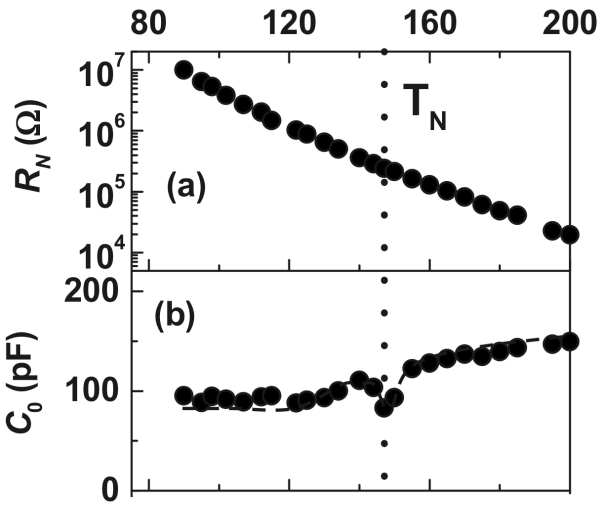

Figure 3.16: The resistance (a) and capacitance(b) values varying with temperature in $LaMnO_3$ as found in [23]. The values were extracted from equivalent circuit fits.

in this investigation there does not appear to be a feature at the magnetic ordering transition in the dielectric constant results directly calculated from the capacitance data, Figure 3.15.

An obvious gradient change is observed in the resistance at the magnetic ordering temperature $T_N = 140$ K, Figure 3.15. The values were extracted from the same equivalent circuit model as the capacitance. Previously reported results have shown no such feature, Figure 3.16 [23]. It is possible that the dielectric anomaly observed by [23] is due to a resistive component of the dielectric response and the Maxwell-Wagner effect which can mimic a multiferroic system. They had discounted this possibility as they did not see a resistive feature. However given the feature in the resistance observed here, Figure 3.15, and the lack of capacitive feature observed here and in other studies under the same conditions [25] this explanation could be valid.

3.4.2 $GdCrO_3$ Impedance Analysis

$GdCrO_3$ is a member of the distorted perovskite rare earth chromite family. Recent publications have claimed to observe multiferroic behaviour in this family [27] however these chromites have a centrosymmetric space group which is not compatible with ferroelectricity. The suggested mechanism is that they remain globally centrosymmetric but have a locally non-centrosymmetric structure. The magnetic properties of this

series are investigated in Chapter 6. $GdCrO_3$ becomes a canted antiferromagnet at $T_N = 170$ K with the antiferromagnetic moments along the orthorhombic a-axis and a weak ferromagnetic moment along the orthorhombic c-axis.

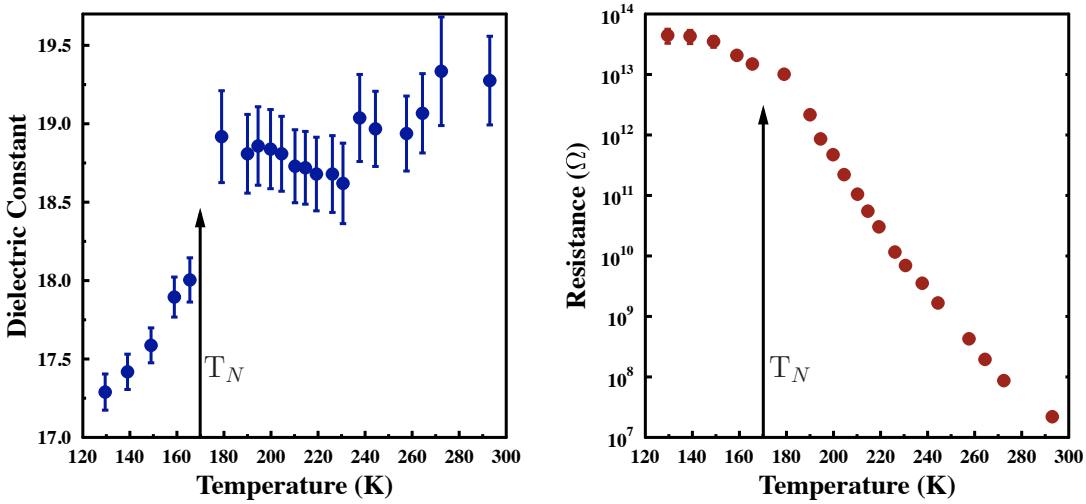

Figure 3.17: Dielectric behaviour of $GdCrO_3$ at the magnetic transition temperature showing an anomaly in the dielectric constant and the resistance.

The impedance spectroscopy work shown here aims to clarify the dielectric properties. These measurements cannot confirm ferroelectricity but can add information to the overall picture of the electrical properties. Dielectric results are important for finding electronic anomalies at magnetic ordering transitions which can indicate coupling between the order parameters. The single crystal of $GdCrO_3$ was aligned with X-ray Laue, the orthorhombic a-axis was aligned perpendicular to the flat gold coated faces with the orthorhombic c and b axes in the plane.

The dielectric constant for a bulk polycrystalline sample of $GdCrO_3$ at room temperature has previously been reported as 23 [28] whereas for nanoparticles it was found to be 12 at 300 K and 1 kHz [29]. For this study, on a single crystal, a dielectric constant of between 19 and 19.5 at room temperature was found, Figure 3.17. Figure 3.17 shows a dielectric constant that increases with increasing temperature. The values for the dielectric constant do show a general agreement with other results with differences perhaps due to this work being done on a single crystal.

There is a feature in the dielectric constant around the magnetic ordering transition however this does not necessarily suggest any type of coupled response, it is likely that it is in fact a resistive effect. The capacitance change is very small with significant

error whereas the change in resistance is large and well defined. The anomaly could also be due to a structural transition or lattice modulation.

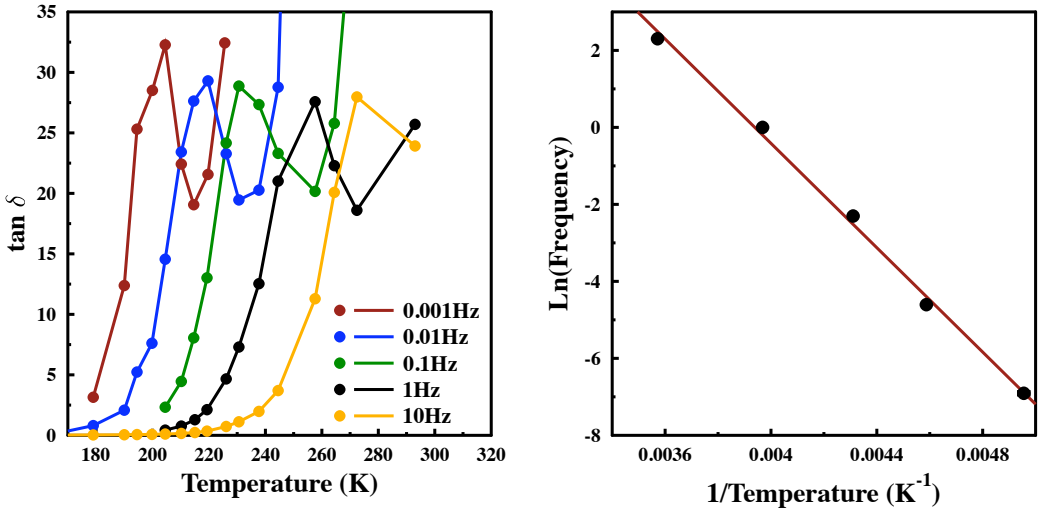

Figure 3.18: The left panel shows the dielectric loss in $GdCrO_3$. A small peak is seen at temperatures from 180 K to 270 K with the start of a larger one forming for each frequency. As the frequency increases the peak moves to high temperatures. In the right panel the Arrhenius plot of the temperature at which the peaks occur against the frequency is shown. A good straight line has been fit to the data.

Another consideration is that it is thought that $GdCrO_3$ experiences a strong thermal excitation of charge carriers from around 170 K which would transform the material from a good insulator to a semiconductor, the charge carriers may for example be oxygen vacancies [30]. This would cause an increase in the dielectric constant as dipoles will form from delocalised charge carriers and the shielding of opposite charges. This will be accompanied by an energy absorption which can be observed in $\tan(\delta)$.

Peaks in $\tan(\delta)$ are observed in the left panel of Figure 3.18 which then lead into larger peaks which continue to rise to room temperature. The peaks were fitted with Gaussian line shapes and the resultant peak positions plotted against the natural logarithm of frequency and the best fit line found, right panel of Figure 3.18. The error bars from the fitting are so small they cannot be seen. The dielectric loss peaks give an Arrhenius relation with an activation energy of E_a=0.58±0.019 eV. This is determined from the lower peak although clearly there will be another one at higher temperatures.

3.4.3 $LuFe_2O_4$ Impedance Analysis

$LuFe_2O_4$ is a type I multiferroic material in which ferroelectricity develops as a result of charge ordering, this mechanism is referred to as 'Electronic Ferroelectricity' as described in Section 1.5.1. In this mechanism the electric dipole depends on the electron correlations rather than the covalency [31]. $LuFe_2O_4$ has been shown to generate a large spontaneous polarization of 0.24 C/m^2 [32] and have a large dielectric constant of about 10,000 at room temperature [33]. Previous dielectric results have found a hump in the dielectric constant at the transition from 2D to 3D charge order [31] and large changes in the dielectric constant have been observed when small magnetic fields were applied [34]. There is also strong coupling of the spins and electric dipoles at room temperature. This makes $LuFe_2O_4$ a particularly interesting material to investigate with this technique.

A single crystal of $LuFe_2O_4$ was aligned with X-ray Laue and was found to be orientated with the hexagonal c-axis 15° perpendicular to the flat gold coated faces. As this was a single crystal, which was not that easy to separate in this material, of the right size and was flat enough that it could be easily polished to have perpendicular faces it was used despite the lack of perfect alignment. In terms of magnetic properties $LuFe_2O_4$ exhibits quasi 2D ferrimagnetic order below $T_N = 240$ K. The spins point along the c-axis and there is a net magnetic moment of approximately 2.8 μ_B [35].

Figure 3.19(a) shows a result that has not been observed before. The anomaly in the capacitance, and therefore ε, at $T_N = 240$ K, the ferrimagnetic ordering temperature, has not previously been observed and indicates the coupling between the electric and magnetic order parameters. The corresponding dielectric constant is 25 at 100 K increasing up to 48,000 at room temperature. The low temperature constant has previously been found to be of the order of 10 [36]. The room temperature constant found from Figure 3.19 is five times larger than reported results [34]. The published dielectric constants have always been given as single frequency measurements.

As coupling between the order parameters is of great interest in multiferroic systems this is a significant result. Although signals of coupling of the magnetic and electrical order parameters at the magnetic transition have been seen before this is the first time it has been seen with this technique. There was no significant error associated with this temperature point as illustrated by the error bars being mostly too small to see. This suggests that what is seen here is a genuine coupling effect.

Unlike in $GdCrO_3$, Figure 3.17, there is not a resistive feature at this ordering

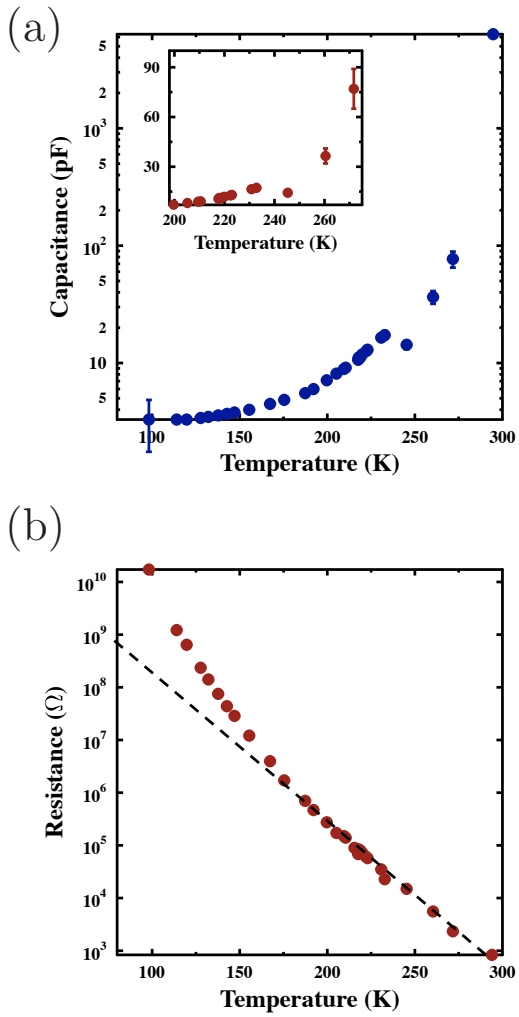

Figure 3.19: (a) Capacitance of $LuFe_2O_4$ showing a capacitive feature at the magnetic ordering transition. The inset is a closer view of the discontinuity. (b) Resistance of $LuFe_2O_4$ showing a change in gradient which is not at the magnetic ordering transition. The dashed line is simply a guide to the eye.

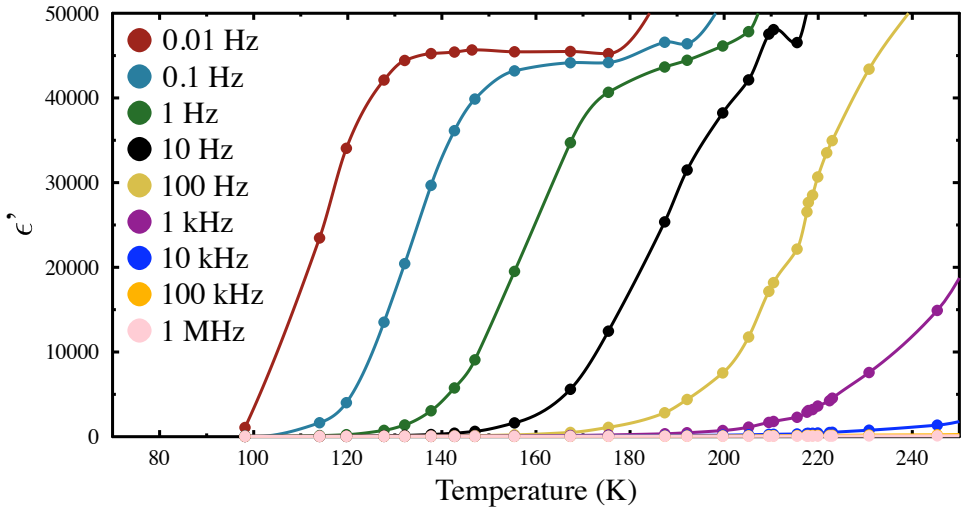

Figure 3.20: $LuFe_2O_4$ boundary motion temperature dependence. This figure shows that as the temperature increases the electrons can hop to follow the field at higher frequencies.

temperature, 240 K, Figure 3.19(b). There is however a change in the gradient of the resistance below 200 K. This resistance temperature relationship has been observed previously [37] however no explanation was suggested. The magnitude of the results over the temperature range also agrees well with the previous results [37]. This suggests that the capacitance results are even more likely to be reliable as the resistance and capacitance values are extracted with the same model. Capacitance data has not been presented before but that the resistance agrees so well with other results adds weight to the model. The $R Fe_2O_4$ family have been found to be well described by a Debye single relaxation time process which was also found in these results by the successful fitting of single complex plane arcs.

Figure 3.20 shows a step-wise increase in ε' which shifts to higher temperatures with increasing frequency. There is a discrepancy between the constants that have previously been observed with the commonly accepted result being around 5000 [31]. However subsequent results taken by the same group on samples which they assumed had the same stoichiometry were found to have a constant of the order of 10 times higher [37]. The isostructural $ErFe_2O_4$ also shows an amplitude in ε' of the same magnitude as that seen in Figure 3.20. The frequency dispersion is commonly observed in the $R Fe_3O_4$ family with sharp rises in ε'.

The frequency dispersion is due to the presence of ferroelectric domains and their boundary motion. The ferroelectric domain boundary movement is the exchange of

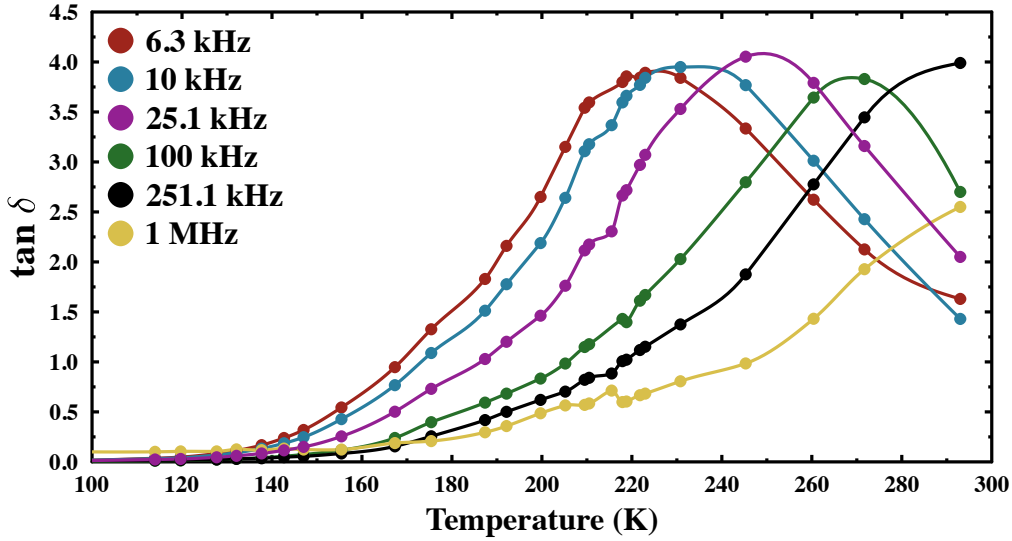

Figure 3.21: $LuFe_2O_4$ $\tan(\delta)$ dielectric loss plot showing the peaks moving to higher temperatures with increasing frequency. The greater the temperature the faster the electrons can hop across domain boundaries.

electrons between the Fe^{2+} and Fe^{3+} atoms at the boundary. The hopping is due to the charge interaction between the Fe^{2+} and Fe^{3+} ions. This hopping mechanism only works when the temperature is high enough for the electrons to be able to follow the applied field. This mechanism gives a large dielectric response in the frequency range in which the wall motion can follow the change of applied field, producing the observed frequency dependence. Electron fluctuations have a central role in ferroelectric domain wall motion.

The dielectric loss peaks, shown in Figure 3.21, give an Arrhenius relation with E_a=0.30±0.018 eV. The activation energies have previously been found to be E_a=0.25 eV [36], E_a=0.29 eV [31] and E_a=0.30 eV [37] parallel to the hexagonal c-axis and E_a=0.29 eV [31] and E_a=0.26 eV perpendicular to the hexagonal c-axis [36]. These low activation energies of the electron motion suggest a lower coupling of the polarization with the lattice distortions [31]. Such low activation energies could find practical applications in devices such as fatigue free capacitors.

Mössbauer spectroscopy has been used to find the valence fluctuation frequency of the iron ions [38]. When this data is added to a frequency against inverse temperature graph it extrapolates to the same gradient as the dielectric loss data. This indicates that the electron fluctuations of the iron ions play an important role in the dielectric response and motion of the ferroelectric domain walls. The same activation energies as seen for the dielectric results are seen for magnetic AC susceptibility results [37]. This

again illustrates the coupling between the magnetic and dielectric order parameters.

3.5 Conclusions

Impedance spectroscopy is ideal for looking at multiferroics as the times scales are perfect for looking at dipole motion and domain wall motion. These experiments have been unable to reproduce a feature previously reported in $LaMnO_3$ at the magnetic ordering transition. This is an interesting result which agrees with a complementary study and suggests that the feature seen before may have been an artefact. An unexpected feature at the magnetic ordering temperature of $GdCrO_3$ has also been found. A dielectric feature at the magnetic ordering temperature in $LuFe_2O_4$ has been observed which is evidence of coupling between the order parameters. The activation energy of the ferroelectric domain boundary movement, the exchange of electrons between the Fe^{2+} and Fe^{3+} atoms at the boundary, has been calculated from the data and found to agree with previously reported results. The instrumentation created for this study can be used to more fully investigate multiferroic materials at cryogenic temperatures and in high magnetic fields.

Bibliography

[1] J. R. Macdonald, Annals of Biomedical Engineering **20**, 289 (1992).

[2] J. R. Macdonald, *Impedance Spectroscopy*, John Wiley and Sons, (1987).

[3] A. K. Jonscher, Nature **267**, 673 (1977).

[4] J. R. Macdonald, J. Schoonman and A. P. Lehnen, Solid State Ionics **5**, 137 (1981).

[5] R. J. D. Tilley, *Understanding Solids: The Science of Materials*, Wiley, (2004).

[6] G. Hsieh, S. J. Ford, T. O. Mason and L. R. Pederson, Solid State Ionics **91**,191 (1996).

[7] J. C. Ruiz-Morales, D. Marrero-López, J. T. S. Irvine and P. Núñez, Materials Research Bulletin **39**, 1299 (2004).

[8] J. C. Ruiz-Morales, D. Marrero-López, J. Canales-Vasquez, P. Núñez, J. T. S. Irvine, Solid State Ionics **176**, 2011 (2005).

[9] T. W. Dakin, IEEE Electrical Insulation Magazine **22**, 11 (2006).

[10] J. Liu, C-g. Duan, W. N. Mei, R. W. Smith and J. R. Hardy, J. Appl. Phys. **98**, 093703 (2005).

[11] R. Pirc, R. Blinc and V. Bobnar, Ferroelectrics **370**, 203 (2008).

[12] R. Pirc and R. Blinc, Phys. Rev. B. **76**, 020101(R) (2007).

[13] G. Catalan and J. F. Scott, Nature **448**, E4 (2007).

[14] P. Lunkenheimer, V. Bobnar, A. V. Pronin, A. I. Ritus, A. A. Volkov and A. Loidl, Phys. Rev. B. **66**, 052105 (2002).

[15] J. R. Dygas and M. W. Breiter, Electrochimica Acta **41**, 993 (1996).

[16] J-H. Hwang, K. S. Kirkpatrick, T. O. Mason and E. J. Garboczi, Solid State Ionics **98**, 93 (1997).

[17] G. Hsieh, S. J. Ford, T. O. Mason and L. R. Pederson, Solid State Ionics **100**, 297 (1997).

[18] Y. Melman, S. Baltianski and Y. Tsur, Instrumentation Science and Technology **33**, 279 (2005).

[19] *User Manual of Impedance Spectroscopy Measurements at ISIS*, (1998).

[20] D. D. Edwards, J-H. Hwang,S. J. Ford and T. O. Mason, Solid State Ionics **99**, 85 (1997).

[21] J. R. Macdonald and J. A. Garber, J. Electrochem. Soc. **124**, 1022 (1977).

[22] A. Sadkowski, M. Dolata and J.-P. Diard, J. Electrochem. Soc. **151**, 20 (2004).

[23] P. Mondal, D. Bhattacharya, P. Choudhury and P. Mandal, Phys. Rev. B. **76**, 172403 (2007).

[24] W-H. Jung, J. Mat. Sci. Lett. **19**, 739 (2000).

[25] J. L. Cohn, M. Peterca and J. J. Neumeier, Phys. Rev. B. **70**, 214433 (2004).

[26] A. S. Alexandrov and A. M. Bratovsky, J. Phys.: Condens. Matter **11**, L531 (1999).

[27] J. R. Sahu, C. R. Serrao, N. Ray, U. V. Waghmare and C. N. R. Rao, J. Mater. Chem. **17**, 42 (2007).

[28] A. K. Tripathi and H. B. Lal, J. Mat. Sci. **17**, 1595 (1982).

[29] A. Jaiswal, R. Das, K. Vivekanand, T. Maity, P. M. Abraham, S. Adyanthaya and P. Poddar, J. Appl. Phys. **107**, 0133912 (2010).

[30] Z. X. Cheng, X. L. Wang, S. X. Dou, H. Kimura, and K. Ozawa, J. Appl. Phys. **107**, 09D905 (2010).

[31] N. Ikeda, H. Ohsumi, K. Ohwada, K. Ishii, T. Inami, K. Kakurai, Y. Murakami, K. Yoshii, S. Mori, Y. Horibe and H. Kitô, Nature **436**, 1136 (2005).

[32] J. van den Brink and D. I . Khomskii, J. Phys.: Cond. Matt. **20**(43), 434217 (2008).

[33] Y. Zhang, H. X. Yang, Y. Q. Guo, C. Ma, H. F. Tian, J. L. Luo, and J. Q. Li, Phys. Rev. B. **76**, 184105 (2007).

[34] M. A. Subramanian, T. He, J. Chen, N. S. Rogado, T. G. Calvarese and A. W. Sleight, Adv. Mater. **18**, 1737 (2006).

[35] J. Iida, M. Tanaka, Y. Nakagawa, S. Funahashi, N. Kimizuka and S. Takekawa, J. Phys. Soc. Jap. **62** 1723 (1993).

[36] N. Ikeda, K. Kohn, N. Myouga, E. Takahashi, H. Kitôh and S. Takahashi, J. Phys. Soc. Jpn. **69**, 1526 (2000).

[37] K.Yoshii, N. Ikeda, Y. Matsuo, Y. Horibe, and S. Mori, Phys. Rev. B. **76**, 024423 (2007).

[38] M. Tanaka, K. Siratori and N. Kimizuka, J. Phys. Soc. Jpn. **53**, 760 (1984).

Chapter 4

Magnetic Excitations in Multiferroic $LuMnO_3$

Contents

One of the most investigated families of multiferroics is the hexagonal manganites RMnO$_3$, which form with R = Sc, Y, Ho, Er, Tm, Yb and Lu. The magnetoelectric behaviour found in this family is associated with frustrated antiferromagnetic interactions of Mn spins on a triangular lattice. The compounds formed with R = Sc, Y and Lu are attractive for fundamental studies because they are not complicated by additional magnetic contributions from the R ions and because they form a family in which changes in structure and magnetoelectric behaviour can be correlated in a systematic way. LuMnO$_3$ is the focus of this study, neutron scattering measurements of the cooperative magnetic dynamics, measurements of the thermal expansion by dilatometry and magnetization measurements are presented. The data provide quantitative information on the exchange interactions, magnetic anisotropy, and magnetostriction, all of which play a part in the magnetoelectric coupling. The results are compared with similar measurements on YMnO$_3$.

4.1 Properties of $LuMnO_3$

4.1.1 Structural Properties

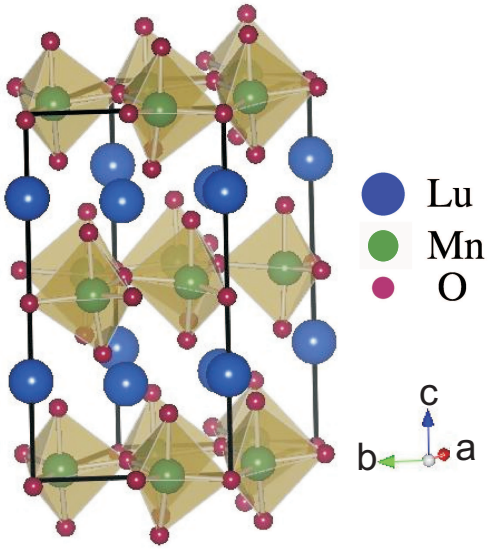

Figure 4.1: The hexagonal layered structure of LuMnO$_3$ showing the MnO$_5$ polyhedra.

The crystal structure of the hexagonal manganites, which is described by the

space group $P6_3cm$, is built from corner-sharing MnO_5 bipyramids which form layers parallel to the hexagonal ab plane separated by rare earth ions, as shown in Figure 4.1. The Mn ions form a near-ideal triangular lattice. At the ferroelectric transition the crystal structure changes from $P6_3/mmc$ in the paraelectric phase to $P6_3cm$ in the ferroelectric phase. As the temperature is lowered the ferroelectric distortion is caused by a tilting of the MnO_5 bipyramids at 1270 K and a buckling of the R plane at 920 K [1], Figure 4.2(a) [2], which together create a $\sqrt{3} \times \sqrt{3}$ superlattice distortion (trimerization) of the Mn ions and a ferroelectric moment along the hexagonal c-axis [1, 3] Figure 4.2(b),(c),(d). The distortion shifts the Mn ions along the hexagonal a-axis away from the ideal $x = 1/3$ position [4], Figures 4.3 and 4.5. It is the coupling between the planes that allows the trimerization to stabilize.

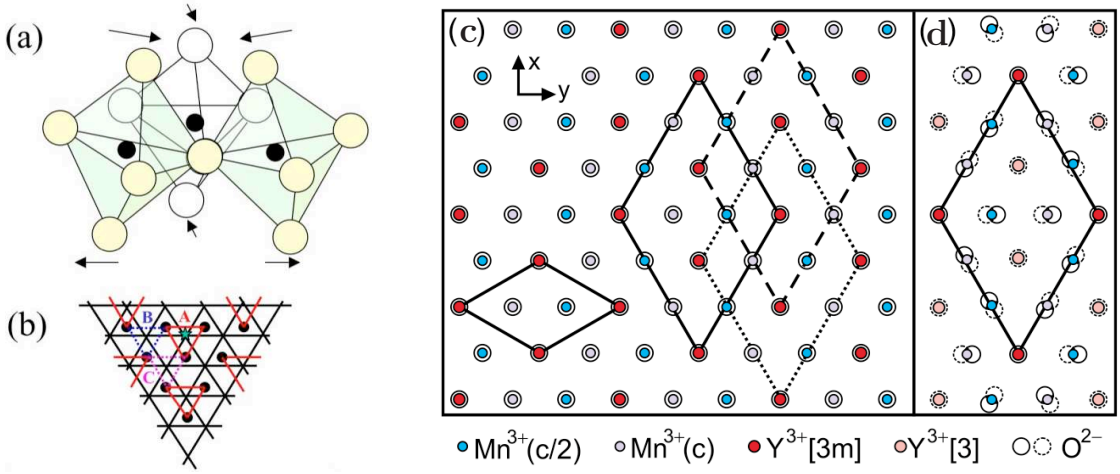

Figure 4.2: (a) Three MnO_5 bipyramids tilt towards the oxygen at the centre forming a trimer, black circles are Mn ions [5]. (b) Shows an MnO layer in the ab plane. The solid circles are the Mn ions and the oxygen ions are on the intersections of the lines. The red, A, blue, B, and pink, C, lines show the trimers that can be formed [5]. (c) Shows the original unit cell (small diamond) and the elongated unit cells corresponding to the three trimerization domains (α, β, γ) [2]. (d) Shows the ferroelectric unit cell [2].

The tilting can be explained by the mismatch of the ionic radii in the crystal. The rare earth ion is too small to form a cubic perovskite structure so the crystal distorts so the space around the rare earth is filled [1]. The resulting trimerization is due to the difference in the ionic radii of R and Mn ions. The tripling of the unit cell at 1270 K [2] leads to the formation of three trimerization domains below this temperature. These domains show a change in the phase but not the orientation of the order parameter. Figure 4.2(b) shows the three trimers A, B and C which correspond

to the three domains (α, β, γ) (the designation is ambiguous, these are not listed respectively) shown in Figure 4.2(c).

In the hexagonal manganite structure the MnO_5 bipyramids consist of five Mn–O bonds. These are the Mn–O1 and Mn–O2 bonds oriented along the crystallographic hexagonal c-axis while Mn–O3 and two pairs of Mn–O4 bonds lie within the ab plane. The O3 and O4 atoms are located close to the centres of the Mn trimers, Figure 4.3. The Mn–O3–Mn and Mn–O4–Mn bond angles have nearly 120° antiferromagnetic superexchange. The differences between the bond lengths and angles in $YMnO_3$ and $LuMnO_3$ changes the strength of the interaction pathways in the two compounds.

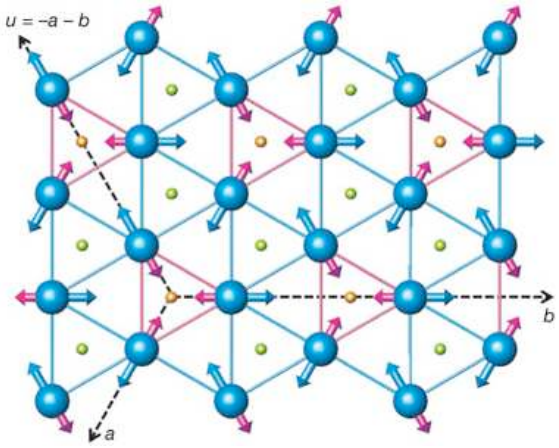

Figure 4.3: The hexagonal layered structure of RMnO$_3$. Showing how the Mn atoms (large blue circles) move below T_N with respect to the O3 (small orange circles) and O4 (small green circles). The movement in $YMnO_3$ is depicted with the blue arrows and the movement in $LuMnO_3$ by the pink arrows [6].

Single crystals of $LuMnO_3$ were prepared by the optical floating-zone technique by D. Prabhakaran. Polycrystalline $LuMnO_3$ was prepared by standard solid-state reaction from high purity (>99.999%) Lu_2O_3 and MnO_2. The polycrystalline powder was pressed into rods of diameter 8 mm and length 80 mm, and sintered at 1300°C for 24 hours. Single crystals were grown in a four-mirror optical floating-zone furnace (Crystal Systems Inc.) at a scanning rate of 3–4 mm hr^{-1} with the feed and seed rods counter-rotating at 30 rpm. The growth was performed in a flowing atmosphere of argon and oxygen in the ratio 12:1. At each stage in the preparation the phase purity of the product was checked by powder X-ray diffraction.

4.1.2 Magnetic Properties

The magnetic properties of $LuMnO_3$ arise from the almost triangular layers of Mn^{3+} ($3d^4$) ions with $S = 2$. Neighbouring spins are coupled by antiferromagnetic exchange interactions which are frustrated by the triangular geometry, as evidenced by the large ratio of the Weiss to Néel temperatures $|\Theta/T_N| \sim 10$ [7], the anomalous magnetic entropy below T_N [7], and the reduction in the value of the ordered magnetic moment to about 75% of the full spin-only moment for $S = 2$ [1]. The Mn spins in all the hexagonal RMnO$_3$ compounds form a classical 120° structure within the triangular layers, Figures 4.4 and 4.5, [1, 8, 9, 10, 11, 12]. The spins are confined by anisotropy to lie in the ab plane, and the large inter-layer separation decouples the layers electronically and makes the magnetism quasi-two-dimensional. In the case of $LuMnO_3$, magnetic ordering occurs below $T_N = 88$ K. If there was no trimerization then there would be no ordering as the fluctuations from the frustration would dominate.

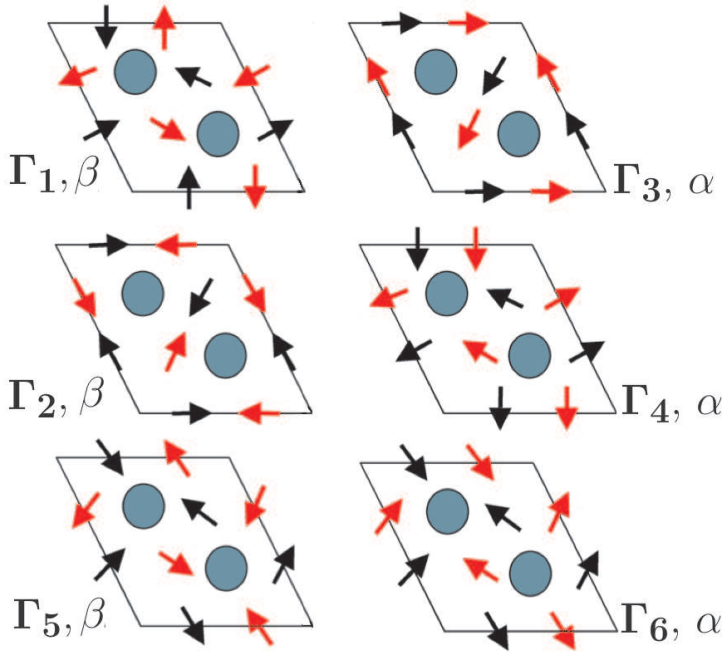

Figure 4.4: Different possible magnetic orderings of the Mn spins in the hexagonal rare earth manganites [12] where black arrows are spins at z=0 and red arrows are spins at z=1/2. The order depends on the ionic radius of the rare earth ion. In the α arrangement the spin at (-x, -y, 1/2) is parallel to that at (x, y, 0). In the β arrangement they point in opposite directions.

Reviews of the magnetic structure of the RMnO$_3$ compounds are given in the

literature [8, 9, 10, 11, 12], with particular reference to $LuMnO_3$. The six Mn sites in the unit cell, Figures 4.4 and 4.5, form two near-equilateral triangles, one in the $z = 0$ layer and the other in the $z = 1/2$ layer. The spins on these triangles lie in the basal plane and order in 120° structures. Symmetry constrains the relation between the $z = 0$ and $z = 1/2$ layers to two possibilities, conventionally labelled α and β. In the α structure the spin on the Mn at $(x, 0, 0)$ ($x \approx 1/3$) is parallel to that at $(1 - x, 0, 1/2)$, whereas in the β structure the spins on these two sites point in opposite directions. Each spin makes an angle ψ to the unit cell axis on which it lies, and the magnetic structure factors depend on ψ and on the stacking relation (α or β). For $x = 1/3$, the magnetic structures occur in homometric pairs, such that the magnetic diffraction intensities for the configuration (α, ψ) are identical with those from (β, $\psi \pm 90°$).

Table 4.1: Magnetic selection rules for hexagonal manganites [12]

Irreducible Representations	Model	Space Group	ψ
Γ_1	β	$P6_3cm$	90°
Γ_2	β	$P6_3\underline{cm}$	0°
Γ_3	α	$P\underline{6}_3c\underline{m}$	0°
Γ_4	α	$P\underline{6}_3\underline{c}m$	90°
Γ_5	β	$P6_3$	0° → 90°
Γ_6	α	$P\underline{6}_3$	0° → 90°

Depending on whether the angle between the Mn^{3+} spin and the axis on which it lies, ψ, is 0°, 90° or in between there are six possible magnetic symmetries for the hexagonal rare earth manganites, Figure 4.4 and Table 4.1. Second harmonic generation studies can differentiate between all the possible spin structures [11]. The $\Gamma_{2,4}$ magnetic orders seem to stabilize for low ionic rare earth radii (Er, Yb and Lu) and the $\Gamma_{1,3}$ for higher ionic rare earth radii (Ho, Y and Y-Er). This appears to be related to the amplitude of the distortion of the Mn lattice with respect to the triangular symmetry [13, 14]. When the position of the Mn ion is at x <1/3 the magnetic structures $\Gamma_{1,3}$ form and for x >1/3 $\Gamma_{2,4}$ form.

4.2 Multiferroic Mechanism

Evidence for magnetoelectric coupling in $R\mathrm{MnO}_3$ compounds is provided by anomalies at T_N in the dielectric constant [15, 7], lattice dynamics [16, 17, 18, 19], thermal conductivity [20] and structural parameters [21, 22, 6]. It has been shown that the

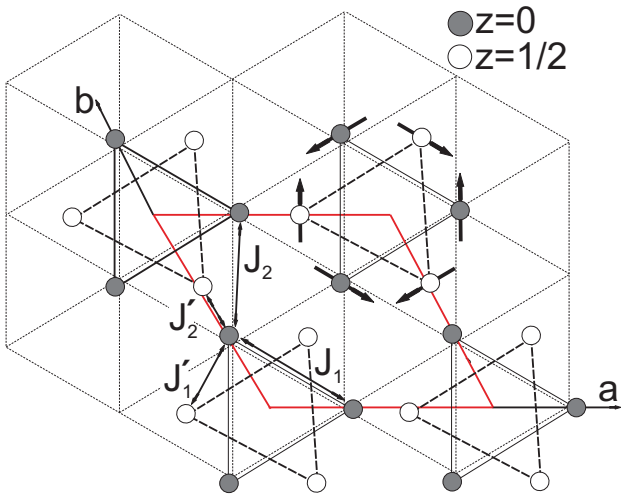

Figure 4.5: Projection of the structure of $LuMnO_3$ down the hexagonal c-axis showing the Mn sites. The large (red) diamond is the projection of chemical/magnetic unit cell, and the filled and empty circles represent Mn at fractional heights $z = 0$ and $z = 1/2$ respectively. The Mn trimerization has been exaggerated for emphasis. The in-plane (J_1, J_2) and out-of-plane (J_1', J_2') Mn–Mn exchange couplings used in the spin-wave model are shown. Arrows on the Mn atoms show the probable magnetic structure of $LuMnO_3$ based on neutron diffraction [1] and optical second harmonic generation [11].

magnetic phase of $HoMnO_3$ can be controlled by an external electric field which realises the magnetoelectric effect [23].

The precise microscopic mechanism of the magnetoelectric coupling in $RMnO_3$ is still under investigation. Careful structural measurements on $Y_{1-x}Lu_xMnO_3$ have shown that an isostructural transition takes place at T_N [6], which causes further displacements of the ions resulting in a small increase in the ferroelectric polarization. It was therefore proposed that the magnetoelectric coupling is driven by a primary magnetoelastic coupling. The origin of the magnetoelastic coupling, however, remains unclear. One possibility is that the isostructural distortion may occur in order to relieve some energy associated with magnetic frustration [14]. Another proposal is that the system might benefit energetically from the Dzyaloshinskii–Moriya interaction below T_N via a small hexagonal c-axis displacement in the oxygen atoms that bond adjacent Mn atoms [24]. This displacement would produce a small additional electric polarization along the c-axis.

There are also interesting observations by optical second-harmonic generation which show a cross-correlation between ferroelectric and magnetic domains due to

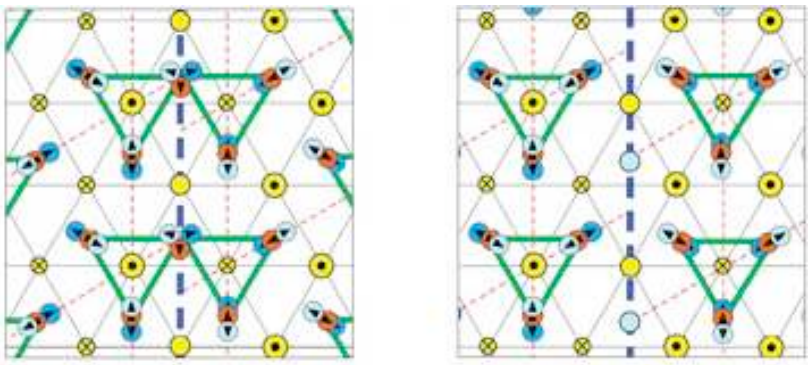

Figure 4.6: Translational domains are shown with the ferroelectric and antiphase boundaries (APBs) coinciding. Yellow, red, dark-blue and light-blue circles are the Y, Mn, bottom O and top O ions respectively. The dashed red lines show the discontinuity of the trimerization at the APBs. The upward and downward distortions of the Y ion are inverted in neighbouring domains because of the opposite polarization. The position of the Mn trimers is unchanged across the boundary even though the top and bottom oxygen atoms distort inversely across the ferroelectric boundary [25].

the formation of magnetic domain walls below T_N which coincide with ferroelectric domain walls [26, 27, 28].

There is a coupling of the order parameters at the domain walls. In the hexagonal manganite $HoMnO_3$, discussed in Chapter 5, which is of the same family as $LuMnO_3$ domain walls are integral to the behaviour observed. Therefore they are discussed here in the context of the multiferroic mechanism that both hexagonal manganites share. The magnetic domain walls are 180° antiferromagnetic (AFM) domain walls, which are energetically unfavourable and have been difficult to study theoretically and energetically. However when AFM domain walls interact with lattice strain they become energetically favourable, lowering the energy of the magnetic system [27]. The ferroelectric domain walls are expected to be only a few unit cells wide due to the strong anisotropy. The AFM domain walls are 10^2-10^4 unit cells wide due to the small in-plane anisotropy of the Mn^{3+} spins in the xy plane.

There is a source of magnetism at or near the centre of the domain wall [27]. The spatial distribution of the dipole moment in the ferroelectric domain wall can be modelled as a step function as the widths are at least two orders of magnitude smaller. The reversal of the electric dipole across the wall and distortion of the domain wall causes an elastic strain. The electric and magnetic parameters can then interact via the piezomagnetic effect. The walls are coincident as there is an energy advantage for

over lapping ferroelectric and AFM walls so when the temperature decreases below T_N AFM domain walls grow at the site of ferroelectric walls, although AFM domain walls can also exist within the ferroelectric domains.

The ferroelectric domain walls are firmly locked to the magnetic domain walls, however the sign of the polarization always changes at the boundary which is surprising as the sign of the polarization is independent of the magnetic orientation. This can be explained by the fact that that structural and ferroelectric boundaries coincide.

There are three structural translational trimerization domains (α, β, γ), Figure 4.6, where the phase but not the order parameters of the orientation differs (antiphase boundaries). As the polarization can be either positive or negative there are three positive and three negative domains. They form cloverleaf vortices where the boundaries are both ferroelectric and antiphase meaning that there is always both a sign change and trimerization change (you don't get $\alpha^+\alpha^-$). So the sequence of domains is $\alpha^+, \gamma^-, \beta^+, \alpha^-, \gamma^+, \beta^-$, Figure 4.7. This has been shown using piezoresponse microscopy, using the same technique to see both types of domain [2].

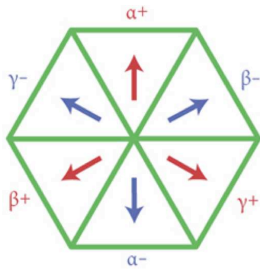

Figure 4.7: The vortex and antivortex configurations that correspond to the cloverleaf defects [29].

The antiphase and ferroelectric boundaries are rigidly coupled except at the vortex region at the centre. The translational domains control the distribution of the orientation ferroelectric domains. The pairing of these domains is due to the electrostatic discontinuity at the trimerization translational domain walls. The discontinuity controls the ferroelectric polarization up to a distance of about 100 unit cells, enforcing a reversal of polarization whenever a wall is crossed. The simplest way to satisfy this is the cloverleaf arrangement. At the vortex where there is electrostatic repulsion between equally polarized domains the system solves this by decoupling the domains, they become flexible and there is a spatial displacement of the walls [2]. They get within 100 nm in the xy plane and 30 nm along z [2]. This means that at the vortex the polarization is not approaching zero, it is either positive or negative. Away from

the vortex where the walls are rigidly coupled the domains maintain a width of at least 100 unit cells.

It has been shown that these domains exist in all three dimensions. It was suggested [25] that the coincidence of the trimerization and polarization walls was because the minimisation of the R ion displacement was energetically favourable. However given these domains exist along the z axis this does not hold. Domain walls provide even more information. They are of the order of a few unit cells wide whereas the separations are closer to 100 unit cells wide. This indicates that the Coulomb interaction determines the domain configurations as it acts in the three spatial dimensions and is a long range force that can act across many unit cells.

It has been found that it is not possible to destroy all positive or negative domains with a negative or positive applied electrical poling field [29]. The domains polarized in the opposite direction to the field are reduced but to maintain the cloverleaf pattern they are never wiped out even when a field of almost twice the coercive field is applied [25].

4.3 Results

4.3.1 Magnetization

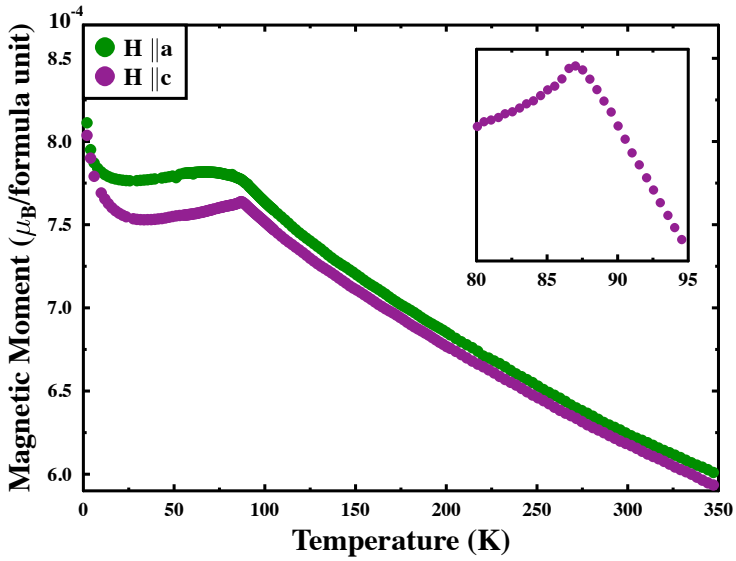

Figure 4.8: Zero-field-cooled magnetization measurements performed in a magnetic field of strength $H = 1000\,\text{Oe}$ applied along the hexagonal c-axis and a-axis. The inset shows an expanded temperature range about the ordering temperature $T_N = 87.5 \pm 0.5\,\text{K}$.

Magnetic measurements were performed with a superconducting quantum interference device (SQUID) magnetometer on a small piece of $LuMnO_3$ crystal cut from the same rod as that used for the neutron scattering measurements.

Figure 4.8 shows the magnetization of $LuMnO_3$ for a magnetic field of strength 1000 Oe applied parallel to the ab plane and along the c-axis. Magnetic ordering is signalled by a sharp peak in the magnetization at $T_N = 87.5 \pm 0.5$ K (Figure 4.8 inset). This is confirmed by the appearance of magnetic Bragg peaks below T_N in neutron diffraction data (Figure 4.11). The magnetization exhibits a small anisotropy, being slightly larger when the field is applied parallel to the ab plane (χ_{ab}) than along the c-axis. This easy-plane anisotropy is consistent with the observation that the moments lie in the plane in the ordered phase. A clear cusp is observed at T_N in χ_c whereas a broader peak is seen in χ_{ab}. It has been suggested that the cusp in χ_c is caused by coupling between adjacent Mn layers, and the more rounded peak in χ_{ab} is due to frustration [7].

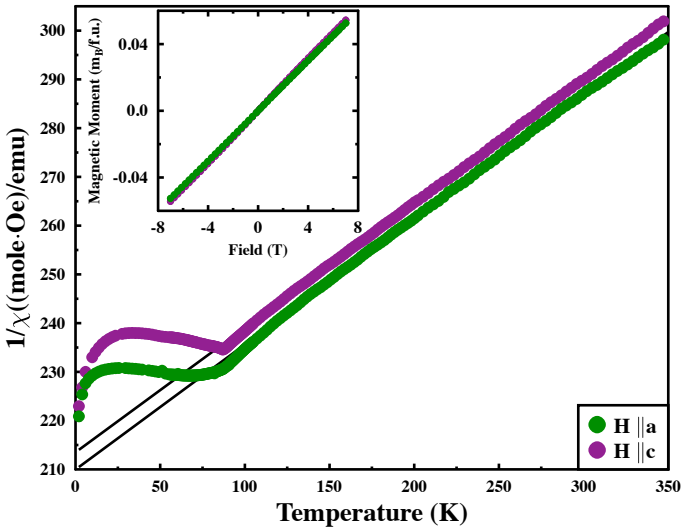

Figure 4.9: The inverse susceptibility along the a and c directions. The inset shows the magnetization at 2 K along the c and b axes

The data follows a Curie–Weiss law at high temperatures, Figure 4.9, with a negative Weiss temperature, Θ. From fits of $1/\chi$ vs T we obtain $\Theta = -819 \pm 2$ K from χ_{ab}, and -837 ± 1 K from χ_c. These values are close to those reported previously from single crystals [7], but somewhat larger in magnitude than obtained from powder samples [30]. The magnetization at 2 K, inset of Figure 4.9, shows that there are no ferromagnetic domains. The field plots are the same along the c- and b-axes.

4.3.2 Thermal Expansion

The magnetization, neutron scattering and thermal expansion measurements were all made on the same crystal. The thermal expansion measurements were made with a miniature capacitance dilatometer [31, 32]. The sample was cut into a cuboid of 2.05 mm x 2.14 mm x 2.87 mm with the hexagonal a and c-axes of the crystal perpendicular to the polished faces, the b-axis was taken to be at 90° to the a-axis. Measuring capacitance is one of the most sensitive ways of measuring small length changes. In this method the sample is put between conducting plates, the distance between which can then be found with the capacitance formula, Chapter 3. The plates are spring loaded so the force on the sample can be evenly applied. This apparatus can measure length changes with an accuracy of 1 Å.

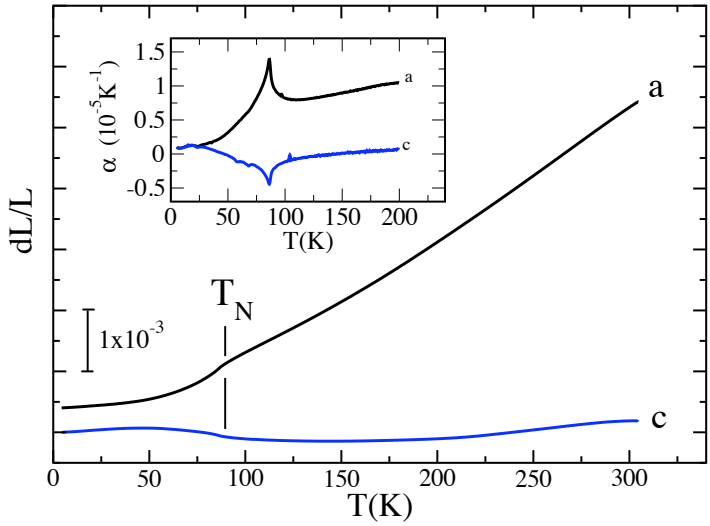

Figure 4.10: Thermal expansion of $LuMnO_3$ measured along the hexagonal a- and c directions. The inset shows the thermal expansion coefficient α as determined from the temperature derivative of the strain $\mathrm{d}L/L$.

Figure 4.10 shows measurements of the thermal expansion of $LuMnO_3$ parallel to the a and c axes. A magnetoelastic anomaly is clearly visible at the Néel temperature, both in the strain $\mathrm{d}L/L$ and in its temperature derivative $\alpha = L^{-1}\mathrm{d}L/\mathrm{d}T$. On cooling through T_N the magnetoelastic strain expands the c-axis and shrinks the hexagonal plane. As a check, the thermal expansion in the hexagonal plane in the direction normal to a was also measured. The data resemble the behaviour of $\mathrm{d}a/a$ to within the experimental error. Above T_N the thermal expansion is highly anisotropic. The

c-axis strain is almost temperature independent. Similar results have been reported for $YMnO_3$ and $Y_{0.5}Lu_{0.5}MnO_3$ [6].

4.3.3 Inelastic Neutron Scattering

Unpolarized neutron scattering measurements were performed on a crystal of mass 1.9 g on the cold-neutron triple-axis spectrometer TASP at the SINQ facility (PSI, Switzerland) and on the thermal triple-axis 2T1 at LLB-Orphée (Saclay, France) as described in Section 2.3.1. At TASP, the crystal was mounted in an 'orange' helium cryostat and neutron spectra were recorded with a fixed final energy of 4.5 meV. The corresponding setup at 2T1 was with a closed-cycle refrigerator and a fixed final energy of 14.7 meV. Measurements were made with either a^* and c^* or a^* and b^* in the horizontal scattering plane, where a^*, b^* and c^* are the axes of the hexagonal reciprocal lattice. On 2T1 some measurements were also made in the plane parallel to the a^*b^* plane but displaced by 0.5 reciprocal lattice units along the c^* axis. The lattice parameters of $LuMnO_3$ of the space group $P6_3cm$ are $a = b = 6.05\,\text{Å}$, $c = 11.4\,\text{Å}$, and the inter-axis angles are $\alpha = \beta = 90\,°$, $\gamma = 120\,°$. Hence, $a^* = b^* = 4\pi/(a\sqrt{3})$, and $c^* = 2\pi/c$.

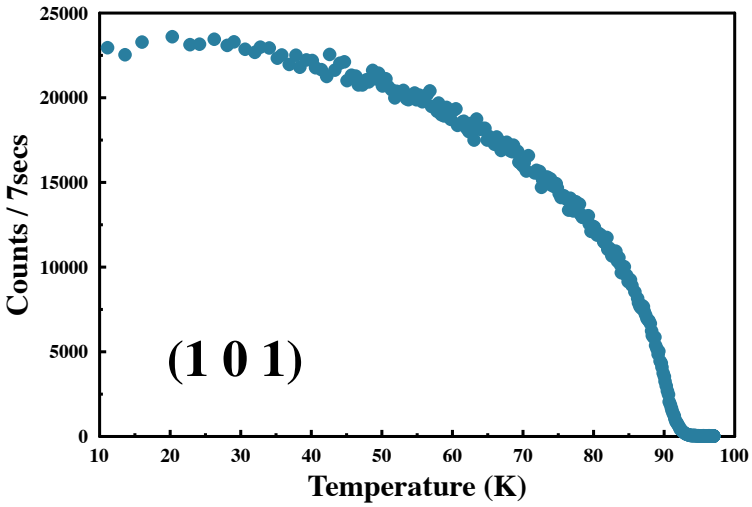

Figure 4.11: The temperature dependence of the (101) magnetic Bragg peak amplitude taken on TASP.

Figure 4.11 shows the temperature dependence of the (1 0 1) magnetic Bragg peak amplitude. This shows the magnetic ordering transition. Examples of neutron scattering spectra from both instruments are presented in Figure 4.12. Figure 4.12(a)

shows energy scans recorded on TASP at the scattering vectors $\mathbf{Q} = (1, 0, 0)$ and $(1, 0, 1.5)$, both of which contain two asymmetric peaks. Figure 4.12(b) shows data at $\mathbf{Q} = (1.33, 0.33, 0.5)$ and $(1.44, 0.11, 0.5)$ measured on 2T1. Since the ordered moment on the Mn sites is relatively large ($\sim 3\,\mu_B$) the scattering from magnons is expected to be much stronger than phonon scattering at these relatively small scattering vectors. This, together with the resemblance of the spectra to previous measurements on $YMnO_3$, provides confidence that the main features in the spectra correspond to magnons.

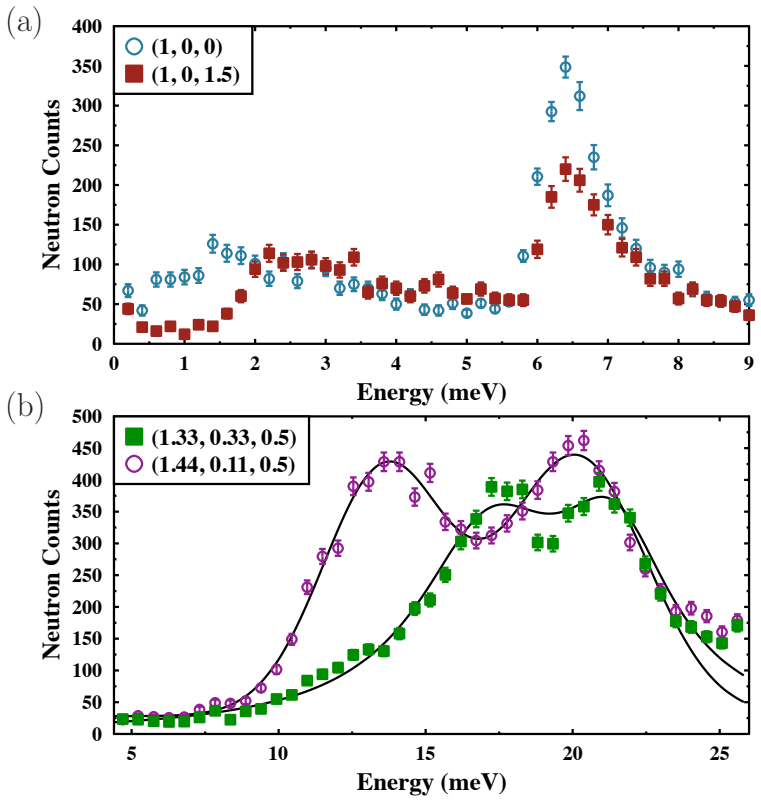

Figure 4.12: Inelastic Neutron Scattering from $LuMnO_3$ measured on (a) TASP at $T = 5\,\mathrm{K}$ and (b) 2T1 at $T = 13.5\,\mathrm{K}$. The data are from constant wavevector scans at the indicated positions in reciprocal space. The lines in (b) are fits to a lineshape comprising two Gaussian functions.

To determine the magnon dispersion the peaks were fitted with Gaussian or Lorentzian functions (depending on the peak shape) on a linear background. Figure 4.13 shows examples of the raw data along the (h, 0, 0) direction. The dispersion of the mode to higher energies can clearly be observed.

The fitted peak positions have been collected together into a dispersion curve which

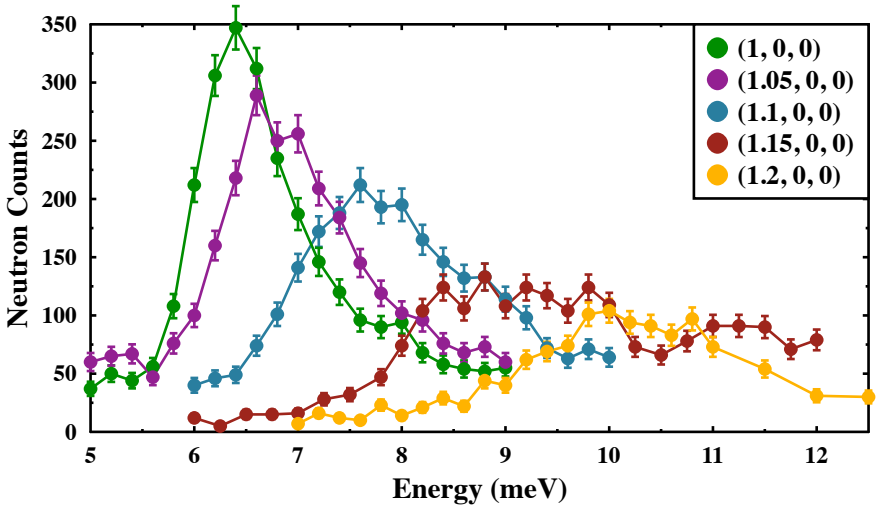

Figure 4.13: The dispersion along the (h, 0, 0) direction

is plotted in Figure 4.14, including data from both TASP and 2T1. Measurements on TASP extended from below 1 meV up to about 13 meV, while measurements at 2T1 covered the range from about 5 meV up to the energy of the highest modes. Measurements were performed in several different zones to find the maximum intensity and to check that the peaks were periodic in reciprocal space.

Figure 4.15 shows diffuse scattering measurements in the vicinity of the point $(1, 0, 0)$ in reciprocal space at temperatures close to T_N. The (100) reflection has zero nuclear structure factor, and zero magnetic intensity was observed here at low temperatures. The scans in Figure 4.15 reveal strong diffuse scattering at temperatures close to $T_N = 87.5 \pm 0.5$ with maximum intensity at T_N itself, as shown in the inset. The diffuse scattering is highly anisotropic, being very broad in the $(0, 0, l)$ direction but much sharper in the $(h, 0, 0)$ direction.

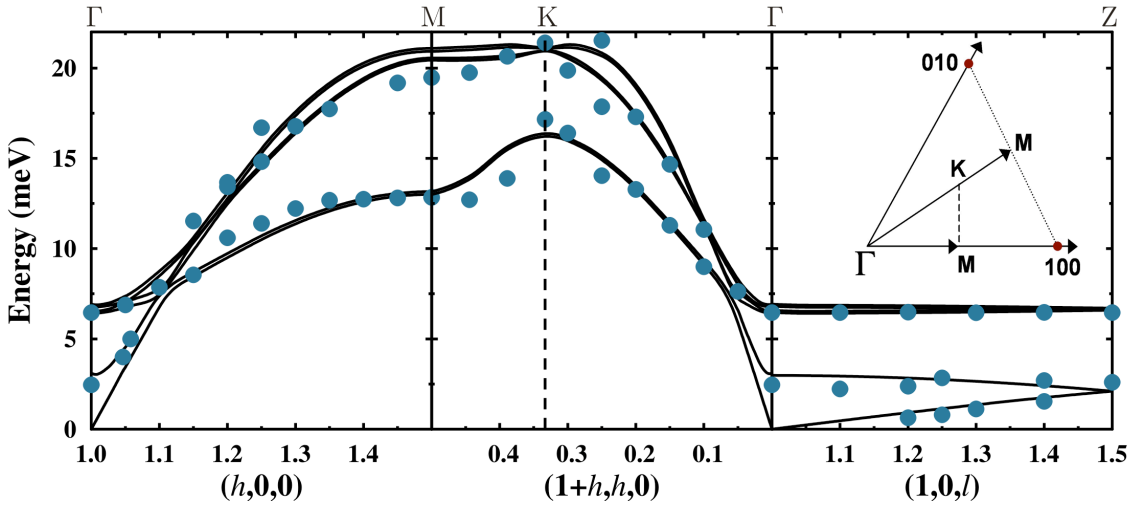

Figure 4.14: Spin-wave dispersion of $LuMnO_3$. Solid circles are the peak centres obtained from fits to scans such as those shown in Figure 4.12. Solid lines are calculated from the model described in the text with parameters $J_1 = -4.09(2)$ meV, $J_2 = -1.54(5)$ meV, $J_2' = +0.019(2)$ meV, $J_1' = 0$, and $D = -0.48$ meV. The inset is a sketch of the $(h, k, 0)$ plane in reciprocal space showing the path ΓMKΓ.

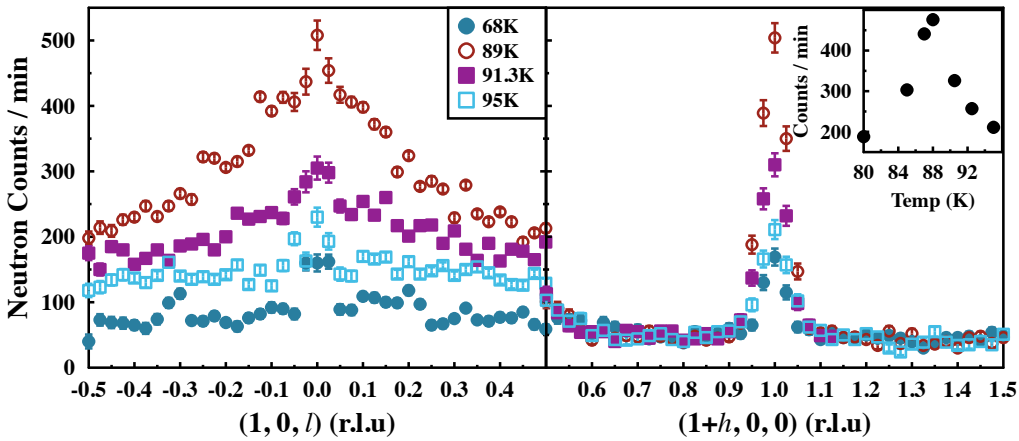

Figure 4.15: Diffuse neutron scattering around the forbidden nuclear reflection $(1, 0, 0)$. The inset shows the temperature variation in the diffuse scattering intensity at $(1, 0, 0)$.

4.4 Analysis and Discussion

4.4.1 Thermal Expansion

Careful powder diffraction measurements [6] have shown that the magnetically-induced ferroelectricity in $R\mathrm{MnO}_3$ is associated with an isostructural transition involving an additional rotation of the MnO_5 bipyramids, and that the increase in ferroelectric polarization below T_N scales with the square of the ordered moment. The thermal expansion of LuMnO_3 reported here (Figure 4.10) reveals a striking magnetoelastic anomaly at T_N, consistent with the diffraction data of Lee *et al.* [6] who argued that magnetoelastic coupling (exchange striction) is the primary source of the magnetoelectric coupling [6]. One might expect, therefore, that the magnetoelectric effect would scale with the strength of the exchange interactions and hence be greater in LuMnO_3 than in YMnO_3. Support for this idea is provided by the magnetically-induced polarization calculated from the measured atomic displacements below T_N, which indeed appears to be systematically larger for LuMnO_3 than for YMnO_3 [6]. However, given the large experimental uncertainties in the values of the small atomic displacements this evidence should be considered tentative.

Another notable feature of the thermal expansion is how small the c-axis thermal expansion is relative to the ab plane expansion above T_N, Figure 4.10,. This effect, which is observed both for LuMnO_3 and YMnO_3, does not correlate with the compressibility of these materials, which is similar along the c direction and in the ab plane [33]. The relatively isotropic compressibility suggests that the anomalous c-axis thermal expansion is not due to a straightforward anharmonicity in the interatomic potentials along the c-axis, and it would be interesting to find out what is responsible for it.

4.4.2 Inelastic Neutron Scattering Spin-Wave Dispersion

In the case of LuMnO_3, Katsufuji *et al.* [1] concluded from neutron powder diffraction measurements that the low temperature structure is one of two possibilities, either (α, $\psi = \pm 90°$) or (β, $\psi = 0°$ or $180°$). These two structures transform respectively like the Γ_4 and Γ_2 irreducible representations of the space group $P6_3cm$ [10]. Only this particular homometric pair have a completely absent (100) magnetic reflection. In our single crystal measurements we also found very little intensity at the (100) reflection (but relatively strong intensity for the (101) reflection — see Figure. 4.11, at the lowest

temperature ($T = 2\,\mathrm{K}$), in agreement with Katsufuji *et al.* [1]. The homometric pairs can in principle be distinguished by optical second harmonic generation (SHG). Using this method, Fiebig *et al.* found that their sample of $LuMnO_3$ was a two-phase mixture of α structures with $\psi = 0°$ and an unspecified other ψ value [11]. Since our low-temperature data, as well as that of [10], conclusively rule out any α structure which does not have $\psi \simeq \pm 90°$ it is difficult to see how to reconcile the diffraction and SHG results. For the purpose of modelling the spin-wave spectrum the (α, $\psi = \pm 90°$) structure is assumed, as shown in Figure 4.5. The magnetic spectrum of this and its homometric partner are not distinguishable at the level of precision of our data.

The spin-wave spectrum has been calculated from the spin Hamiltonian

$$\mathcal{H} = -\sum_{\langle ij \rangle} J_{ij} \mathbf{S}_i \cdot \mathbf{S}_j - D \sum_i \left(S_i^z\right)^2, \tag{4.1}$$

with two in-plane near-neighbour interactions (J_1 and J_2) and two inter-plane interactions (J_1' and J_2') defined as shown in Figure 4.5. The first summation in (4.1) is over pairs of spins with each pair counted once so that the J constants are per spin pair. The second term models the out-of-plane anisotropy with a single-ion anisotropy parameter D. The small in-plane anisotropy is neglected since the in-plane magnon gap was too small to measure in our experiment.

Analytic expressions have been given previously for the spin-wave energies derived from spin Hamiltonians similar to (4.1), [34, 35, 36, 37]. These expressions have been obtained via the usual transformation of the Hamiltonian into a quadratic form of boson normal-mode operators in the linear approximation. Here we use an alternative method based on dynamical matrix diagonalisation (DMD) as outlined in previous work [38], which is implemented in the McPhase software package [39]. This formulation employs the random phase approximation to calculate the magnon cross sections in addition to the dispersion relations. Mean field calculations are repeated with randomly chosen initial moment configurations to find the most stable magnetic structure. The crystal field and exchange parameters are the inputs of the calculations.

There are six Mn spins per unit cell, which gives rise to a total of six spin-wave modes for each wavevector. As the interlayer coupling is small, the in-plane dispersion relations appear as three branches each containing two nearly-degenerate modes. The degeneracy of the lowest two modes is lifted close to the Γ point and along ΓZ by the effect of the J_1' and J_2' interactions, while the upper four modes are almost degenerate along ΓZ. This degeneracy precludes the possibility to fit accurate values for J_1' and

J_2' independently, and so we chose to fix $J_1' = 0$ and to vary J_2' under the constraint that $J_2' > 0$ to maintain the stability of the α structure.

A least-squares fitting procedure returned the following values for the model parameters:

J_1 = -4.09(2) meV,

J_2 =-1.54(5) meV,

J_2' = +0.019(2) meV ($J_1' = 0$),

D =-0.48(4) meV.

The calculated dispersion relations from the model with these parameters are shown in Figure 4.14. The agreement is observed to be very good, and the parameters are well constrained by the data. For example, the 6.5 meV gap to the upper mode at Γ is sensitive to the single-ion anisotropy, and J_2' controls the dispersion in the out-of-plane direction. The splitting of the magnon peaks in the vicinity of the K point, seen in Figure 4.14, is sensitive to the difference between J_1 and J_2. Qualitative agreement between the measured and calculated magnon cross sections gave us further support for the obtained parameters. Figure 4.16 shows the dispersion in the case that $J_1 = J_2$. The only difference from the dispersion in Figure 4.14 is the convergence at the K point. As most studies do not include the (1+h,h,0) direction the need for separate J_1 and J_2 values is not usually apparent.

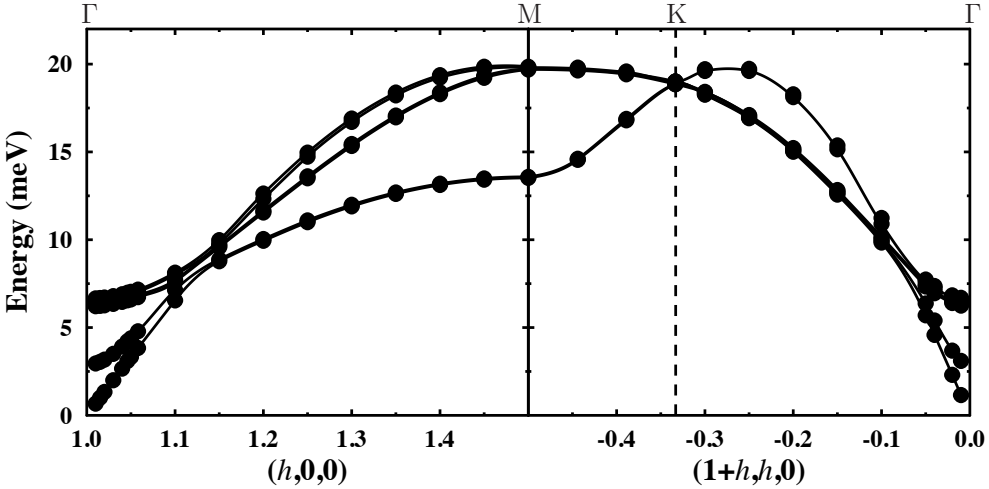

Figure 4.16: The splitting of the magnon peaks in the vicinity of the K point, seen in Figure 4.14, is sensitive to the difference between J_1 and J_2. The black circles and solid dispersion lines are calculated values for the case that $J_1 = J_2$ and there is no splitting at K.

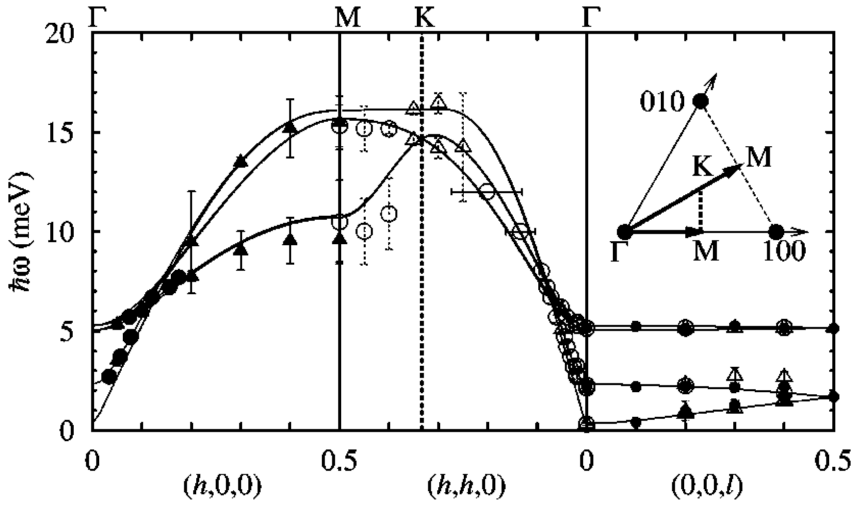

Figure 4.17: Spin-wave dispersion of $YMnO_3$ from [35]. Circles and triangles represent the experimental peak positions and the solid lines are the model dispersion relations.

The exchange parameters obtained here show that the dominant magnetic interaction is the in-plane antiferromagnetic superexchange via the $\sim 120^\circ$ Mn-O-Mn path. The inter-layer superexchange is two orders of magnitude weaker, confirming that the magnetism in $LuMnO_3$ is highly two-dimensional. It is interesting to compare the magnetic spectrum of $LuMnO_3$ investigated here with those obtained from similar measurements on $YMnO_3$ ([35, 37, 19, 14]), Figure 4.17, and $HoMnO_3$ [36]. Qualitatively, the spectra of the three compounds look very similar, but the overall band width of the $LuMnO_3$ spectrum is about 30% larger than that of $YMnO_3$ and $HoMnO_3$ (21 meV compared with 16 meV). Consistent with this, the fitted exchange parameters for $LuMnO_3$ are found to be systematically larger than those of $YMnO_3$ and $HoMnO_3$. This accounts for the difference in the antiferromagnetic ordering temperatures of these compounds: $T_N \approx 88\,\mathrm{K}$ ($LuMnO_3$) compared with $T_N \approx 72\,\mathrm{K}$ ($YMnO_3$) and $T_N \approx 75\,\mathrm{K}$ ($HoMnO_3$) and the larger Weiss temperature of $LuMnO_3$ ($\Theta \approx -850\,\mathrm{K}$) compared with $YMnO_3$ ($\Theta \approx -700\,\mathrm{K}$) [7].

The stronger magnetic interactions in $LuMnO_3$ fits with the systematic trend in the ionic radii and the lattice parameters [1], i.e. the smaller the ionic radius the smaller the unit cell and the stronger the exchange interactions. The single-ion anisotropy parameter D is also found to be larger for $LuMnO_3$ ($D = -0.48\,\mathrm{meV}$) than for $YMnO_3$ ($D = -0.28$ to $-0.33\,\mathrm{meV}$) and $HoMnO_3$ ($D = -0.38\,\mathrm{meV}$). This could be another consequence of the small differences in the structural parameters of these

compounds.

Table 4.2: $RMnO_3$ Comparison of Properties

R	T_N (K)	Θ (K)	c-axis Å	Mn-O3 Å	Mn-O4 Å
Lu	88(1)	-850(20)	11.4074(3)	0.988(3)	1.003(4)
Y	72(1)	-700(20)	11.4432(4)	1.021(4)	0.985(2)

Table 4.3: $RMnO_3$ Comparison of Properties

R	J_1 (meV)	J_2 (meV)	D (meV)
Lu	-4.09(2)	-1.54(5)	-0.48(4)
Y	-3.4(2)	-2.02(7)	-0.28/-0.33(1)

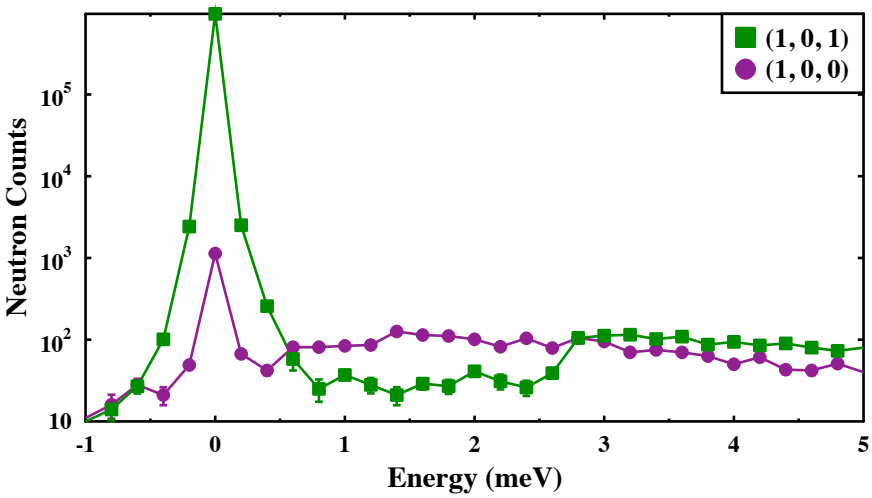

Figure 4.18: The $(1, 0, 1)$ and $(1, 0, 0)$ energy scans are shown on a log scale. The (1, 0, 1) has 10^3 times greater intensity at 0 meV than $(1, 0, 0)$.

A summary of the comparison of $YMnO_3$ and $LuMnO_3$ parameters is seen in Table 4.3, the errors on the temperature values are representative of the spread of values quoted within the literature [1, 6, 35]. The ratio of the respective T_N and J_1 values is approximately 1.2 for both values suggesting good agreement between the results. $LuMnO_3$ trimers are more isolated with stronger coupling within the trimer. The increase in bond length along a particular exchange path corresponds to a decrease

in the value of the exchange, this is seen for both J_1 and J_2. The shorter hexagonal c-axis for $LuMnO_3$ also corresponds to the stronger inter-planar interaction.

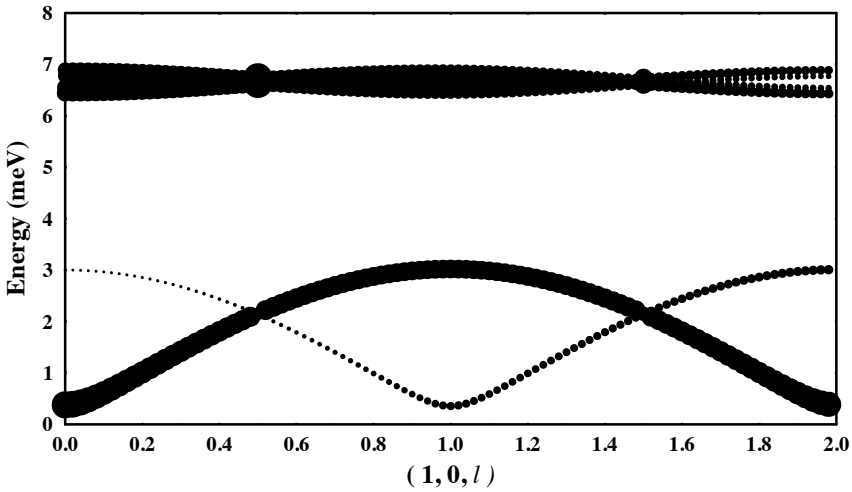

Figure 4.19: The dispersion along the l direction as expected for $LuMnO_3$ for the magnetic structures Γ_2 and Γ_4.

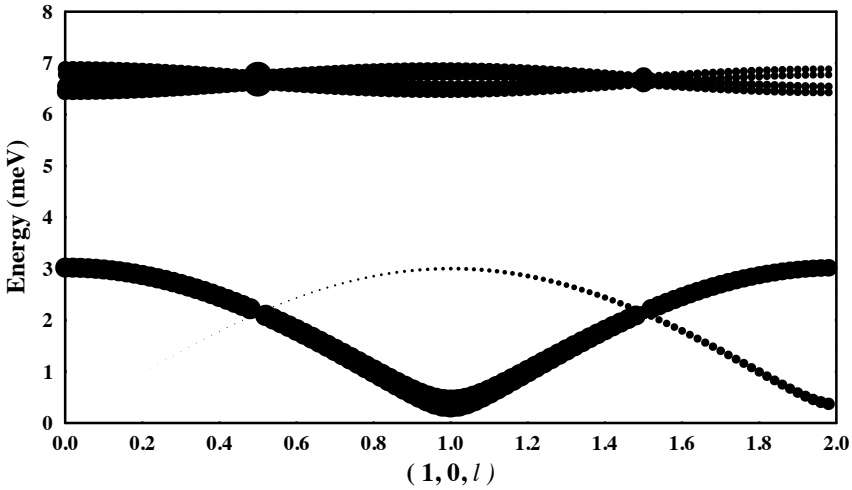

Figure 4.20: The dispersion along the l direction as expected for $YMnO_3$ for the magnetic structures Γ_1 and Γ_3.

The much larger intensity of the (1,0,1) peak compared to the (1,0,0) peak (an order of 10^3) means that the magnetic structure found for this compound is unambiguous, Figure 4.18. However in some regions the expected intensity of the inelastic scans when compared to the data results in a slightly more ambiguous picture.

Figures 4.19 and 4.20 show the calculated dispersions along (1,0,l) for $\Gamma_2\Gamma_4$ and $\Gamma_1\Gamma_3$ respectively. The size of the points indicates the expected intensity of peaks found in inelastic neutron measurements at those positions. The figures show that

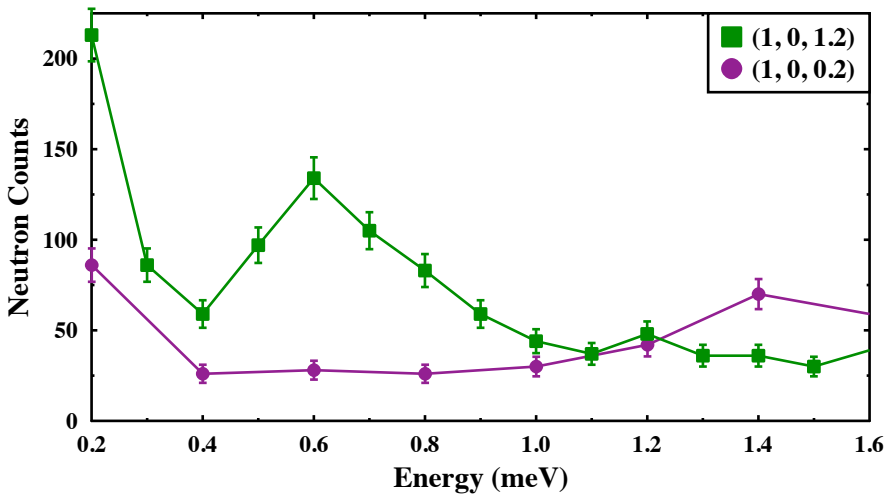

Figure 4.21: For $LuMnO_3$ magnetic symmetry greater intensity is expected to be observed for the $(1, 0, 0.2)$ low energy peak than for the $(1, 0, 1.2)$ low energy peak. However no peak is observed for $(1, 0, 0.2)$.

with the change of irreducible representation the expected intensity of the two lower branches along (1,0,l) swap. If this is the case then a strong peak would be expected at low energy and low l value for $LuMnO_3$ and not for $YMnO_3$. Figure 4.21 shows that this is not the case.

Intensity was detected at the (1, 0, 1.2) but not the (1, 0, 0.2) positions, Figure 4.21. As Figures 4.19 and 4.20 show, for $LuMnO_3$ the relative intensities would be expected to be the other way around. It is possible that this is due to the mosaic of the crystal. There were 4 grains spanning approximately 10° so it is possible while looking at the main grain another grain is at such an angle that intensity is measured where it is not expected.

4.4.3 Diffuse Scattering

The character of the diffuse scattering from $LuMnO_3$ close to T_N, Figure 4.15, strongly resembles that observed from $YMnO_3$ [40]. The appearance of scattering which is very broad along c but relatively sharp in the plane indicates that the inter-layer correlations are very weak, consistent with the small J_1' and J_2' and two-dimensional nature of the magnetic system. The strong enhancement in the diffuse scattering intensity around $(1, 0, 0)$ was also observed in powder diffraction measurements on $LuMnO_3$ [1]. These showed that the diffuse peak persists up to at least $\approx 3T_N$ [1], which was interpreted as evidence for strong geometric frustration.

4.4.4 Point Charge Calculations

As a check, the bulk magnetization was calculated using the best-fit exchange and anisotropy parameters. The T_N predicted by the mean-field model is about 2.5 times larger than the observed T_N, presumably as a consequence of frustration. The calculated susceptibility has a small easy-plane anisotropy consistent with the measured susceptibility, Figure 4.8. The magnetization of the sample as a function of applied field is linear and almost identical in the a and c directions, Figure 4.9 (inset). Increasing the single-ion anisotropy in the model creates a step in the a-axis magnetization which is not observed. This adds to the evidence that the single-ion anisotropy is very small compared to the exchange interactions.

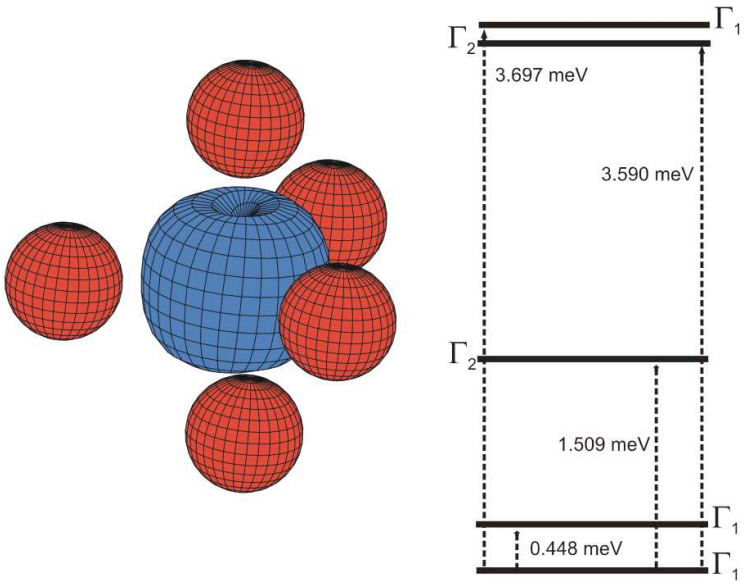

Figure 4.22: Left: Calculation of the thermally-averaged charge density in the MnO_5 bipyramid of $LuMnO_3$ at $T = 4\,\mathrm{K}$. The $3d$ charge is represented (in blue) by a surface of constant charge density obtained from a calculation of the crystal field acting on Mn^{3+} assuming point charges of $-2|e|$ on each of the five nearest oxygen neighbours (shown in red). Right: Low-lying energy levels of Mn^{3+} split by the point-charge crystal field via spin–orbit coupling. The symmetry of each level is labelled according to the irreducible representation of the point group C_s, which describes the local symmetry around the Mn site.

The origin of the small magnetic anisotropy of $LuMnO_3$, which is represented in the Hamiltonian (4.1) by the phenomenological $D(S^z)^2$ term was also investigated. For reference, a point-charge calculation of the crystal field at the Mn sites, assuming

Mn to be in the Mn^{3+} state with d^4 configuration and using the structural parameters reported by Katsufuji *et al.*, was performed [1]. Only the five nearest oxygen neighbours of Mn in the MnO_5 bipyramid were included, as shown in Figure 4.22. The ground-state $S = 2$ manifold is split by the crystal field via the spin–orbit interaction. The calculated splitting, due to the crystal field alone, is also shown in Figure 4.22. This model of the crystal field predicts that the ordered magnetic moment points along the normal to the local mirror plane, as shown in Figure 4.1, and with the inclusion of the exchange field from the neighbouring Mn ions predicts an anisotropy gap in the magnon spectrum of approximately 10 meV. This size of gap is in clear disagreement with the observed spin-wave modes, which have a gap of less than 1 meV at the zone centre, Figure 4.14. The anisotropy gap may be reduced in the model if the local symmetry is increased to C_{3v}, i.e. by lessening the degree of Mn trimerization and tilting of the MnO_5 bipyramid. In conclusion it appears that the single-ion anisotropy is controlled by a tiny distortion of the ideal MnO_5 bipyramid and that the anisotropy is much smaller than that predicted by a simple point-charge model.

4.5 Conclusions

The magnon dispersion in $LuMnO_3$ has been measured and a very good description of the spectrum, using the Heisenberg Hamiltonian Eq. 4.1, has been achieved. A striking magnetoelastic coupling at T_N in the thermal expansion is also observed. The results are qualitatively similar to those previously obtained on the sister compound $YMnO_3$. The bandwidth of the one-magnon spectrum of $LuMnO_3$ is about 30% larger than that of $YMnO_3$, and the difference between the two nearest-neighbour in-plane exchange constants J_1 and J_2 is greater for $LuMnO_3$ than for $YMnO_3$. As the magnetic interactions are stronger in $LuMnO_3$ than in $YMnO_3$ the magnetically-induced ferroelectric polarization is expected to be greater in $LuMnO_3$. The available diffraction data provides tentative support for this [6].

Bibliography

[1] T. Katsufuji, M. Masaki, A. Machida, Y. Moritomo, K. Kato, E Nishibori, M. Takata, M. Sakata, K. Ohoyama, K. Kitazawa, and H. Takagi, Phys. Rev. B **66**, 134434 (2002).

[2] T. Jungk, A. Hoffmann, M. Fiebig and E. Soergel, Appl. Phys. Lett. **97**, 012904 (2010).

[3] B. B. Van Aken, T. T. M. Palastra, A. Filippetti and N. A. Spaldin, Nature Materials **3**, 164 (2004).

[4] Note that there is a discrepancy between different structural studies about whether the Mn shifts to a position with $x > 1/3$ or $x < 1/3$. For $LuMnO_3$, Van Aken *et al.* (Ref. [21]) and Lee *et al.* (Ref. [6]) report $x < 1/3$, whereas Katsufuji *et al.* (Ref. [1]) report $x > 1/3$.

[5] Y. Aikawa, T. Katsufuji, T. Arima, and K. Kato, Phys. Rev. B **71**, 184418 (2005).

[6] S. Lee, A. Pirogov, M. Kang, K.-H. Jang, M. Yonemura, T. Kamiyama, S.-W. Cheong, F. Gozzo, N. Shin, H. Kimura, Y. Noda, and J.-G. Park, Nature **451**, 805 (2008).

[7] T. Katsufuji, S. Mori, M. Masaki, Y. Moritomo, N. Yamamoto, and H. Takagi, Phys. Rev. B **64**,104419 (2001).

[8] E. F. Bertaut and M. Mercier, Phys. Lett. **5**, 27 (1963).

[9] W. C. Koehler, H. L. Yakel, E. O. Wollan, and J. W. Cable, Phys. Lett. **9**, 93 (1964).

[10] A. Muñoz, J. A. Alonso, M. J. Martínez-Lope, M. T. Casáis, J. L. Martínez, and M. T. Fernández-Díaz, Phys. Rev. B **62**, 9498 (2000).

[11] M. Fiebig, D. Fröhlich, K. Kohn, Th. Lottermoser, V. V. Pavlov and R. V. Pisarev, Phys. Rev. Lett. **84**, 5620 (2000).

[12] P. J. Brown and T. Chatterji, J. Phys.: Condens. Matter **18**, 10085 (2006).

[13] X. Fabrèges, I. Mirebeau, P. Bonville, S. Petit, G. Lebras-Jasmin, A. Forget, G. André, S. Pailhès, Phys. Rev. B **78**, 214422 (2008).

[14] X. Fabrèges, S. Petit, I. Mirebeau, S. Pailhès, L. Pinsard, A. Forget, M. T. Fernandez-Diaz, and F. Porcher, Phys. Rev. Lett. **103**, 067204 (2009).

[15] Z. J. Huang, T. Cao, Y. Y. Xue, and C. W. Chu, Phys. Rev. B **56**, 2623 (1997).

[16] A. B. Souchkov, J. R. Simpson, M. Quijada, H. Ishibashi, N. Hur, J. S. Ahn, S.W. Cheong, A. J. Millis, and H. D. Drew, Phys. Rev. Lett. **91**, 027203 (2003).

[17] K.-J. Jang, J. Lim, J. Ahn, J.-H. Kim, K.-J. Yee, J. S. Ahn, and S.-W. Cheong, New Journal of Physics **12**, 023017 (2010).

[18] M. Poirier, F. Laliberté, L. Pinsard-Gaudard, and A. Revcolevschi, Phys. Rev. B **76**, 174426 (2007).

[19] S. Petit, F. Moussa, M. Hennion, S. Pailhès, L. Pinsard-Gaudart and A. Ivanov, Phys. Rev. Lett. **99**, 266604 (2007).

[20] P. A. Sharma, J. S. Ahn, N. Hur, S. Park, S. B. Kim, S. Lee, J.-G. Park, S. Guha, and S-W. Cheong, Phys. Rev. Lett. **93**, 177202 (2004).

[21] B. B. Van Aken and T. T. M. Palstra, Phys. Rev. B **69**,134113 (2004).

[22] S. Lee, A. Pirogov, J. H. Han, J.-G. Park, A. Hoshikawa, and T. Kamiyama, Phys. Rev. B **71**, 180413(R) (2005).

[23] T. Lottermoser, T. Lonkai, U. Amann, D. Hohlwein, J. Ihringer, and M. Fiebig, Nature **430**, 541 (2004).

[24] S. Pailhès, X. Fabrèges, L. P. Régnault, L. Pinsard-Godart, I. Mirebeau, F. Moussa, M. Hennion, and S. Petit, Phys. Rev. B **79**, 134409 (2009).

[25] T. Choi, Y. Horibe, H. T. Yi, Y. J. Choi, W. Wu and S.-W. Cheong, Nature Materials **9**, 253 (2010).

[26] M. Fiebig, Th. Lottermoser, D. Frölich, A. V. Goltsev, and R. V. Pisarev, Nature **419**, 818 (2002).

[27] A. V. Goltsev, R. V. Pisarev, Th. Lottermoser and M. Fiebig, Phys. Rev. Lett. **90**, 177204 (2003).

[28] E. Hanamura, K. Hagita, and Y. Tanabe, J. Phys.: Condens. Matter **15**, L103 (2003).

[29] M. Mostovoy, Nature Materials **9**, 188 (2010).

[30] D. G. Tomuta, S. Ramakrishnan, G. J. Nieuwenhuys and J. A. Mydosh, J. Phys.: Condens. Matter **13**, 4543 (2001).

[31] M. Rotter, H. Mueller, E. Gratz, M. Doerr, M. Loewenhaupt, Rev. Sci. Instr. **69**, 2742 (1998).

[32] M. Rotter, Patent Nr 502515, Austrian Patent Office.

[33] D. P. Kozlenko, S. E. Kichanov, S. Lee, J.-G. Park, V. P. Glazkov and B. N. Savenko, JETP Lett. **82**, 193 (2005).

[34] W. Sikora, O. V. Gurin, and V. N. Syromyatnikov, J. Magn. Magn. Mater. **71**, 225 (1988).

[35] T. J. Sato, S.-H. Lee, T. Katsufuji, M. Masaki, S. Park, J. R. D. Copley and H. Takagi, Phys. Rev. B **68**, 014432 (2003).

[36] O. P. Vajk, M. Kenzelmann, J. W. Lynn, S. B. Kim, and S.-W. Cheong, Phys. Rev. Lett. **94**, 087601 (2005).

[37] T. Chatterji, S. Ghosh, A. Singh, L. P. Regnault, and M. Rheinstädter, Phys. Rev. B **76**, 144406 (2007).

[38] M. Rotter, J. Comp. Mat. Sci. **38**, 400 (2006).

[39] McPhase: a software package for the calculation of phase diagrams and magnetic properties of magnetic systems, M. Rotter *et al.*, (2002 – 2010), available at http://www.mcphase.de.

[40] B. Roessli, S. N. Gvasaliya, E. Pomjakushina, and K. Conder, JETP Lett. **81**, 287, (2005).

Chapter 5

Local Magnetism and Magnetoelectric Effect in $HoMnO_3$

Contents

$HoMnO_3$ is a member of the hexagonal manganite family in which large magnetoelectric effects have been found. Correlations between magnetism and ferroelectricity have been investigated before in materials such as $BaMnF_4$ and $Ni_3B_7O_{13}I$, but $HoMnO_3$ is the only case in which a purely ferromagnetic state has been induced from a paramagnetic or antiferromagnetic state by an electric field. In a recent μ^+SR experiment $YMnO_3$ has proven highly accessible yielding much information on the role of the finely balanced interactions within this system which would be inaccessible using other techniques [1]. $HoMnO_3$ is therefore the ideal candidate for the first muon experiment involving the application of an electric field on a multiferroic, as described in Lewtas *et al.* [2]. This experiment was also the first μ^+SR experiment on $HoMnO_3$. In contrast to previous investigations using X-ray and neutron techniques the use of μ^+SR provides a sensitive local probe of the spin distribution. Additionally there is also the possibility of probing the Mn^{3+} and Ho^{3+} environments separately allowing information to be gathered on the different magnetic sublattices. This was a proof of principle experiment, so information gathered can be applied to other materials where less information is known.

5.1 Properties of $HoMnO_3$

The structure of $HoMnO_3$ is isotropic to $LuMnO_3$ which is shown in Figure 4.1. It is described by the space group $P6_3cm$ and is built from corner-sharing MnO_5 bipyramids which form layers parallel to the hexagonal ab plane separated by rare earth ions. The Mn ions form a near-ideal triangular lattice. Some studies have seen no change in the crystal structure between 75 K–2 K with a value for the trimerization remaining greater than x_{Mn}=1/3 [3]. Other studies have found there to be a drop across the x_{Mn}=1/3 threshold corresponding to a change in the magnetic symmetry somewhere below 10 K [4, 5].

5.1.1 Magnetic Properties

As a member of the hexagonal rare earth family the magnetic properties of $HoMnO_3$ are similar to those of $LuMnO_3$ although there are now two magnetic ions, Ho^{3+} and Mn^{3+}. The magnetic properties arise from the almost triangular layers of Mn^{3+} ($3d^4$)

spins with $S = 2$ and Ho^{3+} ($4f^{10}$) spins between the layers. These Ho^{3+} spins possess an Ising-type anisotropy forcing them to align parallel or antiparallel to the hexagonal c-axis whereas the Mn^{3+} spins are confined to the ab plane. At $T_N = 75$ K the Mn sublattice relieves its frustration by ordering antiferromagnetically in the ab plane. The spin structures overcome the geometric frustration by adopting a 120° ordered structure [6] as shown in Chapter 4 Figure 4.4. This has the space group $P\underline{6}_3\underline{c}m$.

There has been much experimental work done on the magnetic phase diagram of $HoMnO_3$ due to the number of phases distinguished by the presence or absence of the Ho^{3+} order and the angle, ϕ, that the Mn^{3+} spins make to the local x direction. There are also many magnetic field dependent phases [7, 8, 9, 10, 11]. This angle differs by $\pi/2$ in each of the ordered phases (with the exception of a small intermediate phase described below).

The HTI phase ($P\underline{6}_3\underline{c}m$) occurs for $38\ K \lesssim T < T_{\mathrm{N}}$ where $\phi = \frac{\pi}{2}$. In this phase the Ho^{3+} spins are disordered. Below $T \approx 38$ K the Ho^{3+} moments are partially antiferromagnetically ordered in the c direction [12] while Mn spin reorientations take place. In the small temperature region $34 \lesssim T \lesssim 38$ K there is evidence of an intermediate magnetic phase (IP) (space group $P\underline{6}_3$) characterized by an angle taking values $\frac{\pi}{2} < \phi < \pi$ [13]. On cooling below $T \approx 34$ K, ϕ locks into $\phi = \pi$ (the HTII phase, $P\underline{6}_3c\underline{m}$).

It is at this spin reorientation transition that some experiments have seen the x_{Mn} position cross the 1/3 threshold and the magnetic symmetry change from Γ_4 to Γ_1, the magnetic arrangements are seen in Figure 4.4. Finally, a further Mn^{3+} spin rotation transition occurs around 5 K to the low temperature (LT) phase where $\phi{=}\frac{3\pi}{2}$ ($P6_3cm$). Here the Ho^{3+} moments also reorder to another structure, although they are still polarized along the c direction.

5.1.2 Electrical Properties

$HoMnO_3$ has a ferroelectric transition temperature of $T_C = 875$ K and a very large polarization of P∼56 mCm^{-2} along the hexagonal c-axis [14]. The ferroelectric structure is the result of the distorted and tilted MnO_5 as well as the displacement of the Ho^{3+} ions [15]. Sharp anomalies have been seen in the dielectric constant at all the magnetic phase transitions as a function of temperature and magnetic fields. This is indicative of strong magnetodielectric coupling in the compound [16] and demonstrates the correlation between the ferroelectric and the magnetic orders [13]. Magnetoelec-

tric coupling occurs because superexchange interactions depend sensitively on orbital overlap, and these can be tuned with an electric field (E-field) as metal cations and ligand anions move in opposite directions [15, 17].

When a magnetic field of a few Tesla is applied there is a change in the electrical polarization greater than δP$\sim$80 μCm^{-2} [18], which is a strong magnetoelectric effect. Optical second harmonic generation and Faraday rotation experiments have suggested that the local magnetic properties of a system are dramatically changed with the application of an electric field of E=10^7 Vm^{-1} [4].

5.1.3 Magnetoelectric Domain Wall Coupling

The ferroelectric domain walls are firmly locked to the magnetic domain walls. This may be explained by supposing that the lattice strain, which is present by virtue of the existence of the ferroelectric domain wall, couples to local Mn magnetic moments. This means that the free energy of the system is lowered when the magnetic order parameter (i.e., the sublattice magnetic moment for an antiferromagnet) changes sign across a ferroelectric domain wall, creating a spatially coincident antiferromagnetic wall. This implies that all ferroelectric domain walls coincide with antiferromagnetic domain walls, but that antiferromagnetic domain walls may exist within a single ferroelectric domain. This is described further in Section 4.2.

5.2 Experimental Details

Samples of $HoMnO_3$ were prepared as described previously [19]. Stoichiometric amounts of dried Ho_2O_3 and MnO_2 powders were mixed and calcined in air for 24 hours at 1100°C and 1200°C, respectively, with intermediate grinding. The powders were formed into cylindrical feed rods and sintered at 1250°C for 15 hours in air. Single crystals of $HoMnO_3$ were grown using the floating-zone technique. The growth was carried out at a rate of 3 mm h^{-1} under the flow of mixed Ar/O_2 gas. Crystals were characterized using X-ray diffraction and DC magnetic susceptibility measurements.

Zero field μ^+SR measurements were made using the General Purpose Spectrometer (GPS) at the Swiss Muon Source, SμS, and the EMU spectrometer at the ISIS facility. Electric field μ^+SR measurements were also made using the EMU spectrometer. μ^+SR can be combined with electric field experiments especially at pulsed muon sources where the electric field can be switched on or off between muon pulses allowing

small effects to be measured. μ^+SR techniques combined with electric field measurements have been used extensively to study semiconductors [20] however experiments with magnetic systems are a recent development [21]. In μ^+SR experiments the spin polarized muons are stopped in a target sample where the muon usually occupies an interstitial position in the crystal. The observed property of the experiment is the time evolution of the muon-spin polarization, the behaviour of which depends on the local magnetic field, B, at the muon site and which is proportional to the positron asymmetry function, $A(t)$, as described in Section 2.2.3 [22].

For the measurements at SμS a polycrystalline sample was measured, made up of approximately 10 unaligned crystallites of various sizes. For the measurements at ISIS a mosaic of aligned crystals was prepared in order that the electric field could be applied along a single crystallographic direction. To produce the mosaic, $HoMnO_3$ crystals were polished into thin plates of thickness 1 mm with the ab plane forming the polished surfaces. Crystallites were aligned such that the muon-spin was initially parallel to the crystallographic c direction. Gold electrodes of thickness 1 μm were evaporated onto these surfaces allowing the application of E-fields along the c direction. The sample was mounted into a tight fitting polytetrafluoroethylene (PTFE) mask and mounted in an aluminium sample holder.

5.3 Results and Discussion

5.3.1 Magnetic Measurements

The DC magnetic susceptibility, Figure 5.1, shows no feature that indicates the onset of magnetic ordering at 76 K. This is consistent with previous measurements of the susceptibility [23] and is likely to be caused by the high paramagnetic susceptibility of the Ho^{3+} ions masking the magnetic transition. Ho^{3+} has an effective paramagnetic moment of 10.6 μ_B. No difference between the zero-field-cooled and field-cooled data is observed at low temperatures. The absence of any effect in the DC susceptibility around 38 K is puzzling since the Ho^{3+} moments are thought to partially order at this temperature. For the hexagonal manganites it has been seen that the Weiss constant increases with decreasing radius of the rare earth ion. It is possible that the increase of the magnetic contribution of the Mn^{3+} sublattice is due to the monotonic decrease of the paramagnetic effect of the rare earth ion. The -850 K hexagonal c-axis Weiss constant of $LuMnO_3$ (Chapter 4) is very different from the approximately -115 K

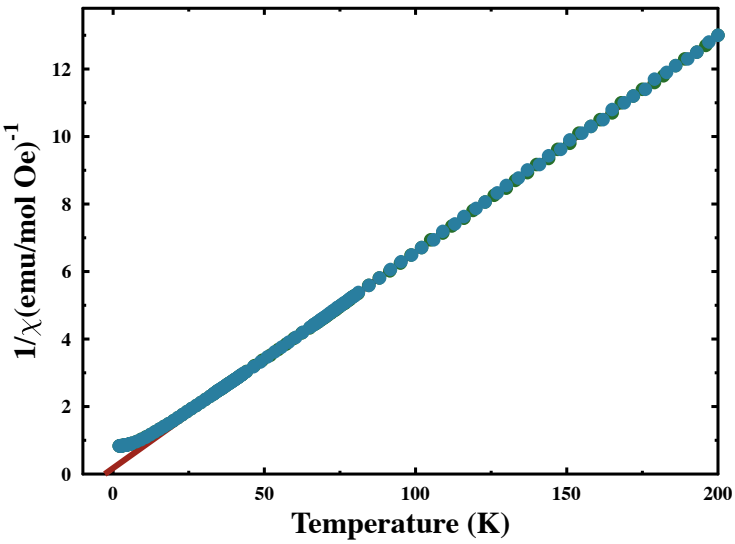

Figure 5.1: Field-cooled (FC) and zero-field-cooled (ZFC) DC inverse susceptibility results for $HoMnO_3$ orientated along the hexagonal a-axis are shown with a fit to the Curie Weiss Law, red line. The FC and ZFC measurements show insignificant deviation and cannot be distinguished. The applied field was 1000 Oe.

Weiss constant of $HoMnO_3$ [24]. The fit to the hexagonal a-axis inverse susceptibility in Figure 5.1 gives a Weiss constant of -3.8 $\pm$ 0.09 K. This is close to previously reported hexagonal a-axis results of 0 $\pm$ 1 K [25].

The AC susceptibility measurements in Figure 5.2 show the effect of an oscillating magnetic field on a single crystal of $HoMnO_3$ and reproduce results reported previously [23]. The maximum frequency that can be reached by the SQUID is 1.5 kHz so these results were taken using the ACMS head on the PPMS. At 10 kHz the imaginary AC susceptibility exhibits a maxima at around 38 K after which the susceptibility decreases and there is a minima around 15 K before a final increase towards 0 K. The maxima at 38 K is due to the spin reorientation of the Mn^{3+} moments. The minima occurs at approximately the same temperature as the saturation of the real susceptibility, Figure 5.1. The relative heights of the maxima and minima at 10 kHz in Figure 5.2 when compared to similar results [10] can be used as an indication of the sample stoichiometry. From the relative peak heights seen in our sample it was initially thought that there may be a small oxygen excess so subsequent samples were annealed. The inset of Figure 5.2 shows the real part of the AC susceptibility at 10 kHz which looks identical to the DC susceptibility except that there is a discontinuity at the magnetic transition. The same Curie Weiss fit is shown on both the DC and AC

graphs. The AC susceptibility is measuring in a different frequency window so it could be that it is able to observe dynamical effects that the DC measurement cannot.

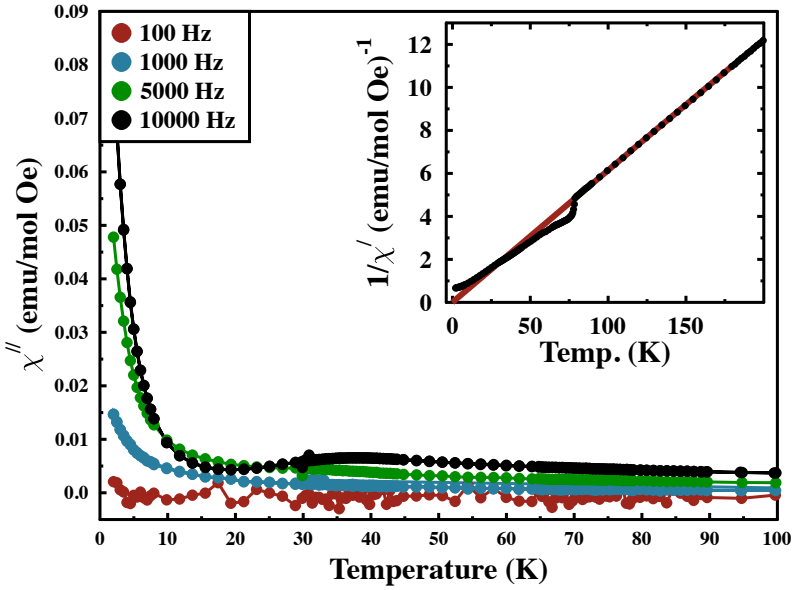

Figure 5.2: The imaginary part of the AC magnetic susceptibility at different oscillating magnetic fields. The behaviour below 72 K at 10 kHz is due to the onset of the magnetic ordering of the Mn lattice. The inset shows the inverse of the real part of the susceptibility with a fit to the Curie Weiss Law shown in red.

5.3.2 Zero Electric Field

Figure 5.3 shows examples of zero field (ZF) μ^+SR spectra measured on $HoMnO_3$. The inset shows an example spectrum measured on the unaligned polycrystalline sample at SμS at $T = 50$ K. Spontaneous oscillations are seen at early times ($0 \leq t \leq 0.1$ μs) in all spectra measured below T_N. Upon cooling to the HTI phase the spectra consist of oscillations at a single frequency with a large relaxation rate. In the HTII phase the oscillations change their form and there is evidence for a second frequency component. These observations are in good agreement with the results of previous μ^+SR measurements [26] made on powder samples of $HoMnO_3$, where oscillations were also observed below T_N.

For muons with their initial spin direction oriented at an angle θ to a static magnetic field, in the absence of fluctuations, the spectrum is expected to be described by

$$A(t) = A_0 \left[\cos^2\theta + \sin^2\theta \cos(\gamma_\mu B t)\right] \tag{5.1}$$

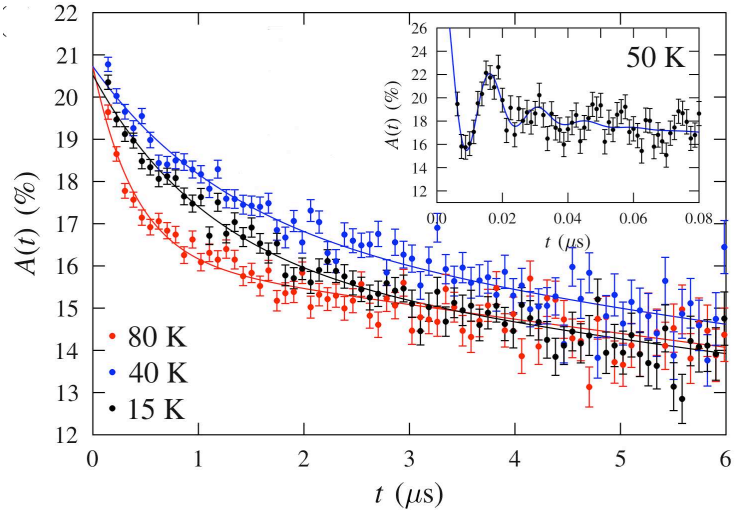

Figure 5.3: $HoMnO_3$ zero field μ^+SR data measured with a pulsed muon source. The relaxation is exponential across the whole measured temperature regime. Inset: Zero field μ^+SR data at $T = 50$ K measured at early times using a continuous muon source. The antiferromagnetic order gives rise to the oscillations in the data.

where γ_μ is the muon gyromagnetic ratio and B is the local magnetic field at the muon site. For a polycrystalline material, averaging over all directions leads to the prediction that

$$A(t) = A_0 \left[\frac{1}{3} + \frac{2}{3} \cos(\gamma_\mu B t) \right]. \tag{5.2}$$

Although this ratio of amplitudes was measured previously [26] it is not observed here. This is attributable to the incomplete angular averaging caused by having only a small number of crystallites.

In contrast to the measurements made at SμS, those made on the aligned mosaic using the pulsed muon source at ISIS did not show resolvable oscillations. This is because the pulse length, τ_{pulse}, limits the dynamic range of the measurement to rates $\approx 1/\tau_{\text{pulse}}$. When oscillations are not resolvable, only the first term in equation 5.1 is measured, giving a signal whose amplitude is due to that component of the muon-spin initially oriented parallel to the local magnetic field at the muon site. The relaxation of such a signal is due to the dynamic fluctuations of the local field at the muon site. In the fast magnetic fluctuation regime, typical of most magnetic materials, dynamics give rise to exponential relaxation [27],

$$A(t) = A_0 \exp(-\lambda t) \cos^2 \theta \tag{5.3}$$

with a relaxation rate given by

$$\lambda = 2\gamma_\mu^2 \langle B_\perp^2 \rangle \tau \tag{5.4}$$

where τ is the correlation time describing the dynamics of the local field distribution and $\langle B_\perp^2 \rangle$ is the second moment of that part of the magnetic field distribution that is perpendicular to the initial muon-spin direction. Dynamic fluctuation in the paramagnetic phase of the material may also be expected to give rise to exponential relaxation, $A(t) = A_0 \exp(-\lambda t)$, and λ might be expected to differ considerably in the two phases. The spectra measured at ISIS show this expected exponential relaxation at all measured temperatures ($15 < T <$ 300 K). The measured asymmetry for these data is best described by a fitting function

$$A(t) = A_1 e^{-\lambda t} + A_{bg} e^{-\lambda_{bg}} \tag{5.5}$$

where $A_{bg} e^{-\lambda_{bg}}$ represents the contribution from those muons that stop in the sample holder or cryostat tail. The background signal due to muons stopping in the PTFE in the sample holder is the distinctive F–μ^+–F state [28], so it can be easily identified and subtracted.

Although it might be hoped that the temperature evolution of $A(t = 0)$ in equation 5.5 would tell us the orientation of the local magnetic field at the muon site via equation 5.1, this is not the case here. $A(t = 0)$ in Figure 5.4(a) shows a decrease in the paramagnetic regime as the temperature is reduced toward T_N. This points to the presence of an additional fast relaxation component that is not resolved. The presence of two relaxation rates signals either two classes of muon site or to two relaxation channels [29]. A significant change in $A(t = 0)$ is not observed when the material magnetically orders, implying that the local magnetic field at the dominant muon sites in our mosaic sample makes only a small angle to the initial muon-spin direction and hence that $\cos \theta$ in equation 5.1 does not differ considerably from unity. Upon cooling below T_N the amplitude $A(t = 0)$ shows quite scattered behaviour in the HTI phase before levelling off in the HTII phase. The presence of an additional relaxing component makes any determination of the local field direction in the crystal very difficult.

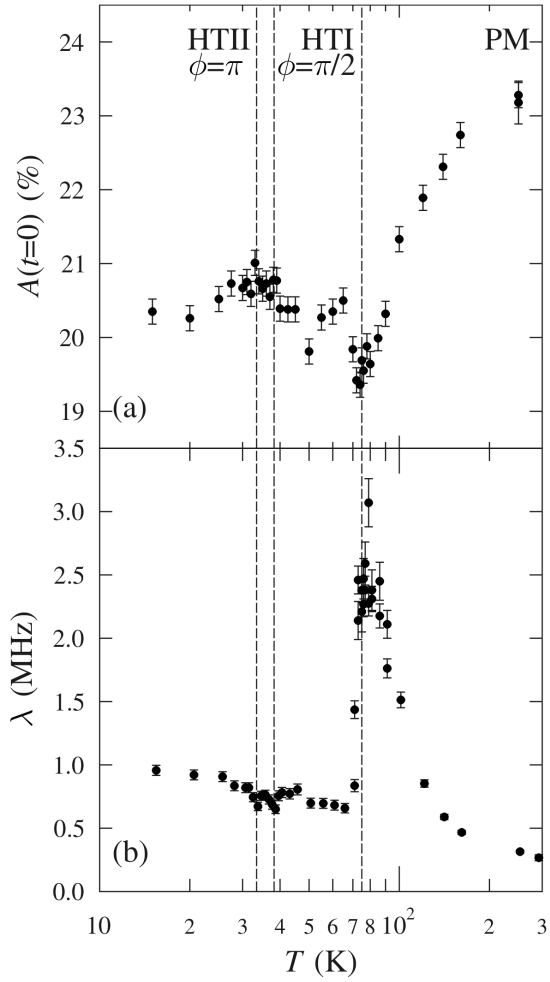

Figure 5.4: Measurements made in zero magnetic and electric field across the phase diagram. (a) The temperature dependence of the initial asymmetry $A(t = 0)$. (b) The evolution of the relaxation rate λ with temperature.

In contrast, the relaxation rate λ provides a good probe of the magnetic behaviour in $HoMnO_3$. On cooling from $T = 300$ K the rate λ, Figure 5.4(b), is seen to increase with decreasing temperature, peaking around 79 K. This reflects the slowing of fluctuations of the Mn^{3+} moments as the material approaches the magnetic phase transition at T_N where these moments magnetically order. On cooling further we observe that λ does not change dramatically on cooling from the HTI to HTII phases, implying that the field distribution and fluctuation rate is similar in the two phases.

However, with decreasing temperature λ shows a weak, approximately linear, increase. Given that it is unlikely that the correlation time should become shorter as temperature is reduced, this behaviour may indicate that the field distribution is be-

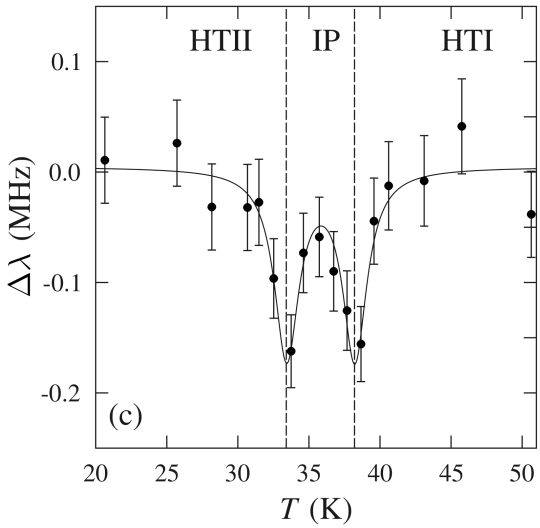

Figure 5.5: The behaviour of λ after background subtraction, giving a more detailed view of Figure 5.4b. Minima are observed at the phase boundaries between the HTI and IP phases and at the boundaries between the IP and HTII phases.

coming narrower (leading to a decrease in $\langle B_\perp^2 \rangle$) as the temperature is reduced in the ordered phase. Subtracting this linear trend from the data results in two pronounced minima, shown in Figure 5.5, which occur at the two proposed transition temperatures between the phases HTI, IP, and HTII. Fitting Lorentzian line shapes to these features allows the transition temperatures to be estimated as $T_{\mathrm{IP}} = 38.2(2)$ K and $T_{\mathrm{HTII}} = 33.4(3)$ K. The minima in λ near the phase boundaries at T_{IP} and T_{HTII} would imply that $\langle B_\perp^2 \rangle$ goes through minima at these temperatures perhaps suggesting that the correlation times are shortest at these phase boundaries or that the field distribution narrows around the transitions. This contrasts with the usual case, such as that seen at T_N, where the relaxation rate peaks at a phase transition and points to a substantial difference in the nature of the transition at T_N to those at T_{IP} or T_{HTII}.

The largest change in λ is seen at $T = 79$ K where the Mn^{3+} spins initially order but where the Ho^{3+} spins do not undergo any change. This contrasts with the changes seen below 38 K, where the Ho^{3+} spins begin to order, which are far more modest. This implies that these measurements are mostly sensitive to the local magnetic fields of the Mn spins. This is consistent with the case of structurally similar $YMnO_3$ [1] where ZF μ^+SR measurements revealed the existence of two separate classes of muon site, showing quite differently behaving relaxation rates. The position of the positive muon is usually close to an electronegative O^{2-} ion. In $YMnO_3$, one site appeared to be closely coupled to the magnetic layers of Mn^{3+} ions, while the other was less

well defined, but was probably due to muons stopping at several positions between the layers. We might expect the muon sites in $HoMnO_3$ to be similar, with the site near the Mn layers giving rise to the relaxation with rate λ and the site between layers coupled more strongly to the Ho^{3+} moments. The latter site would then be responsible for rapid relaxation in the paramagnetic phase which leads to the loss of initial asymmetry described above.

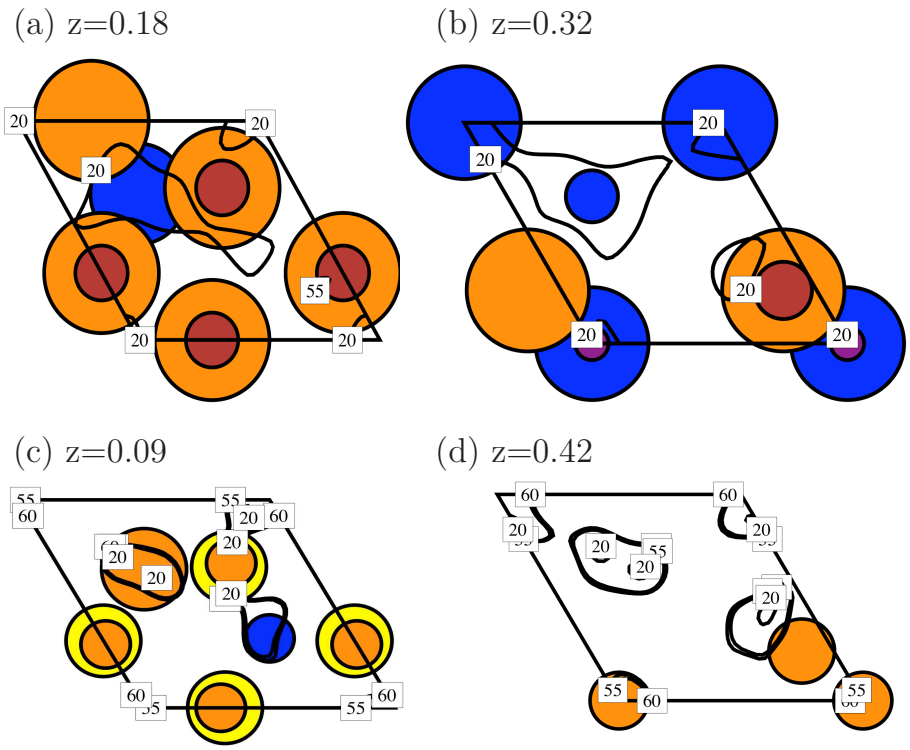

Figure 5.6: Dipole field calculations below T_N without an applied field. The z positions are those identified as possible muon stopping sites from work on $YMnO_3$ [1]. Orange and red disks represent the oxygen ions, yellow and green the manganese ions and blue and purple the holmium ions. The slice in (a) is half way through the oxygen atoms. The contours represent particular frequencies which are also given on the plots.

In $YMnO_3$ two frequencies were fit to the data [1]. The muon site for the higher frequency was found to be 1 Å from an O(4) oxygen along the hexagonal c-axis. This would give sites at (1/3, 2/3, z) and (2/3, 1/3, z) where $z \approx 0.09$, 0.42, 0.59 and 0.92. Only the first two have been shown here as they are symmetrically equivalent to the other two. The site corresponding to the lower frequency was close to the triangularly arranged O(1) and O(2) oxygens. Possible sites would be between the oxygens at (1/3, 2/3, z) and (1/3, 2/3, z) with $z \approx 0.18$ and 0.32.

Each picture of the dipole field calculations (Figures 5.6, 5.7, 5.10 and 5.11) shows a cut of the crystal field structure at a fixed value of z. Contours of constant dipolar field are also shown. A muon site must be away from any atom in the crystal structure and such 'exclusion zones' are shown as the inner coloured disks. A likely muon site is close to an oxygen ion probably at a distance of around 1 Å. The red disk encloses regions closer than 0.5 Å to the oxygen ion, whereas the orange disk encloses regions closer than 1 Å. The muon might therefore be expected to stop within, or at the edge of, the outer shaded disk. Also shown are the cations manganese and holmium. The manganese ions are shown in yellow and green and the holmium ions in blue and purple. However the muon is not likely to stop near to the cations because of their positive charge.

Figure 5.6 shows results of dipole field calculations for temperatures below T_N but above T_{SR} at the sites described above. Slice (a) is at a position half way through the oxygen atoms. It can be noticed that the frequency contour lines are grouped around the (1/3, 2/3) and (2/3, 1/3) positions. A frequency of 20 Hz is observed at all the z positions whereas at $z \approx 0.09$ and $z \approx 0.42$ additional higher frequencies of 55 and 60 Hz are also seen.

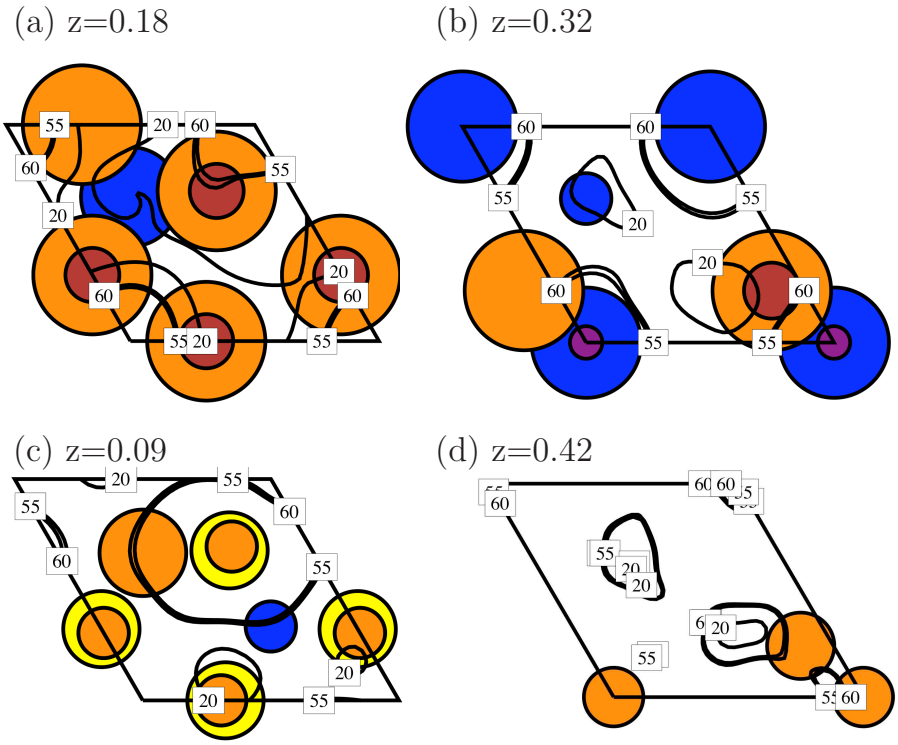

Figure 5.7: Dipole field calculations below the spin reorientation transition temperature, T_{SR}, without an applied field. The z positions are those identified as possible muon stopping sites from work on $YMnO_3$ [1].

Figure 5.7 shows the results of dipole field calculations for temperatures below T_{SR}. Frequency contours are also seen at the expected positions but in this case with the higher frequency contributions present at every z value. The higher and lower frequencies coincide at $z \approx 0.42$. There are small differences in the contours below T_N and T_{SR} perhaps seen most noticeably in the introduction of higher frequencies at the $z \approx 0.09$ and 0.32 positions below T_{SR}.

5.3.3 Electric Field Measurements

E-field μ^+SR measurements were made in the presence of a longitudinal magnetic field, B_a, directed along the crystallographic hexagonal c-axis. Static electric fields of E = 5 x 10^6 Vm^{-1} were applied in the same direction. The saturation field of $HoMnO_3$ occurs at $E = 10^6$ Vm^{-1} [4], above which a state consisting of almost a single ferroelectric domain was expected. As described in Section 4.2 a single domain state cannot be achieved as it has been found that it is not possible to destroy all positive or negative domains with a negative or positive applied electrical poling field [30]. They are reduced but to maintain the cloverleaf pattern they are never eliminated [25]. A summary of the effect of an electric field on the different magnetic phases is given in Table 5.1. Figure 5.8 pictorially illustrates the change in magnetic structure [4].

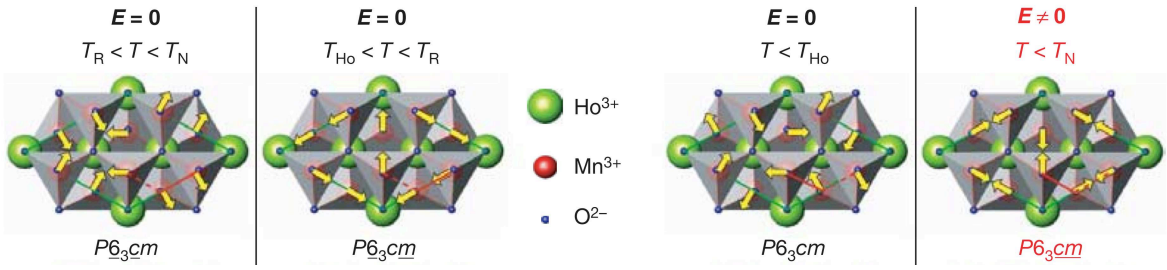

Figure 5.8: The magnetic structures of $HoMnO_3$ in the absence and presence of an electric field. Yellow arrows are the magnetic moments of the Mn ions, green lines indicate the unit cell [4].

As in the ZF case, the spectra for E-field μ^+SR measurements showed exponential relaxation described by relaxation rate λ. There is no significant difference in initial asymmetry upon the application of the electric field. Figures 5.9(a) and 5.9(c) show the effect of applying a magnetic field, B_a, on the relaxation rate, λ, in the presence

Table 5.1: Magnetic Phases of $HoMnO_3$ in an Electric Field

Temp	Space Group	E-Field	Description
873 K	$P6_3cm$	Off	Ferroelectric Transition
75 K	$P\underline{6_3}\underline{c}m$	Off	**HTI**: The Mn sublattices exhibit AFM order in the ab plane with $\phi = \frac{\pi}{2}$. Ho^{3+} do not order.
75 K	$P6_3\underline{cm}$	On	Mn spins reorient to $\phi = 0$. Most experiments see no Ho^{3+} order.
38 K	$P\underline{6_3}$	Off	**IP**: Mn^{3+} spin reorientation in the ab plane, $\frac{\pi}{2} < \phi < \pi$. Ho^{3+} order partially AFM along c-axis.
38 K	$P6_3\underline{cm}$	On	Same Mn spin state as below T_N.
34 K	$P\underline{6_3}\underline{cm}$	Off	**HTII**: ϕ locks into $\phi = \pi$.
5 K	$P6_3cm$	Off	**IP**: Mn^{3+} rotate in the ab plane, $\phi = \frac{3\pi}{2}$. Ho^{3+} reorder still AFM along c-axis.

and absence of a static electric field, E, in the HTII phase at $T = 30$ K and the HTI phase at $T = 50$ K.

In both phases there is little systematic variation in λ as a function of applied magnetic field, B_a, independent of the presence, or absence, of the E-field. It is expected that a dynamic relaxation rate should vary with applied magnetic field as in equation 5.6,

$$\lambda = 2\gamma_\mu^2 \left\langle B_\perp^2 \right\rangle \tau / \left(\gamma_\mu^2 B_a^2 \tau^2 + 1\right), \tag{5.6}$$

which suggests that the system is in the limit such that

$$\gamma_\mu^2 \left\langle B_a^2 \right\rangle \tau^2 \ll 1, \tag{5.7}$$

or, given that the maximum field was 300 mT, τ<5 ns. The main result of these measurements is that, in both HTI and HTII phases, the presence of the electric field, results in a reduction in the relaxation rate λ(E) compared to λ(E=0). The reduction due to the application of the field is approximately 0.05 MHz. Application of the paired-samples t-test shows that the E-field causes a statistically significant decrease

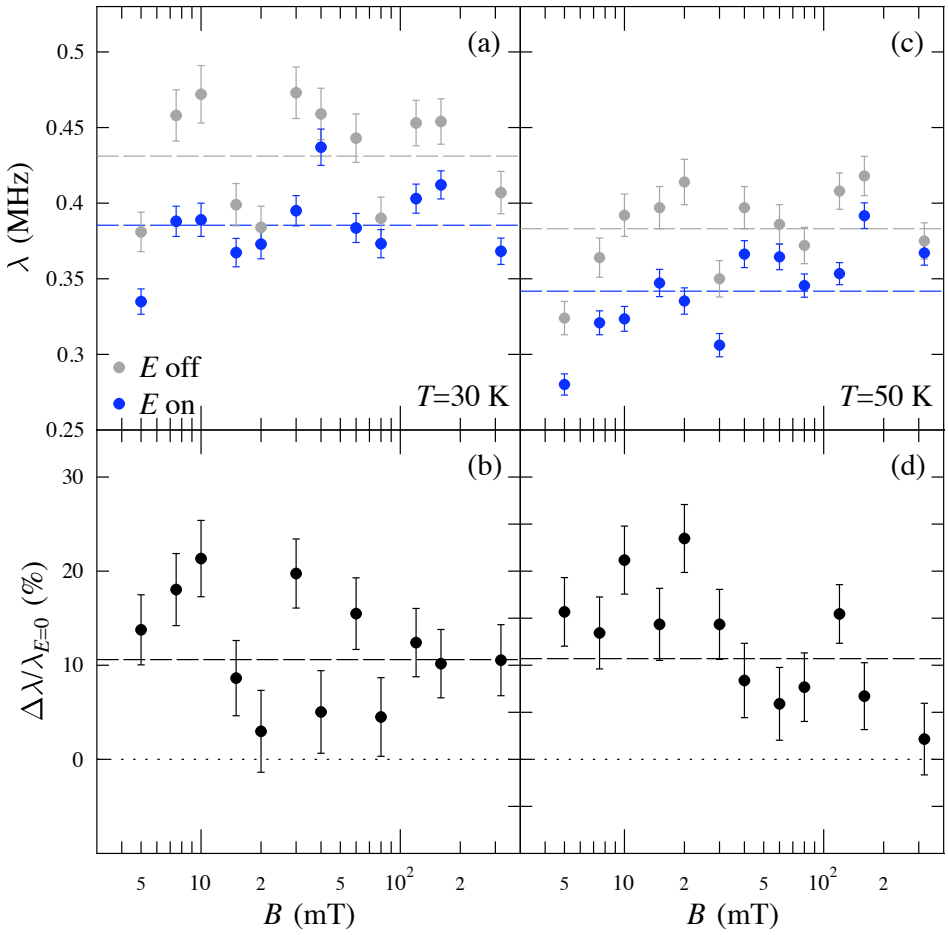

Figure 5.9: (a) Relaxation rate λ at $T = 30$ K (HTII phase) in the presence and absence of an electric field. The average value for each condition is shown as a dashed line. The field is seen to reduce the mean value of λ. (b) Fractional difference in λ defined as $[\lambda(E=0) - \lambda(E \neq 0)]/\lambda(E=0)$. The average difference is around 10% (dashed lines). (c) and (d) are the same as (a) and (b) but measured at $T = 50$ K (HTI phase).

at a >99% confidence level in both phases. Figures 5.9(b) and 5.9(d) show the normalized difference in the relaxation rates with the field on and off, i.e., [λ(E=0) - λ(E≠0)] / λ(E=0) as a function of B_a. Taking the average of these results across the B-field range shows the same average decrease in this quantity of 11(1) % for each phase.

On the application of an E-field the effect is the same within experimental uncertainties in the HTI and HTII phases. This is in keeping with the optical results [4] where the magnetoelectric effect was seen at all temperatures below T_N and would imply that the change in Ho ordering at T_{SR} is not a prerequisite for the observation

of a magnetoelectric effect. Noting that in the fast fluctuation limit the relaxation rate $\lambda \sim \gamma_\mu^2 \langle B_\perp^2 \rangle \tau$, it is likely that the decrease in λ caused by the application of the E-field reflects a decrease in the quantity $\sqrt{\langle B_\perp^2 \rangle}$, the local magnetic field distribution at the muon sites. It seems unlikely that the E-field would cause a decrease in the correlation time, τ.

There are two ways to decrease $\sqrt{\langle B_\perp^2 \rangle}$:

(i) a reduction in the magnitude of the average local magnetic field at the muon sites, caused, for example, by the E-field altering the magnetic moment structure via the magnetoelectric effect in such a way that the average dipole field at the muon sites decreases;

(ii) a decrease in the width of the magnetic field distribution.

For case (ii) the E-field leads to an effective increase in the order in the magnetic structure. This appears to provide the most likely mechanism to explain our measurements.

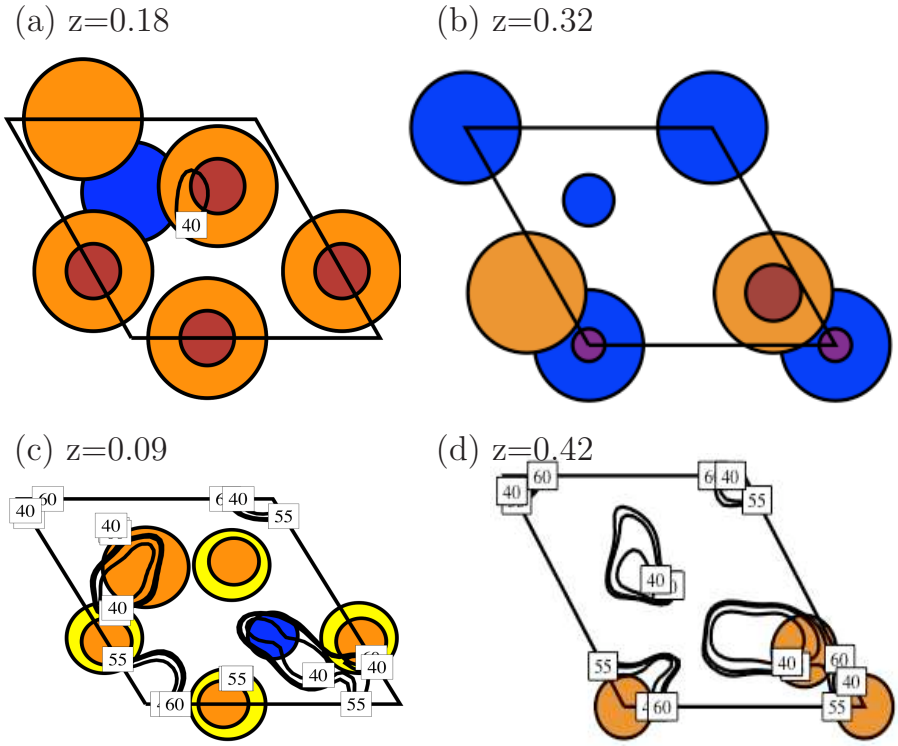

Figure 5.10: Results of dipole field calculations below T_N with the magnetic structure expected in an applied field. The z positions are those identified as possible muon stopping sites from work on $YMnO_3$ [1].

The magnetic order changes found under the application of an electric field as

described in [4], and pictured in Figure 5.8, result in changes to the dipole fields which are seen in the contour plots. Figure 5.10 shows the results of dipole field calculations for temperatures below T_N but above T_{SR} under the application of an electric field. There are higher frequency contours at the expected $YMnO_3$ positions than calculated for the zero field structure, with quite high frequency gradients. Figure 5.11 shows the dipole field calculation results for the magnetic structure below T_{SR} under the application of an electric field. There appears to be less change between the contour maps below T_{SR} without and with field (Figures 5.7 and 5.11) than there is between the contour maps above T_{SR} and below T_N without and with an applied field (Figures 5.6 and 5.10). This might be because there is a less dramatic change of magnetic symmetry.

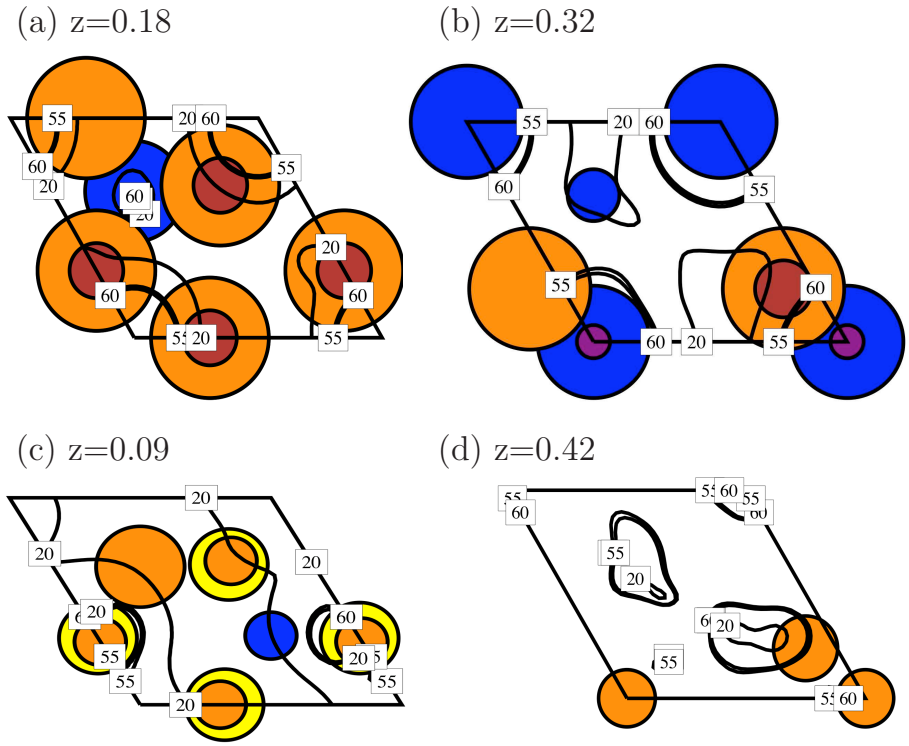

Figure 5.11: Results of dipole field calculations below the spin reorientation transition temperature, T_{SR}, with the magnetic structure expected in an applied field. The z positions are those identified as possible muon stopping sites from work on $YMnO_3$ [1].

$HoMnO_3$ is a more complex system than $YMnO_3$ as there are two magnetic ions present which makes the analysis more involved. However as candidate stopping sites could be clearly found in $YMnO_3$ they provide a good guide as to the likely sites in $HoMnO_3$. Another difficulty in locating muon stopping sites with the dipole field

calculations is due to the hyperfine contribution. The hyperfine contribution is not accounted for in the model and may have a significant effect on the system.

The primary effect of applying a large E-field to a ferroelectric is to produce close to a single ferroelectric domain. Furthermore, it has been demonstrated experimentally in the case of $YMnO_3$ [7] and proposed for $HoMnO_3$ [24] that ferroelectric domain walls coincide with antiferromagnetic domain walls. The application of the E-field therefore causes the size of the ferroelectric domains poled oppositely to the applied field to be hugely reduced and also causes a big reduction in the number of antiferromagnetic domains. This will reduce the width of the magnetic field distribution $\sqrt{\langle B_\perp^2 \rangle}$ probed by the muons and cause the small observed decrease in the relaxation rate λ. These E-field μ^+SR results may therefore be consistent with the magnetoelectric coupling in $HoMnO_3$ being mediated via domain walls, as was originally proposed to explain the results of dielectric constant measurements [24].

5.4 Conclusions

In conclusion the zero field and E-field μ^+SR of $HoMnO_3$ has been studied. It is possible to confirm the presence of magnetic transitions at $T \approx 76$ K, $T = 34$ K and 38 K. The muon probe is primarily sensitive to the ordering and dynamics of the Mn^{3+} magnetic moments, with the Ho ordering having little effect on the measurements. The ordering of the Ho moments, at most, contributes via a minority relaxation channel. The application of electric fields of $E = 5$ x 10^6 Vm^{-1} causes only an approximately 10 $\%$ change in the relaxation rate, which may be accounted for by the change in magnetic domains as a result of the coupled ferroelectric and antiferromagnetic domain walls. This work further corroborates the ideas discussed in Chapter 4 on the coupling of the magnetic and ferroelectric domain walls.

Bibliography

[1] T. Lancaster, S. J. Blundell, D. Andreica, M. Janoschek, B. Roessli, S. N. Gvasaliya, K. Conder, E. Pomjakushina, M. L. Brooks, P. J. Baker, D. Prabhakaran, W. Hayes and F. L. Pratt, Phys. Rev. Lett. **98**, 197203 (2007).

[2] H. J. Lewtas, T. Lancaster, P. J. Baker, S. J. Blundell, D. Prabhakaran and F. L. Pratt, Phys. Rev. B **81**, 014402 (2010).

[3] P. J. Brown and T. Chatterji, J. Phys.: Condens. Matter **18**, 10085 (2006).

[4] T. Lottermoser, T. Lonkai, U. Amann, D. Hohlwein, J. Ihringer and M. Fiebig, Nature **430**, 541 (2004).

[5] X. Fabrèges, S. Petit, I. Mirebeau, S. Pailhès, L. Pinsard, A. Forget, M. T. Fernandez-Diaz, and F. Porcher, Phys. Rev. Lett. **103**, 067204 (2009).

[6] A. Muñoz J. A. Alonso, M. J. Martínez-Lope, M. T. Casais, J. L. Martínez and M. T. Fernández-diaz, Phys. Rev. B **62**, 9498 (2000).

[7] M. Fiebig, Th. Lottermoser, D. Fröhlich, V. Goltsev and R. V. Pisarev, Nature **419**, 818 (2002).

[8] O. P. Vajk, M. Kenzelmann, J. W. Lynn, S. B. Kim and S.-W. Cheong, Phys. Rev. Lett. **94**, 087601 (2005).

[9] F. Yen, C. dela Cruz, B. Lorenz, E. Gastylan, Y. Y. Sun, M. Gospodinov and C. W. Chu, J. Mater. Res. **22**, 2163 (2007).

[10] A. Muñoz, J. A. Alonso, M. J. Martínez-Lope, M. T. Casais, J. L. Martínez and M. T. Fernández-diaz, Chem. Mater. **13**, 1497 (2001).

[11] T. Lonkai, D. Hohlwein, J. Ihringer and W. Prandl, Appl. Phys. A: Mater. Sci. Process **74**, s843 (2002).

[12] S. Nandi, A. Kreyssig, L. Tan, J. W. Kim, J. Q. Yan, J. C. Lang, D. Haskel, R. J. McQueeney and A. I. Goldman, Phys. Rev. Lett. **100**, 217201 (2008).

[13] B. Lorenz, C. R. dela Cruz, F. Yen, Y. Q. Wang, Y. Y.Sun, C. W. Chu, Proc. ACERS Ann. Meet. April (2005).

[14] P. Coeuré, F. Guinet, J. C. Peuzin, G. Buisson and E. F. Bertaut, Proceedings of First International Meeting on Ferroelectricity (Institute of Physics, London), p332 (1996).

[15] H. Lueken, Angew. Chem. Int. Ed. **120**, 8690 (2008).

[16] F. Yen, C. R. dela Cruz, B. Lorenz, Y. Y. Sun, Y. Q. Wang, M. M. Gospodinov and C. W. Chu, Phys. Rev. B **71**, 180407(R) (2005).

[17] G. A. Gehring, Ferroelectrics **161**, 275 (1994).

[18] N. Hur, I. K. Jeong, M. F. Hundley, S. B. Kim and S.-W. Cheong, Phys. Rev. B **79**, 134120 (2009).

[19] H. D. Zhou, J. C. Denyszyn and J. B. Goodenough, Phys. Rev. B **72**, 224401 (2005).

[20] D. G. Eshchenko, V. G. Storchak and G. D. Morris, Phys. Lett. A **264**, 226 (1999).

[21] V. G. Storchak, O. E. Parfenov, J. H. Brewer, P. L. Russo, S. L. Stubbs, R. L. Lichti, D. G. Eshchenko, E. Morenzoni, V. P. Zlomanov, A. A. Vinokurov and V. G. Bamburov, Physica B **404**, 899 (2009).

[22] S. J. Blundell, Contemp. Phys. **40**, 175 (1999).

[23] R. Pauthenet and C. Veyret, J. Phys. (France) **31**, 65 (1970).

[24] B. Lorenz, A. P. Litvinchuk, M. M. Gospodinov and C. W. Chu, Phys. Rev. Lett. **92**, 087204 (2004).

[25] B. Lorenz, F. Yen, M. M. Gospodinov and C. W. Chu, Phys. Rev. B **71**, 014438 (2005).

[26] S. G. Barsov, S. I. Vorob'ev, V. P. Koptev, E. N. Komarov, S. A. Kotov, S. M. Mikirtych'yants, G. V. Shcherbakov, A. E. Pestun and Ya. M. Mukovskii, JETP Lett. **85**, 658 (2007).

[27] R. S. Hayano, Y. J. Uemura, J. Imazato, N. Nishida, T. Yamazaki and R. Kubo Phys. Rev. B **20**, 850 (1979).

[28] T. Lancaster, F. L. Pratt, S. J. Blundell, I. McKenzie and H. E. Assender, J. Phys.: Condens. Matter **21**, 346004 (2009).

[29] T. Lancaster, S. J. Blundell, P. J. Baker, H. J. Lewtas, W. Hayes, F. L. Pratt, H. T. Yi and S.-W. Cheong, Phys. Rev. B **80**, 020409(R) (2009).

[30] M. Mostovoy, Nature Materials **9**, 188 (2010).

Chapter 6

Rare Earth Chromites

Contents

Experimental work in the 1960s on the family of rare earth chromites, RCrO$_3$, began to gather evidence that this might be an interesting series to investigate for multiferroic and magnetoelectric properties [1]. Several recent papers have been published claiming to have found multiferroicity [2, 3]. However these chromites have a centrosymmetric space group which is not compatible with ferroelectricity. The suggested mechanism is that they remain globally centrosymmetric but have a locally non-centrosymmetric structure. As definitive proof of ferroelectricity had not been shown the aim of this work was to investigate the properties of this series to determine if the title multiferroic is justified.

6.1 Properties of Rare Earth Chromites

6.1.1 Structural Properties

Rare earth chromites, RCrO$_3$, have a GdFeO$_3$ distorted perovskite structure and belong to the centrosymmetric space group Pbnm(D$^{16}{}_{2h}$), Figure 6.1(a). The oxygen polyhedra surrounding the chromium ions have octahedral tilting distortions. This family is also referred to as the orthochromites and the axes described are orthorhomic axes. The experiments in this chapter use single crystals grown by a flux method by B. M. Wanklyn in the 1960s [4] and pressed polycrystalline pellets prepared by D. Prabhakaran in 2007 for these experiments. The literature indicated that in the single crystals there was evidence of impurity phases and the accumulation of lead deposits in cracks that formed on cooling [5]. To compensate for this all the crystals were examined with X-ray Laue diffraction to confirm their quality. They were found to be good single crystals with only minimal twinning in small sections. Residual lead was found on the crystals but was removed thoroughly by placing the crystals in nitric acid which reacts with the lead to form water soluble lead nitrate.

A change of the rare earth ion can have a significant effect on the chromite properties. There is a trend across the series between the magnitude of the covalency in the Cr–O bond and the radius of the rare earth ion. It has been estimated that of the three 3d electrons of Cr^{3+} on average only two remain localized on the Cr^{3+} site and the remaining electron takes part in the covalent bonding of the Cr–O linkages. The covalent nature of the Cr–O linkages increases towards the higher members of the series, increasing from LaCrO$_3$ to LuCrO$_3$ [6].

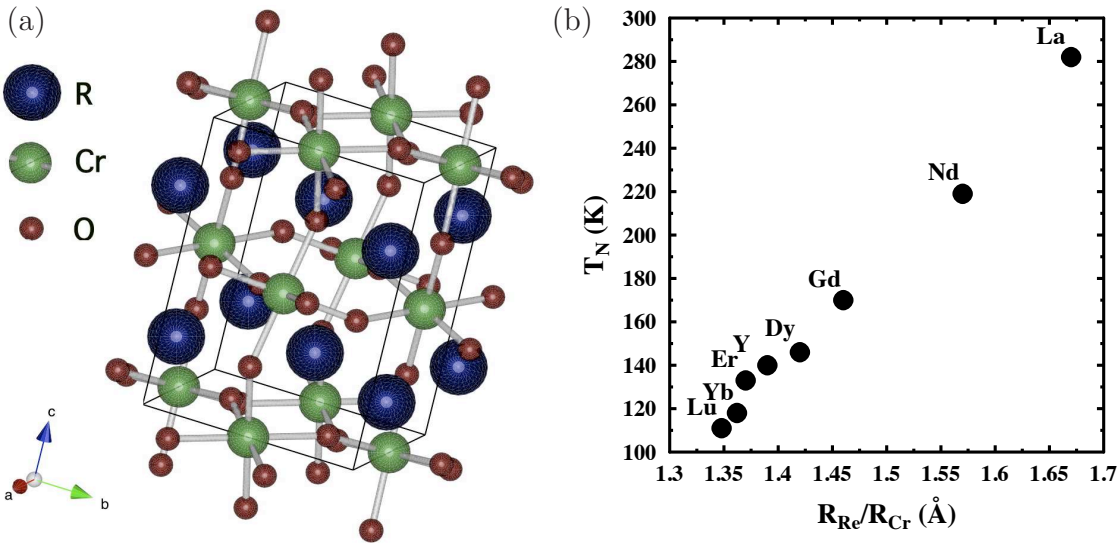

Figure 6.1: (a)RCrO$_3$ distorted orthorhombic structure of space group Pbnm [7]. (b) Variation of the transition temperature to canted antiferromagnetic order from the paramagnetic state as a function of the radius of the rare earth ion. The observed trend can be related to the magnitude of covalent mixing [8].

6.1.2 Magnetic Properties

The materials in this thesis have both magnetic (R=Yb,Gd,Nd) and non-magnetic (R=Y,Lu,La) rare earth ions. The Cr^{3+} ions have $S = 3/2$ with $\mu_{\text{eff}} = 2\mu_{\text{B}}[S(S+1)]^{1/2}$=3.87 μ_B for an ideal spin-only ion. The rare earth chromites are canted antiferromagnets (due to superexchange coupling between nearest neighbours) with a weak ferromagnetic moment resulting from the canting of the Cr^{3+} spins. The net moment of this sublattice lies along either the orthorhombic c- (G_xF_z) or a-axis (G_zF_x) (Bertaut notation) perpendicular to the moment direction of the antiferromagnetic structure. The unit cell is doubled along the $\langle 111 \rangle$ direction as it has G-type antiferromagnetic ordering, a result of the intra-plane and inter-plane antiferromagnetic coupling. When the rare earth ion is magnetic the net moment of this subsystem is then oriented parallel or antiparallel to the Cr^{3+} sublattice depending on the Cr^{3+}–R^{3+} interaction. An early review of these states can be found in reference [9]. As in the RMnO$_3$ series the decrease of the magnetic ordering temperature of the transition metal ions, T_N, is due to the increase of the bending of the Cr–O–Cr bond angle which is a result of the decrease of the ion size as shown in Figure 6.1(b). The magnetic ordering temperature of the Cr^{3+} sublattice decreases monotonically across the periodic table from 282 K for LaCrO$_3$ to 112 K for LuCrO$_3$. The ordering of the R^{3+} sublattice does not follow

the same trend across the periodic table [10].

A major question when looking at materials with two distinct spin systems is the nature of the coupling between them. Symmetric and antisymmetric coupling is allowed by the crystallographic symmetry. By studying $ErCrO_3$ it was observed that the Er^{3+}–Cr^{3+} coupling in all phases is antisymmetric and due mainly to Dzyaloshinsky-Moriya type exchange [11]. When both subsystems are magnetic there are three types of interaction that need to be considered; the Cr^{3+}–Cr^{3+}, R^{3+}–Cr^{3+} and R^{3+}–R^{3+} interactions, listed from strongest to weakest. The different interactions result in complex magnetic properties but having differing magnitudes their effects can be identified by measurements in different temperature ranges [12]. In $GdCrO_3$ for example above 100 K the Cr^{3+}–Cr^{3+} interaction dominates resulting in Cr^{3+} subsystem ordering at 170 K. Below 100 K the Cr^{3+}–Gd^{3+} interactions become more important and at very low temperatures the Gd^{3+}–Gd^{3+} interaction results in the ordering of the Gd^{3+} subsystem.

Table 6.1: $R CrO_3$ Magnetic Properties

$RCrO_3$	T_N	Spin Reorientation	Details
$LuCrO_3$	111 K		Cr^{3+} moment in ac plane 63^o to a-axis. Weak FM along a-axis.
$YbCrO_3$	118 K	16.5 K Yb^{3+} order antiparallel to Cr^{3+}	Cr^{3+} moment in ac plane 68^o to a-axis. Weak FM along a-axis [13] Yb^{3+} moments in ab plane.
$YCrO_3$	140 K		Cr^{3+} AFM order along a-axis. Weak FM along c-axis.
$GdCrO_3$	170 K	7 K Cr^{3+} reorients 2.3 K Gd^{3+} orders	Weak FM along c-axis then along a-axis below 7 K [14]. Gd^{3+} moment lies in ab plane.
$NdCrO_3$	219 K	34 K Cr^{3+} reorients to Γ_1 uncanted AFM	Γ_2 canted AFM along c-axis. Weak FM along a-axis [15] Nd^{3+} moments lie in ab plane.

Anisotropic parts of the magnetic interaction between the Cr^{3+} ions and the rare earth ions are responsible for spin reorientations [16]. As the temperature is lowered the effective field increases because of increased rare earth magnetization. When the interaction energy of the Cr^{3+} spins, within the effective fields, exceeds the anisotropic

energy of the Cr^{3+} ions then spin reorientations take place. Again using the example of $GdCrO_3$ the net magnetic moment of Cr^{3+} ions lies parallel to the crystallographic orthorhombic c-axis and an antisymmetric exchange interaction between Gd^{3+} and Cr^{3+} produces an effective magnetic field at the Gd^{3+} site of 5.5 kOe, whose direction is opposite to that of the canted Cr^{3+} moments. This is different from many perovskites, RBO_3 where the direction of the R^{3+} moments are perpendicular to the canted B^{3+} moments. The interaction in $GdCrO_3$ becomes even more important at lower temperatures which leads to the spin reorientation of Cr^{3+} at about 7 K. At lower temperatures the magnetic interaction between Gd^{3+}–Gd^{3+} becomes significant and results in the ordering of the Gd^{3+} moments at 2.3 K.

6.2 Multiferroic Mechanism

The space group Pbmn is centrosymmetric and so fundamentally cannot be ferroelectric. The orthochromite magnetic symmetry does allow however for linear magnetoelectric coupling. Although some studies have found evidence of, and suggested explanations for, multiferroicity in this family, other investigators have set out the reasons that it cannot occur and experimental evidence for why observed ferroelectricity is flawed [17]. Examples of the experimental evidence for ferroelectricity are shown in Figure 6.2.

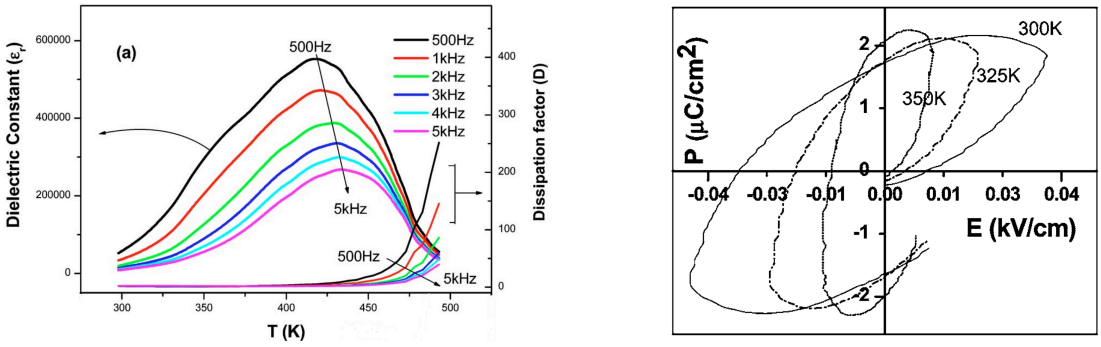

Figure 6.2: Dielectric behaviour and a polarization loop of $YCrO_3$ as published in reference [2].

A study of the pair distribution functions based on neutron diffraction data of $YCrO_3$ claims to provide an explanation [3]. It claims that in the short distance range of 1–6 Å and below the supposed ferroelectric transition temperature the data is best described by the non-centrosymmetric space group $P2_1$ but conforms to the

centrosymmetric group above this temperature. However, over the longer range of 1–22 Å the fitting conforms to the centrosymmetric space group. Using first principles calculations they also found that while in $LaCrO_3$ (not suggested to be a ferroelectric) the La^{3+} ion displacement is stable at its high symmetry site the Lu^{3+} ion in $LuCrO_3$ (supposed ferroelectric) has a double energy well producing a tendency to be off-centred. The off-centring of the Lu^{3+} resulted in a small polarization in their calculations [3]. From this it was suggested that the mechanism under which these materials become ferroelectric is that they remain globally centrosymmetric but locally non-centrosymmetric.

First-principle spin-dependent density functional theory calculations have been used to look at the structural optimization of $YCrO_3$ given ferroelectricity should not occur in a centrosymmetric structure [2]. Two structural instabilities were found, the strongest one exhibiting rotational motion of the oxygen octahedra and the weaker one being Y^{3+} displacement with respect to the oxygen cage. The former would result in an antiferrodistortive phase and the weaker one in a break in the inversion symmetry giving rise to the ferroelectric phase. Hence the polarisation arising from the weak instability is relatively small. The off-centring of the Cr was found not to be favoured energetically [2]. However another paper [18] described neutron pair distribution function analysis and concluded that an off-centring of the Cr does occur in a disordered (local) manner providing the source for the electrical polarization.

In a review of multiferroic mechanisms Khomskii reasons why non-centrosymmetry does not occur in these compounds [19]. $RCrO_3$ have half filled t_{2g} levels and empty e_g levels, with no empty chromium d shell for hybridization with the oxygen p orbitals. It seems that the latter e_g levels have strong hybridization with the oxygen ions so there could be scope for an off-centring distortion via the mechanism in which displacement is caused by the formation of one strong dative covalent bond. A singlet state would be formed from the strong covalent bond with the oxygen (the e_g electrons participating in the bond formation). However Khomskii argues that this is made unlikely as the interaction does not favour a singlet state [19]. If there are other localized electrons at the transition metal ion forming localized spins (in this case $S = 3/2$) as there would be from the t_{2g}^3 occupancy of Cr^{3+} then these spins would have a strong Hund's rule exchange with the electrons in the bond. The singlet from the covalent bond has an up and a down electron from the metal ion. Hund's rules however want to act to maximise S so all the electrons would be pointing up. This would break up the bond, with this interaction acting as a 'pair breaker' to destroy the singlet state. It has been

shown with band structure calculations that without the pair breaking of the localized spins in an analogous material the energy of the system would actually decrease with the off-centring octahedra distortion, thus favouring ferroelectricity [19].

6.3 Magnetization of $R\mathbf{CrO}_3$

By looking at the magnetic properties of the series more thoroughly than was possible in previous studies different features of these compounds can be observed. Most of the recent attention on this family has focussed on $YCrO_3$ as it has a simple magnetic structure with a single magnetic species. By comparing chromites where the rare earth ion plays significantly different roles much can be learnt about the interaction of the subsystems.

The Field Cooled (FC) and Zero Field Cooled (ZFC) magnetization allows the magnetic order and reorientation transitions to be observed. Due to the canting a weak ferromagnetic signal can be detected below the ordering temperatures in the ZFC and FC results. This is observed for Nd, Y, Yb and Lu chromites in Figures 6.3, 6.4, 6.5 and 6.6 respectively. From the results the critical parameters can be found giving important information on the magnetic system.

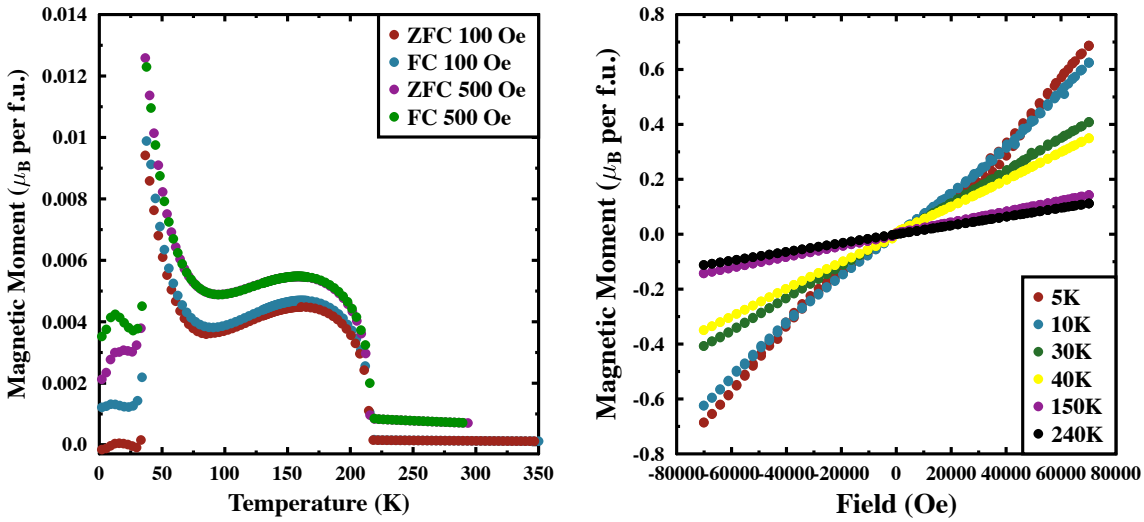

Figure 6.3: Temperature dependence of the magnetization of $NdCrO_3$ in various fields is shown in the left panel. To the right the hysteresis loops from all the sections of the magnetic phase diagram of $NdCrO_3$ are shown. The crystal was not oriented along a high symmetry crystallographic axis.

6.3.1 $NdCrO_3$

In Figure 6.3 all the transitions in Nd can be distinguished with greater clarity than has been reported previously [20]. The spontaneous magnetisation increases from $T_N = 219$ K with decreasing temperature reaching a maximum at around 180 K. It then decreases reaching a minimum around 85 K where there is a compensation point and the moments have been observed to change direction [20]. It then reaches a maximum as the temperature decreases to the spin reorientation transition $T_{SR} = 34$ K (Morin-type phase transition) [21]. At T_{SR} the ordering changes from Γ_2 to Γ_1, Table 6.1. From 214 K to 34 K the moments are found to lie along the orthorhombic a-axis (with antiferromagnetic order along the c-axis). This behaviour appears to be unique in this family to $NdCrO_3$. This behaviour is perhaps more like a ferrimagnetic material [11]. The hysteresis measurements on the right of Figure 6.3 show behaviour suggestive of $NdCrO_3$ having a metamagnetic transition where the least steep part of the curve is at 0 Oe and it curves in the opposite way to an S-shape graph. There is a lack of consistency in the literature as to whether there is any magnetization below T_{SR}. The results presented here differ from previous results where below 35 K the magnetic moment remained zero. Figure 6.3 shows an increase in the magnetic moment below 35 K and a non-zero moment value at 2 K.

The Nd^{3+} moments are polarised by the Cr^{3+}–Nd^{3+} exchange and dipolar interactions so that the moments lie in the ab plane [20]. Below T_{SR} the Nd^{3+}–Nd^{3+} interaction means that the rare earth ions are further polarized. It appears that the Nd^{3+} moments are in the ab plane but that there is no long-range cooperative order as it is inhibited by the large Nd^{3+}–Cr^{3+} interaction which is much larger than the Nd^{3+}–Nd^{3+} interaction [15]. This is not necessarily expected as there is a relatively low Cr^{3+} sublattice ordering temperature.

6.3.2 $YCrO_3$

In $YCrO_3$ the FC and ZFC magnetization were indistinguishable, Figure 6.4 shows the lack of spin reorientation transition in the magnetization of the FC data. Of all the chromites studied $YCrO_3$ has the most clear ferromagnetic component of the canting as shown in the right panel of Figure 6.4. The antiferromagnetic transition temperature was found to be $T_N = 140.49 \pm 0.07$ K from the fitting of a phenomenological function,

$$M(T) = M(0)(1 - (T/T_N)^{\alpha})^{\beta}, \tag{6.1}$$

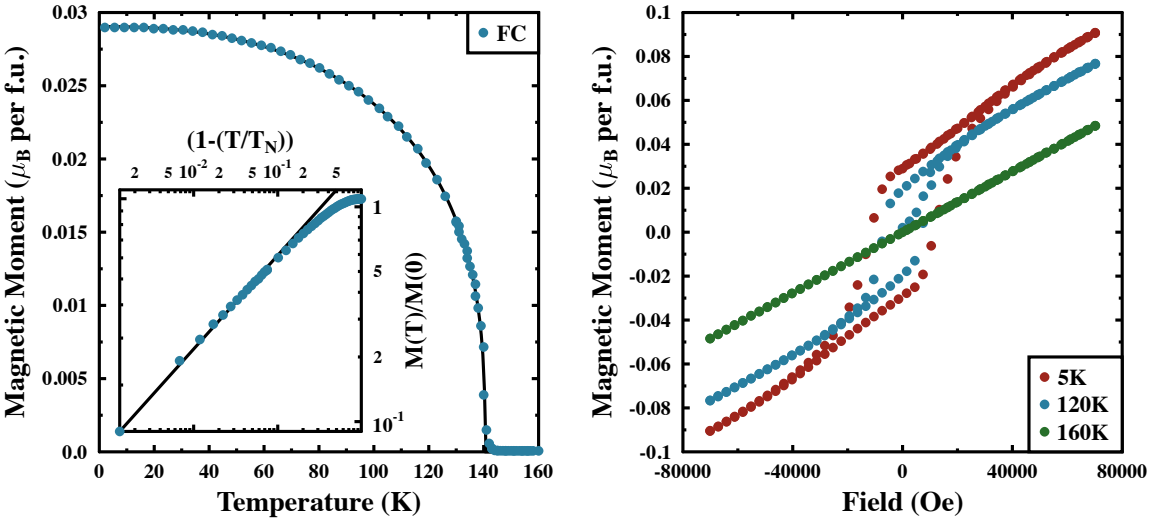

Figure 6.4: The left panel shows field-cooled magnetization of a pressed pellet of $YCrO_3$ in 100 Oe (the zero field cooled measurements were indistinguishable). The fit to equation 6.1 is displayed in black. The inset shows the fitting of the critical region where the scaling is logarithmic. Magnetic hysteresis results are shown on the right for temperatures above and below T_N.

where M(0) was found to be 0.029 μ_B/formula unit. This fitting is plotted as the black line on the main graph of the left panel of Figure 6.4. With the transition temperature accurately identified the critical parameter β can then be found from a log graph of $M(T)\backslash M(0)$ against $(1-(T/T_N))$.

This method allows the fit to be made just to the critical region around T_N which makes the determination of the critical parameter more accurate [22], Figure 6.4 (inset). The value of β is then extracted from the linear region of the graph which equates to the temperature region closest to T_N. For $YCrO_3$ β=0.341 $\pm$ 0.003 which is close to the value representative of a 3D Ising model [22, 23]. It is slightly higher that the $\beta = 0.326$ expected for a 3D Ising model but is lower than the $\beta = 0.5$ expected for a mean field model [22, 23]. However, as section 6.4.4 shows, the heat capacity data is represented very well by a mean field model. Given the magnetization and heat capacity data suggest conflicting models no firm conclusions can be drawn.

6.3.3 $YbCrO_3$

$YbCrO_3$ is an interesting material because of the strong anisotropic exchange interaction between the Cr^{3+} and Yb^{3+} ions. The Yb^{3+} ions only have one $4f$ hole so the $4f$ orbital is widely spread which results in the strong $3d$–$4f$ exchange interaction

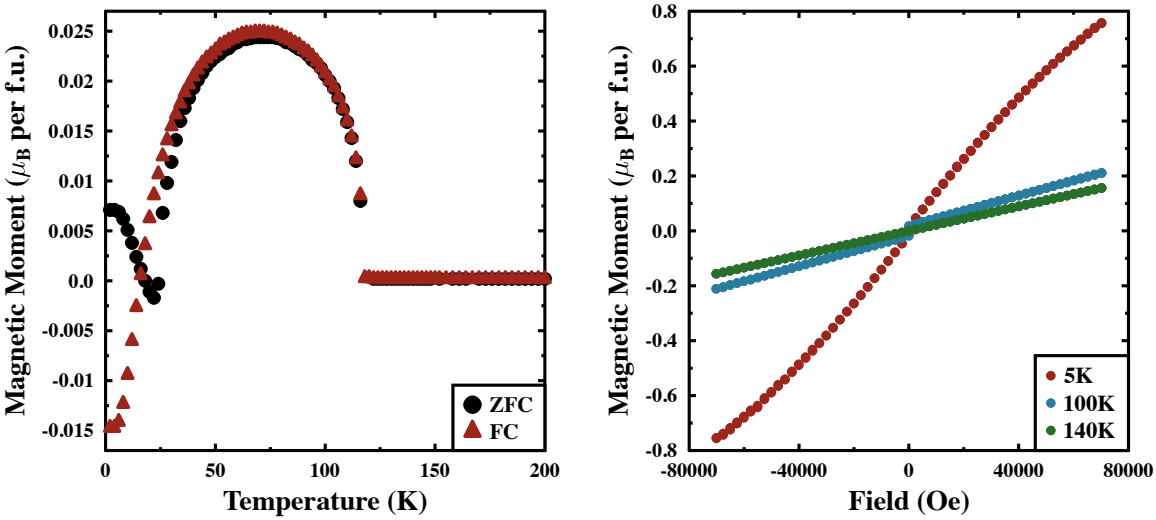

Figure 6.5: Zero and field-cooled magnetization of $YbCrO_3$ in 100 Oe on the left showing the compensation point and magnetic hysteresis in $YbCrO_3$ showing no remnant magnetization on the right. The crystal was aligned perpendicular to the orthorhombic a-axis and at 43° to the b-axis.

[24]. There is a metamagnetic transition (H_c=6.7 T) where the weak ferromagnetic moment of the Cr^{3+} spins reverse direction from antiparallel to parallel to the direction of the net magnetic moment of the Yb^{3+} spins which lie in the ab plane. There is a metamagnetic transition at 16.5 K where the net moment of the Yb^{3+} couples antiparallel to the weak ferromagnetic moment of the Cr^{3+} spins [13] as shown by the change in the sign of the magnetization, Figure 6.5. Our sample of $YbCrO_3$ was a single crystal for which a PTFE holder was made to fit inside the straw that holds the sample within the SQUID so the sample could be oriented with particular axes along the field direction. This however generated spurious results. It was therefore oriented with the orthorhombic a-axis perpendicular to the field and the b-axis at 43^o to the field direction. The hysteresis is consistent with the moments being perpendicular to the applied field.

6.3.4 $LuCrO_3$

A pressed pellet sample of $LuCrO_3$ was used for the magnetization experiment, Figure 6.6. As for $YCrO_3$, $LuCrO_3$ shows no evidence for a spin reorientation transition in the magnetization data. This provides further evidence that it is the presence of a magnetic rare earth ion that causes the reorientation. Fitting the critical parameters to $LuCrO_3$ magnetization data found T_N=113.74 ± 0.17 K, very slightly higher than

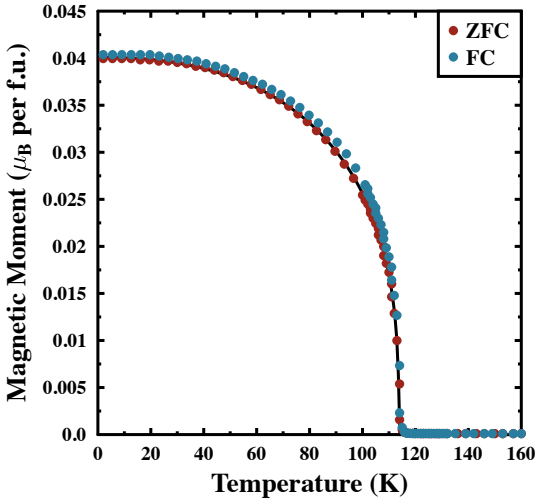

Figure 6.6: Field-cooled and zero field cooled temperature variations of the magnetization in $LuCrO_3$ measured in 100 Oe. Only small differences between FC and ZFC measurements are observed. The fit to equation 6.1 is displayed in black.

the 111 K reported in most of the literature. The transition temperature extracted from μ^+SR data gives T_N=114.8 K, see Section 6.6, also higher than the expected value. From this the critical parameter β=0.335 $\pm$ 0.003 was found. The value 0.335 is close to that expected for a 3D Ising structure as found in $YCrO_3$. However as discussed in section 6.3.2 no firm conclusions can be drawn.

6.4 Heat Capacity of $RCrO_3$

The molar heat capacity, C, results in this section show the magnetic transitions, Schottky anomalies and entropy contributions, exposing the underlying physics. The general trends and magnitudes agree with earlier heat capacity work taken using differential scanning calorimetry although the work in this thesis is much more detailed [25]. Heat capacity results have been divided by the gas constant, R=8.314 $Jmol^{-1}K^{-1}$, to make them more easily comparable to previously published results [15, 26].

6.4.1 Transition Temperatures

There are several interesting features in the heat capacity results to be found in different temperature ranges. The λ-shaped peaks indicate second order phase transitions where the canted antiferromagnetic ordering of the Cr^{3+} spins occurs. There are also spin reorientation transitions which are harder to detect at lower temperatures. The

axes of the order varies between chromites.

$YbCrO_3$ was oriented with the a-axis perpendicular to the field and the c-axis 43^o from vertical. This orientation was a necessity of good thermal contact to the heat capacity puck. The upper panel of Figure 6.7 identifies T_N from the λ transition at 118 K but the reorientation transition is subsumed by the Schottky anomaly which is discussed in the next section. The peaks that appear with the application of the magnetic fields may be induced ordering transitions but that cannot be determined from these results. The small peaks in the field scans were repeatable however with few points around the peaks, even when more detailed scans were undertaken, no firm conclusions can be drawn as to their origin. The idea that they could be induced ordering transitions is speculation.

In the lower graph of Figure 6.7 the $GdCrO_3$ λ shaped peak shows the onset of magnetic order at around 170 K. The $GdCrO_3$ was measured with the b-axis along the magnetic field direction. In the inset the Cr^{3+} reorientation is observed at 7 K at 0 T. However when a field is applied the reorientation transition disappears. The ordering at 2.3 K is not observed as sufficiently low temperatures were not reached.

In the upper graph of Figure 6.8 the ordering transition of the powder sample of $LuCrO_3$ is observed at about 114 K. There is no Schottky anomaly in zero field. The inset shows the change in the transition peak shape in a field of 5 T. This will be more fully explained in Section 6.4.4 for the more complete data set of $YbCrO_3$.

The $NdCrO_3$ was measured with the c-axis along the magnetic field. The lower graph in Figure 6.8 shows the λ anomaly at T_N=219 K. Although other Nd $3d$ metal oxide systems have low temperature ordering of the Nd^{3+} moments this does not occur in $NdCrO_3$. The Nd^{3+}–Cr^{3+} exchange field is large suppressing the co-operative ordering of the Nd^{3+} [27]. Below 1 K there is a hyperfine contribution [15] but these results do not reach that temperature. Very little change is observed on the application of fields up to 7 T in $NdCrO_3$ at either the high temperature transition or around the Schottky anomaly as explained in the following section.

6.4.2 Schottky Anomaly Calculations

Schottky anomalies are smooth broad maxima in the heat capacity signal close to $k_BT \sim \mu_BB$ where it is possible to thermally excite transitions between two states of a system. When the temperature is too low there is not enough energy to excite the transitions from the ground state and when temperatures are too high both states

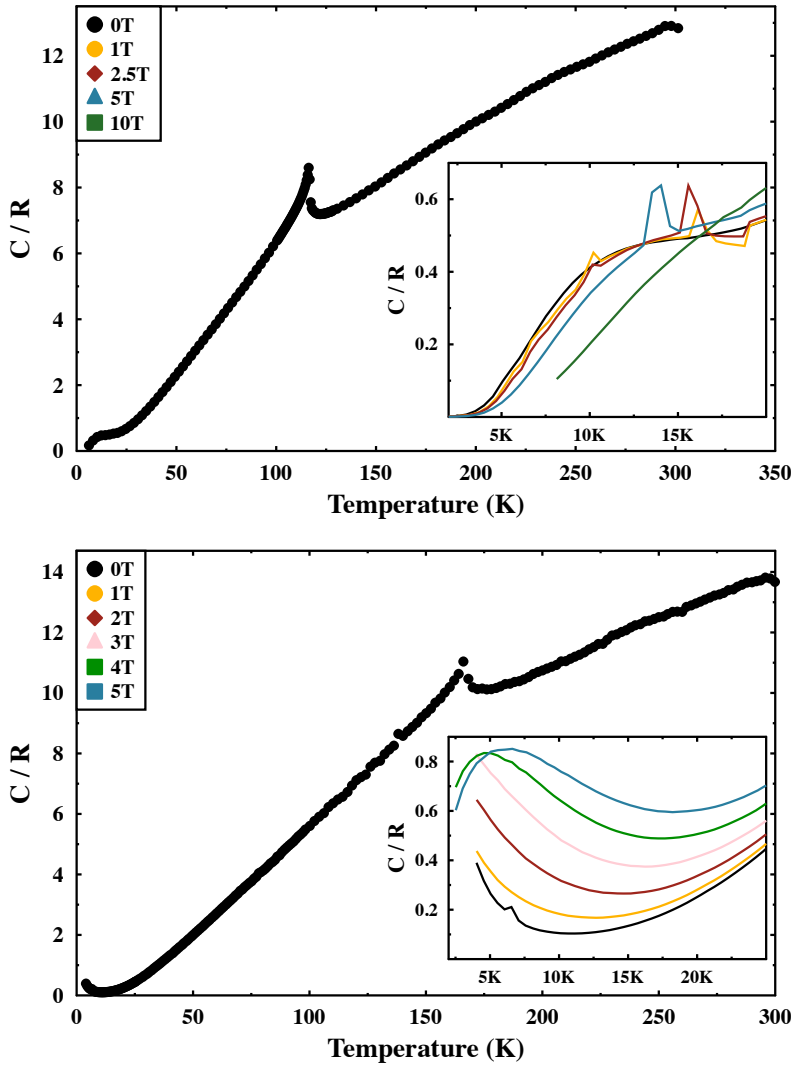

Figure 6.7: The upper panel is the molar heat capacity of $YbCrO_3$ showing the Cr^{3+} ordering temperature at 118 K. The inset shows the effect of applied magnetic fields at the Schottky anomaly. The lower panel is the molar heat capacity of $GdCrO_3$ showing the Cr^{3+} ordering temperature at 170 K. The inset shows the effect of applied field at the Gd^{3+} ordering transition and Schottky anomaly. Small repeatable peaks were observed in both materials at low temperatures in the field scans but with few points around the features no conclusions can be drawn as to their origin.

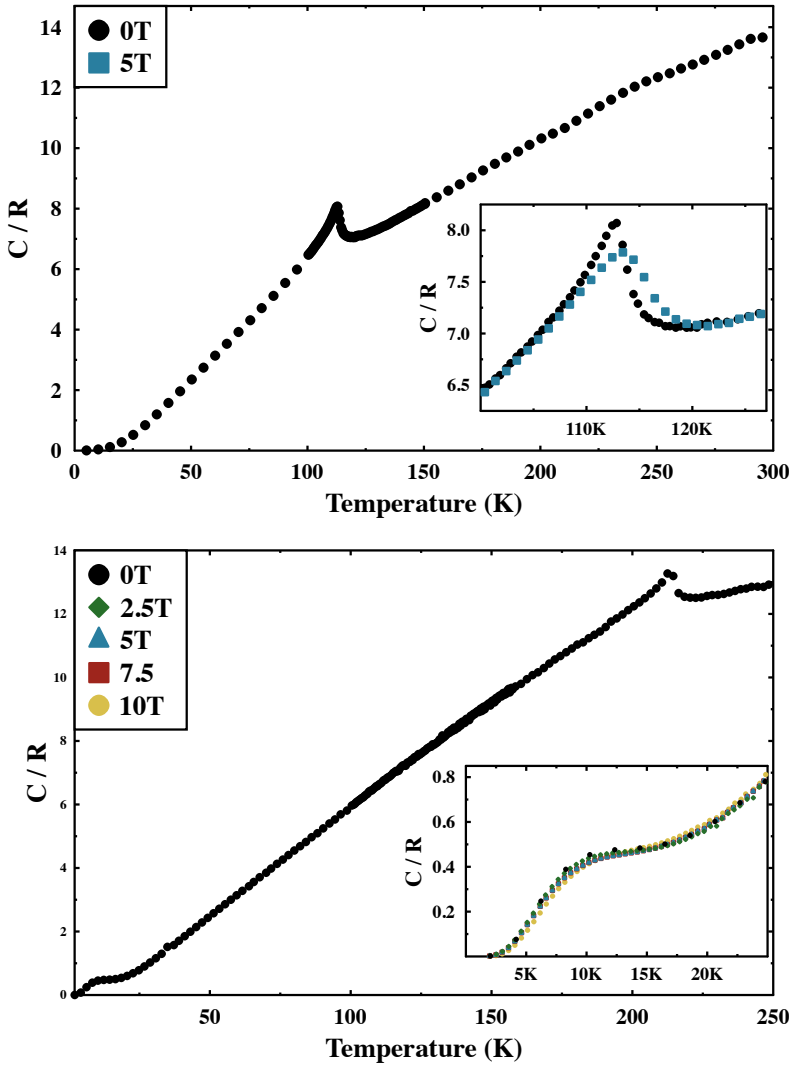

Figure 6.8: The upper panel is the molar heat capacity of $LuCrO_3$ showing the Cr^{3+} ordering temperature at 111 K . The inset shows the effect of applied magnetic field at the ordering temperature. The lower panel is the molar heat capacity of $NdCrO_3$ showing the Cr^{3+} ordering temperature at 219 K. The inset shows the effect of applied field at the Schottky anomaly.

are already equally occupied so in these two cases it is hard to change the energy of the system. Low temperature Schottky anomalies are observed clearly in $YbCrO_3$, $GdCrO_3$ and $NdCrO_3$.

The field dependence of the Schottky anomaly is an interesting feature which can be modelled from the physics of the rare earth ions. The model is created from the statistical properties of a system in thermal equilibrium which can be defined through functions Z_n given by,

$$Z_n = \sum_i \mathrm{E}_i^n \exp(-\beta \mathrm{E}_i), \tag{6.2}$$

with the appropriate energy levels, i, for the particular rare earth ion and where $\beta = \frac{1}{k_B T}$. With this notation, the conventional partition function is given by Z_0. The average energy of the system is

$$\langle E \rangle = \frac{\sum_i E_i \exp(-E_i \beta)}{\sum_i \exp(-E_i \beta)} = \frac{Z_1}{Z_0} \tag{6.3}$$

which can then be used to calculate the heat capacity of the system

$$C = \frac{d\langle E \rangle}{dT} = -\frac{\beta}{T}\frac{d}{d\beta}\left(\frac{Z_1}{Z_0}\right) = -\frac{\beta}{T}\left(\frac{Z_2}{Z_0} - \left(\frac{Z_1}{Z_0}\right)^2\right). \tag{6.4}$$

Therefore for fitting the low temperature heat capacity around the Schottky anomaly the following model is used,

$$C = N k_B \beta^2 \left(\frac{Z_2}{Z_0} - \left(\frac{Z_1}{Z_0}\right)^2\right) + C_{ph} T^3, \tag{6.5}$$

where N is Avogadro's constant introduced when C is molar heat capacity. The prefactor of this function is then the gas constant R=Nk_B=8.314 $\mathrm{Jmol^{-1}K^{-1}}$. The $C_{ph}T^3$ term accounts for the phonon contribution. The free parameter in the model is the energy level splitting. The parameter, C_{ph}, was fitted at 0 T and then held constant for the calculations in applied field.

Yb^{3+} and Nd^{3+} have a doublet lying lower than the subsequent energy levels. The splitting of the ground doublet of the Yb^{3+} ion is the cause of the Schottky anomaly observed below 15 K in the upper panel of Figure 6.7. As shown in the inset of Figure 6.7 the anomaly is gradually shifted to higher temperatures by an increase in the magnetic field. The doublet splitting is caused by the exchange interaction from the Cr^{3+} and on applying an extra external field the splitting increases. The model

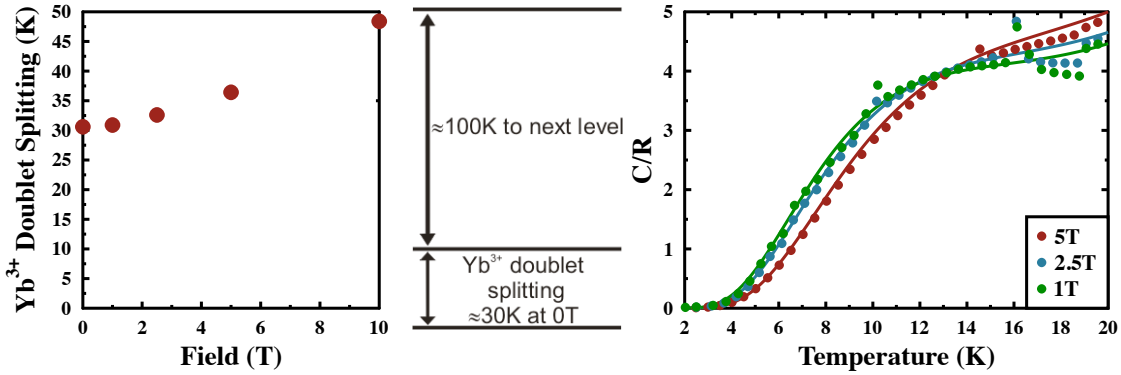

Figure 6.9: The values of Yb^{3+} ground state doublet splitting at 0 T and in an applied magnetic field are shown on the left. The behaviour in field shows the expected trend. A depiction of the energy level splitting is displayed in the middle. The fits to the Schottky anomalies are presented on the right of the figure.

was applied to the experimental data acquired in different fields. To judge the quality of the fitting the value of the gas constant, R, for Yb^{3+} was varied, it ranged from 7.9 to 8.2 which is very close to the gas constant suggesting good fits. For the final fitting R was held constant at its value of 8.314 $Jmol^{-1}K^{-1}$. The zero field doublet splitting was 30.3 K increasing to 48 K at 10 T. Figure 6.9 shows the change in splitting of the doublet and the expected trend on the increase of the field as well as examples of the fitting.

The $NdCrO_3$ has a Schottky anomaly between 4 K and 15 K and was modelled in the same way as the Yb^{3+}. However no change was observed in the splitting until 10 T where there was a slight increase from 27 K to 30 K. This is shown in the far smaller change to the Schottky anomaly in applied field compared to $YbCrO_3$. The value of 27 K for 0 T splitting is in good agreement with a previous study showing a two level system with a splitting of 27 K [15]. The energy gap between the ground state doublet and excited level was found to be 100 K so in this temperature range only the lowest doublet was particularly populated.

In $GdCrO_3$ the lack of orbital angular momentum and $S = 7/2$ means that there are 8 evenly spaced levels. The splitting from the Cr^{3+} is much smaller for the Gd^{3+} than the Yb^{3+} with a zero field splitting of 1.2 K, Figure 6.10. When the value of the gas constant, R, for Gd^{3+} was allowed to vary it was 7.8 at 5 T which is very close to the gas constant suggesting a good fit, it was held constant at its value of 8.314 $Jmol^{-1}K^{-1}$ for the final fitting.

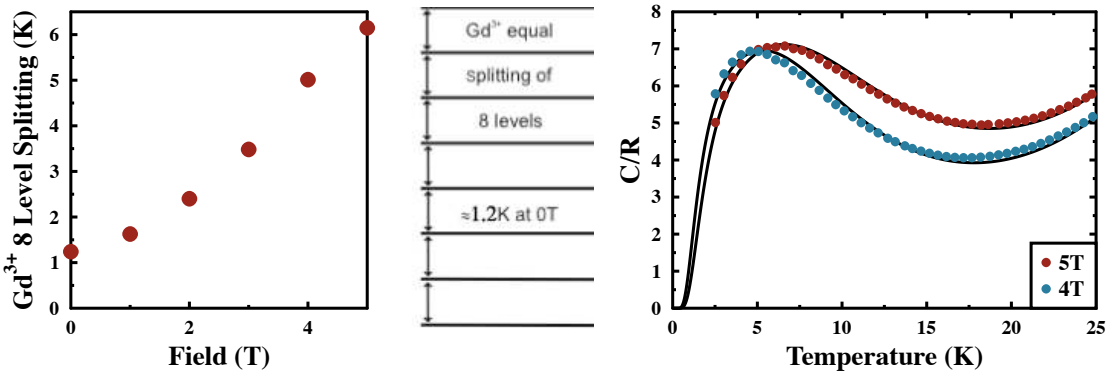

Figure 6.10: The values of Gd^{3+} 8 level splitting at 0 T and in an applied magnetic field are shown on the left. The splitting shown is that of the adjacent levels. The behaviour in field shows the expected trend. A depiction of the energy level splitting is displayed in the middle. The fits to the Schottky anomalies are presented on the right of the figure.

6.4.3 Magnetic Heat Capacity and Entropy

To extract the magnetic specific heat capacity a non-metallic analogue of the chromites, $LaGaO_3$, was made and the heat capacity measured in the same temperature range so the phonon contribution could be subtracted. This was thought to be a more rigorous subtraction than if the lattice contribution had been generated by modelling Debye and Einstein phonon contributions. These materials can be considered insulators for this purpose over the measured temperature range so no electronic contribution to the specific heat needs to be considered. However to account for the difference in mass between the particular rare earth and La, and the Cr and Ga, the temperature of the experimental curves of the $LaGaO_3$ graphs are scaled by a Lindemann factor, L so that

$$\theta_D = L\left(\frac{T_M}{MV^{2/3}}\right)^{1/2}, \tag{6.6}$$

where T_m is the melting temperature, M the atomic weight, V the atomic volume and θ_D the effective Debye temperature. The $LaGaO_3$ data were not scaled to that of the chromites further after the Lindemann correction factors had been applied. The magnetic heat capacity results are in very good agreement with that of a previous study of $NdCrO_3$ [15].

A high temperature contribution to the magnetic specific heat and entropy is observed above 150 K in Figures 6.11 and 6.12 and in the other chromites investigated.

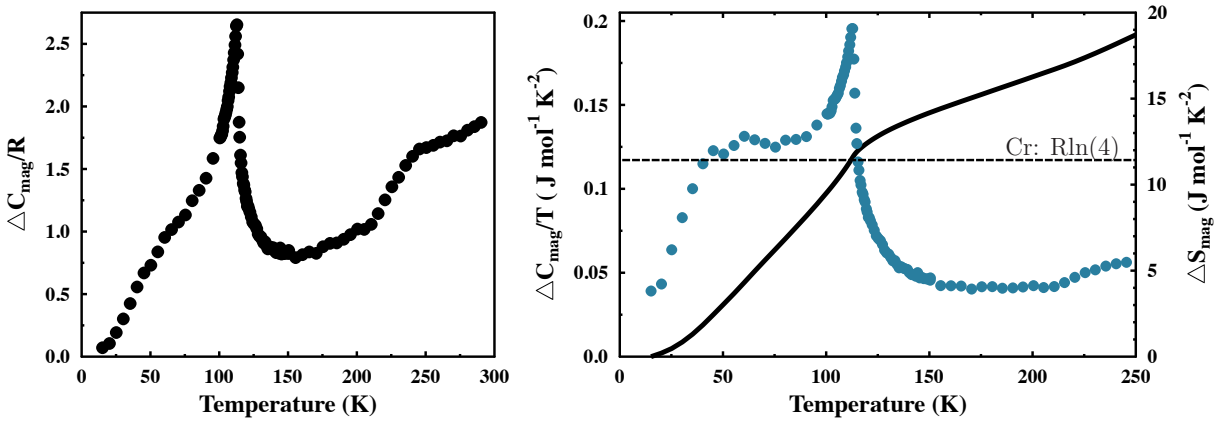

Figure 6.11: The magnetic specific heat contribution of $LuCrO_3$, after subtraction of the phonon contribution, is shown in the left panel. In the right panel $(\Delta C_{mag}/T)$ is integrated to give the entropy ΔS_{mag}, the solid line. The dashed line is the expected entropy.

It is possible that this is due to the grease applied between the sample and the heat capacity puck to provide good thermal contact, as described in Section 2.1.2. The heat capacity profile of 'N grease' has been previously measured showing a peak around this temperature range [28]. The source is hard to confirm as the mass of the grease used was of the order of a fraction of a milligram and could not be measured. It is also possible that the subtraction of the phonon contribution using the $LaGaO_3$ measurements has resulted in this feature. This might account for the almost constant offset, which is more obvious at higher temperatures. Given the $LaGaO_3$ subtraction could provide an effect over a large temperature range and the grease would be more likely to be observed as a peak the phonon subtraction might be a more likely explanation for the high temperature contribution.

The magnetic entropy can be calculated by integrating $\Delta C_{\rm mag}/T$, in these cases over the whole temperature range, Figures 6.11 and 6.12. The entropy increases as the temperature rises reflecting the disordering of the spins. These results have again been divided by R=8.314 $\mathrm{Jmol^{-1}Kmol^{-1}}$. Contributions going towards 0 K are difficult to account for and could be the source of errors. The expected entropy is shown as a dashed line in Figures 6.11 and 6.12 and calculated using

$$\Delta \mathrm{S} = \mathrm{Rln(2S{+}1)} = 11.526 \mathrm{J\ mol^{-1}K^{-1}} (\text{for } S{=}3/2). \tag{6.7}$$

The entropy found from these experiments in $LuCrO_3$, with a non-magnetic rare earth ion, is greater than the calculated value, Figure 6.11. It appears that this may

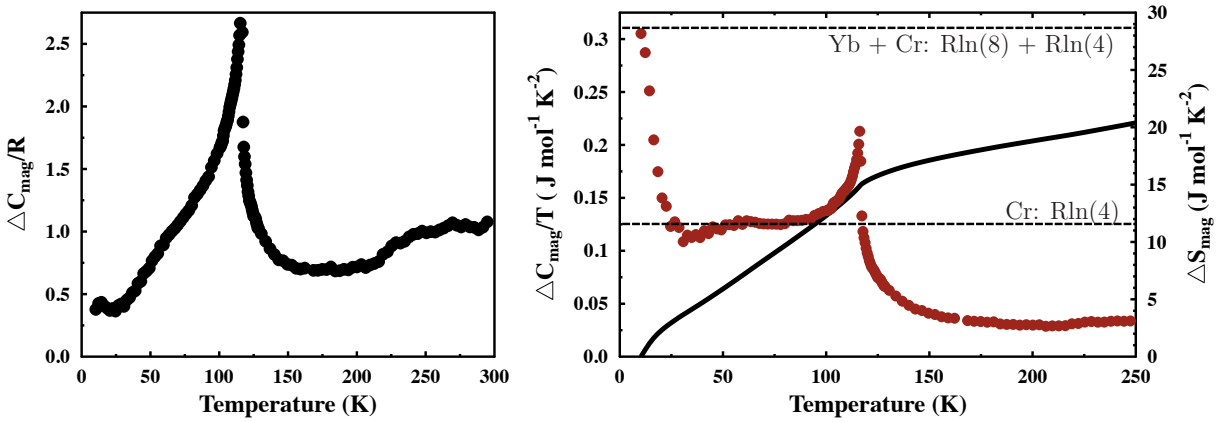

Figure 6.12: The magnetic specific heat contribution of $YbCrO_3$ after subtraction of the phonon contribution is shown in the left panel. In the right panel $(\Delta C_{mag}/T)$ is integrated to give the entropy ΔS_{mag}, the solid line. The dashed line is the expected entropy.

be from a background signal at temperatures above 150 K where you might expect the $\Delta C_{\mathrm{mag}}/T$ values to drop much closer to zero which could be a complication from the grease or from the subtraction of $LaGaO_3$ data. Apart from this high temperature signature the heat capacity results for $LuCrO_3$ are extremely similar to those of $LuMnO_3$ [29]. There is a hump in $\Delta C_{\mathrm{mag}}/T$ around 50 K which is also observed in $LuMnO_3$, it has been suggested that it is due to the frustration of the Mn^{3+} spins on the triangular lattice [29]. If there were spin degrees of freedom available below T_N then the system would still be searching for its true ground state.

In contrast the entropies found are considerably lower than the calculated values for $YbCrO_3$ and $GdCrO_3$ (not shown) which have two magnetic ions, Figure 6.12. It could be that entropy is reduced due to the presence of short range magnetic correlations above T_N which is observed in some of the rare earth manganite series. The smaller than expected entropy release at T_N is typical of a system with highly degenerate ground states in geometrically frustrated spin systems, leading to enhanced spin fluctuations above the transition temperature. There is also still an extra contribution to the magnetic specific heat and entropy which is probably due to the $LaGaO_3$ subtraction. A factor contributing to the lack of entropy in $YbCrO_3$ could also be the fact that above the low lying doublet there is a large gap to subsequent energy levels so at the temperatures of these experiments not all the levels have been populated.

6.4.4 Mean Field Model

The mean field model approach assumes that all the spins experience an identical average exchange field created by all their neighbours. This field is proportional to the magnetization and so heat capacity experiments in successive magnetic fields provides a good way to test how well this system corresponds to the model.

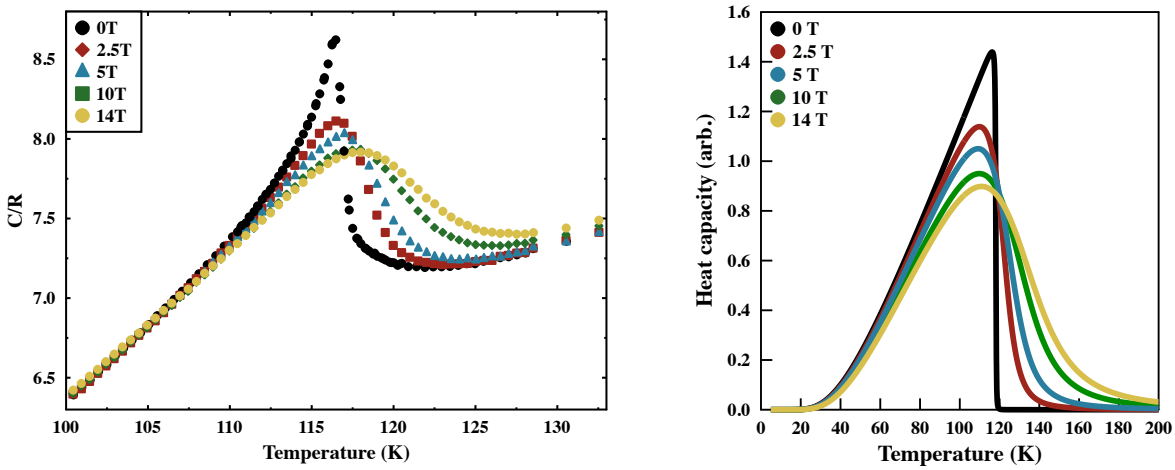

Figure 6.13: The left panel shows $YbCrO_3$ heat capacity in fields at the magnetic ordering transition for comparison to the mean field model. The right panel shows the mean field model of $YbCrO_3$ heat capacity calculated by S. J. Blundell.

The heat capacity results, in different magnetic fields, of $YbCrO_3$ from a mean field model have been generated and show a remarkable similarity to the data, Figure 6.13, although the phonon contribution has not been included in this model. The λ shaped anomaly is lowered and broadened in magnetic fields but with the position of the peak remaining mostly unchanged. A similar effect is observed in $PrMnO_3$ [30]. The mean field model overestimates the temperature range in which there is a magnetic contribution to the heat capacity. The magnetization data in section 6.3 more closely fits a 3D Ising model so no firm conclusions can be drawn.

6.5 Electrical Properties of RCrO$_3$

To unequivocally demonstrate a material is ferroelectric certain electrical measurements need to be made. Pyroelectric current measurements are often shown as evidence of ferroelectricity but this technique does not prove that the emergence of a ferroelectric phase is the source of any feature within the data and the same is true

for dielectric measurements [31, 32]. Also anomalies have been observed in electrical conductivity and Seebeck coefficient measurements which were believed to be due to a large change in the symmetry of the Cr–O polyhedra [33]. Polarization loops are needed to confirm ferroelectricity and dielectric measurements can be used to indicate the nature of the possible ferroelectric response.

6.5.1 Polarization Loops

A recent study has shown that when ferroelectric polarization loops are believed to have been measured [2] it can be just the properties of a leaky highly resistive material [17]. The results for RCrO$_3$ are compatible with being the consequence of conductive artefacts since these orthochromites are not good insulators [34]. At room temperature, polarization hysteresis loops from a ferroelectric are indistinguishable from that due to conduction artefacts. When the sample is not a perfect insulator an applied voltage induces leakage currents which are then integrated by the ferroelectric tester [35]. The lack of remnant polarization has also been shown using PUND (Positive-Up, Negative-Down) which is used to separate ferroelectric switching from artefacts [36]. A series of voltage pulses are applied and the transient current that results from them is measured which allows the separation of the components of the electrical response. It was observed that for YbCrO$_3$ there was zero remnant polarization which shows that the polarization that has been measured is due to charge leakage only. Recently a group working on polycrystalline bulk and thin film samples could not get well developed P-E hysteresis loops for YCrO$_3$ and GdCrO$_3$ because of a large contribution from a leakage current [37]. It was also said by the group suggesting multiferroicity that the shapes of the loops resembled leaky dielectrics [3].

6.5.2 Dielectric Measurements

High temperature dielectric measurements of some of the rare earth chromites have been shown in previous work to corroborate the onset of ferroelectricity [2]. Figure 6.14 shows the results of the same experiments for GdCrO$_3$. The aim of this was to try and repeat previous measurements, but on a different chromite, to see if the same behaviour was realised and why conclusions of ferroelectricity were drawn.

The ferroelectric phase of GdCrO$_3$ has been suggested to exist below 334 K [38]. This is approximately where the dielectric peak starts to form and above this point the dispersion is frequency independent. Below the transition temperature the dielectric

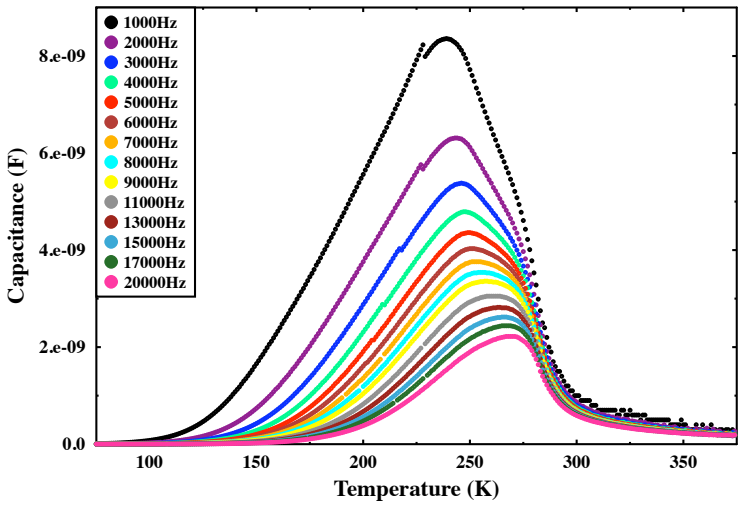

Figure 6.14: Initial measurements done with collaborators at Warwick University showing the high temperature dispersive capacitive behaviour of $GdCrO_3$.

peak is broadened and the transition temperature reduced with decreasing frequency indicating the presence of relaxation processes on multiple time scales. The magnetic transition temperature at 170 K is not seen as a feature in these results. This frequency behaviour has been observed in $LuCrO_3$, $ErCrO_3$ and $YbCrO_3$ [3] and is shown for $YCrO_3$ in Figure 6.2 [2]. A large dispersion is typically found below the transition temperature whereas the dielectric constant is almost temperature independent above it. This is typical relaxor ferroelectric behaviour. There is in fact no phase transition to a relaxor state as there is no macroscopic change in symmetry. Relaxor behaviour is usually attributed to polar micro-regions caused by defects, therefore not allowing for long range order as described more fully in Section 3.1.5.

The dielectric constant for a bulk polycrystalline sample of $GdCrO_3$ at room temperature has previously been reported as 23 [39] whereas for nanoparticles it was found to be 12 at 300 K and 1 kHz [40]. For measurements made using the impedance spectroscopy apparatus described in Section 3.2, on a single crystal, a dielectric constant of between 19 and 19.5 at room temperature was found. Figure 6.15 shows the dielectric constant increasing with increasing temperature.

Figure 6.15 shows a feature in the dielectric constant around the magnetic ordering transition however this does not necessarily suggest any type of coupled response, it is likely that it is in fact a resistive effect. The capacitance change is very small with significant error whereas the change in resistance is large and well defined. The values for the dielectric constant do show a general agreement with other results with

differences perhaps due to this work being done on a single crystal (for single crystals there is no capacitive contribution from grain boundaries).

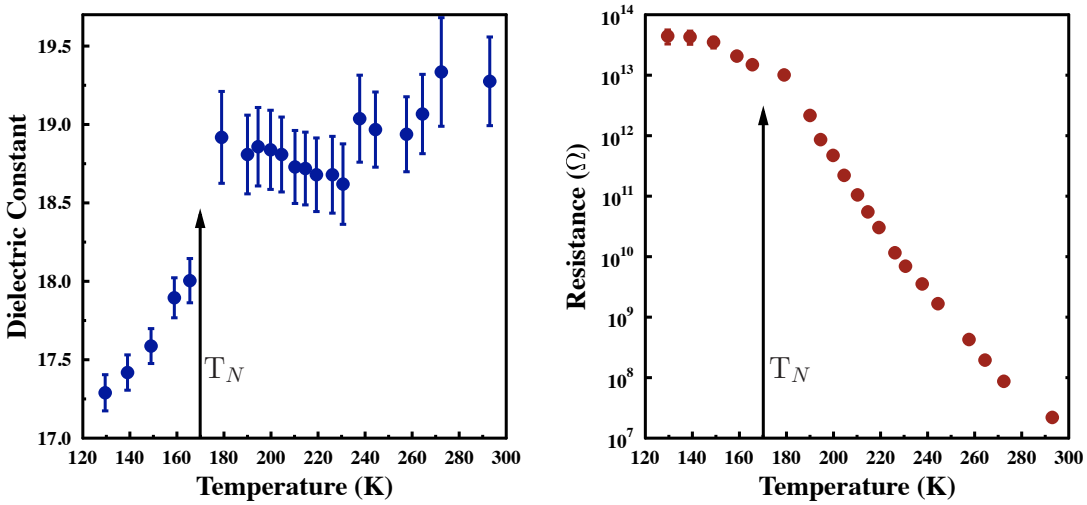

Figure 6.15: Low temperature dielectric behaviour of $GdCrO_3$ from simultaneous fits of capacitance and resistance have shown a change in behaviour around 170 K.

It is thought that $GdCrO_3$ experiences a strong thermal excitation of charge carriers from around 170 K which would transform the material from a good insulator to a semiconductor, the charge carriers may for example be oxygen vacancies [37]. This would cause an increase in the dielectric constant as dipoles will form from delocalised charge carriers and the shielding of opposite charges. This will be accompanied by an energy absorption which can be observed in $\tan\delta$ and the activation energy of the charge carriers can also be obtained as seen in Section 3.4.2.

6.6 Muon Experiment

μ^+SR can provide valuable information on how the local magnetic fields are changing when the rare earth ion is varied. The $LuCrO_3$ and $YCrO_3$ samples were pressed pellets and $YbCrO_3$ was comprised of small single crystals. The muon signals were fitted with the function

$$A(t) = A_{bg}+A_1e^{\lambda_1 t}\cos(2\pi\upsilon_1 t+\phi_1)+A_2e^{\lambda_2 t}\cos(2\pi\upsilon_2 t+\phi_2)+A_3e^{\lambda_3 t}\cos(2\pi\upsilon_3 t+\phi_3), \quad (6.8)$$

where λ is the relaxation (depolarization) rate, ϕ is the phase and υ is the frequency. A_{bg} is the background contribution from muons that stop in the sample holder or cryostat. Three frequency terms were needed to fit $YCrO_3$ but only one was required for $YbCrO_3$ and $LuCrO_3$.

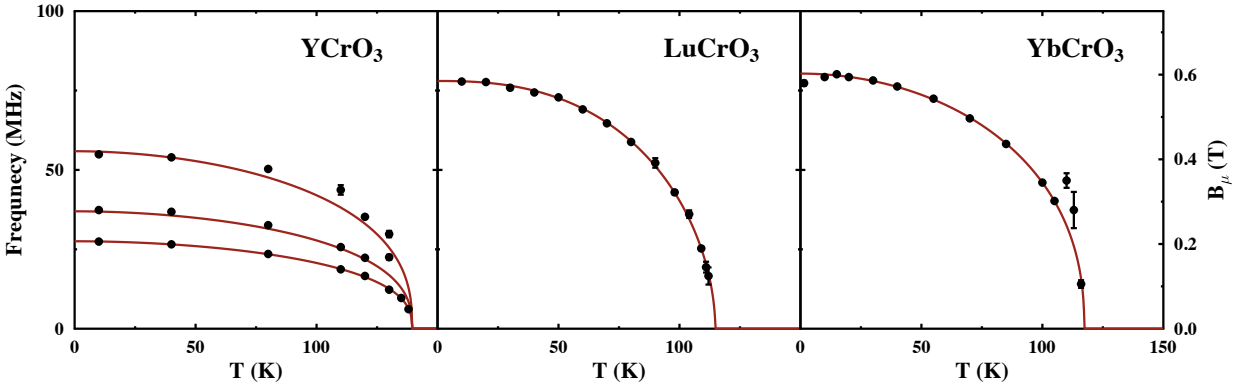

Figure 6.16: Muon results for three chromites showing different magnetic ordering resulting in different μ^+SR signals.

With similar magnetic structures comparable signals would be expected for $LuCrO_3$ and $YbCrO_3$ and this is observed despite the different forms of the sample. Single frequencies of the order of 76 MHz and 78 MHz are clearly distinguishable in $LuCrO_3$ and $YbCrO_3$ respectively, Figure 6.16. The transition temperatures were found to be 114.8 K and 117.3 K for $LuCrO_3$ and $YbCrO_3$ respectively. The magnetism in these two compounds is very alike with only a 5° difference in canting angle so analogous μ^+SR results would be expected. The $YbCrO_3$ signal becomes more complex below 16.5 K at the metamagnetic transition. There is a 2.4 % decrease in frequency at the point where the Yb^{3+} spins order to oppose the Cr^{3+} ferromagnetic moment. This is observed as a dip in the magnetic field and therefore frequency. This can be calculated from the Lorentz contribution to the field ($B_L = \mu_0 M_{sat}/3$) where M_{sat} is the saturation magnetization. This term would be absent if there was no ferromagnetic component. This calculation suggests that the decrease in field would be 4.9 % which is close to the decrease observed.

In contrast $YCrO_3$ clearly shows three clearly resolved frequencies which all decay to zero at the same critical temperature. From the μ^+SR data this is found to be 139.5 K and from the magnetization data 140.5 K with the expected value being 140 K. The difference is also observed in the Fourier transforms of the frequency signals where three frequencies can be clearly recognised in $YCrO_3$ and only one for $LuCrO_3$ and

$YbCrO_3$, Figure 6.17.

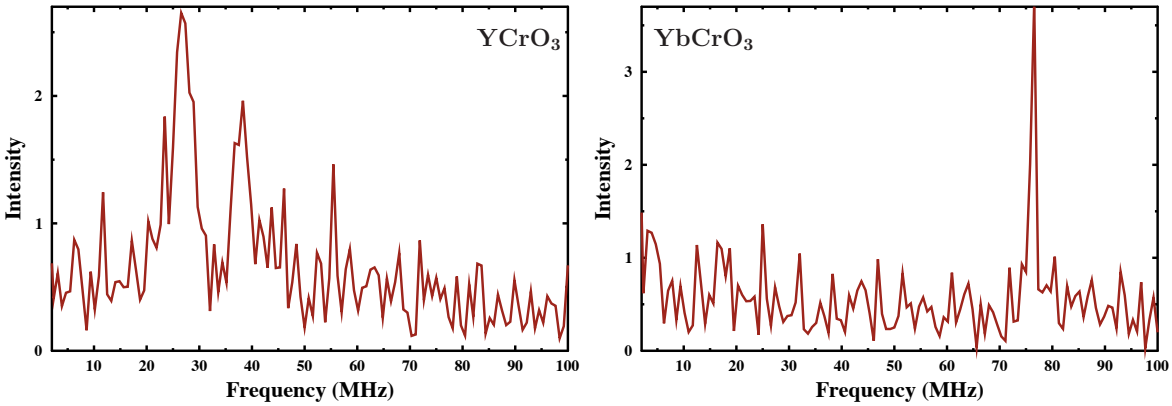

Figure 6.17: The Fourier transforms of the $YCrO_3$ and $YbCrO_3$ data showing three frequency contributions in $YCrO_3$ at 10 K and one in $YbCrO_3$ at 40 K, above the metamagnetic transition.

This suggests that it is not a case of the additional frequencies in $YbCrO_3$ and $LuCrO_3$ being hidden by damping. Powders would have the moments pointing in different directions giving rise to a broadening which might make frequencies harder to see but as the $LuCrO_3$ and $YCrO_3$ samples are in powder form this is unlikely to be the source of the difference. From the smaller magnetic field experienced by the muon in $YCrO_3$, Figure 6.16, it can be calculated that the muon has stopped approximately 0.2 Å further away from the chromium than it has in the case of the other two chromites.

To understand the differences between $YCrO_3$ and $LuCrO_3$/$YbCrO_3$ dipole field calculations have been performed. Contour mapping of the dipole fields was done every 1% of the orthorhombic c-axis. Each picture of the dipole field calculations shows a cut of the crystal field structure at a fixed value of z. Contours of constant dipolar field at values matching the discovered frequencies are also shown. A muon site must be away from any atom in the crystal structure and such 'exclusion zones' are shown as the inner coloured disks. A likely muon site is close to an oxygen ion probably at a distance of around 1 Å. The red disk encloses regions closer than 0.5 Å to the oxygen ion, whereas the orange disk encloses regions closer than 1 Å. The muon might therefore be expected to stop within, or at the edge of, the outer shaded disk. Also shown are the cations chromium and the rare earth. The chromium ions are shown in yellow and green and the rare earth ions in blue and purple. The green disk encloses regions closer than 0.9 Å to the chromium ion, whereas the yellow disk encloses

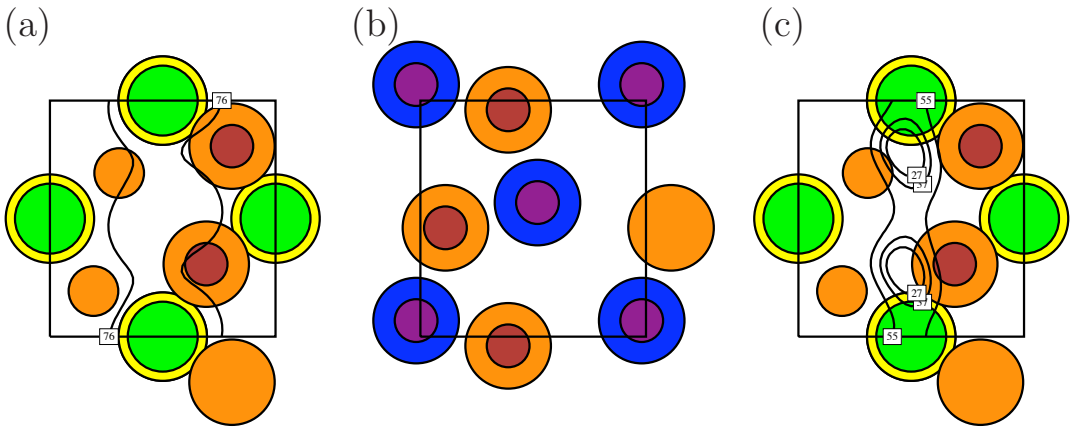

Figure 6.18: Dipole field contour plotting of (a)z=5% of orthorhombic c-axis of $LuCrO_3$, (b) z=25% of c-axis of $LuCrO_3$ and (c) z=45% of c-axis of $YCrO_3$. Orange and red disks represent the oxygen ions, yellow and green the chromium ions and blue and purple the rare earth ions. These slices occur half way through the oxygen atoms. The contours represent particular frequencies which are also given on the plots.

regions closer than 1 Å. The purple disk encloses regions closer than 0.5 Å to the rare earth ion, whereas the blue disk encloses regions closer than 1 Å. However the muon is not likely to stop near to the cations because of their positive charge.

The sites are expected approximately 1 Å from an oxygen. As expected the dipole field results are almost identical for $LuCrO_3$ and $YCrO_3$. However there is no overlap of sites in the $LuCrO_3$ or $YCrO_3$ calculations as the field lines are observed on opposite sides of the oxygen at the matching positions along the c-axis. Figure 6.18(a) shows a cut of $LuCrO_3$ at z=5% of the c-axis, the same position for $YCrO_3$ has the field lines on the opposite side of the oxygen. Figure 6.18(c) shows a cut of $YCrO_3$ at z=45% of the c-axis, the same position for $LuCrO_3$ has the field lines on the opposite side of the oxygen.

The lack of field lines in the planes of $LuCrO_3$ containing the rare earth ions, Figure 6.18(b), means that the muon site can be identified as being in the plane with the chromiums but in that plane there are a number of possible sites that cannot be pinned down. This is probably because of the hyperfine contribution which is not accounted for in the model and could provide a significant contribution. This planar relationship is very clearly identified in $LuCrO_3$ and as the rest of the series are isostructural the same result will probably hold.

These results are the first μ^+SR experiments on the rare earth chromite family and

have provided information on the effect of the rare earth ions on the local magnetic system. Although it might have been expected that the chromites with only one magnetic ion, $LuCrO_3$ and $YCrO_3$, would have a more comparable local magnetic structure than $YbCrO_3$ with two magnetic ions this was not the case. The magnetic structures of $LuCrO_3$ and $YbCrO_3$ are very similar with only a 5° difference in the canting angle of the Cr^{3+} ion. This was observed in the experiments through almost identical single frequency signals, Figure 6.16. This was observed despite the different physical forms of the samples. The main difference between these two chromites is the small dip in the magnetic field of $YbCrO_3$ around 16.5 K which is due to a metamagnetic transition. The contrasting three resolved frequencies observed for $YCrO_3$ point to a more complex response to the local magnetic structure. Dipole field calculations were performed but were not able to pinpoint the muon stopping sites although it appears that the muons stop in the plane with the chromium ions.

6.7 X-Ray Experiment

An exploratory resonant X-ray study of the anomalous scattering in $GdCrO_3$ was carried out on the I16 beamline at the Diamond Light Source in collaboration with Dr. S. Bland, R. Johnson and Prof. P. Hatton from Durham University. The sample was a single crystal of $GdCrO_3$ orientated with the [001] surface normal. The aim of the experiment was to investigate whether or not the system is locally non-centrosymmetric while remaining globally centrosymmetric as has been claimed [18].

Resonant X-ray scattering is a powerful technique as it provides a large enhancement to the diffraction signal by tuning the X-rays close to the absorption edge of a particular ion. Anisotropies at the resonant site can give rise to resonant scattering at forbidden reflections [41]. The Thomson contribution to the scattering vanishes at reflections which are forbidden due to glide plane or screw axis extinction rules [42]. A technique was explored by Templeton and Templeton in 1994 that looks at third rank tensors resulting from a tetrahedral anisotropy of anomalous scattering [43, 44]. Disparate elements such as the X-ray polarization, magnetism of the resonant atom and lattice features can combine to form a sensitive anisotropy [45].

The third rank tensor dipole-quadrupole transition term vanishes by symmetry if the atom is centrosymmetric and so the observation of a non-vanishing signal requires an ordered structure and the breaking of spatial inversion symmetry [46]. As the experiment was performed at the resonant chromium K edge any anisotropy observed

would just be around the chromium atom. Although this term corresponds to the global inversion symmetry at resonance you are really just looking at the local term around the chromium.

The sample was cooled to 130 K, well below all ferroic transitions, and a temperature dependent study of several Pbnm allowed Bragg peaks was made, Figure 6.19. However there was no significant change in intensity or width over the whole temperature range. A search for any reflections corresponding to the P2_1 unit cell (suggested as the non-centrosymmetric space group) was then done but despite the high intensity on the I16 beamline no reflections were found. This suggests that Pbnm is the correct space group over the whole temperature range.

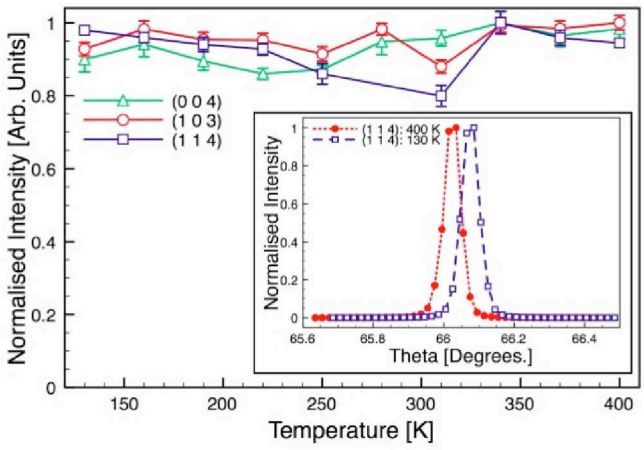

Figure 6.19: Temperature dependence of three Bragg reflections. Inset shows the (1 1 4) reflections at 130 K and 400 K, only a change in position is observed which is associated with the lattice expansion.

In order to study whether only local inversion is broken the Pbnm forbidden (0 0 1) Templeton reflection was located. The reflection at (0 0 1) was selected as it is not an allowed Bragg reflection in either the Pbnm or the P2_1 space group. We then performed azimuthal dependencies above and below the ferroelectric transition, Figure 6.20. An azimuthal angle scan is the rotation of the crystal around the Bragg wave vector where ϕ is the azimuthal angle. The intensity of a Bragg reflection as a function of the azimuthal angle is a direct measure of the angular properties of the environment of the resonant ion [47]. The azimuthal dependency of a Templeton reflection is highly dependent on the site symmetry of the resonant atom. As such, loss of inversion at the chromium site should be easily detectable. However, we found no such change in the azimuthal dependence, Figure 6.20. When the crystal was rotated

around the scattering vector the intensity exhibits the characteristic $\sin^2\phi$ dependence expected in the absence of an anisotropy. There is no clear change in the azimuth that can definitely be attributed to local inversion symmetry breaking. However the azimuthal scan is probably not clear enough to completely rule out the possibility.

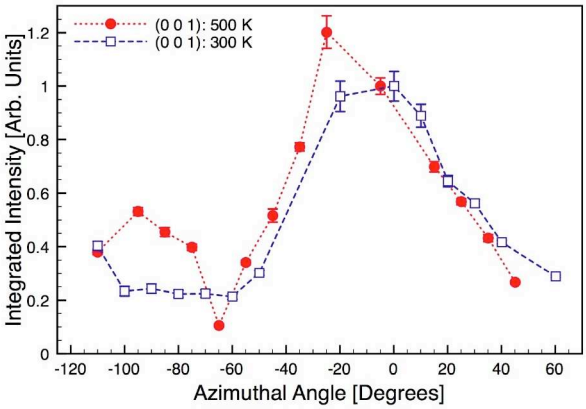

Figure 6.20: The azimuthal dependence of the forbidden (0 0 1) reflection at 300 K and above the ferroelectric transition at 500 K. No evidence is observed for the breaking of spatial inversion symmetry.

This experiment has demonstrated that the reported multiferroic $GdCrO_3$ does not break global inversion symmetry, and does not favour the $P2_1$ structure as a low temperature ground state. There is no evidence that local non-centrosymmetry occurs but further measurements would be necessary to make definite conclusions.

6.8 Conclusions

In conclusion the rare earth chromite series have not been proven to be ferroelectric and therefore cannot be said to be multiferroic. Experiments suggest that any features in electrical measurements are compatible with conductive artefacts since these orthochromites are not good insulators [34]. The heat capacity results have revealed interesting physical effects with the low temperature Schottky anomalies and the mean field model fitting around the magnetic ordering transitions. The entropy results have revealed similarities with the $R\mathrm{MnO}_3$ series and possible effects of frustration in the lattice. The μ^+SR work has shown differences between the local magnetic effects in three of the chromites. The magnetization work has shone further light onto the magnetic transitions in these systems.

Bibliography

[1] G. V. Subba Rao, G. V. Chandrashekhar and C. N. R. Rao, Solid State Communications **6**, 177 (1968).

[2] C. R. Serrao, A. K. Kunda, S. B. Krupanidhi, U. V. Waghmare and C. N. R. Rao, Phys. Rev. B **72**, 220101(R) (2005).

[3] J. R. Sahu, C. R. Serrao, N. Ray, U. V. Waghmare and C. N. R. Rao, J. Mater. Chem. **17**, 42 (2007).

[4] B. Wanklyn, J. Cryst. Growth **5**, 323 (1969).

[5] P. N. Kotru, A K. Razdan and B. M. Wanklyn, J. Mat. Sci. **24**, 2401 (1989).

[6] H. B. Lal, K. Gaur and R. D. Dwivedi, J. Mat. Sci. Lett. **14**, 9 (1995).

[7] E. F. Bertaut and J. Mareschal, Solid State Communications **5**, 93 (1967).

[8] G. V Subba Rao, C. N. R. Rao and J. R. Ferraro, Appl. Spectroscopy **24**, 436 (1970).

[9] T. Yamaguchi and K. Tsushima, Phys. Rev. B **8**, 5187 (1973).

[10] N. Shamir, H. Shaked and S. Shtrikman, Phys. Rev. B **24**, 6642 (1981).

[11] R. M. Hornreich, J. Mag. and Mag. Mater. **7**, 280 (1978).

[12] A. H. Cooke, D. M. Martin and M. R. Wells, J. Phys. C: Solid State Phys. **7**, 3133 (1974).

[13] S. Shtrikman, B. M. Wanklyn and I. Yaeger, Intern. J. Magnetism **1**, 327 (1971).

[14] K. Yoshii, J. Sol. Stat. Chem. **159**, 204 (2001).

[15] F. Bartolomé, J. Bartolomé and M. Castro, J. J. Melero, Phys. Rev. B **62**, 1058 (2000).

[16] T. Yamaguchi, J. Phys. Chem. Solids **35**, 479 (1974).

[17] S. Nagar, K. V. Rao, L. Belova, G. Catalan, J. Hong, J. F. Scott, A. K. Tyagi, O. D. Jayakumar, R. Shukla, Y-S. Liu and J. Guo, Mater. Res. Symp. Proc. **1161**, (1161-I07-04) (2009).

[18] K. Ramesha, A. Llobet, Th. Proffen, C. R. Serrao and C. N. R. Rao, J. Phys.: Condens. Matter **19**, 102202 (2007).

[19] D. I. Khomskii, J. Mag. and Mag. Mater. **306**, 1 (2006).

[20] R. M. Hornreich, Y. Komet, R. Nolan, B. M. Wanklyn and I. Yaeger, Phys. Rev. B **12**, 5094 (1975).

[21] V. S. Gerasimchuk and A. L. Sukstanskiĭ, Phys. Solid State **41**, 245 (1999).

[22] H. E. Stanley, *Introduction to Phase Transitions and Critical Phenomena*, Oxford University Press, Oxford, (1971).

[23] S. J. Blundell, *Magnetism in Condensed Matter*, Oxford University Press, Oxford, (2003).

[24] N. Kojima, H. Okada, M. Kawarazaki, I. Mogi, M. Takenda, G. Kido, Y. Nakagawa and K. Tsushima, J. Phys. Soc. Jpn. **64**, 3082 (1995).

[25] H. Satoh, S-i. Koseki, M. Takagi, W. Y. Chung and N. Kamegashira, J. Alloys and Compounds **259**, 176 (1997).

[26] J. W. Kim, Y. S. Oh, K. S. Suh, Y. D. Park and K. H. Kim, Thermochimica Acta **4554**, 2 (2007).

[27] F. Bartolomé, M. D. Kuz'min, J. Bartolomé, J. Blasco, J. García and F. Sapiña, Solid State Communications **91**, 117 (1994).

[28] J. G. Bunting, T. Ashworth and H. Steeple, Cryogenics **9**, 385 (1969).

[29] D. G. Tomuta, S. Ramakrishnan, G. J. Nieuwenhuys and J. A. Mydosh, J. Phys.: Condens. Matter **13**, 4543 (2001).

[30] J.G. Cheng, Y. Sui, X. J. Wang, Z. G. Liu, J. P. Miao, X. Q. Huang, Z. Lü, Z. N. Qian and W. H. Su, J. Phys.: Condens. Matter **17**, 5869 (2005).

[31] H.B. Lal, R. D. Dwivedi and K. Gaur, J. Mater. Sci.: Mater. Elec. **1**, 204 (1990).

[32] H.B. Lal, R. D. Dwivedi and K. Gaur, J. Mater. Sci.: Mater. Elec. **7**, 35 (1996).

[33] A. K. Tripathi and H. B. Lal, Mat. Res. Bull. **15**, 233 (1980).

[34] G. V. Subba Rao, B. M. Wanklyn and C. N. R. Rao, J. Phys. Chem. Sol. **32**, 345 (1971).

[35] J. F. Scott, J. Phys.: Condens. Matter **20**, 021001 (2008).

[36] K. M. Rabe, C. H. Ahn and J-M. Triscone, Ferroelectrics: a modern perspective, Springer, Berlin, (2007).

[37] Z. X. Cheng, X. L. Wang, S. X. Dou, H. Kimura and K. Ozawa, J. Appl. Phys. **107**, 09D905 (2010).

[38] H. B. Lal, K. Gaur, R. D. Dwivedi and N. Srivastava, J. Mater. Sci. Lett. **8**, 1085 (1989).

[39] A. K. Tripathi and H. B. Lal, J. Mat. Sci. **17**, 1595 (1982).

[40] A. Jaiswal, R. Das, K. Vivekanand, T. Maity, P. M. Abraham, S. Adyanthaya and P. Poddar, J. Appl. Phys. **107**, 0133912 (2010).

[41] J. Garcia and G. Subías, Phys. Rev. B **68**, 127101 (2003).

[42] C. Detlefs, Physica B **345**, 45 (2004).

[43] D. H. Templeton and L. K. Templeton, Phys. Rev. B **49**, 14850 (1994).

[44] I. S. Elfimov, N. A. Skorikov, V. I. Anisimov and G. A. Sawatzky, Phys. Rev. Lett. **88**, 015504 (2002).

[45] P. Carra and B. T. Thole, Rev. Modern Phys. **66**, 1509 (1994).

[46] L. Paolasini and F. de Bergevin, C. R, Physique **9**, 550 (2008).

[47] V. Scagnoli and S. W. Lovesey, Phys. Rev. B **79**, 035111 (2009).

Chapter 7

Inelastic Neutron Study of $LuFe_2O_4$

Contents

$LuFe_2O_4$ is a type I multiferroic material in which ferroelectricity develops as a result of charge ordering. This mechanism is referred to as 'Electronic Ferroelectricity'. In this mechanism the electric dipole depends on the electron correlations rather than the covalency [1]. The advantage of this type of multiferroic system is in the application possibilities inherent in a ferroelectric material that can be controlled by the charge, spin and orbital degrees of freedom of the electron. There is the potential for this material to have switchable electrical polarization in magnetic fields and vice versa so it is an extremely interesting material to study, especially given the large dielectric response and the magnetoelectric coupling at room temperature. Inelastic neutron scattering results from complementary instruments are presented and the spin wave dispersion investigated.

7.1 Properties of $LuFe_2O_4$

7.1.1 Crystal Structure

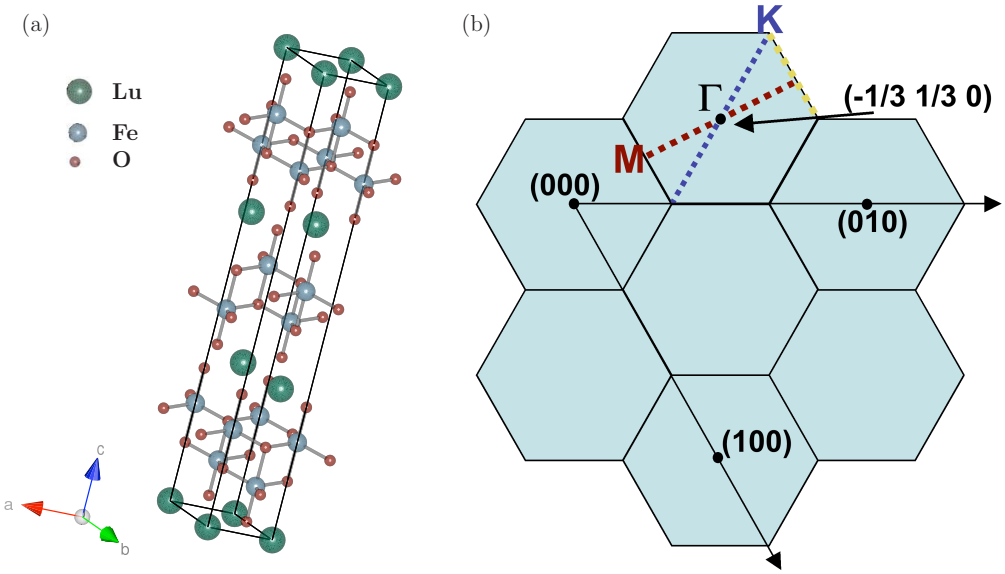

Figure 7.1: (a) The layered structure of $LuFe_2O_4$, the green, blue and red atoms are Lu, Fe, and O respectively. (b) The Brillouin zone of the hexagonal lattice showing the symmetry positions and the directions along which the neutron scans were made, shown as dashed lines.

$LuFe_2O_4$ is a member of the RFe_2O_4 family where R is a trivalent rare earth ion (R=Dy–Lu and Y) with the rhombohedral space group R$\overline{3}$m and lattice parameters;

$a = 3.444$ Å and $c = 25.259$ Å [2]. The room temperature structure of this material is a hexagonal layered structure stacked with two alternating layers along the hexagonal c direction, Figure 7.1. The hexagonal layers of Fe_2O_4, made up of corner sharing FeO_5 trigonal bipyramids, alternate with layers of Lu_2O_3 with three layers of Fe_2O_4 per unit cell. The Fe atoms form triangular lattice layers resulting in spin and charge frustration.

The samples were grown by D. Prabhakaran at Oxford University. Stoichiometric amounts of high-purity (>99.99 %) Lu_2O_3 and Fe_2O_3 chemicals were mixed and sintered at 1200°C for 12 hours under a flow of CO/CO_2 mixed gas. The sintered powder was ground and heat treated again at 1200°C for 24 hours in an Argon atmosphere. Finally the ground powder was pressed into a rod of 8 mm diameter and 100 mm length and sintered at 1200°C for 12 hours in a CO/CO_2 mixed atmosphere. Single crystal growth was carried out in an optical floating-zone furnace (Crystal Systems Inc.) with a flow of CO/CO_2 mixed gas atmosphere. The growth was carried out at a speed of 1-2 mm/hour with the feed and seed rods counter rotating at 30 rpm. The growth process was initiated on a polycrystalline seed rod initially, but on subsequent runs cleaved single crystal seeds were used.

7.1.2 Magnetic Properties

$LuFe_2O_4$ exhibits quasi-2D ferrimagnetic order below $T_N \approx 240$ K with ordering wavevectors (1/3, 1/3) and (0, 1). The spins point along the hexagonal c-axis and there is a net magnetic moment of approximately 2.8 μ_B [3]. The layered structure of the lattice is responsible for the 2D nature of the magnetic system with weak inter-layer interactions allowing the ferrimagnetic stacking. The ions sit on a triangular lattice and as such are frustrated with antiferromagnetic nearest neighbour interactions. In a weak crystal field Fe^{3+} has a spin of $S = 5/2$ and Fe^{2+} a spin of $S = 2$.

The Fe^{2+} spins are aligned ferromagnetically, possibly due to the large orbital moment of the Fe^{2+} causing a strong uniaxial magnetic anisotropy. The orbital moment of the Fe^{3+} ion is negligible and it is possible that its alignment is decided by the competition between the Fe^{2+}–Fe^{3+} double exchange and the Fe^{3+}–Fe^{3+} superexchange interaction. The result is a 2:1 ferrimagnetic spin order where one Fe^{3+} is parallel and the other two Fe^{3+} are antiparallel to the ferromagnetic Fe^{2+} ions [4]. The most likely ferrimagnetic structure is shown in Figure 7.2 with the parallel Fe^{3+} spin in the Fe^{3+} rich plane [4]. The magnetic anisotropy is large so the spins are Ising-like.

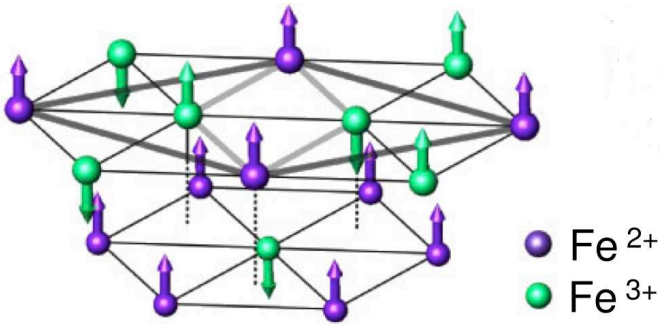

Figure 7.2: Ferrimagnetic order of $LuFe_2O_4$ with the parallel Fe^{3+} spin in the Fe^{3+} rich plane [4].

Below 176 K a broadening of the magnetic peaks has been seen, suggesting the build up of a diffuse component of the magnetic scattering [5]. Charge fluctuations persist down to 176 K occurring even in the charge ordered state. The broadening of the magnetic peaks occurs at the same temperature as the disappearance of charge fluctuations, suggesting that this low temperature magnetic phase transition quenches the charge fluctuations. It has also been suggested that this feature is affected by the oxygen stoichiometry [6]. There is strong spin-charge coupling in $LuFe_2O_4$ and it is suggested the spin frustration allows reinforcement of the polar charge ordering by a magnetic ordering [7].

7.1.3 Charge and Orbital Ordering

Charge frustrated systems are caused by the Coulombic preference for pairing an ion with an excess of charge with an ion with a deficiency of charge on a triangular lattice where these criteria cannot be simultaneously satisfied.

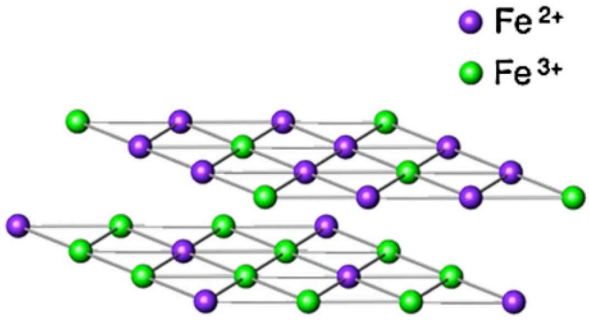

Figure 7.3: Charge ordering in a $LuFe_2O_4$ bilayer illustrating the charge disproportionation between layers [4].

$LuFe_2O_4$ shows charge frustration because Coulomb interactions favour the Fe^{2+}

(d^6 S=2) and Fe^{3+} (d^5 S=5/2) ions being on adjacent sites but on a triangular lattice this cannot be simultaneously satisfied. An equal amount of Fe^{2+} and Fe^{3+} ions coexist at the same site in the triangular lattice with the ions considered to have an excess and deficiency of half an electron respectively from the average ion valence. These competing frustrated interactions are relieved by the creation of the charge superstructure seen in Figure 7.3. The frustrated nature of the lattice means that the usual checkerboard charge ordering is not favoured. Instead there is a charge distribution between the layers so that there is a Fe^{2+}:Fe^{3+} ratio of 2:1 in one layer and in the next layer the ratio is reversed. This redistribution relieves the charge ordering frustration [8]. The ground state is characterized at low temperatures by a charge density wave with the ordering wavevector (1/3, 1/3, 3/2) below 320 K [9, 10]. Diffuse scattering with propagation vector (1/3, 1/3, 0) indicates short range correlations between neighbouring layers at 360 K .

Above 320 K two dimensional charge ordering is seen on the Fe_2O_4 layers, this becomes full three dimensional ordering below 320 K. A model of the charge superstructure has been proposed [1] where the supercell is referred to as a $\sqrt{3}$ x$\sqrt{3}$ structure. The unit cell is enlarged by a factor of three in the ab plane along the [1 1 0] direction. A charge order to disorder transition is also seen at about 530 K [2]. At $T > 500$ K the valence electrons can thermally move so all the Fe sites will appear to have a charge of $2.5e^-$.

Charge fluctuations are present even in the charge ordered state and persist down to 175 K [11]. It has been shown that the charge ordering lowers the crystallographic space group symmetry to monoclinic C2/m due to atom shifts that accompany the charge order [9]. It has been suggested that the charge order can take two forms and that the charge fluctuations arise from the interconversion between the two [12]. The two types of charge order, the $\sqrt{3}$ x$\sqrt{3}$ structure and chain type, which occurs in the Fe_2O_4 layers, have almost equal stability. The ground state has the $\sqrt{3}$ x$\sqrt{3}$ charge order and ferroelectric arrangement [12]. The discussion over the influences of the distortion and the magnetic order on the charge fluctuations is not resolved [7, 9, 11, 12, 13].

Fe^{3+} has five $3d$ electrons and is therefore spherical however Fe^{2+} has six 3d electrons and therefore has a doubly degenerate orbital degree of freedom [14]. This is expected to result in the order of the Fe^{2+} orbitals but it appears that they have a random orientation, forming an orbital glass state [7, 14].

7.2 Multiferroic Mechanism

The ferroelectric mechanism for this multiferroic is 'electronic ferroelectricity' which occurs in the situation where the electric dipole depends on the electron correlations, instead of the covalent bonding between anions and cations, to stabilize the dipolar arrangement [1]. Spontaneous electrical polarization has been shown to appear below 320 K [1, 14, 15].

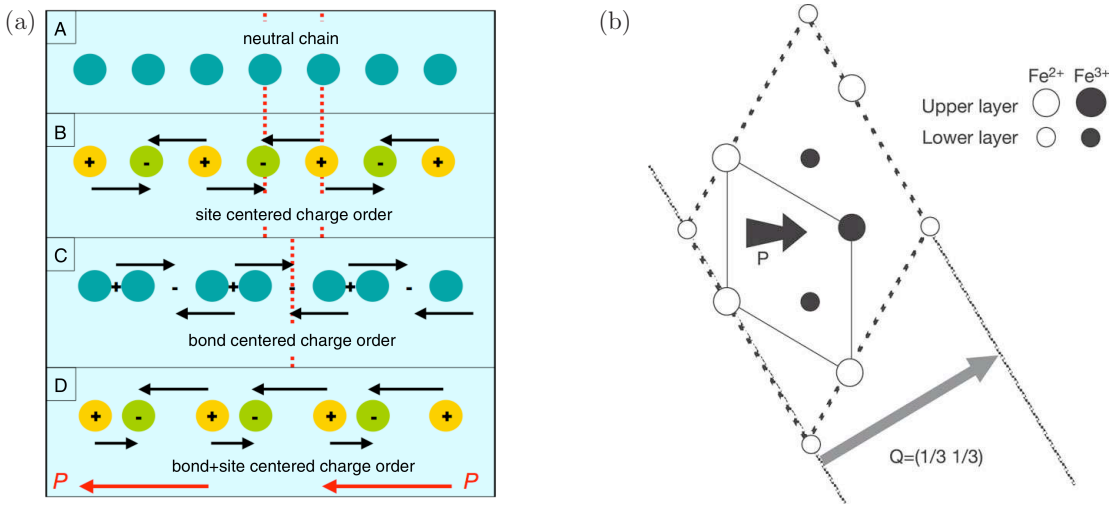

Figure 7.4: (a) The mechanism for ferroelectricity showing site and bond centred charge ordering with the mirror planes shown as red dashed lines [8]. (b) The superstructure of $LuFe_2O_4$. The solid lines show the chemical unit cell and the dotted lines show the charge superstructure. Polarization is indicated by the black arrow. The long grey arrow is the wave vector showing the charge wave [1].

The general mechanism through which charge order can induce ferroelectricity is illustrated in Figure 7.4(a). In panel A there is no charge on each site whereas in panel B the sites become inequivalent in charge but are still spatially invariant as shown by the red dashed mirror planes [8]. Without breaking spatial inversion symmetry there can be no net dipole moment. In panel C the material has dimerized so that the sites remain equivalent but the bonds are not, with the strong and weak bonds alternating. These systems can be described as site-centred charge ordering, B, and bond-centred charge ordering, C. The bond-centred ordering is also centrosymmetric as shown by the mirror plane. Ferroelectricity arises when both types of charge order occur simultaneously. This is shown in panel D where inversion symmetry is broken and there is a net polarization.

The charge structure of $LuFe_2O_4$ allows for local electrical polarization as the centres of the Fe^{2+} and Fe^{3+} (electron excess and deficiency) do not coincide in the unit cell of the superstructure. This means that ferroelectricity can emerge from the electron density modulation of d electrons without the need for a cation anion pair. The ferroelectricity specifically comes from the different ratio of the ions in the Fe_2O_2 bilayers [16]. There are Fe^{3+}:Fe^{2+} ratios of 2:1 on one layer and 1:2 on the adjacent layer. This results in each bilayer acquiring a dipole moment. It has been shown to generate a large spontaneous polarization of 0.24 C/m^2 along the hexagonal c-axis [8] and a large dielectric constant of about 10,000 at room temperature [2].

An alternate result finds the ground state to be antiferroelectric with no net polarization [9]. Remnant polarization in pyroelectric measurements have been explained as being dependent on the oxygen stoichiometry [17] although some find this unlikely [9]. High temperature correlations appear to favour ferroelectricity so it is possible that cooling in an electric field stabilizes the net moment. In a recent experiment ferroelectricity was ruled out in favour of bipolar stacking as an answer to this controversy [16].

7.2.1 Magnetoelectric effect

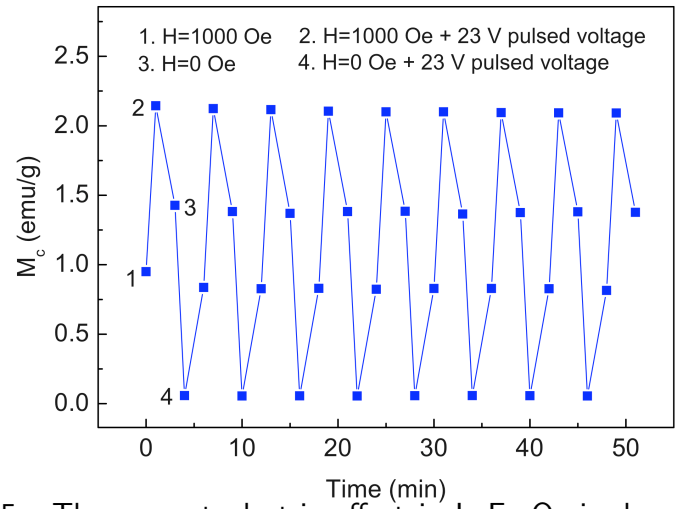

Figure 7.5: The magnetoelectric effect in $LuFe_2O_4$ is shown by the reversible switching of the magnetic states at 200 K [18].

There have been observations of magnetic control of polarization in a variety of multiferroics [19, 20, 21] however electrical control of magnetization is rarely reported. It has been previously shown that charge order can be destroyed by an external stimulus such as an electric field. Through this process the breakdown of the charge ordering

in $LuFe_2O_4$ leads to a large change in magnetization. The intrinsic magnetoelectric coupling in this system is a response to the electrical breakdown of the charge order.

The observation of P-E loops, the usual technique for determining the presence of ferroelectricity, are rarely reported for $LuFe_2O_4$. It is possible that residual electronic conductivity arising from non-charge ordered regions may prevent the observation [22]. Pyroelectric measurements have seen polarization switching in external electric fields as well as a shoulder at the magnetic ordering transition. A significant change in the polarization is seen when the system enters the long-range ferrimagnetic state [6]. This indicates the coupling of the magnetic and electrical order parameters. Polarization fluctuations in $LuFe_2O_4$ are directly correlated with the charge fluctuations. The energy required for charge motion could be much lower than for the ion displacements of other multiferroics so a smaller electric field would be needed to affect the permittivity [23].

There are contradictory suggestions as to the origin of the giant magnetocapacitance effect that is seen at room temperature above the magnetic ordering temperature. It has been suggested that it is the charge fluctuations of the Fe sites that is the main contribution to the polarizability at high temperatures when there is no charge ordering [24] and also that the magnetic field is affecting the static charge order [6].

It is suggested that the magnetoelectric effect is due to the field affecting the static charge order. When the charge order is reduced the magnitude of the local electric dipole moment is smaller and so the dielectric constant is reduced. As static charges do not respond directly to a magnetic field the changes seen are unusual. There are exceptions where the effect is mediated by a different order parameter but there is no such parameter between the magnetic and charge ordering temperatures in $LuFe_2O_4$[6]. Local spin clusters, which favour particular charge ordered states depending on their spin structure, might be formed at room temperature. It is speculated that charge structures near charge domain boundaries are more unstable and so could be affected by a change in local spin structures induced by an applied magnetic field [6]. The magnetoelectric coupling could then be due to the magnetic field effect on local spins unlike in most other multiferroics where the bulk magnetic order is important.

Figure 7.5 shows the electrical control of the magnetization in $LuFe_2O_4$. It is attributed to an intrinsic magnetoelectric coupling in response to the electrical breakdown of charge order [18]. The electrical switch down of the magnetization can always occur in the ferrimagnetic state however the electrical switch up of the magnetization in a magnetic field is a switch from the ZFC to FC magnetizations so a divergence

between the two has to exist [18]. Although this result was tested to exclude sample heating as a source of the results other work has found internal sample heating to be the cause of changes in charge and magnetic order upon the application of an electric field in inelastic neutron scattering measurements [25].

7.3 Results

7.3.1 Impedance Spectroscopy

Dielectric properties of $LuFe_2O_4$ have been explored through impedance spectroscopy using apparatus designed and built for the study of these materials, Section 3.2. Previous dielectric results have found a hump in the dielectric constant at the transition from 2D to 3D charge order [1] and large changes in the dielectric constant have been observed when small magnetic fields were applied [24]. There is also strong coupling of the spins and electric dipoles at room temperature. This makes $LuFe_2O_4$ a particularly interesting material to investigate with this technique. The main result is presented here, Figure 7.6, with a more detailed analysis seen in Section 3.4.3.

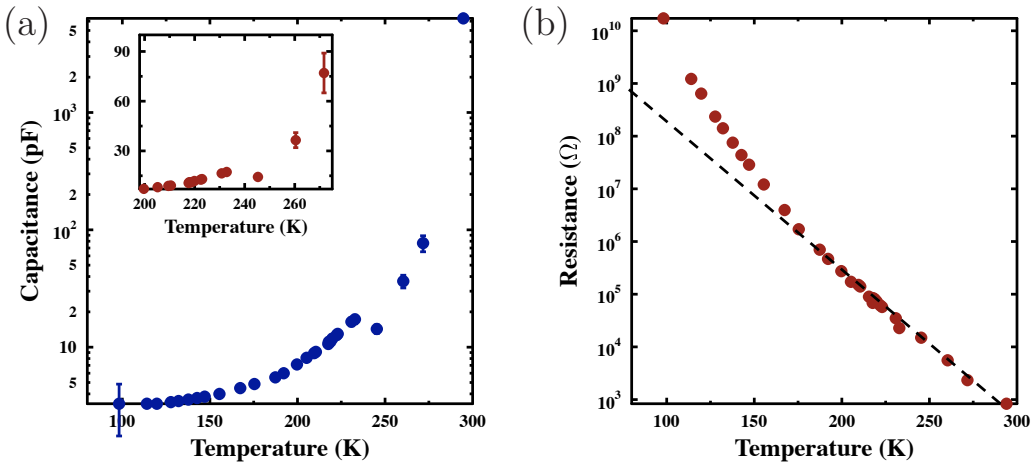

Figure 7.6: (a) Capacitance of $LuFe_2O_4$ showing a capacitive feature at the magnetic ordering transition. The inset is a closer view of the discontinuity. (b) Resistance of $LuFe_2O_4$ showing a change in gradient which is not at the magnetic ordering transition temperature. The dashed line is simply a guide to the eye.

In Figure 7.6 the measured capacitance shows a discontinuity at approximately $T_N = 240$ K the ferrimagnetic ordering temperature. Although signs of coupling between the magnetic and electrical order parameters at the magnetic transition have

been reported before, this appears to be the first time that it has been observed using this technique. There is not a resistive feature at the ordering temperature, 240 K, Figure 7.6(b). There is however a change in the gradient of the resistance below 200 K. This has been seen previously [26] however no explanation was suggested. The magnitude of the resistance results over the temperature range also agrees well with the previous results [26]. This suggests that the capacitance results are even more likely to be accurate as the resistance and capacitance values are extracted using the same model.

There was no significant error associated with the temperature point at 245 K in the capacitance plot as illustrated by the error bars being too small to see, Figure 7.6. This suggests that what is seen here is a genuine coupling effect. It is unfortunate that more data points were not able to be collected around the ferrimagnetic ordering temperature. Due to problems with liquid helium supplies there was not time to perform more measurements. The discontinuity is however still convincing.

7.3.2 Neutron Experiments

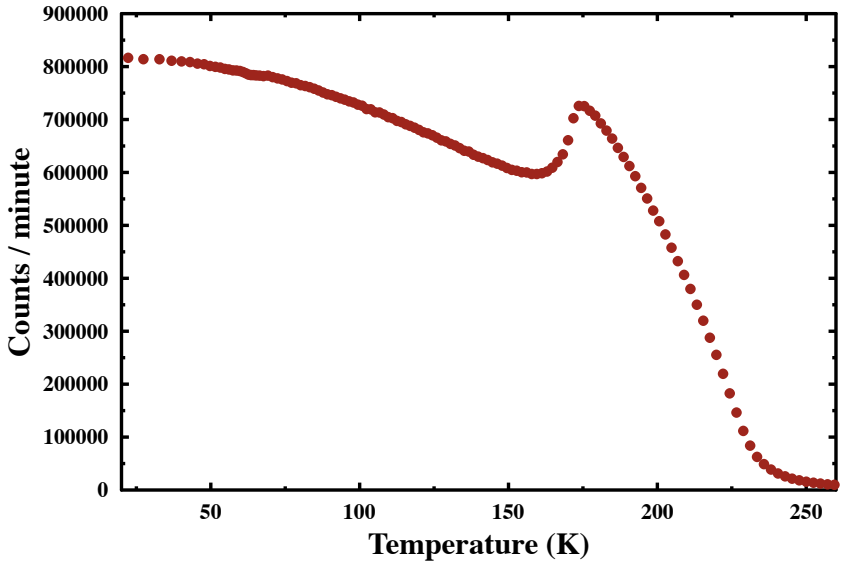

Figure 7.7: Temperature scan at the magnetic (-1/3, 2/3, 0) position showing the magnetic transition at 240 K and the build up of the broad component at 176 K.

Large, single-grain crystals of $LuFe_2O_4$ are hard to grow so many trial runs were needed. A large number of crystals were screened on the Orient Express Laue diffractometer at the ILL to identify crystals containing one single grain. Eventually a very

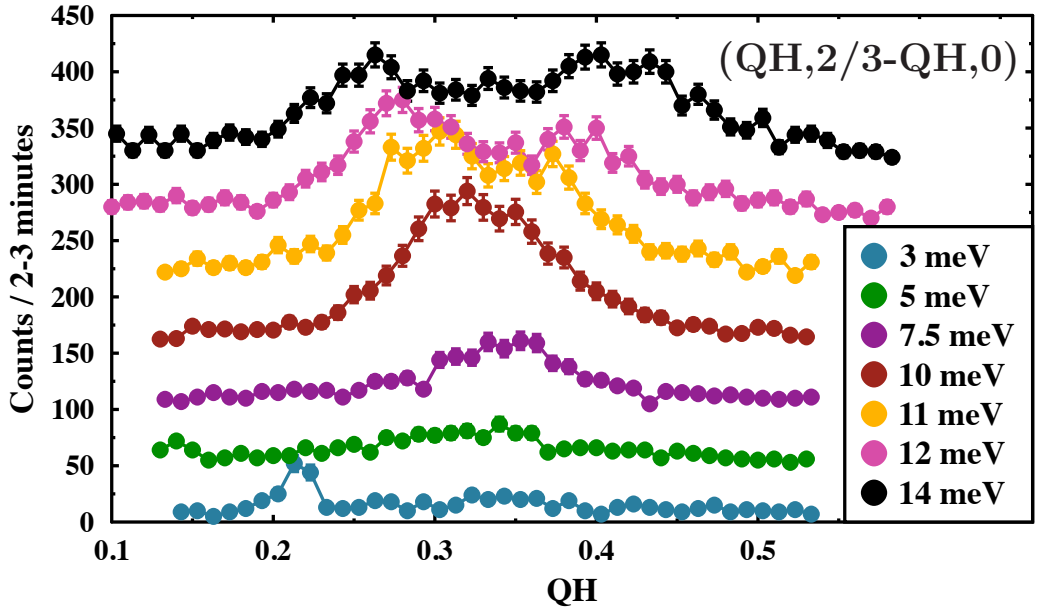

Figure 7.8: Inelastic scattering recorded on IN22. The conical spin waves are seen dispersing from the position (1/3, 1/3, 0) with the scans taken along the (1/3+x, 1/3-x, 0) direction. The QH values are therefore the (QH, 2/3-QH, 0) positions. The scans are displaced vertically by 50 counts. Each point was collected for 2-3 minutes at 10 K.

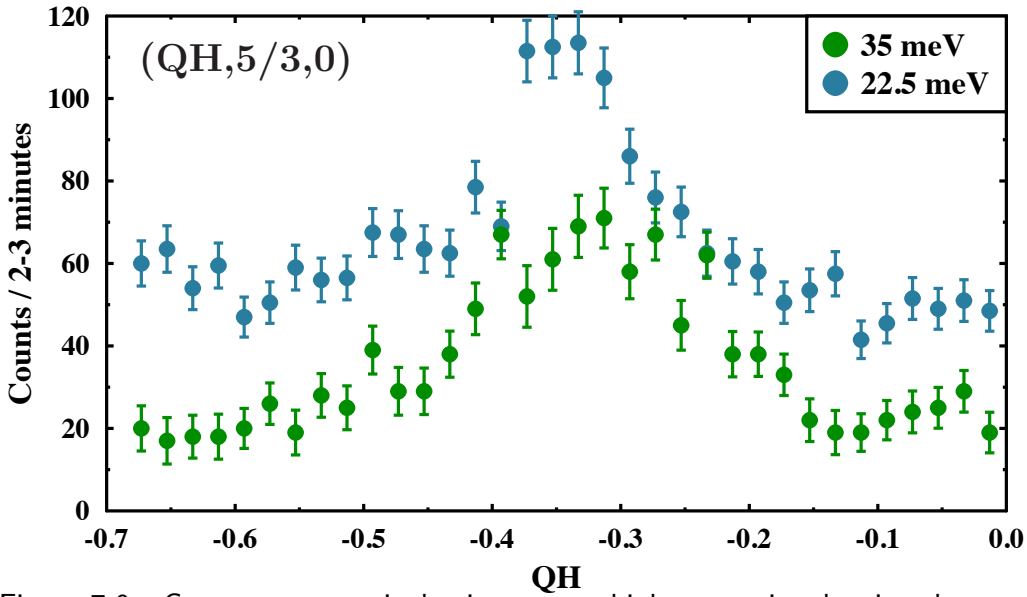

Figure 7.9: Constant-energy inelastic scans at higher energies showing the presence of a second dispersive feature along the same symmetry direction as seen in Figure 7.8. The dispersion is from the (-1/3, 5/3, 0) position with the scans made along the (-1/3+x, 5/3, 0) direction at 10 K. A feature persisted to at least 35 meV. The scans are displaced vertically.

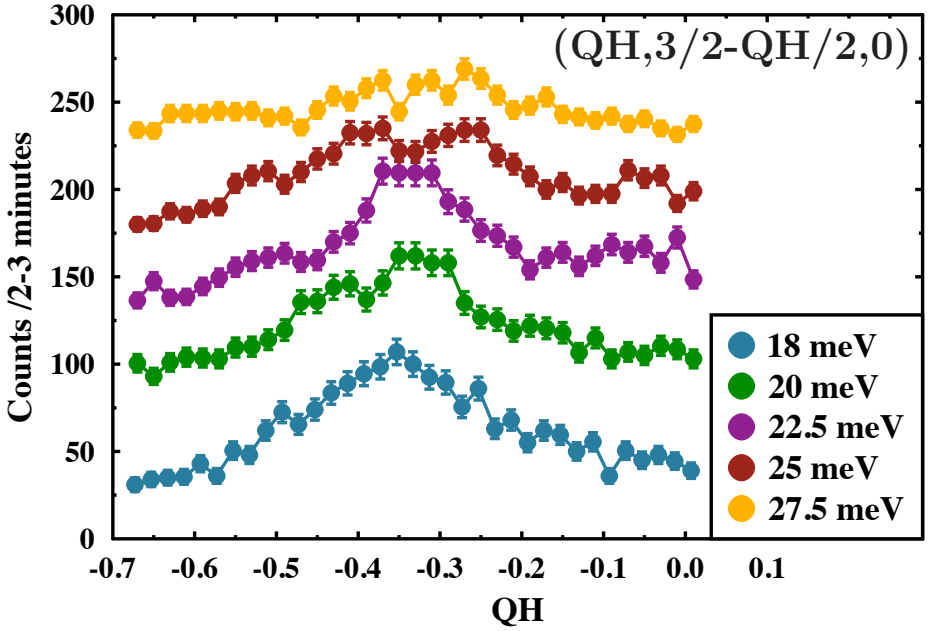

Figure 7.10: Constant-energy inelastic scans along the direction (-1/3+x, 5/3-x/2, 0) at 10 K. The conical spin waves are seen dispersing along this symmetry direction as well. The dispersion is from the (-1/3, 5/3, 0) position. The scans are displaced vertically.

high quality crystal of mass 0.35 g was found. Experiments were performed on IN22 with a fixed k_f=2.662 Å^{-1} selected by a graphite analyser. The crystal was aligned with (h, k, 0) as the horizontal scattering plane.

Figure 7.7 shows the magnetic ordering transition around 240 K as determined by the intensity measured at the (-1/3, 2/3, 0) position while the sample was cooled. The magnetic position was carefully aligned then the counts per minute recorded, at what had been found as the peak centre, this was not an integrated intensity. A broadening of the magnetic reflections is seen at 176 K where there is a build up of the diffuse component of the magnetic scattering [5]. 176 K is also the onset temperature of the charge fluctuations suggesting that the magnetic feature at this point quenches the charge fluctuations. This result has been corroborated by hexagonal c-axis magnetization experiments [5]. It appears that the basic charge ordering configuration remains the same on cooling through 175 K and the correlation along the hexagonal c-axis is improved by about 7 % compared to at 200 K [9]. This suggests that the charge ordering is better established below 175 K.

Figure 7.8 shows the inelastic scans along the symmetry direction (1/3+x, 1/3-x, 0). This direction is described as that connecting the Γ and K points of the Brillouin zone as described in Figure 7.1. The scans were performed at 10 K. The conical spin

wave is seen dispersing from the magnetic Bragg position. A peak forms at QH=1/3 and then separates into two peaks and moves away from the 1/3 position. The traces at different energies have been displaced by 50 counts/2-3 minutes for clarity.

Figure 7.9 shows scans in the same symmetry direction as in Figure 7.8 however the spin wave is dispersing from the point (-1/3, 5/3, 0) which was necessary for the higher energy scans. The direction of the scans was (-1/3+x, 5/3, 0) between the Γ and K points . It shows the presence of a second dispersive feature at higher energies along the same symmetry direction as seen in Figure 7.8. The presence of higher energy features has been backed up by theoretical calculations described later in this chapter.

Figure 7.10 shows constant energy scans in a different symmetry direction, (-1/3+x, 5/3-x/2, 0), but dispersing from the same position as seen in Figure 7.9, (-1/3, 5/3, 0). This direction could be described as heading between the Γ and M points of the Brillouin zone as described in Figure 7.1. The conical spin wave dispersion is seen again with a peak forming at QH=-1/3 then diverging into two peaks at higher energies. A higher energy mode than that in Figure 7.8 is observed.

These measurements proved that spin wave dispersions can be measured in $LuFe_2O_4$. The spin waves have been seen to disperse along different symmetry directions of the Brillouin zone. It is clear that the spin excitations extend to much higher energies than was possible to probe in this experiment. The continuation of these scans to higher energies would be an opportunity for further work.

7.3.3 FlatCone Neutron Experiments

Experiments were performed at the ILL on the instruments IN8 and IN20 with the FlatCone secondary spectrometer. The multidetector set-up of the FlatCone instrument is described in Section 2.3.2. The bank of detectors can be used to obtain large maps of reciprocal space. The experiments were performed with silicon as the analyser and k_f=3.0 Å^{-1}. The crystal was aligned with (h, k, 0) as the horizontal scattering plane. The lifting capabilities of the detector bank meant it was possible to also vary the l coordinate. The crystal was mounted in a helium cryostat. All of the scans were made at 10 K.

Figures 7.11–7.18 are constant-energy maps of the scattered intensity measured by rotating the sample through a range of angles in 0.5° steps. The hexagonal symmetry of the magnetic peaks can be observed as can their dispersion as the maps reach higher

energies. The circles indicating the positions have to be enlarged to encapsulate the expanding dispersion. Longitudinal and transverse phonon dispersions are also clearly seen. Aluminium powder lines from the cryostat have been subtracted in a way that aims not to affect any underlying feature. However the remnants of the lines can be seen and are indicated in some of the figures. Unfortunately the powder lines do lie over two of the magnetic positions. Spurions can be seen in all of the scans as extremely intense sharp points.

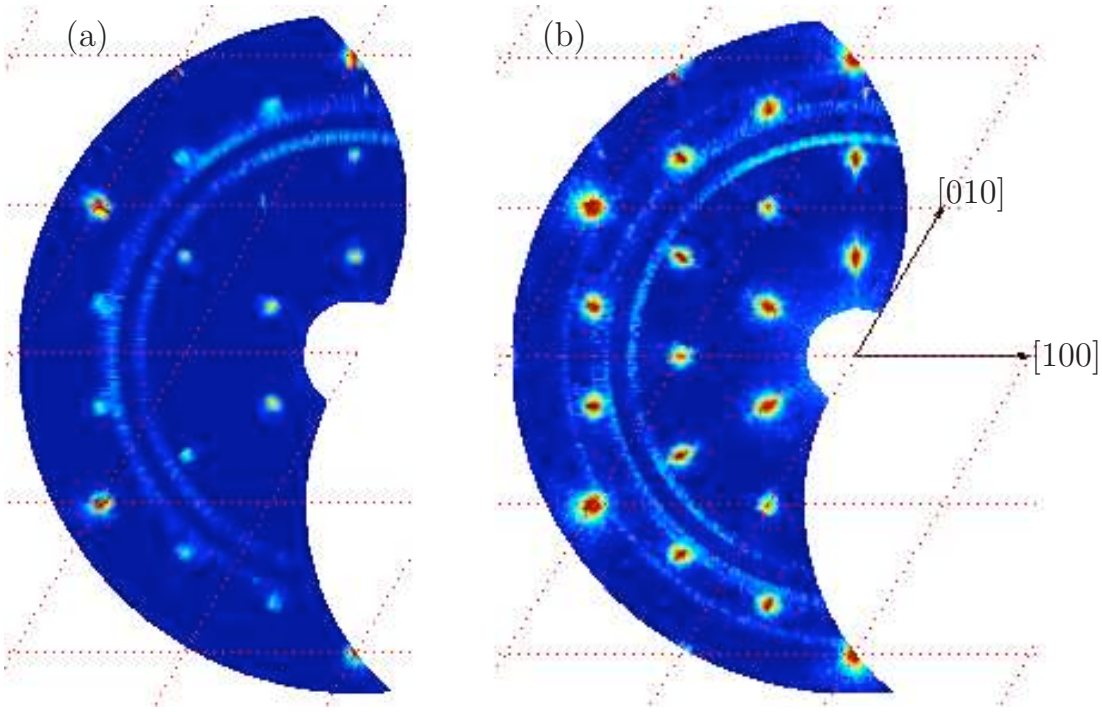

Figure 7.11: The 0 meV FlatCone map at room temperature (a) and 10 K (b). The intensity of the peaks is observed to greatly increase with the decrease in temperature. The scans were made at $l = 0$.

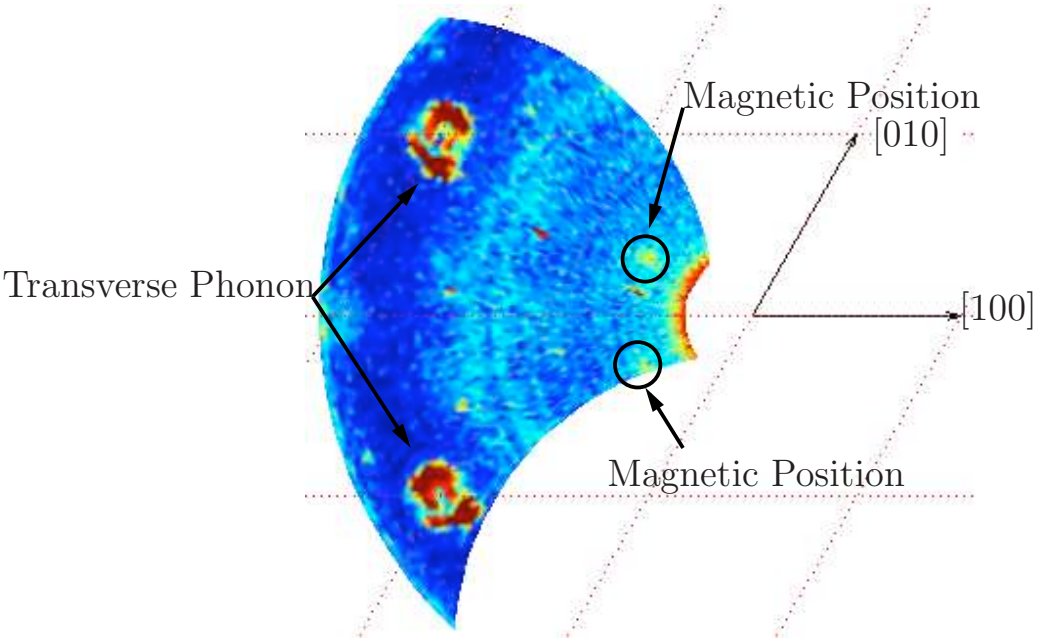

Figure 7.12: 5 meV FlatCone results showing magnetic scattering at (1/3, 1/3, 0)-type positions. The Al powder lines make some of the magnetic positions hard to distinguish. Phonons are also seen at the (-2, 1, 0)-type positions. The transverse and longitudinal components are hard to distinguish. The scans were made at $l = 0$.

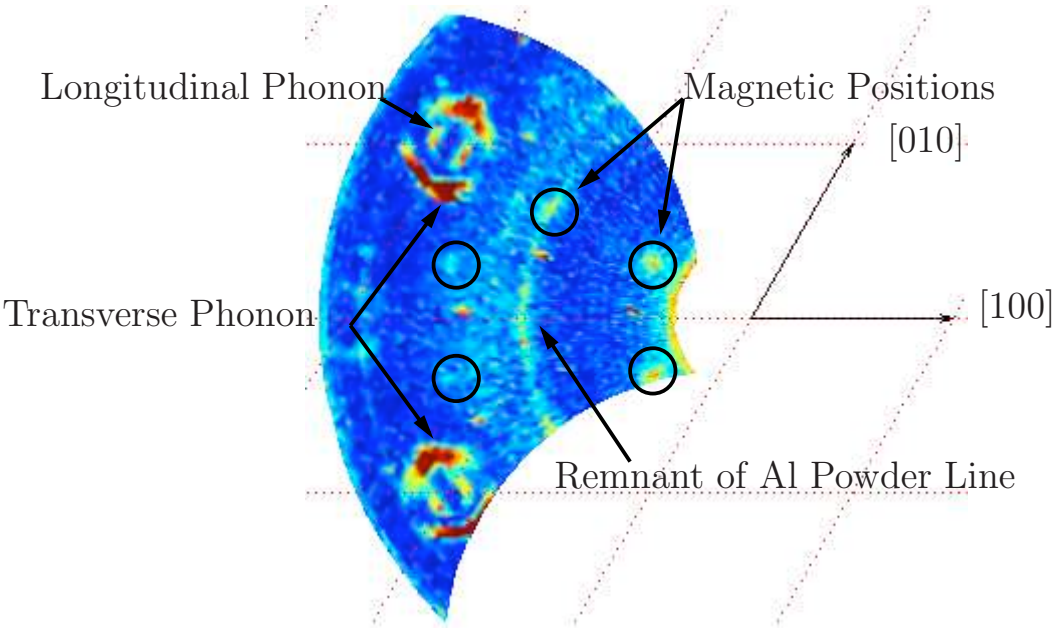

Figure 7.13: 7.5 meV FlatCone results showing clearer (1/3, 1/3, 0)-type position magnetic peaks than were seen for 5 meV. They also appear larger as they are dispersing away from the magnetic Bragg position. The longitudinal and transverse components of the phonon are now easy to distinguish. The scans were made at $l = 0$.

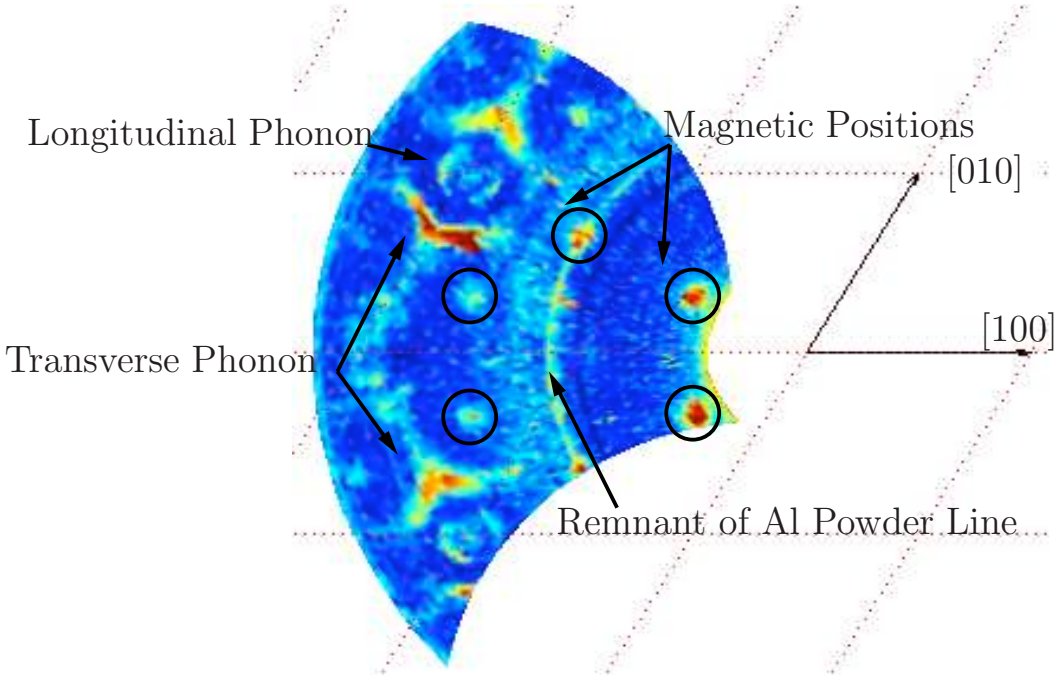

Figure 7.14: 10 meV FlatCone results showing the dispersion from the magnetic Bragg positions as higher energies are reached. The phonon has dispersed even further from the nuclear position. The scans were made at $l = 0$.

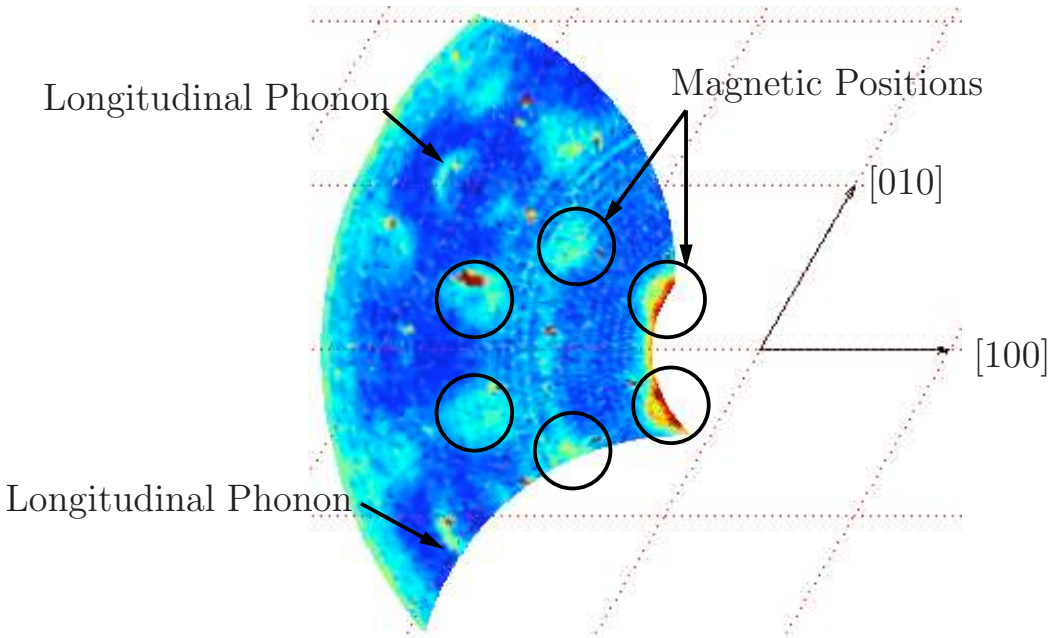

Figure 7.15: 15 meV FlatCone results showing the conical dispersion of the magnetic peaks. The arcs around the (1/3, 1/3, 0)-type positions can be seen at the positions closest to the origin. Only the longitudinal component of the phonon remains observable at this energy. The scans were made at $l = 0$.

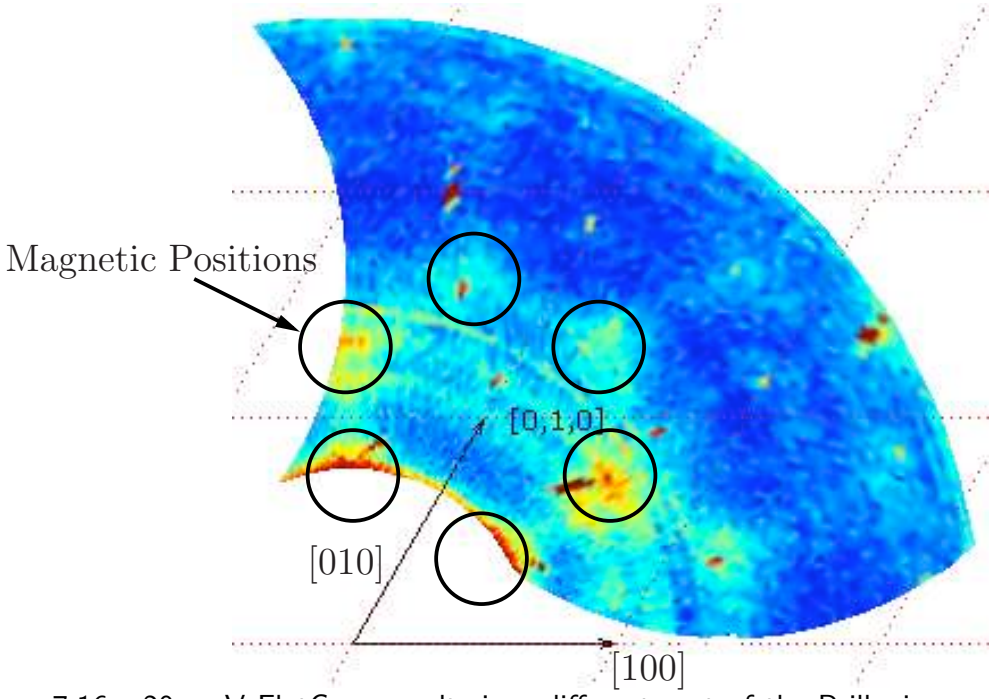

Figure 7.16: 20 meV FlatCone results in a different part of the Brillouin zone and at $l = 2$. The magnetic positions are still very clear although they are considerably more dispersed than at lower energies. The magnetic points are stronger at 20 meV in an $l = 2$ scan than an $l = 0$ scan.

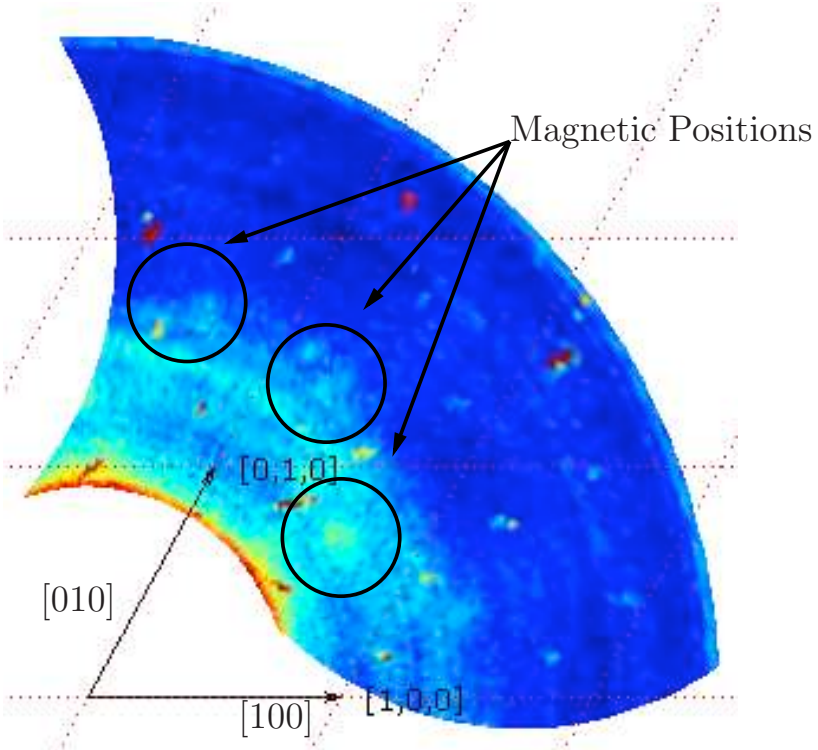

Figure 7.17: 25 meV FlatCone results at $l = 2$. The magnetic peaks are now not as clear as they have dispersed out much further. The higher energy scans were made at $l = 2$. The magnetic points are stronger at 25 meV in a $l = 2$ scan than an $l = 0$ scan.

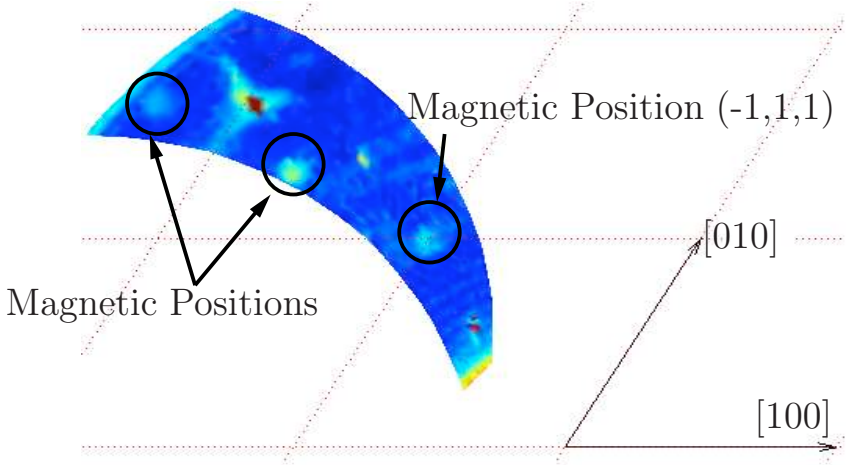

Figure 7.18: 10 meV FlatCone results showing the (-1,1,0)-type magnetic position where $l = 1$.

Dispersion data can be extracted from the maps by defining cuts along particular directions. Even though the original data points may not lie on a straight line in **Q**-space a 1-D scan can be extracted from the data. This can be done in three ways, by interpolation, integration and projection. Although all the methods were trialled the data was eventually extracted using an interpolation method.

Constant energy maps at 0 meV are shown in Figure 7.11. The increased intensity of the peaks when the temperature is decreased from room temperature to 10 K is observed.

The extraction of the 1-D cuts has been used to follow the spin wave dispersion and phonons. A phonon is observed dispersing from the (-2,1,0) and (-1,-1,0) positions. At 5 meV the longitudinal and transverse components are harder to distinguish than at higher energies where they can be individually seen dispersing from the nuclear positions. The phonons have not been seen in the higher energy scans. The magnon dispersion at the (1/3, 1/3, 0)-type positions is seen in all of the maps however the magnetic position (-1,1,0) cannot be observed in most of them. This was remedied by moving to $l = 1$ where the position can be more clearly observed, Figure 7.18. The (1/3, 1/3, 0)-type positions are also observed at $l = 1$, Figure 7.18.

7.4 Analysis and Discussion

7.4.1 Spin Wave Dispersion Analysis

The spin wave spectrum has been calculated from the spin Hamiltonian

$$\mathcal{H} = -\frac{1}{2}\sum_{ij} J_{ij}\mathbf{S}_{iz}\cdot\mathbf{S}_{jz}, \tag{7.1}$$

where J_{ij} are the spin exchange parameters between spin sites i and j, and $\mathbf{S}_{jz}$ is the spin component along the c direction. There are 15 possible superexchange (SE) (nearest neighbour) interactions, occurring both in and between the layers, and 19 super-superexchange (SSE) (next-nearest neighbour) interactions where the O...O distances are shorter that 3.2 Å .

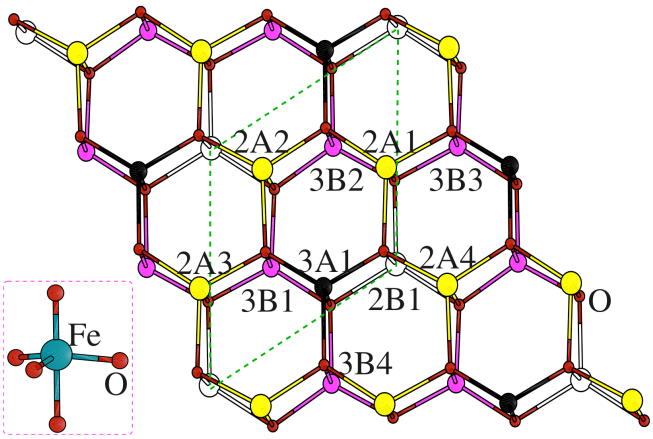

Figure 7.19: Schematic of $LuFe_2O_4$ structure [27] depicting the ions corresponding to the exchange interactions, Table 7.1. In the A layer the yellow and black circles represent the Fe^{2+} and Fe^{3+} ions respectively. In the B layer the white and pink circles represent the Fe^{2+} and Fe^{3+} ions respectively. The red circles represent the O^{2-} ions. The green dashed line shows the unit cell of the charge ordered structure.

The interactions are described by the designation of the layer, the value of the charge and the site as seen in Figure 7.19. A is designated as the layer with an Fe^{3+} ion at the centre of each Fe^{2+} ion hexagon and B is the layer with the opposite arrangement. The SE inter-layer interactions are weaker than the SE intra-layer interactions. The SSE interactions are generally much weaker than the SE interactions. Ab initio calculations by Xiang *et al.* found all the SSE interactions to be less than 1.4 meV [27]. Table 7.1 shows the 15 calculated superexchange interactions.

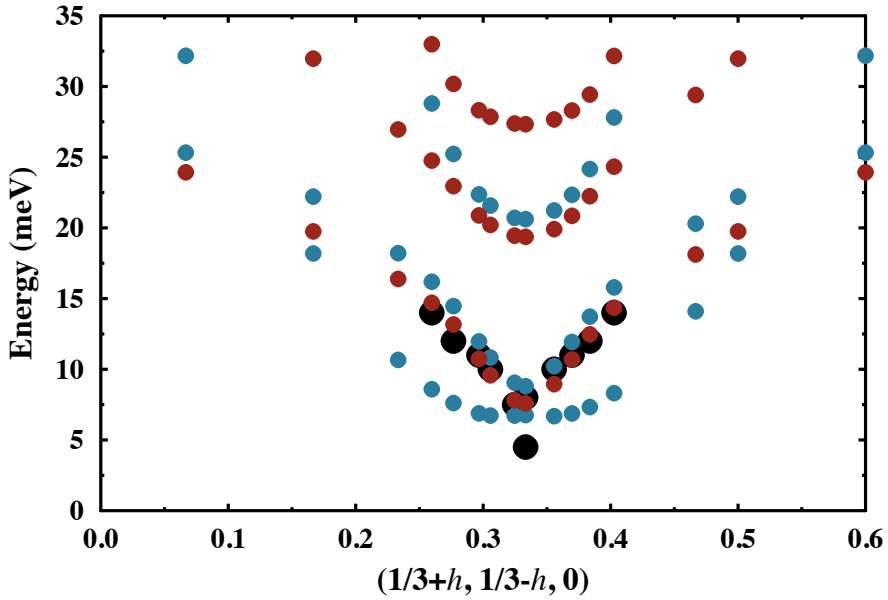

Figure 7.20: Scans taken along the edge of a Brillouin zone. Black points are the fitted experimental data. Fit 1 is shown in red and Fit 2 is shown in blue. The blue points are from the calculated exchange parameters given in this chapter.

The calculations in this chapter were carried out with the McPhase package as described in Chapter 4. The anisotropy was constrained to vary by no more than $\pm$0.5 meV from the starting values of B20=-1.5 meV for Fe^{2+}, and B20=0 meV for Fe^{3+}. All the interactions within the layers are antiferromagnetic. The results from this study and those of Xiang *et al.* [27] are consistent in finding the interlayer interaction $J_{2A1-3B2}$ to be ferromagnetic. There is also a general agreement between the size of the interactions, Table 7.1. When compared to the data our calculation showed a much closer agreement than was seen when the ab initio values of Xiang *et al.* [27] were compared to the data. The ab initio values are said to have an error of 7 % however giving errors on the exchange parameters found from fitting the neutron data would not be realistic at this stage. This was the best fit that could be found however it is only a preliminary fit as the data is limited. It may be that another set of parameters will give a better fit once a more complete set of data is available.

Two good fits to our experimental data were found, with Fit 1 having a higher standard deviation than Fit 2. The following Figures 7.20, 7.21 and 7.22 show the data and fits along several directions, and show why the parameters in Table 7.1 (Fit 2) have been chosen. The difference between the calculations is in the way in which the fitting is manipulated. Fit 1 is shown in red and Fit 2 in blue.

Figures 7.20 and 7.21 show the dispersion along the directions (1/3+h, 1/3-h, 0)

Table 7.1: Calculated Superexchange Parameters. The top section gives interactions within the A layer, the middle section interactions within the B layer and the lower section the interactions between the layers.

Exchange Interaction	Fit 2-blue (meV)	Xiang Results (meV)
$J_{3A1-2A1}$	-4.43	-6.4
$J_{3A1-2A2}$	-7.60	-8.0
$J_{3A1-2A3}$	-13.77	-9.4
$J_{2A1-2A2}$	-4.79	-3.8
$J_{2A1-2A4}$	-10.52	-7.2
$J_{3B1-3B2}$	-12.18	-14.0
$J_{3B1-3B4}$	-13.41	-15.2
$J_{2B1-3B1}$	-1.07	-3.0
$J_{2B1-3B2}$	-5.68	-5.6
$J_{2B1-3B3}$	-6.27	-2.6
$J_{3A1-3B1}$	-3.35	-4.0
$J_{3A1-2B1}$	-5.39	-3.8
$J_{2A1-2B1}$	$+0.45$	~ 0
$J_{2A1-3B2}$	$+2.08$	$+1.2$
$J_{2A1-3B3}$	-1.08	-2.4

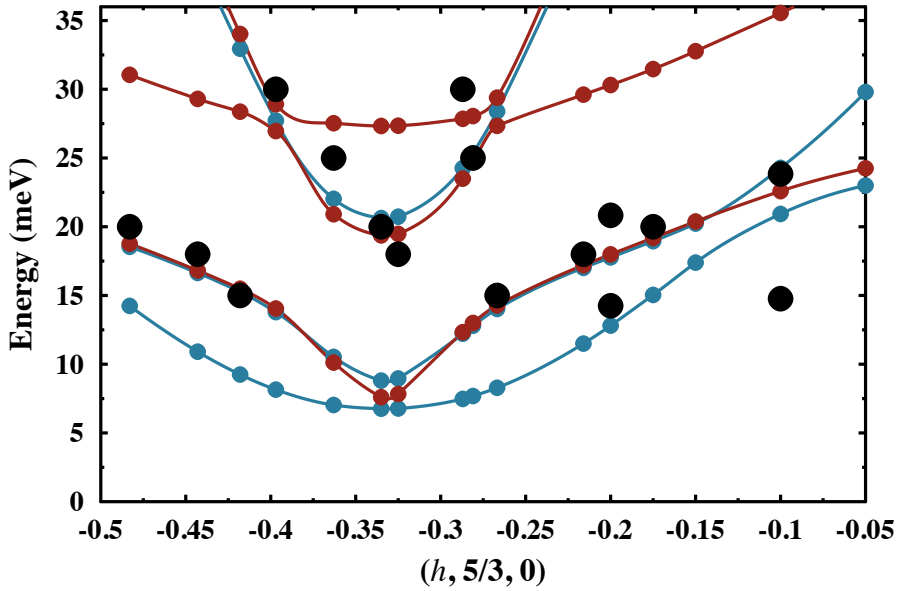

Figure 7.21: Scans performed along the edge of a Brillouin zone. Black points are the fitted experimental data. Fit 1 is shown in red and Fit 2 is shown in blue. The blue points are from the exchange parameters given in this chapter.

and $(h, 5/3, 0)$ respectively. They are both scans heading between the Γ and K points of the Brillouin zone as described in Figure 7.1. The fits show a good agreement to the data but there is definite ambiguity as to which calculation represents the data in a more comprehensive way. Fit 1 has one mode at energies below 15 meV whereas Fit 2 has two lower energy modes.

A direction was sought that allowed the fits to be more thoroughly examined. The upper panel in Figure 7.22 shows the experimental and two calculated dispersions along the direction $(0, k, 0)$. The black points are the experimental data and the red and blue points are Fits 1 and 2 respectively. Fit 2 has two modes in the energy range of the two peaks seen in Figure 7.22. Fit 1 however only has one mode in this range with the next mode at around 35 meV. Figure 7.22 shows an energy scan at (0, 1.5, 0) where the blue line is a fit of the data to 2 Lorentzian functions. Two peaks can clearly be distinguished and the scan was very repeatable. This appears to be a good way to evaluate which calculation is closer to the experimental dispersion. It allows Fit 2 to be considered the more accurate representation.

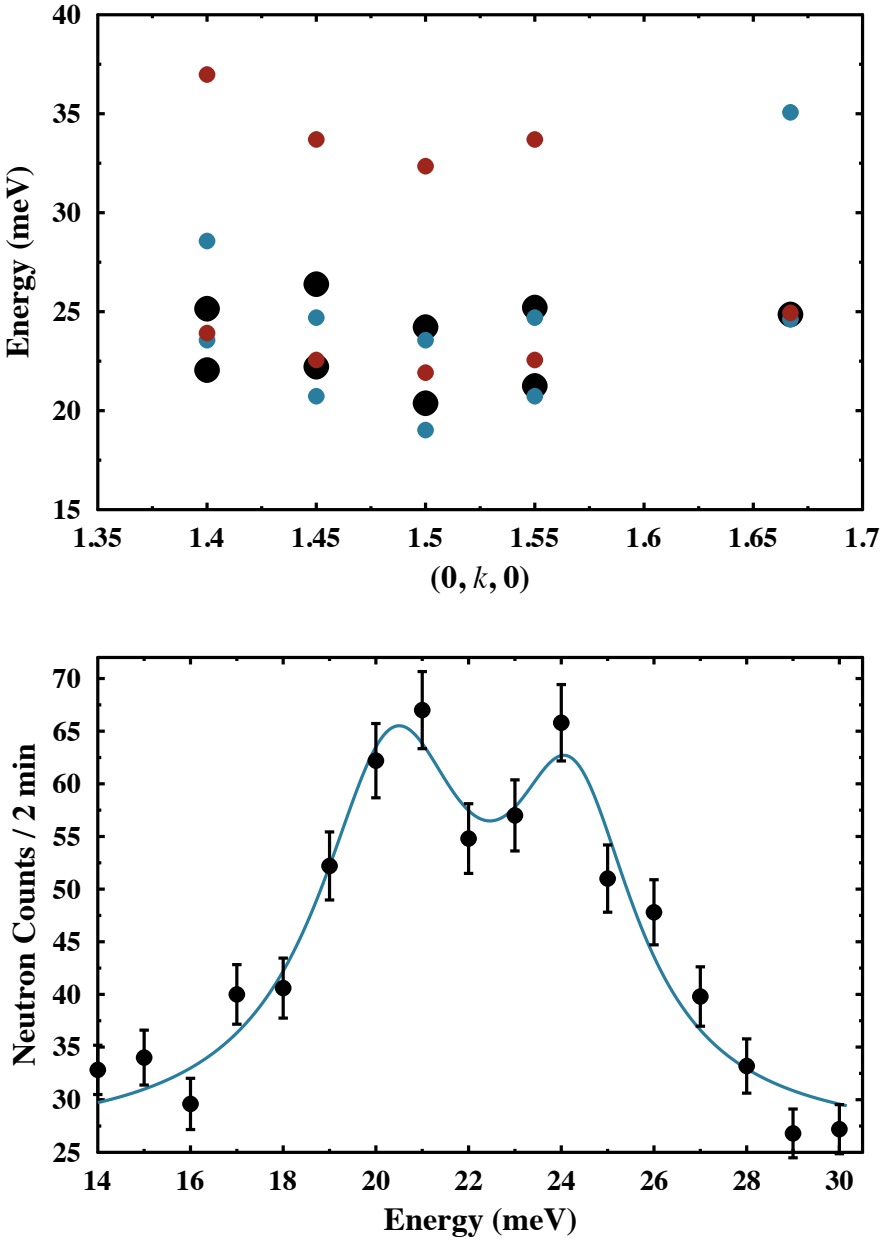

Figure 7.22: The upper panel shows scans taken along the edge of a Brillouin zone along (0, k, 0). Black points are the fitted experimental data. Fit 1 is shown in red and Fit 2 is shown in blue. The blue points correspond to the exchange parameters given in this chapter. The lower panel shows a scan performed along the edge of a Brillouin zone at (0, 1.5, 0). Black points are the fitted experimental data. The blue line is a fit to 2 Lorentzian functions.

7.4.2 Phonon Dispersion Analysis

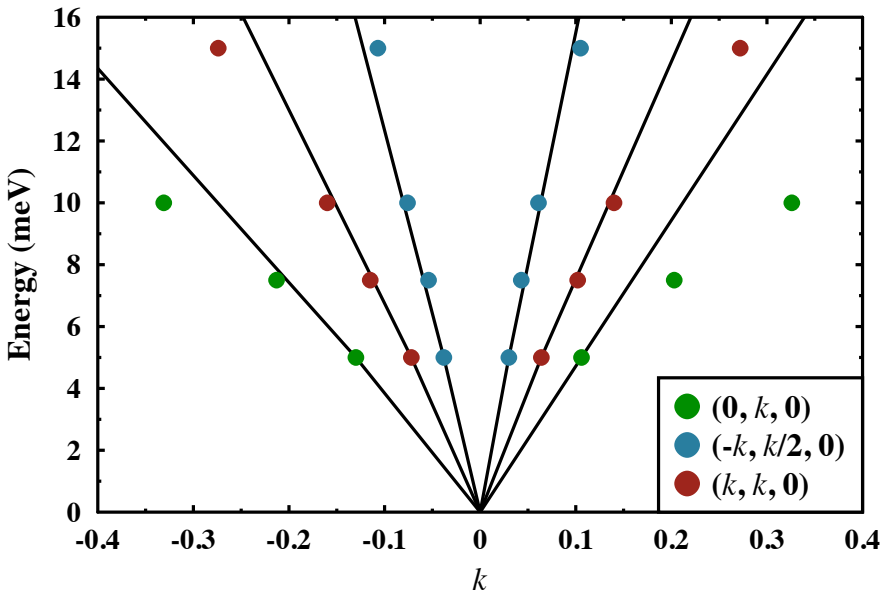

Figure 7.23: Phonon dispersion taken from the FlatCone maps at the (-2, 1, 0) position along three symmetry directions.

The dispersion of the phonon seen in the FlatCone figures is shown in Figure 7.23 along three symmetry directions. The dispersion becomes non-linear at different rates. These results have also been used to identify signals that are a result of phonons in the IN22 triple axis scans. This is extremely useful as it ensures peaks are not erroneously attributed to the spin wave dispersion. The phonon disperses out of the (-2, 1, 0)-type position. The (0, k, 0) points show the dispersion of the transverse phonon and the (-k, k/2, 0) points show the dispersion of the longitudinal phonon. The (k, k, 0) points show a mix of both phonons.

7.4.3 Further Work

The results presented in this chapter should be considered as initial work in a study into $LuFe_2O_4$. The spin wave dispersion should now be followed in greater detail and to higher energies. The initial fit from the data in the chapter provides a map for future experiments to follow. More results at relevant positions will allow the exchange parameters to be determined more accurately. Additional impedance spectroscopy work would involve applying magnetic fields to see the magnetoelectric effect on the capacitance. The apparatus was constructed with these measurements in mind.

7.5 Conclusions

The impedance spectroscopy measurements, taken with purpose built apparatus, have shown the ferrimagnetic ordering transition of $LuFe_2O_4$ as a discontinuity in the capacitance of the sample. This is the first time this transition has been observed with this technique. Multidetector elastic and inelastic neutron scattering measurements on a single crystal of $LuFe_2O_4$ have been used to create constant energy maps at seven different energies at 10 K. The extraction of 1D scans from the maps coupled with the complimentary, more conventional, triple axis measurements have allowed the spin wave dispersion to be followed throughout the Brillouin zone. This meant fitting could be carried out to find the spin exchange parameters. The parameters calculated in this chapter support previous theoretical calculations [27] but have refined them based on the fitting to the neutron data. Further experiments would be needed to follow the branches to higher energies and to refine the exchange parameters.

Bibliography

[1] N. Ikeda, H. Ohsumi, K. Ohwada, K. Ishii, T. Inami, K. Kakurai, Y. Murakami, K. Yoshii, S. Mori, Y. Horibe and H. Kitôh, Nature **436**, 1136 (2005).

[2] Y. Zhang, H. X. Yang, Y. Q. Guo, C. Ma, H. F. Tian, J. L. Luo and J. Q. Li, Phys. Rev. B **76**, 184105 (2007).

[3] J. Iida, M. Tanaka, Y. Nakagawa, S. Funahashi, N. Kimizuka and S. Takekawa, J. Phys. Soc. Jap. **62**, 1723 (1993).

[4] K.-T. Ko, H.-J. Noh, J.-Y. Kim, B.-G. Park, J.-H. Park, A. Tanaka, S. B. Kim, C. L. Zhang and S-W. Cheong, Phys. Rev. Lett. **103**, 207202 (2009).

[5] A. D. Christianson, M. D. Lumsden, M. Angst, Z. Yamani, W. Tian, R. Jin, E. A. Payzant, S. E. Nagler, B. C. Sales and D. Mandrus, Phys. Rev. Lett. **100**, 107601 (2008).

[6] J. Wen, G. Xu, G. Gu and S. M. Shapiro, Phys. Rev. B **80**, 020403(R) (2009).

[7] A. Nagano, M. Naka, J. Nasu and S. Ishihara, Phys. Rev. Lett. **99**, 217202 (2007).

[8] J. van den Brink and D. I . Khomskii, J. Phys.: Cond. Matt. **20(43)**, 434217 (2008).

[9] M. Angst, R. P. Hermann, A. D. Christianson, M. D. Lumsden, C. Lee, M.-H. Whangbo, J.-W. Kim, P. J. Ryan, S. E. Nagler, W. Tian, R. Jin, B. C. Sales and D. Mandrus, Phys. Rev. Lett. **101**, 227601 (2008).

[10] Y. Yamada, K. Kitsuda, S. Nohdo, and N. Ikeda, Phys. Rev. B **62**, 12167 (2000).

[11] X. S. Xu, M. Angst, T. V. Brinzari, R. P. Hermann, J. L. Musfeldt, A. D. Christianson, D. Mandrus, B. C. Sales, S. McGill, J.-W. Kim and Z. Islam, Phys. Rev. Lett. **101**, 227602 (2008).

[12] H. J. Xiang and M.-H.Whangbo, Phys. Rev. Lett. **98**, 246403 (2007).

[13] M. Naka, A. Nagano, and S. Ishihara, Phys. Rev. B **77**, 224441 (2008).

[14] A. M. Mulders, S. M. Lawrence, U. Staub, M. Garcia-Fernandez, V. Scagnoli, C. Mazzoli, E. Pomjakushina, K. Conder and Y. Wang, Phys. Rev. Lett. **103**, 077602 (2009).

[15] N. Ikeda, K. Kohn, N. Myouga, E. Takahashi, H. Kitôh and S. Takekawa, J. Phys. Soc. Jpn. **69**, 1526 (2000).

[16] X. S. Xu, J. de Groot, Q.-C. Sun, B. C. Sales, D. Mandrus, M. Angst, A. P. Litvinchuk and J. L. Musfeldt, Phys. Rev. B **82**, 014304 (2010).

[17] T. Kambe, T. Komatsu, T. Michiuchi, H. Hayakawa, D. Ohishi, N. Hanasaki, K. Yoshii and N. Ikeda, Journal of Physics: Conference Series **200**, 012077 (2010).

[18] C.-H. Li, F. Wang, Y. Liu, X.-Q. Zhang, Z.-H. Cheng and Y. Sun, Phys. Rev. B **79**, 172412 (2009).

[19] T. Kimura, T. Goto, H. Shintani, K. Ishizaka, T. Arima and Y. Tokura, Nature **426**, 55 (2003).

[20] N. Hur, S. Park, P. A. Sharma, J. S. Ahn, S. Guha and S-W. Cheong, Nature **429**, 392 (2004).

[21] J. Hemberger, P. Lunkenheimer, R. Fichtl, H.-A. Krug von Nidda, V. Tsurkan and A. Loidl, Nature **434**, 364 (2005).

[22] N. Ikeda, J. Phys.: Condens. Matter **20**, 434218 (2008).

[23] C.-H. Li, X.-Q. Zhang, Z.-H. Cheng and Y. Sun, Appl. Phys. Lett. **92**, 182903 (2008).

[24] M. A. Subramanian, T. He, J. Chen, N. S. Rogado, T. G. Calvarese and A. W. Sleight, Adv. Mater. **18**, 1737 (2006).

[25] J. Wen, G. Xu, G. Gu and S. M. Shapiro, Phys. Rev. B **81**, 144121 (2010).

[26] K.Yoshii, N. Ikeda, Y. Matsuo, Y.Horibe and S.Mori, Phys. Rev. B **76**, 024423 (2007).

[27] H. J. Xiang, E. J. Kan, S.-H. Wei, M.-H.Whangbo and J. Yang, Phys. Rev. B **80**, 132408 (2009).

List of Publications

- Magnetic excitations in multiferroic $LuMnO_3$ studied by inelastic neutron scattering
  H. J. Lewtas, A. T. Boothroyd, M. Rotter, D. Prabhakaran, H. Müller, M. D. Le, B. Roessli, J. Gavilano and P. Bourges, Phys. Rev. B **82**, 184420 (2010).

- Local magnetism and magnetoelectric effects in $HoMnO_3$ studied with muon spin relaxation
  H. J. Lewtas, T. Lancaster, P. J. Baker, S. J. Blundell, D. Prabhakaran and F. L. Pratt, Phys. Rev. B **81**, 014402 (2010).

For the work on $LiFeSi_2O_6$ and $NaFeSi_2O_6$ I was heavily involved in all aspects of the experiment and analysis.

- Muon-spin relaxation and heat capacity measurements on the magentoelectric and multiferroic pyroxenes $LiFeSi_2O_6$ and $NaFeSi_2O_6$
  P. J. Baker, H. J. Lewtas, S. J. Blundell, T. Lancaster, I. Franke, F L. Pratt, L. Bohatý and P. Becker, Phys. Rev. B **81**, 214403 (2010).

For the following publications I performed the experiments with other members of the group and helped to conduct the initial analysis.

- Spin freezing and dynamics in $Ca_3Co_{2-x}Mn_xO_6$ (x = 0.95) investigated with implanted muons: disorder in the anisotropic next-nearest neighbor Ising model
  T. Lancaster, S. J. Blundell, P. J. Baker, H. J. Lewtas, W. Hayes, F. L. Pratt and H. T. Yi, Phys. Rev. B **80**, 020409 (2009).

- Enhancement of Superfluid Stiffness, Suppression of Superconducting Tc and Field-induced Magnetism in the Pnictide Superconductor LiFeAs
  F. L. Pratt, P. J. Baker, S. J. Blundell, T. Lancaster, H. J. Lewtas, P. Adamson, M. J. Pitcher, D. R. Parker and S. J. Clarke, Phys. Rev. B **79**, 052508 (2009).

- Determination of characteristic muon precession and relaxation signals in FeAs and $FeAs_2$, possible impurity phases in pnictide superconductors
  P. J. Baker, H. J. Lewtas, S. J. Blundell, T. Lancaster, F. L. Pratt, D. R. Parker, M. J. Pitcher and S. J. Clarke, Phys. Rev. B **78**, 212501 (2008).